University of Nevada, Reno

Electrocatalytic Oxygen and Nitrate Reduction Reactions Using Cu-Based Electrodes

A dissertation submitted in partial fulfillment of the

requirements for the degree of Doctor of Philosophy in

Chemistry

by

Profulla Mondol

Dr. Christopher J. Barile/Dissertation Advisor

May, 2024

THE GRADUATE SCHOOL

We recommend that the dissertation
prepared under our supervision by

Profulla Mondol

entitled

Electrocatalytic Oxygen and Nitrate Reduction Reactions Using Cu-Based Electrodes

be accepted in partial fulfillment of the
requirements for the degree of

Doctor of Philosophy

Christopher J. Barile
Advisor

Matthew J. Tucker
Committee Member

Nicholas Borotto
Committee Member

Paul Brett
Committee Member

M. Rashed Khan
Graduate School Representative

Markus Kemmelmeier, Ph.D., Dean
Graduate School

May, 2024

Abstract

There has been a resurgence of interest in electrocatalysis because interesting chemistry frequently happens at the electrochemical interface between electrodes and electrolytes that are relevant to energy conversion processes. The focus of this dissertation is on the electrocatalytic reduction of oxygen (O_2) and nitrate (NO_3^-) to water (H_2O) and ammonia (NH_3), respectively, using molecular- and surface-based Cu electrocatalysts. The oxygen reduction reaction (ORR) is important due to its application in the cathode of fuel cells. The nitrate reduction reaction (NRR) can be used to generate NH_3 as an alternative to the traditional Haber-Bosch process.

The first part (chapter 1) of this thesis discusses the importance of electrocatalysis in the field of energy conversion and storage technologies.

The second part of this thesis (chapters 2 and 3) focusses on the ORR. Due to the high reduction potential and slow kinetics of the ORR, fuel cells are not being fully commercialized. This part discusses efforts to understand the ORR reaction mechanism and develop new ORR electrocatalysts using Cu tripeptide complexes. Laccase is a well-known Cu-containing ORR enzyme with a low overpotential, but it is only stable in a narrow pH range. Here, we synthesized Cu-tripeptide complexes and investigated their ORR activities in a wide pH range from 2.5 to 10 and determined the effect of peptide aggregation and Cu-peptide binding constant on ORR performance. In the last parts of chapter 2 and 3, we discuss some future prospects of the ORR using non-precious Cu-based electrocatalysts.

The third part (chapters 4 and 5) of this thesis discusses the NRR. Here, we fabricated Nafion-modified metals electrodes and tested the activity of theses electrodes for the NRR to produce NH_3 electrochemically. We interrogate the mechanism of NH_3 production from NO_3^- reduction using electrochemical experiments, surface-enhanced Raman spectroscopy, and density functional theory calculations. We also explore this NO_3^- reduction reaction for Nafion-modified electrodeposited Cu electrodes to increase the current density and NH_3 Faradaic efficiency. Lastly, we discuss the future prospect of this electrocatalytic NRR using different fluoropolymers instead of Nafion and propose methods to increase the durability of the catalysts.

Acknowledgements

This dissertation would not be possible without the help of large number of people. Although I can’t mention all of them here, I am always thankful to them.

First, I want to express my gratitude to my respected PhD advisor, Professor Christopher Barile, for providing the resources to make this work possible, for encouraging me to be productive while allowing me to work at my own pace, for teaching me about research, for improving written papers, improving my verbal skills, for valuable feedback on oral presentation, and for helping sort out career options. Next, I want to thank, Professors Mathew Tucker, Professor Nicholas Borotto, Professor Paul Brett, and M. Rashed Khan for serving on my PhD committee. I am thankful for Mathew Tucker’s research group (especially Majid Hassani) and Samuel Odoh’s research group (especially Dipak panthi) for fruitful collaborations and who made several publications possible.

Members of the Barile Group made enduring the up’s and down’s of research fun (or at least tolerable, depending on the week). Former members Dr. Hanqing Pan, Shakir Islam, Rajendra Gautam, Jason Mennel, Joseph Jeanetta, Darren Miller, and Judy Li helped me to familiarize with the lab. I spent very good times with Dr. Cheon Woo Moon, who joined to the Barile group as a postdoctoral researcher in 2022-2023, in lab and outside the lab. Desmond Madu was here for the whole ride and provided motivation, friendly competition, lengthy discussions, and lots of fun. Thanks also go to current group members William Nguyen, Tania Akter, Nikhil Bhoumik, Rituparna Patra, David Stem, and Macy Hopping for continuing to provide a motivating research environment. I am thankful to all of the undergraduate students of the Barile group especially Adan Albarran, Jashmeen Thind, Caden Kuster, Quinn Padovan, Alexis Palma (former undergraduate student), Lorenzo Arvisu (former undergraduate student), Isaac Bowers (former undergraduate student), Micah Lilo (former undergraduate student), Nate Merkle (former undergraduate student), and Andrew Thompson (former undergraduate student) for talking about research and giving me some beautiful memories. I am also thankful to Tanzil Mahmud (graduate student from Jeffery research group), who help me a lot during my class tests.

I want to thank the Department of Chemistry for giving me a Teaching Assistantship for first two and half years of my PhD journey. My Ph.D. degree would not be possible without this support. Also, I want to thank Dr. Munro, who was my teaching mentor for all my teaching courses and taught me how to become a good course instructor.

This research was partially supported by Research and Innovation at the University of Nevada, Reno (UNR). SEM-EDS analysis was performed in the Mackay Microbeam Laboratory at UNR, I acknowledge J. Desormeau for his kind assistance. I acknowledge the National Science Foundation for financial support through a CAREER Award under Grant No. CHE2046105 and Grant No. 18003887. I also acknowledge the Shared Instrumentation Laboratory in the Department of Chemistry at the University of Nevada, Reno (UNR). The support of the National Science Foundation (CHE-1429768) for the purchase of the powder X-ray diffractometer is gratefully acknowledged.

I want to acknowledge some of my friends: Md. Tuhinur Raham Joy, Roknuzzaman, Md. Al-Amin, Shad Ershad, and Ruhul Amin, who always believed in me and helped me travel to the USA to become a successful Ph.D. candidate. In addition, I want to thank my fellow Bangladeshi students in the UNR chemistry department: Chowdhury Raihan Bikash and Md. Azizul Islam, for their kindhearted support. I want to thank all my cricket and soccer partners: Nasif Zaman, Abrar Shariar, Tamzid Toha, Abu Sayed, Iffat Hasan, Shawon Dey, Mahadi Hassan, and Hasanul Banna who helped me to cherise my hobby in spite of the big transition from Bangladesh to the United States.

My PhD journey would not be possible without the support of my previous teachers and advisors Professor Shariff Enamul Kabir, Tapan Kumar Saha, and Ananda Kumar Ghosh from Jahangirnagar University, Bangladesh,

My beautiful wife, parents, sister and other family members provided the inspiration to start and the motivation to push on to the end. Without my parents' support, this PhD journey would have been impossible for me. I wouldn't exist without my parents.

Table of Content

List of Tables

List of Figures

Chapter One

1.1 Introduction

Fossil fuels, once acknowledged as a benefit to industrialization and modern living, now are a global problem because they are the primary drivers of increasing greenhouse gas emissions. Greenhouse gases trap heat within the Earth's atmosphere and lead to global warming. This increasing temperature causes rising sea levels, changes conditions for plants and animals, and results in more evaporation, all of which adversely affect ecosystems (Figure 1.1). Transitioning to renewable energy sources offers a sustainable solution to reducing greenhouse gas emissions. Renewable energy comes from nearly unlimited, naturally replenished resources, such as the sun, tides, and wind. About 20% of all U.S. electricity comes from the renewable energy, and this percentage is steadily growing. However, renewable energy sources produce electricity intermittently, and solar and wind production varies with weather conditions. Electrocatalysis plays a crucial role in converting this electricity into storable and transportable forms of energy.

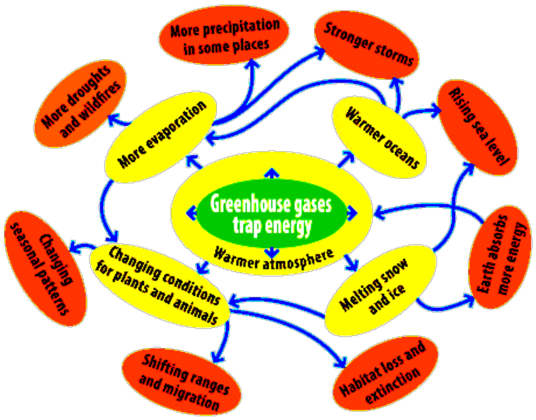

Figure 1.1: Effects of increasing greenhouse gases in the atmosphere (Source: US Environmental Protection Agency).

Electrocatalysis

Electrocatalysis is a process that involves catalysts to accelerate electrochemical reactions. Electrocatalysis has emerged as a pivotal area of research in the field of renewable energy. The electrocatalytic oxygen reduction reaction (ORR) and the nitrate reduction reaction are two important reactions in electrocatalysis. These reactions hold significant implications for both energy conversion and environmental sustainability, making them focal points in recent research.

Electrocatalytic Oxygen Reduction Reaction (ORR)

The most abundant element in the Earth's crust is oxygen. The O_2 reduction reaction (ORR) is an important reaction in energy converting systems such as fuel cells, metal air batteries, and corrosion.[1–3] The thermodynamic potential and mechanism of the ORR largely depend on the electrolytes (Table 1.1). In aqueous medium, the ORR can occur in two pathways: i) a four-electron four-proton (H^+) reduction pathway to form water (H_2O), and ii) a two-electron two-proton pathway to form hydrogen peroxide (H_2O_2). On the other hand, in non-aqueous aprotic medium, a one-electron reduction pathway can also occur to produce superoxide (O_2^-).

The ORR is the central reaction in the cathode of fuel cells. At the anode of a hydrogen (H_2) fuel cell, H_2 is oxidized to produce protons and electrons. Electrons travel to the cathode through an external circuit and generate electrical energy. Protons travel to the cathode through the electrolyte and a proton-exchange membrane to reduce O_2 (Figure 2). Fuel cells are interesting because fuel cells have the potential to extract most of the available energy from the fuels without Carnot cycle limitations. In contrast, combustion engines can extract only 20-40% the energy in fuel as the rest of the energy is lost in heating and other processes.

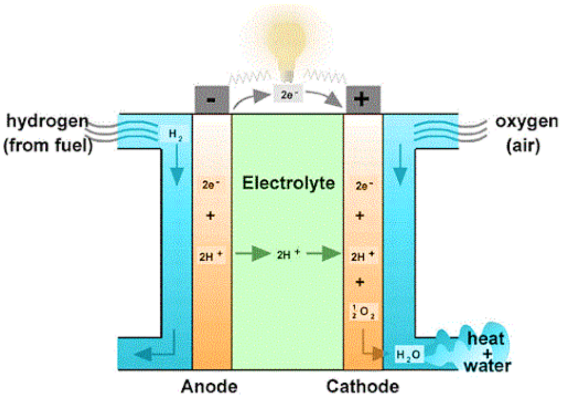

Figure 1.2: Proton exchange membrane fuel cells (PEMFCs) (https://prepp.in/news/e-492-fuel-cells-environment-notes)

Although fuel cells have been used since the 1960s in a variety of applications, there are several factors which limit the widespread use of fuel cells. One of the largest challenges is the sluggishness and high overpotential of the ORR. Due to these issues, fuel cells are not able to deliver the full 1.23 V that a H_2/O_2 fuel cell should deliver from a thermodynamic standpoint. At practical current density, fuel cells are only able to deliver 40-60% of their potential based on thermodynamic values. The origin of this high overpotential comes from the strong strength of the dioxygen double bond energy (498 kJ mol^{-1}).[4] In an attempt to overcome these limitations, catalysts are used at the cathode of fuel cells. At the current stage of fuel cell technology, platinum (Pt) or its alloys are the most applied catalysts, which have an overpotential of ~300 mV for the ORR.[5,6] Unfortunately, a large amount of Pt or Pt alloys are required for practical implication of fuel cells. Furthermore, due to issues such as catalyst durability and susceptibility towards poisoning, it is challenging to use fuel cells in commercial applications. Over the past several decades, extensive research has focused on developing alternative ORR catalysts including non-noble metal catalysts.

Table 1.1: Thermodynamic electrode potentials of electrochemical O_2 reductions[7]

Electrolyte	ORR reactions	Thermodynamic electrode potential at standard conditions, V
Acidic aqueous solution	$O_2 + 4H^+ + 4e^- \rightarrow H_2O$ $O_2 + 2H^+ + 2e^- \rightarrow H_2O_2$ $H_2O_2 + 2H^+ + 2e^- \rightarrow 2H_2O$	1.229 0.70 1.76
Alkaline aqueous solution	$O_2 + H_2O + 4e^- \rightarrow 4OH^-$ $O_2 + H_2O + 2e^- \rightarrow HO_2^- + OH^-$ $HO_2^- + H_2O + 2e^- \rightarrow 3OH^-$	0.401 0.065 0.867
Non-aqueous aprotic solvents	$O_2 + e^- \rightarrow O_2^-$ $O_2^- + e^- \rightarrow O_2^{2-}$	Values strongly depend on the solvent used

A few biological systems such as laccase enzymes show promising ORR activity with even smaller overpotential compared to Pt-based catalysts.[8] Laccases are multicopper oxidases that couple one-electron oxidation of four substrate equivalents with the four-electron reduction of dioxygen to water. The mechanism of the ORR in laccase follows a ping-pong mechanism. First, substrates are oxidized near the solvent-accessible T1 site, and then electrons transfer through protein via a Cys-His pathway to a trinuclear Cu center where the ORR takes place.[9]

Inspired by the ORR activity of laccase, researchers tested different Cu-based systems as ORR electrocatalysts including Cu complexes with porphyrins, phthalocyanines, amino-alkyl ligands, 1,10-phenanthrolines, other aromatic N-donor ligands, tris(2-pyridylmethyl)amine, and substituted triazoles.[10–15] Despite these numerous studies, the native laccase enzyme shows the best ORR catalytic activity, and replicating this activity with synthetic compounds remains elusive.

Electrochemical Nitrate Reduction reaction (NO_3RR)

The nitrogen cycle (N-cycle) is important in connecting aspects of human life with the ecosphere. On Earth, N can exist in various oxidation states, ranging from +5 (e.g., NO_3^-) to -3 (e.g., ammonia, NH_3).[16–18] Since global N circulation is being severely affected due to the use of N-containing fertilizers and chemicals in agriculture and many other fields, recently, N-containing chemistry has been a center of scientific researcher. Electrochemistry has become a promising solution to modulate the N-cycles and concomitant effects such as ground water pollution, eutrophication, and photochemical smog.[19,20]

Every year, the global production of NH_3 is around 176 million tons, making it one of the highest produced chemicals by volume.[21] NH_3 is central to the fertilizer industry and also as precursor to produce a series of N-containing chemicals including nitric acid, amino acids, urea, and organonitrogen compounds.[22] Additionally, NH_3 can be used as a clean energy carrier in fuel cells due to its high hydrogen content (17.6 wt%) and easy liquification at ambient temperature (25°C).[23,24] The current industrial technology for NH_3 production is the Haber-Bosch process in which N_2 and H_2 combine at high temperature and pressures in the presence of a Fe-based catalyst. This technology is energy intensive (1-2% of global energy consumption), and it is also responsible for substantial global CO_2 emissions (~1.5%). Besides, the conversion rate of NH_3 is very low in the Haber-Bosch process (12% single-pass conversion at 550°C and 20.3 MPa).[25,26]

Although electrochemical N_2 reduction reaction (NRR) is a promising alternative to the Haber-Bosch process, the high dissociation energy of the N≡N triple bonds (945 kJ mol^{-1}) and the low solubility of N_2 in aqueous solution decrease the efficiency of NH_3 production.[27,28] Another challenge of electrochemical N_2 reduction is the quantification of NH_3 due to low yield rate and various potential contamination from different sources.[29,30] Recently, N_2 reduction on Li electrodes has been shown to reach high Faradaic efficiency under ambient condition assisted by forming lithium nitride (Li_3N). This high efficiency is achieved in organic electrolytes, and the mechanism is not fully understood, especially at the solid-electrolyte interphase.[31]

As opposed to N_2 reduction, NO_3^- is an alternate nitrogen source for NH_3 production as NO_3^- exists ubiquitously in wastewater and polluted water. Additionally, the electrochemical nitrate reduction reaction (NO_3RR) is more kinetically favorable due to the lower N=O bond energy (204 kJ mol^{-1}) and higher solubility of NO_3^- in water.[32,33] Therefore, electrochemical NO_3RR shows higher Faradaic efficiency for NH_3 production compared to the NRR. Powered by renewable energy, NO_3RR holds the opportunity of achieving decentralized NH_3 production to lower fertilizer manufacturing costs as well as converting pollutant NO_3^- into valuable NH_3.[34]

Chapter Overview

Chapter 2: In this chapter, an amino-ferrocene modified glutathione-Cu complexes (Cu-GSH-NHFc) was synthesized in five steps for use as an ORR catalyst. Inductively coupled plasma mass spectrometry (ICP-MS) indicates that Cu binds with GSH-NHFc in 1:1 ratio. Cyclic voltammetry demonstrates that the integrated charge of Cu-GSH-NHFc under the redox waves approximately doubles compared to GSH-NHFc. This finding suggests that the redox wave with Cu is due to two electrons being transferred through the Cu^{2+}/Cu^{+} and Fe^{3+}/Fe^{2+} processes and this electron availability at the metal centers could facilitate the activation of O_2. Rotating disk electrode (RDE) and rotating ring disk electrode (RRDE) measurements demonstrate that O_2 is reduced by four electrons to H_2O at pH values between 4 and 7 in two different buffer systems.

Chapter 3: In this chapter, we synthesized four different novel tripeptide derivatives of glutathione and tested the ORR activity of the resulting Cu-tripeptide complexes (Cu-GSHAmide, Cu-NCG, Cu-ECG and Cu-QCG) using RRDE in pH range of 2.5 to 10. According to ICP-MS results, Cu binds with tripeptide by 1:1 ratio like Cu-GSH-NHFc. After investigating the ORR properties of these Cu-tripeptides complexes, we determined that the ORR activities not only depend on the structures of the tripeptides, but also on the binding constants of Cu^{2+} with peptides in the complexes as well as the orientation of the peptides on the electrode surface.

Chapter 4: In this chapter, we fabricated Nafion-modified metal electrodes for electrochemical NO_3RR to NH_3 using simple drop casting methods. Among the different electrodes tested, Cu modified with a 6 μm-thick layer of Nafion reduces NO_3^- with up to a 91% Faradaic efficiency for NH_3. X-ray photoelectron spectroscopy shows that polycrystalline Cu foils contain mostly Cu metal along with a small amount of CuO. Cross-sectional scanning electron microscopy imaging demonstrates that Nafion forms a uniform overlayer on the Cu surface, and electrochemical impedance spectroscopy experiments indicate that ions can be stored on the electrode surface due to the charge properties of the Nafion structures. Corroborating electrochemical experiments, surface-enhanced Raman spectroscopy, and DFT calculations indicate that Nafion helps to activate the N-O bonds, which drives selective NH_3 production. This Nafion-modified Cu electrode is also highly efficient at removing NO_3^- from a real groundwater sample.

Chapter 5: In this chapter, we increased the surface area of the Cu electrodes using Cu electrodeposition from electrolyte on Cu foils. The NO_3^- reduction activities of these electrodeposited Cu electrodes with and without a Nafion overlayer were tested. Atomic force microscopy and cycling voltammetry using $Ru(NH_3)_6Cl_3$ shows that the surface roughness increases with increasing electrodeposition voltages. X-ray diffraction experiments and chloride tests demonstrate that Cu(220) faces are the most active face for electrochemical NO_3^- reduction to selectively produce NH_3.

References

1. Jaouen, F.; Proietti, E.; Lef Vre, M.; Chenitz, R.; Dodelet, J. P.; Wu, G.; Chung, H. T.; Johnston, C. M.; Zelenay, P. Recent Advances in Non-Precious Metal Catalysis for Oxygen-Reduction Reaction in Polymer Electrolyte Fuel Cells. *Energy Env. Sci* **2011**, *4*, 114.

2. Li, Q.; Ning, D.; Wong, D.; An, K.; Tang, Y.; Zhou, D.; Schuck, G.; Chen, Z.; Zhang, N.; Liu, X. Improving the Oxygen Redox Reversibility of Li-Rich Battery Cathode Materials via Coulombic Repulsive Interactions Strategy. *Nat. Commun.* **2022**, *13* (1), 1123.
3. Parra-Puerto, A.; Ng, K. L.; Fahy, K.; Goode, A. E.; Ryan, M. P.; Kucernak, A. Supported Transition Metal Phosphides: Activity Survey for HER, ORR, OER, and Corrosion Resistance in Acid and Alkaline Electrolytes. *ACS Catal.* **2019**, *9* (12), 11515–11529.
4. Gewirth, A. A.; Thorum, M. S. Electroreduction of Dioxygen for Fuel-Cell Applications: Materials and Challenges. *Inorg. Chem.* **2010**, *49* (8), 3557–3566.
5. Wang, C.; Spendelow, J. S. Recent Developments in Pt–Co Catalysts for Proton-Exchange Membrane Fuel Cells. *Curr. Opin. Electrochem.* **2021**, *28*, 100715.
6. Gasteiger, H. A.; Kocha, S. S.; Sompalli, B.; Wagner, F. T. Activity Benchmarks and Requirements for Pt, Pt-Alloy, and Non-Pt Oxygen Reduction Catalysts for PEMFCs. *Appl. Catal. B Environ.* **2005**, *56* (1–2), 9–35.
7. Song, C.; Zhang, J. Electrocatalytic Oxygen Reduction Reaction. In *PEM Fuel Cell Electrocatalysts and Catalyst Layers: Fundamentals and Applications*; Zhang, J., Ed.; Springer London: London, 2008; pp 89–134.
8. Thorum, M. S.; Anderson, C. A.; Hatch, J. J.; Campbell, A. S.; Marshall, N. M.; Zimmerman, S. C.; Lu, Y.; Gewirth, A. A. Direct, Electrocatalytic Oxygen Reduction by Laccase on Anthracene-2-Methanethiol-Modified Gold. *J. Phys. Chem. Lett.* **2010**, *1* (15), 2251–2254.
9. Quintanar, L.; Stoj, C.; Taylor, A. B.; Hart, P. J.; Kosman, D. J.; Solomon, E. I. Shall We Dance? How A Multicopper Oxidase Chooses Its Electron Transfer Partner. *Acc. Chem. Res.* **2007**, *40* (6), 445–452.

10. Durand Jr, R. R.; Bencosme, C. S.; Collman, J. P.; Anson, F. C. Mechanistic Aspects of the Catalytic Reduction of Dioxygen by Cofacial Metalloporphyrins. *J. Am. Chem. Soc.* **1983**, *105* (9), 2710–2718.
11. Savy, M.; Andro, P.; Bernard, C.; Magner, G. Etude de La Reduction de l'oxygene Sur Les Phtalocyanines Monomeres et Polymeres—I. Principes Fondamentaux, Choix de l'ion Central. *Electrochimica Acta* **1973**, *18* (2), 191–197.
12. Cai, C.; Xue, K.; Xu, X.; Luo, Q. Electrocatalysis for the Reduction of O_2 and H_2O_2 Based on Complex of Copper (II) with the Tris (3-Aminopropyl) Amine and Imidazole Ligands. *J. Appl. Electrochem.* **1997**, *27*, 793–798.
13. McKenzie, C. J.; Toftlund, H.; Pietraszkiewics, M.; Stojek, Z.; Slowinski, K. Binuclear Complexes of a New Hexadentate Macrocyclic Ligand. The Crystal and Molecular Structure of $[LCu_2\,(CH_3CO_2)_2](ClO_4)_2\cdot 5H_2O$. *Inorganica Chim. Acta* **1993**, *210* (2), 143–149.
14. Thorseth, M. A.; Letko, C. S.; Rauchfuss, T. B.; Gewirth, A. A. Dioxygen and Hydrogen Peroxide Reduction with Hemocyanin Model Complexes. *Inorg. Chem.* **2011**, *50* (13), 6158–6162.
15. Thorum, M. S.; Yadav, J.; Gewirth, A. A. Oxygen Reduction Activity of a Copper Complex of 3, 5-diamino-1, 2, 4-triazole Supported on Carbon Black. *Angew. Chem. Int. Ed.* **2009**, *48* (1), 165–167.
16. Gruber, N.; Galloway, J. N. An Earth-System Perspective of the Global Nitrogen Cycle. *Nature* **2008**, *451* (7176), 293–296.
17. Canfield, D. E.; Glazer, A. N.; Falkowski, P. G. The Evolution and Future of Earth's Nitrogen Cycle. *science* **2010**, *330* (6001), 192–196.

18. Xiong, Y.; Wang, Y.; Zhou, J.; Liu, F.; Hao, F.; Fan, Z. Electrochemical Nitrate Reduction: Ammonia Synthesis and the Beyond. *Adv. Mater.* **2023**, 2304021.
19. Dimitriades, B. Effects of Hydrocarbon and Nitrogen Oxides on Photochemical Smog Formation. *Environ. Sci. Technol.* **1972**, *6* (3), 253–260.
20. Galloway, J. N.; Dentener, F. J.; Capone, D. G.; Boyer, E. W.; Howarth, R. W.; Seitzinger, S. P.; Asner, G. P.; Cleveland, C. C.; Green, P.; Holland, E. A. Nitrogen Cycles: Past, Present, and Future. *Biogeochemistry* **2004**, *70*, 153–226.
21. David, W. Ammonia: Zero-Carbon Fertiliser, Fuel and Energy Store. *Policy Brief.* **2020**.
22. Qing, G.; Ghazfar, R.; Jackowski, S. T.; Habibzadeh, F.; Ashtiani, M. M.; Chen, C.-P.; Smith III, M. R.; Hamann, T. W. Recent Advances and Challenges of Electrocatalytic N2 Reduction to Ammonia. *Chem. Rev.* **2020**, *120* (12), 5437–5516.
23. Valera-Medina, A.; Xiao, H.; Owen-Jones, M.; David, W. I.; Bowen, P. Ammonia for Power. *Prog. Energy Combust. Sci.* **2018**, *69*, 63–102.
24. Shadravan, V.; Cao, A.; Bukas, V. J.; Grønborg, M. K.; Damsgaard, C. D.; Wang, Z.; Kibsgaard, J.; Nørskov, J. K.; Chorkendorff, I. Enhanced Promotion of Ru-Based Ammonia Catalysts by in Situ Dosing of Cs. *Energy Environ. Sci.* **2022**, *15* (8), 3310–3320.
25. Wu, S.; Tsang, S. C. E. Renewable N-Cycle Catalysis. *Trends Chem.* **2021**, *3* (8), 660–673.
26. Erisman, J. W.; Sutton, M. A.; Galloway, J.; Klimont, Z.; Winiwarter, W. How a Century of Ammonia Synthesis Changed the World. *Nat. Geosci.* **2008**, *1* (10), 636–639.
27. Skulason, E.; Bligaard, T.; Gudmundsdóttir, S.; Studt, F.; Rossmeisl, J.; Abild-Pedersen, F.; Vegge, T.; Jónsson, H.; Nørskov, J. K. A Theoretical Evaluation of Possible Transition

Metal Electro-Catalysts for N 2 Reduction. *Phys. Chem. Chem. Phys.* **2012**, *14* (3), 1235–1245.

28. Wang, X.; Peng, X.; Chen, W.; Liu, G.; Zheng, A.; Zheng, L.; Ni, J.; Au, C.; Jiang, L. Insight into Dynamic and Steady-State Active Sites for Nitrogen Activation to Ammonia by Cobalt-Based Catalyst. *Nat. Commun.* **2020**, *11* (1), 653.
29. Choi, J.; Suryanto, B. H.; Wang, D.; Du, H.-L.; Hodgetts, R. Y.; Ferrero Vallana, F. M.; MacFarlane, D. R.; Simonov, A. N. Identification and Elimination of False Positives in Electrochemical Nitrogen Reduction Studies. *Nat. Commun.* **2020**, *11* (1), 5546.
30. Nielander, A. C.; McEnaney, J. M.; Schwalbe, J. A.; Baker, J. G.; Blair, S. J.; Wang, L.; Pelton, J. G.; Andersen, S. Z.; Enemark-Rasmussen, K.; Colic, V. A Versatile Method for Ammonia Detection in a Range of Relevant Electrolytes via Direct Nuclear Magnetic Resonance Techniques. *Acs Catal.* **2019**, *9* (7), 5797–5802.
31. Lazouski, N.; Schiffer, Z. J.; Williams, K.; Manthiram, K. Understanding Continuous Lithium-Mediated Electrochemical Nitrogen Reduction. *Joule* **2019**, *3* (4), 1127–1139.
32. Wu, T.; Zhang, F.; Wang, J.; Liu, X.; Tian, Y.; Chu, K. Electrochemical Reduction of Nitrite to Ammonia on Amorphous MoO_3 Nanosheets. *Dalton Trans.* **2024**, *53* (3), 877–881.
33. Beagan, D. M. *Nitrogen Oxyanion Reduction Facilitated by Earth-Abundant Transition Metals: Sifting Through the Redox States of Nitrgoen*; Indiana University, 2021.
34. Xia, R.; Overa, S.; Jiao, F. Emerging Electrochemical Processes to Decarbonize the Chemical Industry. *JACS Au* **2022**, *2* (5), 1054–1070.

Chapter Two

Four-electron Electrocatalytic O_2 Reduction by a Ferrocene-modified Glutathione Complex of Cu

2.1 Introduction.

Energy conversion technologies mediated by electrocatalysis are pivotal in transitioning to a clean and renewable energy economy.[1–7] Fuel cells (Figure 2.1A) are a promising technology that could play a critical role in this transition. Although the fuels utilized at the anode vary, the O_2 reduction reaction (ORR) occurs at the cathode in almost every fuel cell design. Through the ORR, a molecule of O_2 reacts with four protons and four electrons to yield two molecules of water. The performance of fuel cells is largely limited by the high overpotential needed to drive the ORR.[8]

Over the last forty years, a wide range of ORR electrocatalysts have been developed in an attempt to decrease the overpotential of this reaction. Pt-based materials and laccase enzymes (Figure 1.1B) are the catalysts that exhibit the lowest overpotentials.[9-12] The figure 2.1B is colour-ramped from the N-terminus (blue) to the C-terminus (red). The Cu atoms are shown as shaded spheres, with the T1 site in blue and the T3 pair in yellow. This figure (Figure 2.1B) is in divergent (wall-eyed) stereo.

However, the high cost and scarcity of Pt and the low current densities of laccases hinder their widespread use as ORR catalysts.[13-18] For these reasons, the development of stable, active, and earth-abundant ORR catalysts is an ongoing grand challenge.

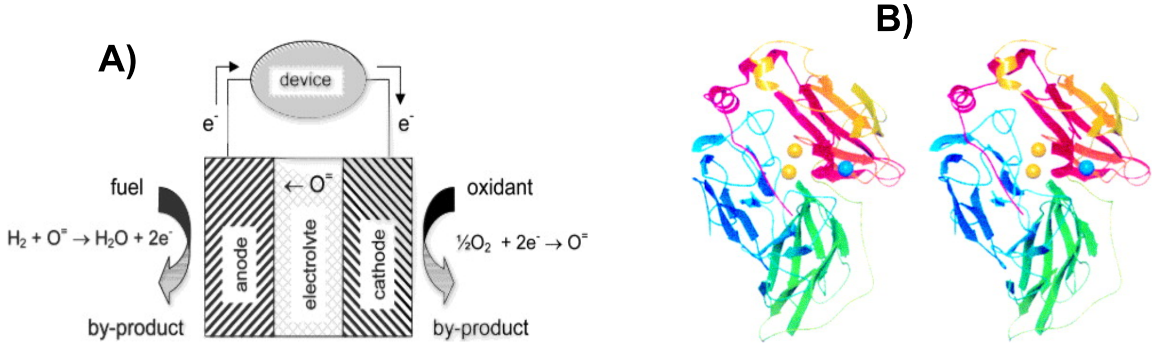

Figure 2.1: Fuel cell, comprised of an electrolyte, an anode and a cathode (A).[19] Cartoon representation of the three-dimensional structure of the Coprinus cinereus laccase (B).[20]

Non-precious metal ORR catalysts, particularly those comprised of Fe or Cu complexes with nitrogen-rich ligands, are actively being studied as practical alternatives to Pt and laccases.[21] For example, Fe complexes with porphyrins or other nitrogen-containing macrocycles have been explored for decades as promising catalysts.[22] More recently, Cu catalysts have been investigated for the ORR. One promising class of Cu catalysts are those based on dinuclear Cu complexes with triazoles, which possess a similar overpotential to Pt, but suffer from poor durability.[23] Additionally, Cui et. al prepared single atom Cu catalysts by pyrolyzing Cu phthalocyanine. In alkaline media, these materials catalyze the ORR at an overpotential that is 30 mV lower than a commercial Pt/C catalyst.[24] Recently, Lu et. al demonstrated that electron density on the d orbitals of Cu weakens the O-O bonds, which results in the high ORR activity of Cu complexes.[25]

We were inspired to use Cu complexes of glutathione to develop a new class of non-precious metal ORR catalysts. Glutathione is a tripeptide and nitrogen-rich ligand that is known to bind Cu ions in a wide variety of coordination environments.[26,27] Additionally, the ability of glutathione to be oxidized and reduced via the thiol/disulfide couple increases the chemical diversity of these complexes through, for example, the formation of dimers. Previous work has also shown that glutathione can be modified with a range of pendant species such as quantum dots and ferrocene for use in a multitude of applications.[26-28]

This chapter evaluates the ORR activity of Cu complexes of glutathione and glutathione covalently bound to a pendant ferrocene moiety. By increasing the electron transfer rate to the Cu active site, the complex with bound ferrocene catalyzes the ORR via four electrons to water. From these experiments, we propose a mechanism for ORR by these complexes that invokes the differential rates of electron and proton transfer to explain differences in the reactivities of the Cu complexes with and without bound ferrocene.

2.2 Experimental Methods.

2.2.1 General Procedures

The synthesis of GSH-Fc is described in the "Synthesis of GSH-NHFc" section. All other chemicals were obtained from commercially available sources and used directly in experiments without further purification. A VSP-300 Biological potentiostat was used for all electrochemical studies. All electrochemical studies were performed in a three-electrode system in which modified glassy carbon, Pt wire, and Ag/AgCl/3 M KCl (eDaq, Inc.) were the working, counter, and reference electrodes, respectively. Prior to use, glassy carbon working electrodes were polished using a suspension of 0.05 μm alumina followed by sonication for 10 minutes in water. A similar electrochemical experiment was done using carbon as a counter electrode which shows the similar result like Pt counter electrode which makes sure that the Pt counter electrode couldn't enhance the ORR current by dissolving in electrolyte solution.

2.2.2 Homogeneous Catalysis

The solution for homogeneous catalysis was prepared using 1 mM $CuSO_4$, 1 mM GSH-Fc, and 100 mM tetrabutylammonium perchlorate ($TBAClO_4$) in 70% MeOH and 30% water. 5 mL of this solution was used in each electrochemical cell and sparged with O_2 or N_2 for 7 minutes prior to running voltammetry.

2.2.3 Heterogeneous Catalysis

GSH-NHFc (5.0 mg), CuSO4 (3.0 mg), carbon (5.0 mg, Vulcan XC-72), MeOH (5.0 mL), and Nafion solution (25 μL, 5 wt %, D520, Fuel Cell Store, Inc.) were added to a vial. The resulting mixture was sonicated for 10 min to yield a homogeneous suspension. About 80 μL of the suspension was dropcast on a glassy carbon electrode (5 mm in diameter) and dried under ambient conditions using a custom-built upright rotator at a rotation speed of 8 rpm. This modified electrode was then used as the working electrode for rotating disk electrode (RDE) and rotating ring-disk electrode (RRDE) experiments using an electrode rotator (MSRX Pine Research, Inc.). Unless noted otherwise, Britton−Robinson buffers (40 mM H3BO3, 40 mM H3PO4, 40 mM CH3COOH) were used and adjusted to the desired pH using NaOH. Voltammetry was performed with 45 mL of buffer solution sparged with O2 for at least 7 min.

2.2.4 UV-Visible Spectroscopy

Solutions with a total concentration of 5 mM in DMSO contained $CuSO_4$ and GSH-Fc, GSH, or GSSG in DMSO. The molar ratio between the two components was varied for each trial, and the absorbances versus a DMSO solvent blank were recorded using quartz cuvettes with a path length of 0.1 cm and a Shimadzu UV-2550 spectrometer.

2.2.5 ICP-MS Studies

GSH-NHFc was dissolved in EtOAc (3 mM), and an aqueous CuSO4 solution (6 mM) with the same volume was added to the GSH-NHFc solution. Cu-GSH-NHFc formed in the organic layer, which was separated from the aqueous layer and subsequently dried with anhydrous Na2SO4. The solvent was then removed under vacuum, and inductively coupled plasma-mass spectrometry (ICP-MS) analysis was conducted to quantify the Cu and Fe in the complex.

2.2.6 Synthesis of GSH-NHFc

The synthesis of GSH-NHFc was accomplished in four steps starting from GSSG. Boc-GSH was first synthesized in two steps from GSSG following established methods from the literature except the equivalents of di-t-butyl dicarbonate were increased by three times.[31] Next, to synthesize Boc-GSH-NHFc, Boc-GSH (0.10 g, 0.25 mmol) was dissolved in DMSO (20 mL) and Et_3N (0.12 mL, 3.0 mmol), HBTU (0.532 g, 1.32 mmol), and aminoferrocene (0.055 g, 0.274 mmol) were added. This mixture was continuously stirred for 18 hours at room temperature. The mixture was then diluted with EtOAc (200 mL) and washed with water (200 mL) followed by brine (3x 200 mL). The organic layer was dried over anhydrous Na_2SO_4, filtered, and removed under vacuum. The crude product was purified by flash chromatography on silica (ethyl acetate: hexane = 2:1, $R_f = 0.5$) to yield Boc-GSH-Fc (32 mg, 22% yield) with a ^1H NMR spectrum similar to literature.[28] Finally, we deprotected the amino group from Boc-GSH-Fc to yield GSH-NHFc according to a literature method.[28]

2.3 Results and Discussion.

2.3.1 Voltammetric Studies

We first synthesized a conjugate of glutathione and ferrocene (GSH-NHFc, Figure 2.2) in four steps following procedures modified from the literature.[28,31]

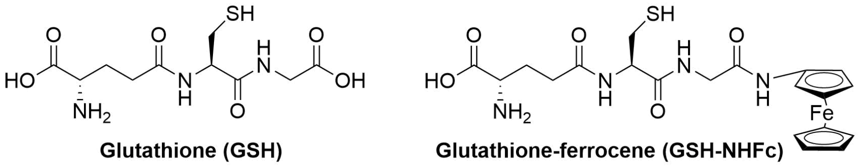

Glutathione (GSH)

Glutathione-ferrocene (GSH-NHFc)

Figure 2.2: Structures of ligands used in this study

We then used cyclic voltammetry (CV) to evaluate the redox properties of glutathione (GSH), GSH-NHFc, and their Cu complexes. A CV of GSH-NHFc dissolved in a solution containing MeOH, water, and a $TBAClO_4$ supporting electrolyte exhibits one redox coupling with a midpoint potential ($E_{1/2}$) of about 0.33 V vs. Ag/AgCl (Figure 2.3A, black line). This couple is due to the Fe^{3+}/Fe^{2+} redox and not the glutathione moiety because a control experiment with GSH shows no redox activity (Figure 2.3B, black line).

The red line in Figure 2.3A shows a CV with 1 equivalent of $CuSO_4$ added to the GSH-NHFc solution. Compared to the CV of the solution without $CuSO_4$ (Figure 2.3A, black line), the magnitude of the current density increases. In fact, the integrated charge under the redox waves approximately doubles (7.0 μC without Cu and 15.5 μC with Cu for the anodic peaks). This finding suggests that the redox wave with Cu is due to two electrons being transferred through the Cu^{2+}/Cu^{+} and Fe^{3+}/Fe^{2+} processes. A control experiment with $CuSO_4$ without GSH-NHFc only shows a redox couple with a very small amount of current density (Figure 2.3B, red line). The differences between the $CuSO_4$ CVs with and without GSH-NHFc suggest that $CuSO_4$ forms a Cu complex with GSH-NHFc, which we denote as Cu-GSH-NHFc.

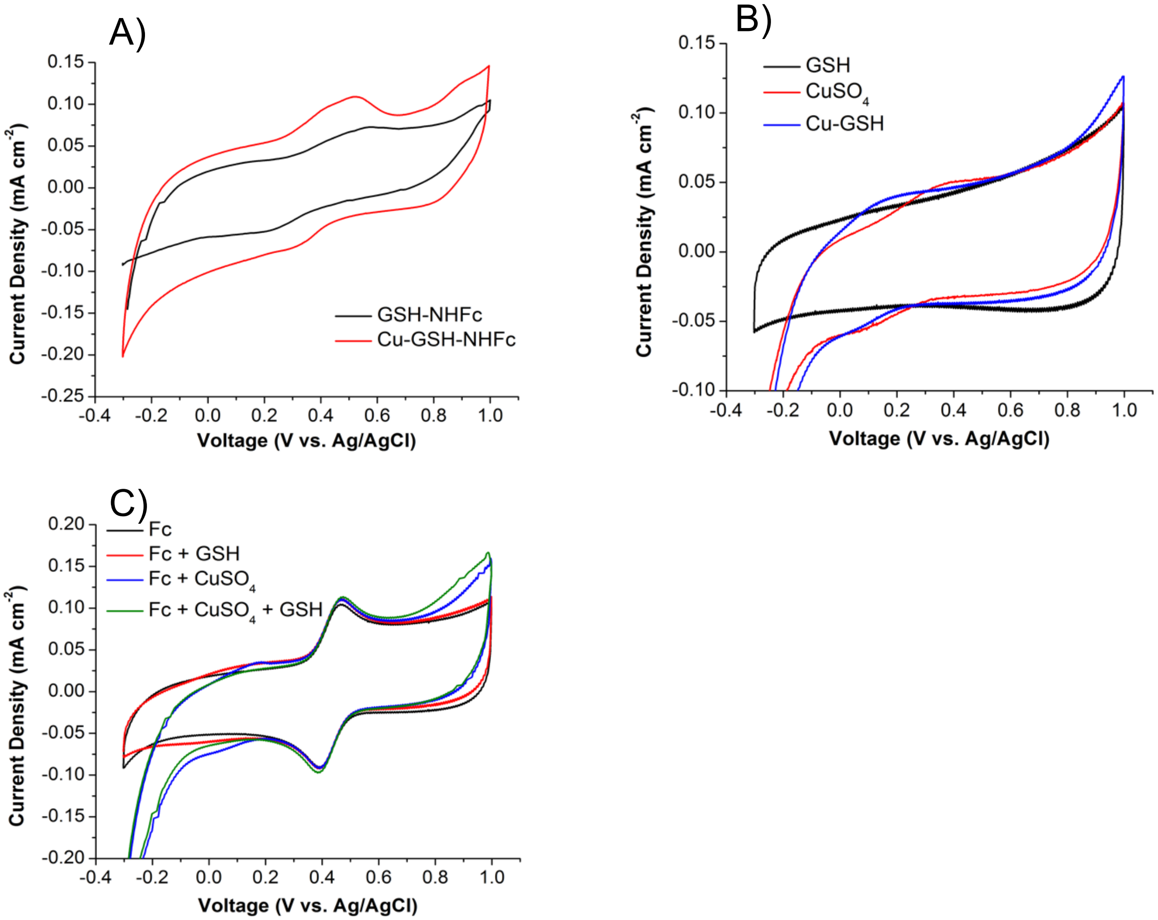

Figure 2.3: Cyclic voltammograms of a glassy carbon electrode at a 500 mV s^{-1} in solutions containing 100 µM GSH-NHFc (A, black), 100 µM Cu-GSH-NHFc (A, red), 100 µM GSH (B, black), 100 µM CuSO4 (B, red), 100 µM Cu-GSH (B, blue),100 µM ferrocene (C, black), 100 µM ferrocene and 100 µM GSH (C, red), 100 µM ferrocene and 100 µM $CuSO_4$ (C, blue), and 100 µM ferrocene, 100 µM $CuSO_4$, and 100 µM GSH (C, green). All solutions also contained 70% MeOH and 30% aqueous 100 mM $TBAClO_4$.

To analyze the effect of having a glutathione moiety covalently bound to ferrocene, we studied CVs of free ferrocene and GSH. A CV of free ferrocene by itself contains one reversible redox couple with an $E_{1/2}$ value of about 0.43 V (Figure 2.3C, black line), which matches literature values.[26] Adding glutathione to the ferrocene solution does not significantly alter the ferrocene CV (Figure 2.3C, red line). This result indicates that the covalent nature of the GSH-NHFc system causes it to exhibit significantly different electrochemical behavior as compared to a solution containing free ferrocene and free GSH. In particular, the $E_{1/2}$ value of free ferrocene is 0.1 V more positive than that of GSH-NHFc. This positive shift in redox potential is due to the electron donating nature of the amide linkage of GSH-NHFc.

CVs of free ferrocene and $CuSO_4$ with and without GSH (Figure 2.3C, blue and green lines) also display the Fe^{2+}/Fe^{3+} redox couple at 0.43 V. In addition, these CVs contain a weak Cu^{+}/Cu^{2+} couple with an $E_{1/2}$ value of about 0.1 V that is similar to those observed in CVs of $CuSO_4$ by itself and $CuSO_4$ with only GSH (Figure 2.3B, red and blue lines). The similarity of the Cu^{+}/Cu^{2+} couples with and without free ferrocene indicate that the Fe^{2+}/Fe^{3+} couple in ferrocene and the Cu^{+}/Cu^{2+} couple are largely independent from one another unlike in Cu-GSH-NHFc. These results imply that the covalent nature of Cu-GSH-NHFc allows for electronic interactions between the Fe^{2+}/Fe^{3+} and Cu^{+}/Cu^{2+} redox couples.

Further evidence of electronic coupling between the two redox couples in Cu-GSH-NHFc can be gleaned from Randles-Ševčík analysis. Figure 2.4 shows Randles-Ševčík plots for the anodic and cathodic peak current densities of CVs of free ferrocene as a function of scan rate. As expected, a better linear fit is obtained when the data are plotted versus the square root of the scan rate as opposed to the scan rate. As observed previously, this result indicates that free ferrocene diffuses to and from the electrode surface during the CVs and is not bound to the electrode.[30] Analogous experiments with GSH-NHFc show the same trend (Figures 2.5), which also indicate that the GSH-NHFc molecule undergoes diffusion during its redox.

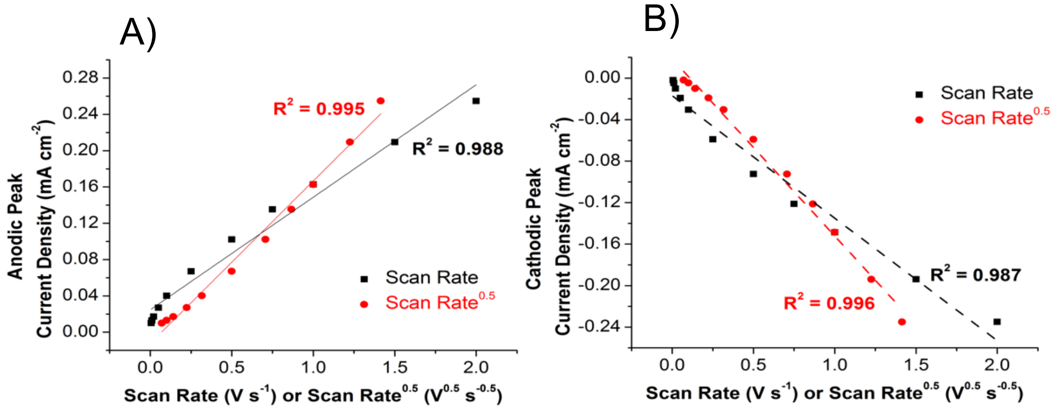

Figure 2.4: Anodic (A) and cathodic (B) Randles-Sevcik plots of 100 µM ferrocene in 70% MeOH and 30% aqueous 100 mM TBAClO4.

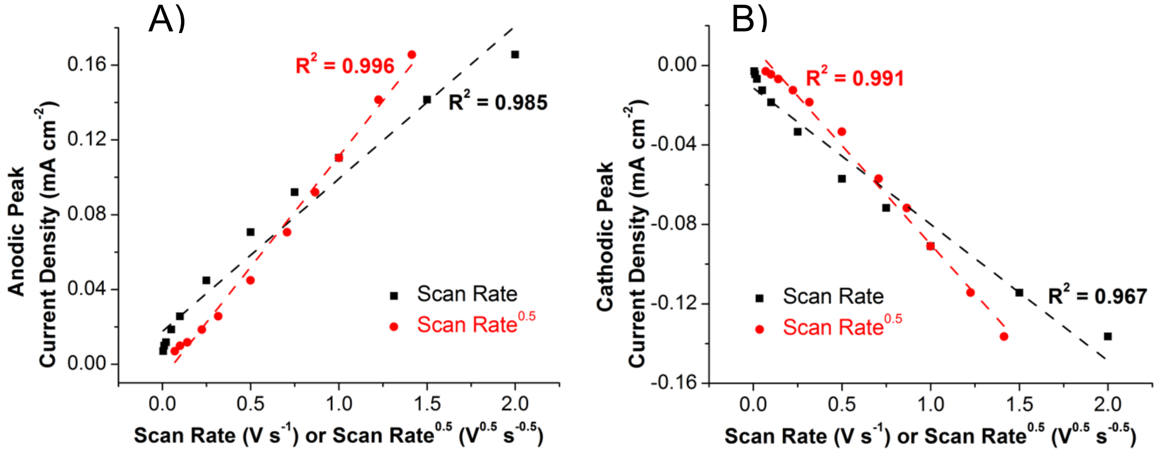

Figure 2.5: Anodic (A) and cathodic (B) Randles-Sevcik plots of 100 µM GSH-NHFc in 70% MeOH and 30% aqueous 100 mM TBAClO4.

Interestingly, a different trend is observed in the Randles-Ševčík analysis of Cu-GSH-NHFc (Figures 2.6). At slow scan rates (≤ 250 mV s^{-1}), a better linear fit is obtained when the data are plotted versus the square root of the scan rate as is observed for free ferrocene and GSH-NHFc. However, at fast scan rates (≥ 250 mV s^{-1}), the data is linear with respect to the scan rate. We hypothesize that at faster scan rates intramolecular electron transfer within Cu-GSH-NHFc results in a quasi-reversible redox, which is perhaps mediated by electrode absorption, resulting in the observed nonlinearity with respect to the square root of the scan rate. Regardless, these findings demonstrate that the electrochemistry of Cu-GSH-NHFc is more complex than that of free ferrocene or GSH-NHFc and that this complexity arises from the covalent linkage of the two redox couples.

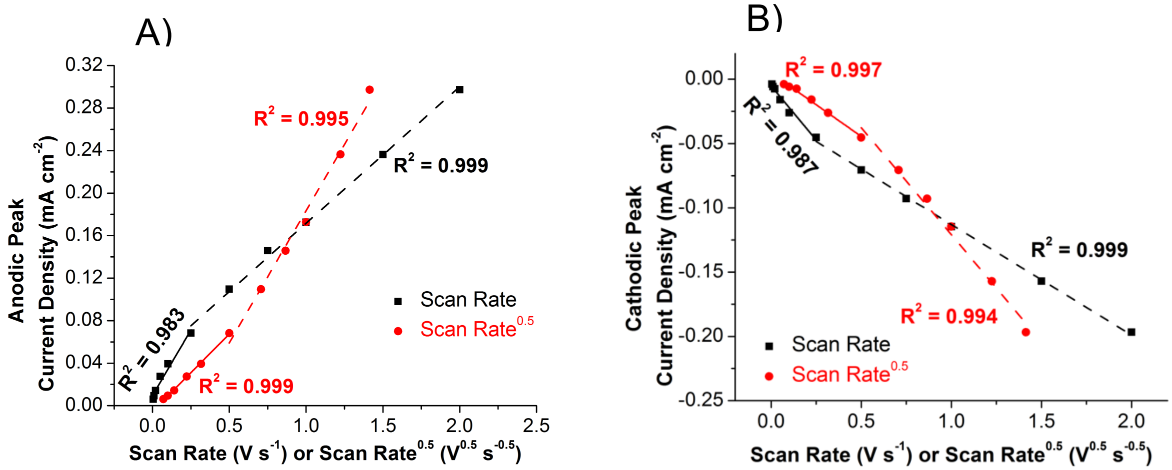

Figure 2.6: Anodic (A) and cathodic (B) Randles-Sevcik plots of 100 µM Cu- GSH-NHFc in 70% MeOH and 30% aqueous 100 mM $TBAClO_4$.

2.3.2 Homogeneous Oxygen Reduction Catalysis

Having established the differences in electrochemistry between Cu-GSH-NHFc and its individual components, next evaluated the ability of Cu-GSH-NHFc to electrocatalyze the ORR. A CV of an O_2-sparged solution containing Cu-GSH-NHFc exhibits enhanced cathodic current density compared to a control experiment with a N_2-sparged solution (Figure 2.7A). These results indicate that Cu-GSH-NHFc is a competent ORR electrocatalyst. Furthermore, the onset potential for O_2 reduction, defined here as the potential of the negative-going scan at which the current density reaches 10% of its maximum value, is -0.29 V vs. AgAgCl. This onset potential is comparable to those observed with previously reported Cu-based molecular ORR catalysts.[31,32]

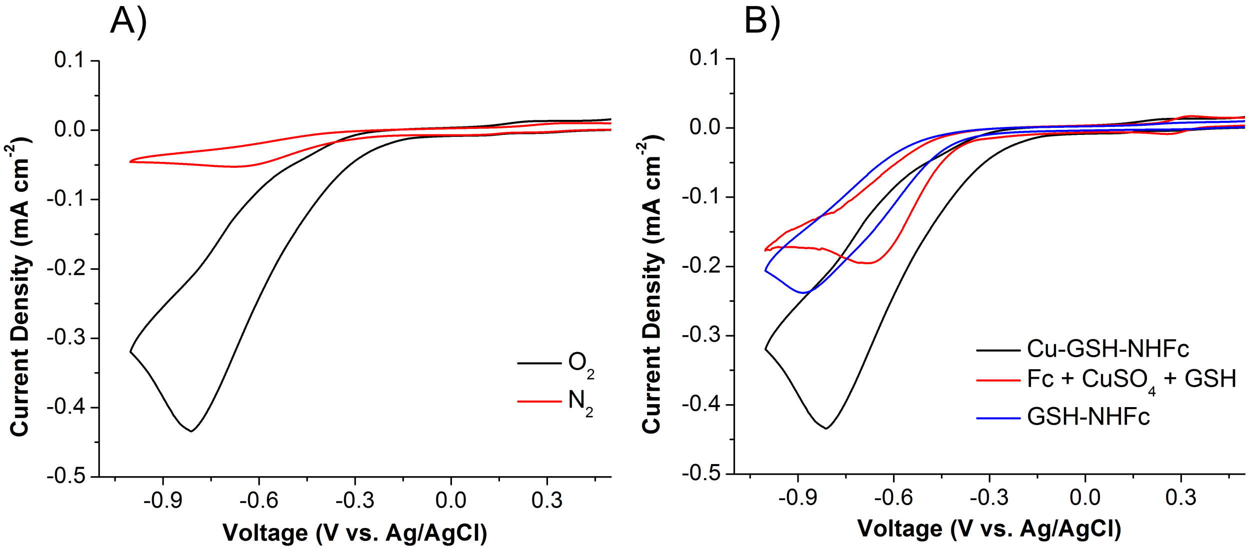

Figure 2.7: Cyclic voltammograms of electrocatalytic O_2 reduction on a glassy carbon electrode at a scan rate of 10 mV s^{-1} in solutions containing 100 µM Cu-GSH-NHFc (A, black and B, black), 100 µM ferrocene, 100 µM CuSO4, and 100 µM GSH (B, red), and 100 mm GSH-NHFc (B, blue). The red line in panel A displays a control experiment in which the Cu-GSH-NHFc solution was sparged with N_2 instead of O_2. All solutions also contained 70% MeOH and 30% aqueous 100 mM $TBAClO_4$.

A CV under the same conditions with GSH-NHFc yields a lower quantity of cathodic current and a more negative onset potential as compared to the CV of Cu-GSH-NHFc (Figure 2.7B, blue line). This finding demonstrates that the presence of Cu aids in the ORR electrocatalysis. Moreover, a CV of a mixture of the three individual free components of Cu-GSH-NHFc (e.g. ferrocene, $CuSO_4$, and GSH) also exhibits less cathodic current and a more negative onset potential (Figure 2.7B, red line). This result demonstrates that these three components must be covalently linked to achieve superior ORR activity. Lastly, CVs of any one or two individual components also result in significantly less cathodic current compared to Cu-GSH-NHFc (Figure 2.8), which further reveal the superior electrocatalytic properties of Cu-GSH-NHFc.

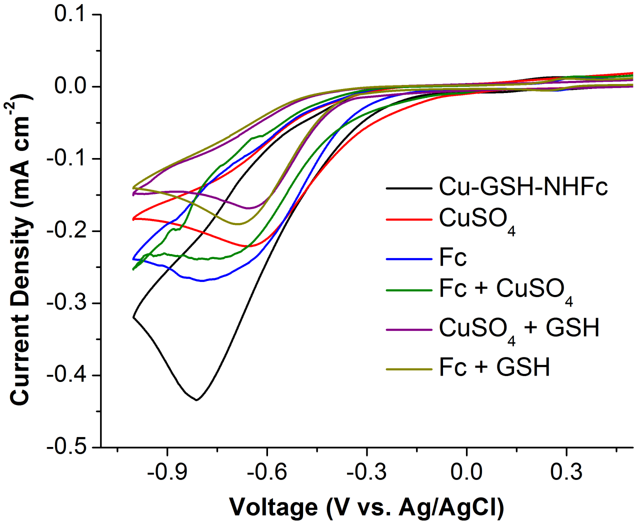

Figure 2.8: Cyclic voltammograms of electrocatalytic O_2 reduction on a glassy carbon electrode at a scan rate of 10 mV s^{-1} in solutions containing 100 µM Cu-GSH-NHFc (black), 100 µM CuSO4 (red), 100 µM ferrocene (blue), 100 µM ferrocene and 100 µM CuSO4 (green), 100 µM CuSO4 and 100 µm GSH (purple), and 100 µM ferrocene and 100 µM GSH (yellow). All solutions also contained 70% MeOH and 30% aqueous 100 mM $TBAClO_4$.

2.3.3 Heterogeneous Oxygen Reduction Catalysis and Rotating Disk Experiments

We next heterogenized the Cu-GSH-NHFc catalyst on a glassy carbon electrode so that its ORR activity could be evaluated in a completely aqueous electrolyte. Figure 2.9A shows LSVs in O_2-sparged pH 5.5 buffer of a glassy carbon rotating disk electrode (RDE) modified with Cu-GSH-NHFc on Vulcan-XC 72 carbon with a Nafion binder. As expected, the ORR current density increases with increasing rotation speed due to enhanced mass transfer at higher rotation speeds.

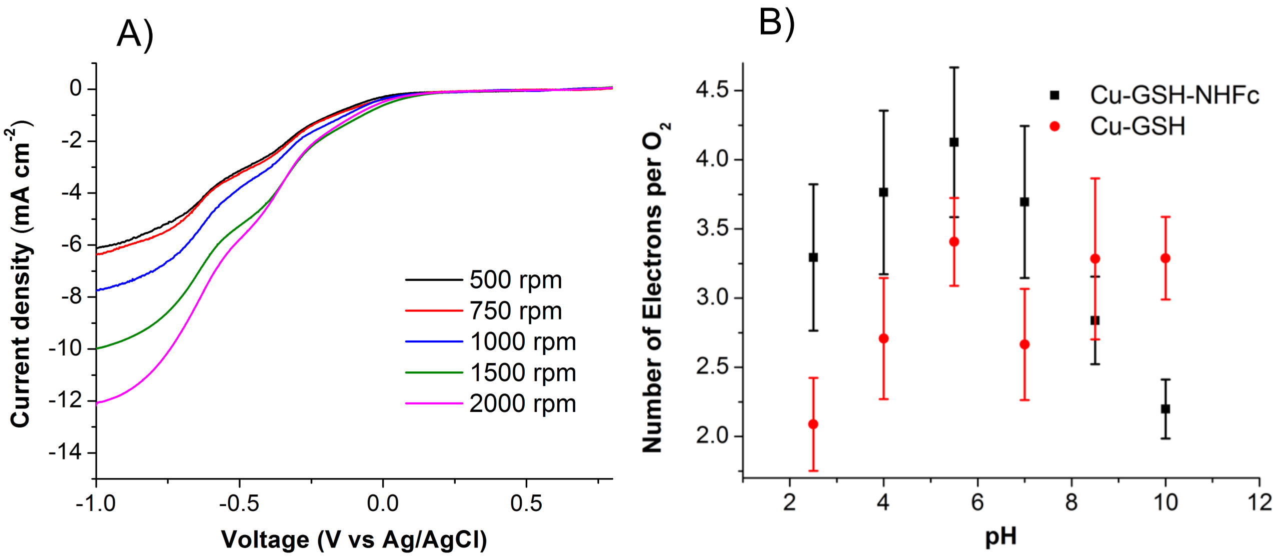

Figure 2.9: Electrocatalytic O_2 reduction by Cu-GSH-NHFc at pH 5.5 on a rotating disk electrode at 10 mV s^{-1} at different rotation speeds (A). Number of electrons transferred per O_2 consumed using Cu-GSH-NHFc (black) and Cu-GSH (red) catalysts as determined by Koutecký-Levich analysis from rotating disk electrochemistry (B).

The number of electrons transferred during O_2 reduction is calculated from the rotating disk electrode experiments using the Levich equation, which is shown below.

$$I = (0.620)nFAD^{2/3}\omega^{1/2}\nu^{-1/6}C$$

In this equation, *I* is the steady-state current, taken to occur at -0.75 V vs. Ag/AgCl, *n* is the number of electrons transferred, *F* is Faraday's constant in C/mol, *A* is the area of the electrode in cm^2, *D* is the diffusion coefficient of the reactant in cm^2/s, ω is the rotation speed of the electrode in rad/s, ν is the kinematic viscosity of the electrolyte in cm^2/s, and C is the concentration of the reactant in mol/cm^3.

Linear plots are obtained when the steady-state current (*I*) is plotted against the square root of the electrode rotation speed ($\omega^{1/2}$). The slope of this line is equal to:

$$Slope = nx$$

where n is the number of electrons and x embodies all of the other values in the above expression, which remain constant across experiments.

Because it is known that unmodified glassy carbon electrodes operate via a two-electron O_2 reduction pathway,[1] the number of electrons can be calculated by comparing the slopes of the modified and unmodified glassy carbon electrodes as follows.

$$2\frac{Slope_{modified}}{Slope_{unmodified}} = n$$

This procedure has been widely used elsewhere.[33]

Through Koutecký-Levich analysis, we calculated the average number of electrons consumed per O_2 during catalysis by Cu-GSH-NHFc as a function of pH (Figure 2.9B, black points). Figure 2.10 represents the respective LSVs in RDE experiments. Within experimental error, Cu-GSH-NHFc reduces O_2 through a four electron pathway at pH values of 4.0, 5.5, and 7.0, which for most applications, such as fuel cells, is desirable. In contrast, at pH values of 2.5, 8.5, and 10.0, Cu-GSH-NHFc catalyzes the ORR with an average of less than four electrons per O_2.

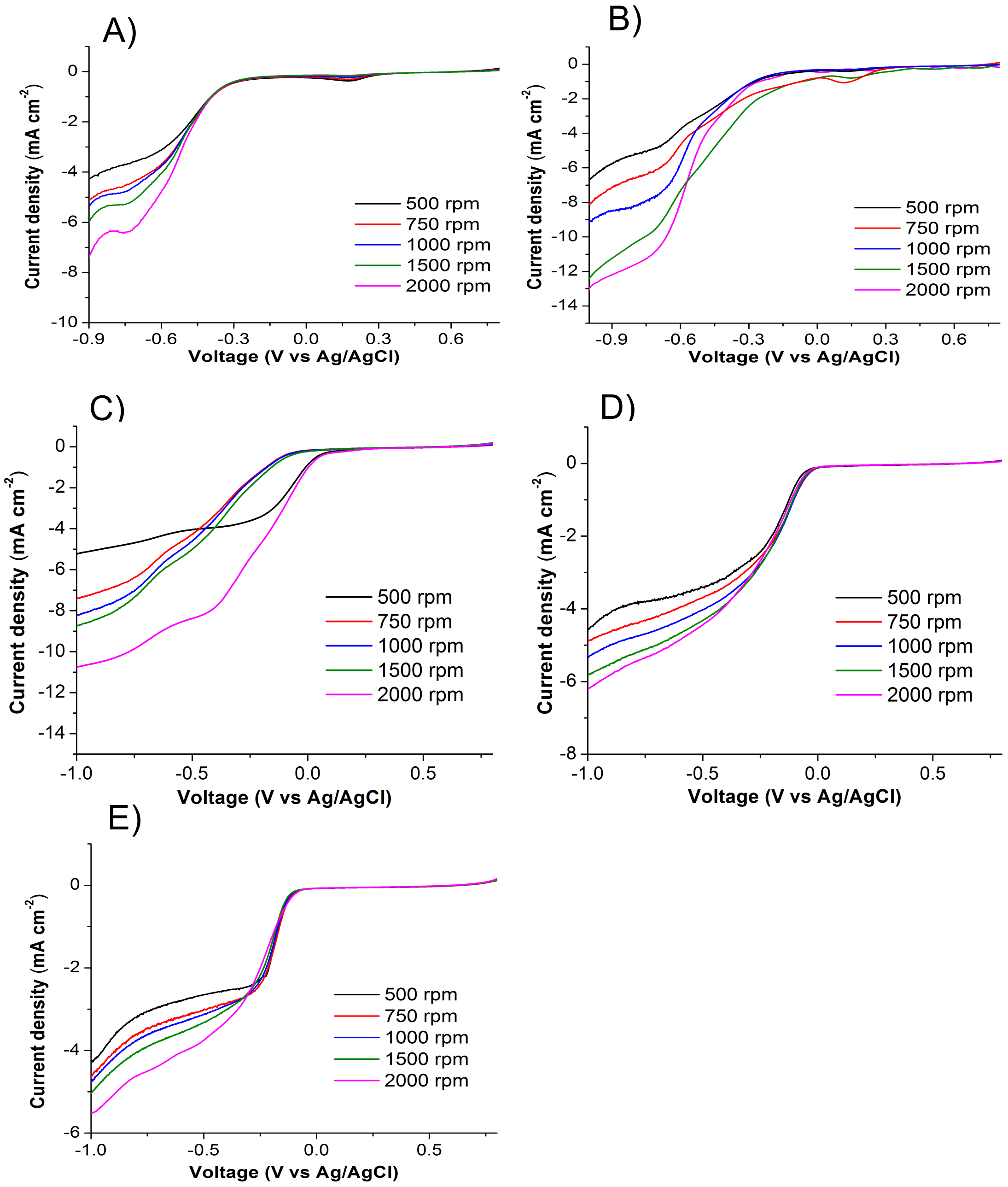

Figure 2.10: Electrocatalytic O_2 reduction by Cu-GSH-NHFc at pH 2.5 (A), pH 4 (B), pH 7 (C), pH 8.5 (D), and pH 10 (E) on a rotating disk electrode at 10 mV s^{-1} at different rotation speeds.

To evaluate the of pH and counter ions effect, we did the rotating ring disk electrode (RRDE) experiments with 400 RPM ratation using 1.2 M Britton – Robinson (BR) buffer which shows the similar number of electrons transfering duing the ORR with small experimental errors (Figure 2.11). The ideal rotating rind disk electrode experimental graphs show in figures 2.12 and 2.13 for CuGSH and Cu-GSH-NHFc, respectivley.

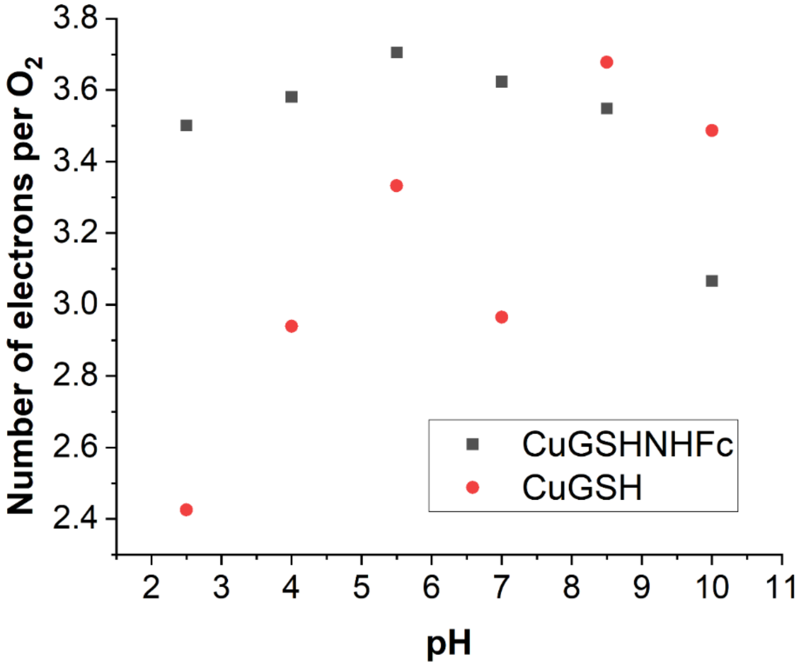

Figure 2.11: Number of electrons transfering per molecule of O_2 during ORR in rotating ring disk electrode (RRDE) experiments using 1.2 M Britton-Robinson (BR) buffers at -0.75 V.

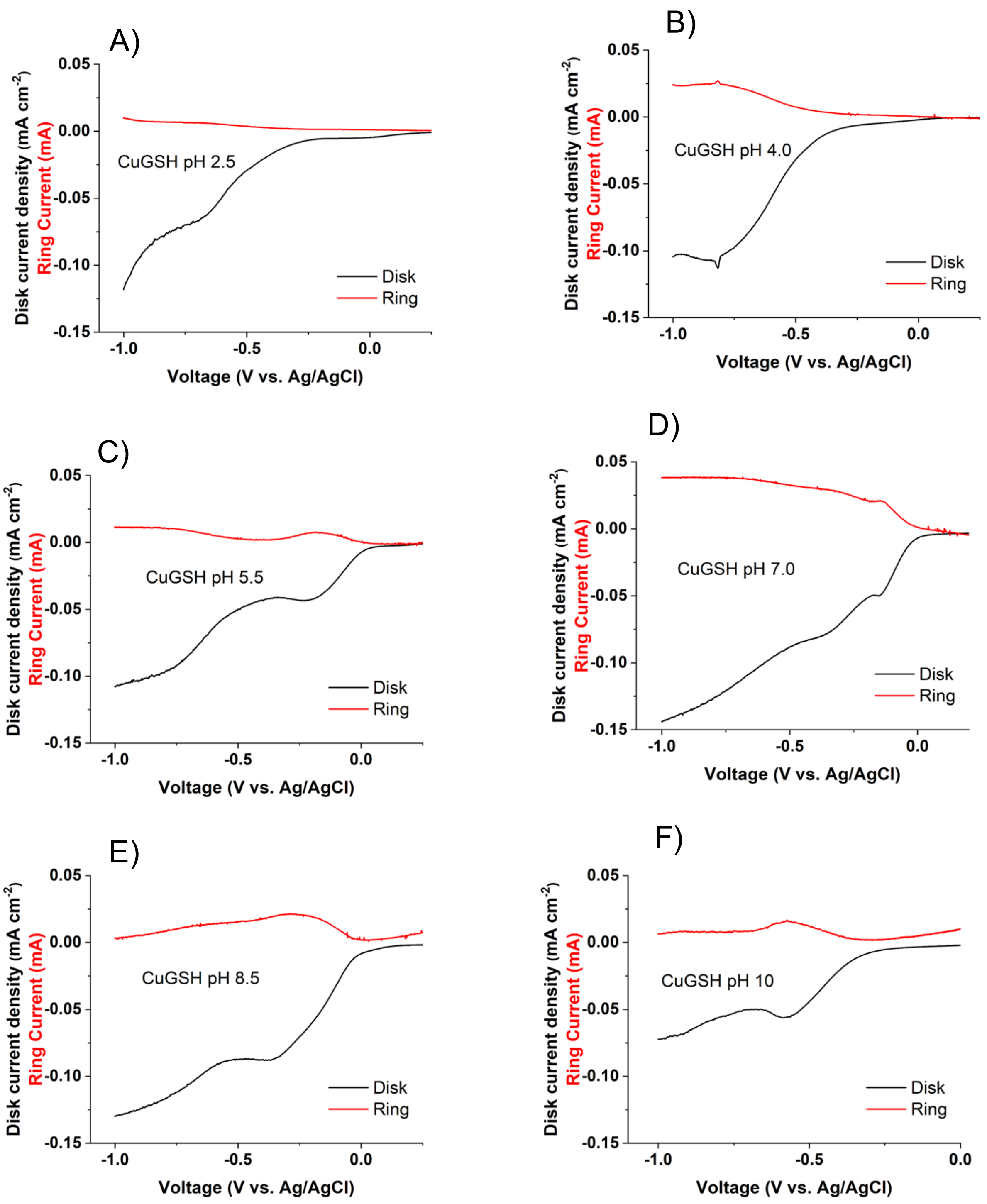

Figure 2.12: Electrocatalytic O_2 reduction by Cu-GSH at pH 2.5 (A), pH 4 (B), pH 5.5 (C), pH 7 (D), pH 8.5 (E), and pH 10 (F) on a rotating ring disk electrode at 10 mV s^{-1} at different rotation speeds.

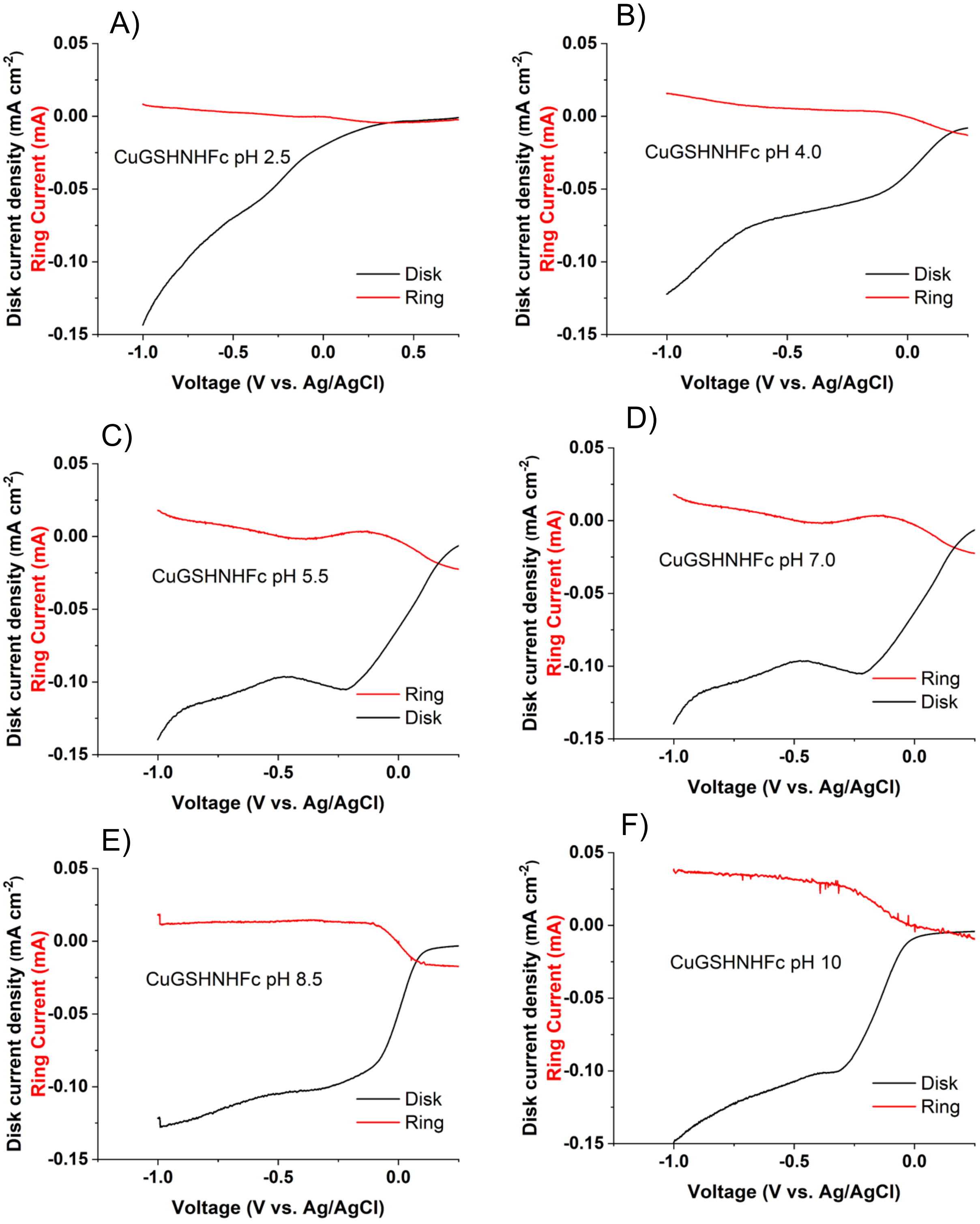

Figure 2.13: Electrocatalytic O_2 reduction by Cu-GSH-NHFc at pH 2.5 (A), pH 4 (B), pH 5.5 (C), pH 7 (D), pH 8.5 (E), and pH 10 (F) on a rotating ring disk electrode at 10 mV s^{-1} at different rotation speeds.

These results indicate that at pH values outside the 4-7 range, Cu-GSH-NHFc generates a significant fraction of H_2O_2 during the ORR. Because these two pH regimes correspond well with the pK_a values of glutathione, we hypothesize that protonation and deportonation events of glutathione outside of the pH 4-7 range cause the Cu coordination environment in Cu-GSH-NHFc to change in a manner that is less amenable to the four electron reduction pathway. Assuming similar pK_a values for unmodified GSH as compared to GSH-NHFc, the relevant pK_a values are 2.12 for the carboxylic acid, 8.66 for the primary amine, and 9.62 for the thiol.[34] Therefore, at pH values from 4-7, GSH-NHFc will be zwitterionic. In contrast, a large fraction of GSH-NHFc molecules will be cationic or anionic at pH values of 2.5 or 8.5 and 10.0, respectively. As is observed here, protonation events of other ORR catalysts comprised of Cu complexes of nitrogen-containing ligands dramatically affect ORR activity.[35,36]

We also compared the number of electrons reduced during ORR by Cu-GSH-NHFc to Cu-GSH (Figure 2.9B, red points). The later of which does not contain the appended ferrocene moiety. Figure 2.14 represents the ideal RDE figures of Cu-GSH for ORR in different pH buffer solution. At all pH values tested, Cu-GSH catalyzes the ORR with an average of less than four electrons per O_2. This finding indicates that the covalently attached ferrocene moeity in Cu-GSH-NHFc is instrumental in enabling the catalyst to reduce O_2 by four electrons and avoid the production of H_2O_2.

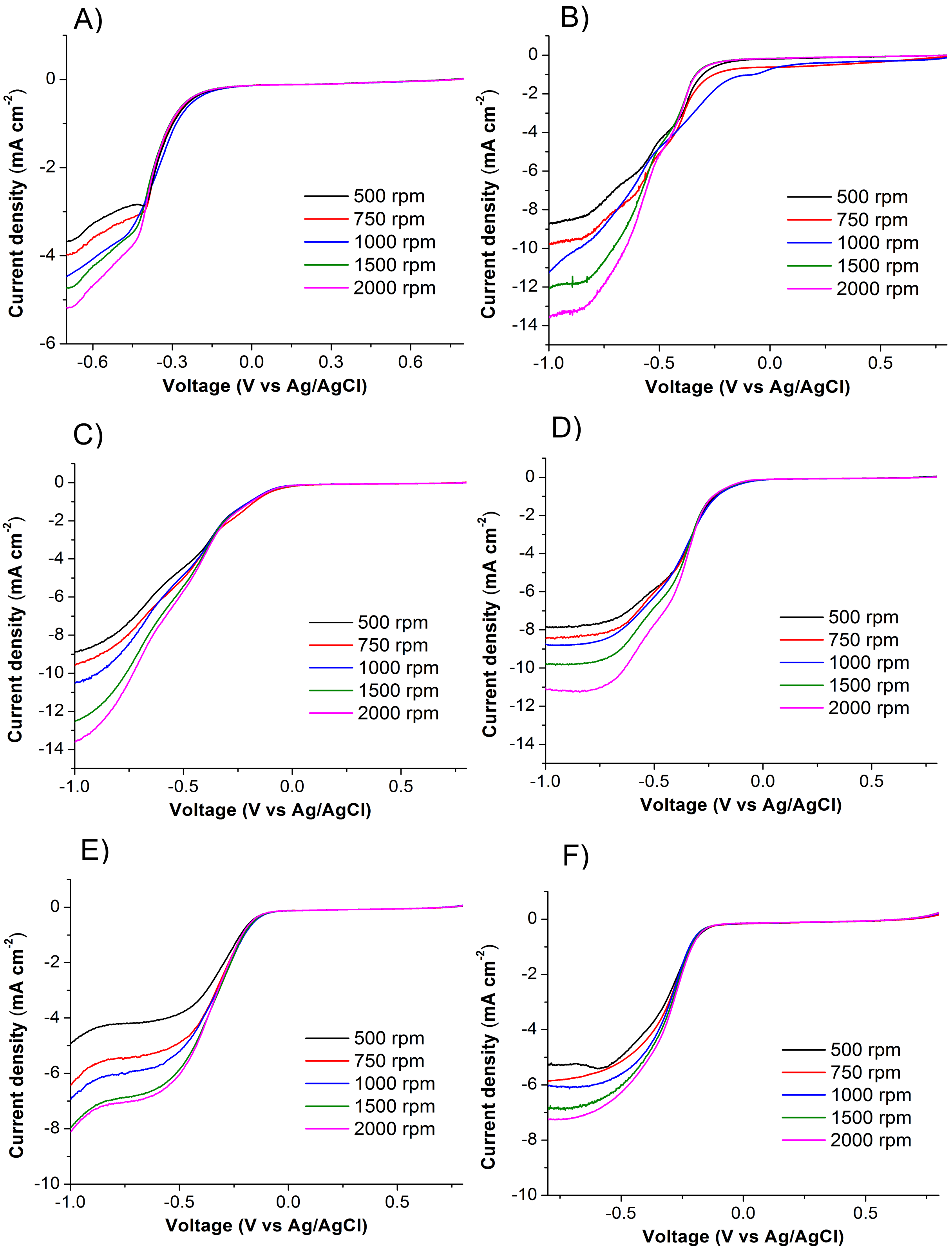

Figure 2.14: Electrocatalytic O_2 reduction by Cu-GSH at pH 2.5 (A), pH 4 (B), pH 5.5 (C), pH 7 (D), pH 8.5 (E), and pH 10 (F) on a rotating disk electrode at 10 mV s^{-1} at different rotation speeds.

UV-Vis spectroscopy was used to detect partially reduced O_2 product H_2O_2. The procedure is following:

UV-Vis spectrum of resorufin formed from an Amplex Red assay for H_2O_2. Rotating disk electrochemistry was performed with a glassy carbon electrode modified with Cu-GSH in a solution containing pH 7 phosphate buffer (4.85 mL, 100 mM), Amplex Red (50 µL, 10 mM in DMSO), and 0.1 mg horseradish peroxidase. Before electrochemistry was performed, the solution was clear. After electrochemistry, the solution turned pink due to absorbance by resorufin with a peak absorbance at 571 nm (Figure 2.15). This experiment demonstrates that H_2O_2 was formed during the electrochemistry. The same assay has previously been used to detect H_2O_2 produced by other O_2 reduction electrocatalysts.[37]

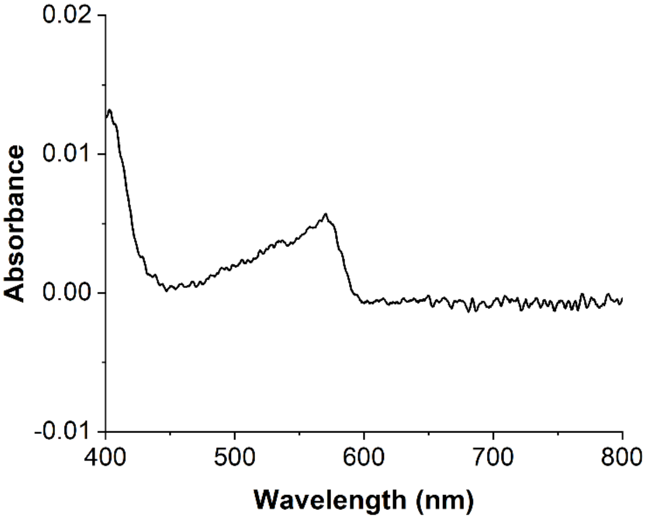

Figure 2.15: UV-Vis spectrum for detecting H_2O_2.

2.4 Mechanism of Oxygen Reduction by Cu-GSH-NHFc and Cu-GSH.

We now discuss a possible mechanistic rationalization for why the ferrocene moiety in Cu-GSH-NHFc allows the catalyst to favor the four-electron pathway for the ORR. A careful analysis of the literature describing molecular Cu ORR catalysts reveals that multinuclear (typically dinuclear) Cu centers are involved in catalysts that reduce O_2 via the four-electron pathway.[37,38] Even catalysts containing nominally mononuclear Cu complexes were later shown to operate via a dinuclear mechanism.[39] For these reasons, we propose that the Cu complexes here also reduce O_2 via a dinuclear Cu center, but studies in our laboratory are ongoing to further interrogate this point.

In order to propose a mechanism, it is useful to determine the stoichiometry of Cu-GSH-NHFc. By collecting UV-visible absorbance spectra across different molar ratios of Cu ions and GSH-NHFc, we used Job plot analysis to determine that in Cu-GSH-NHFc, Cu and the GSH-NHFc ligand exist in a 1:1 molar ratio (Figure 2.16). This Job plot analysis was also confirmed by ICP – MS analysis which shows that the Cu : Fe ration is 0.98 : 1 close to the theoretical 1:1 value.

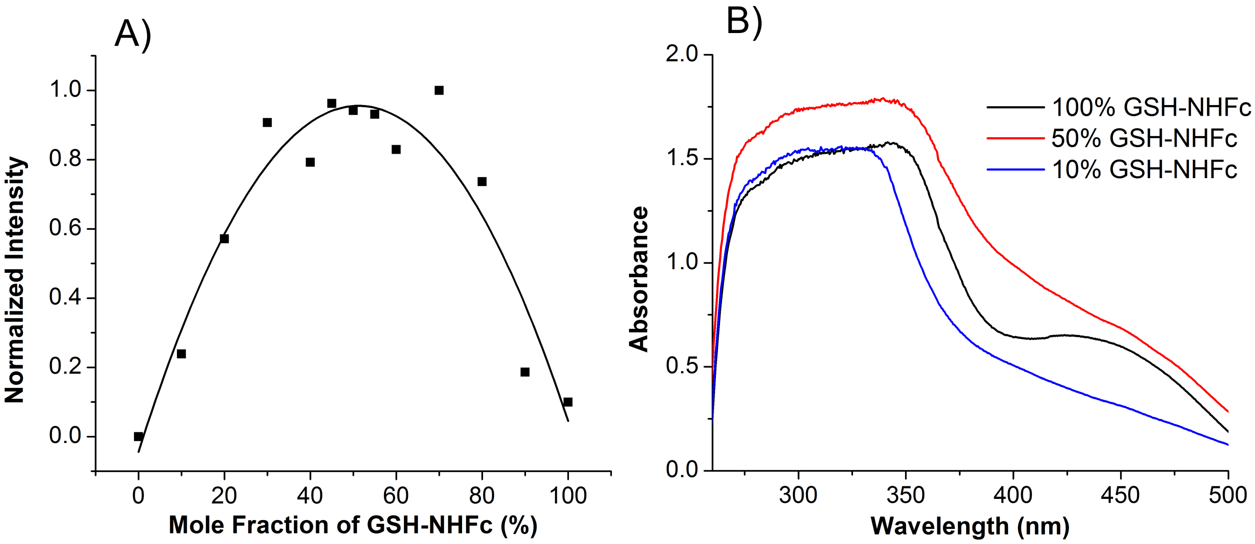

Figure 2.16: Job plot (A) and corresponding representative UV-Vis data (B) for Cu-GSH-NHFc.

Similar UV-vis experiments with Cu-GSH also suggest a 1:1 molar ratio between Cu and the ligand (Figure 2.17). Although there is debate over the Cu coordination environment in Cu-GSH,[24,25,41] most studies suggest involvement of the carboxylate and amine moieties of the glutamate residue and/or the thiol group. Our finding that a 1:1 Cu to ligand stoichiometry exists in both Cu-GSH and Cu-GSH-NHFc is consistent with the Cu in Cu-GSH-NHFc having an analogous coordination environment as in Cu-GSH, especially when considering that the Fc is attached via the pendant glycine residue. In biological contexts, Cu-GSH has been shown to chemically react with O_2 to form Cu complexes of oxidized glutathione (Cu-GSSG).[41,42]

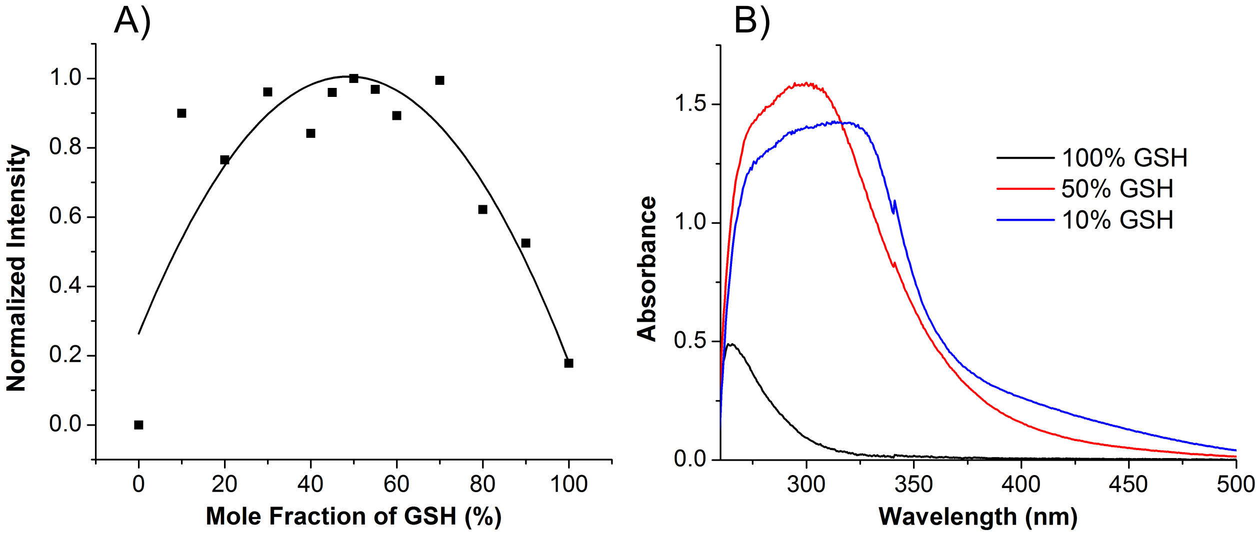

Figure 2.17: Job plot (A) and corresponding representative UV-Vis data (B) for Cu-GSH.

A further set of experiments with Cu and oxidized glutathione demonstrates that under our conditions, the Cu:GSSG ratio is 2:1 in the Cu-GSSG complex (Figure 2.18). Because this stoichiometry is different from those found for Cu-GSH and Cu-GSH-NHFc, this finding suggests that within the time scale of our experiments, the GSH in Cu-GSH-NHFc is not chemically oxidized by dissolved O_2 to form GSSG. In other words, the GSH moiety is stable within Cu-GSH-NHFc and does not form GSSG, at least in the absence of any electrochemistry.

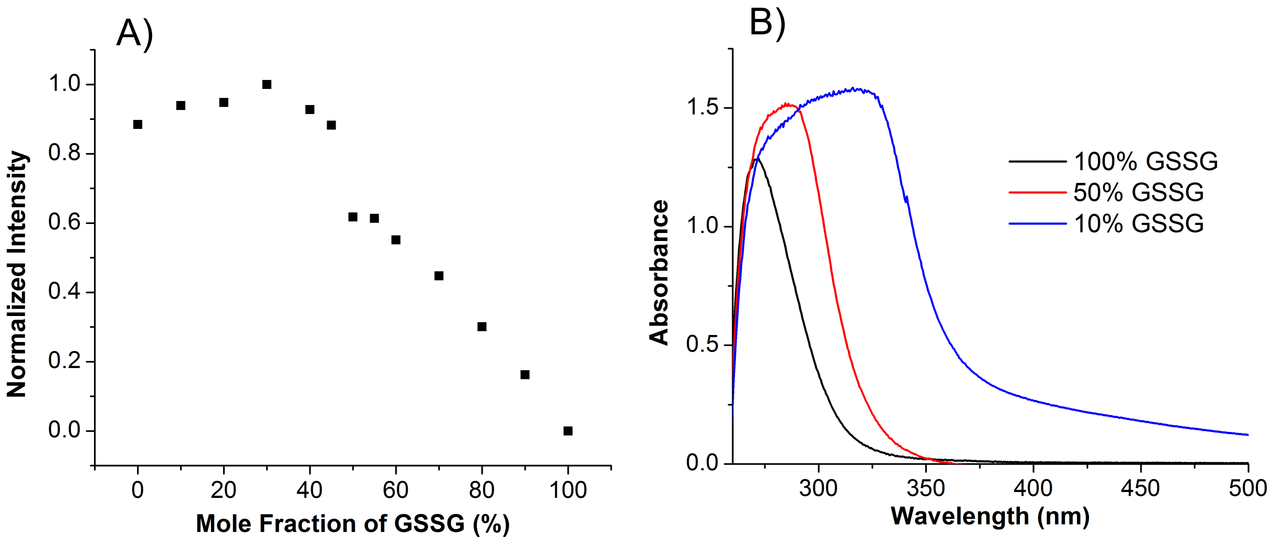

Figure 2.18: Job plot (A) and corresponding representative UV-Vis data (B) for Cu-GSSG.

Based on these findings and previous dinuclear Cu ORR mechanisms[31,43] we propose a mechanism for ORR by both Cu-GSH-NHFc and Cu-GSH (Figure 2.19). First, two Cu-containing complexes react with O_2 to form a dimeric Cu-O-O-Cu intermediate in a two-electron transfer step. When electron transfer is relatively rapid, further electron transfer can occur to yield the four-electron product, H_2O (blue box). We hypothesize that the covalently bound ferrocene moieties increase electron transfer rates to the Cu active site, thus explaining why Cu-GSH-NHFc is capable of catalyzing the ORR by four electrons.

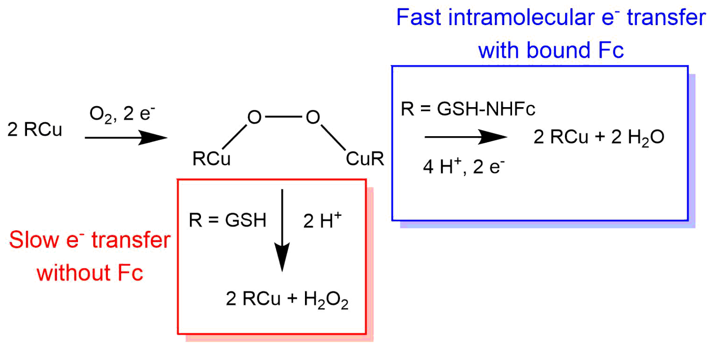

Figure 2.19: Proposed mechanism for electrocatalytic O2 reduction by Cu-GSH-NHFc and Cu-GSH.

In contrast, without the appended ferrocene groups, the electron transfer rates to the Cu active site are slower. In this case, protonation of the Cu-O-O-Cu intermediate occurs as a side reaction, which results in the formation of the two-electron product, H_2O_2 (red box). This production of H_2O_2 at relatively slow electron transfer rates explains why Cu-GSH does not reduce O_2 by four electrons regardless of the pH. Our finding that covalently attached ferrocene groups can improve the ORR catalyzed by Cu complexes is similar to previous work demonstrating that ferrocene-modified Fe porphyrins also catalyze the ORR by four electrons.[42]

We view using ferrocene to accelerate electron transfer as a complimentary approach to previous studies in which the rates of proton transfer were decreased to dinuclear Cu ORR catalysts using membranes.[43] In these studies, the slower proton transfer rates are thought to decrease the rates of protonating the Cu-O-O-Cu intermediate, thus avoiding the production of H_2O_2 (red box) Here, with a ferrocene-modified Cu ORR catalyst, the opposite approach is taken whereby faster electron transfer rates favor O-O bond breaking (blue box), which also avoids H_2O_2 production and yields a catalyst that selectively produces H_2O.

2.5 Conclusions.

We synthesized Cu complexes of glutathiones and evaluated their catalytic activity towards ORR. CV studies demonstrate that intermolecular electron transfer in Cu-GSH-NHFc occurs between Cu and the Fe in the ferrocene-modified glutathione ligand. Homogeneous catalysis results show that Cu, GSH and ferrocene by themselves do not have the same ORR activity as Cu-GSH-NHFc, thus proving the utility of covalently binding these components together. Rotating disk electrode and rotating rind disk electrodes experiments indicate that Cu-GSH-NHFc catalyzes the ORR through a four-electron pathway at pH 4.0-7.0, while the Cu-GSH catalyst without the appended ferrocene catalyzes the ORR with less than four electrons regardless of pH. These findings imply that the attached ferrocene in Cu-GSH-NHFc is instrumental in the catalyst's ability to reduce O_2 to H_2O. We propose a mechanism based on competing rates of proton and electron transfer events that is consistent with these findings. We anticipate that this understanding will contribute to the development of future non-precious metal ORR catalysts based on rational design rules.

2.6 References.

1. Liu, T.; Zhou, Z.; Guo, Y.; Guo, D.; Liu, G. Block Copolymer Derived Uniform Mesopores Enable Ultrafast Electron and Ion Transport at High Mass Loadings. *Nat. Commun.* **2019**, *10* (1), 1–10.
2. Wu, G.; Santandreu, A.; Kellogg, W.; Gupta, S.; Ogoke, O.; Zhang, H.; Wang, H.-L.; Dai, L. Carbon Nanocomposite Catalysts for Oxygen Reduction and Evolution Reactions: From Nitrogen Doping to Transition-Metal Addition. *Electrocatalysis* **2016**, *29*, 83–110.
3. Faustini, M.; Giraud, M.; Jones, D.; Rozière, J.; Dupont, M.; Porter, T. R.; Nowak, S.; Bahri, M.; Ersen, O.; Sanchez, C. Hierarchically Structured Ultraporous Iridium-Based Materials: A Novel Catalyst Architecture for Proton Exchange Membrane Water Electrolyzers. *Adv. Energy Mater.* **2019**, *9* (4), 1802136.
4. Jaouen, F.; Proietti, E. M. Lef Vre, R. Chenitz, J.-P. Dodelet, G. Wu, HT Chung, CM Johnston, P. Zelenay. *Energy Env. Sci* **2011**, *4* (11), 4.
5. Costentin, C.; Drouet, S.; Passard, G.; Robert, M.; Savéant, J.-M. Proton-Coupled Electron Transfer Cleavage of Heavy-Atom Bonds in Electrocatalytic Processes. Cleavage of a C–O Bond in the Catalyzed Electrochemical Reduction of CO2. *J. Am. Chem. Soc.* **2013**, *135* (24), 9023–9031.
6. Fan, L.; Xia, C.; Yang, F.; Wang, J.; Wang, H.; Lu, Y. Strategies in Catalysts and Electrolyzer Design for Electrochemical CO2 Reduction toward C2+ Products. *Sci. Adv.* **2020**, *6* (8), eaay3111.
7. Le, J. M.; Alachouzos, G.; Chino, M.; Frontier, A. J.; Lombardi, A.; Bren, K. L. Tuning Mechanism through Buffer Dependence of Hydrogen Evolution Catalyzed by a Cobalt Mini-Enzyme. *Biochemistry* **2020**, *59* (12), 1289–1297.

8. Yeager, E. Electrocatalysts for O2 Reduction. *Electrochimica Acta* **1984**, *29* (11), 1527–1537.
9. Chen, Z.; Higgins, D.; Yu, A.; Zhang, L.; Zhang, J. A Review on Non-Precious Metal Electrocatalysts for PEM Fuel Cells. *Energy Environ. Sci.* **2011**, *4* (9), 3167–3192.
10. Jones, S. M.; Solomon, E. I. Electron Transfer and Reaction Mechanism of Laccases. *Cell. Mol. Life Sci.* **2015**, *72* (5), 869–883.
11. Varnell, J. A.; Edmund, C. M.; Schulz, C. E.; Fister, T. T.; Haasch, R. T.; Timoshenko, J.; Frenkel, A. I.; Gewirth, A. A. Identification of Carbon-Encapsulated Iron Nanoparticles as Active Species in Non-Precious Metal Oxygen Reduction Catalysts. *Nat. Commun.* **2016**, *7* (1), 1–9.
12. Kramm, U. I.; Herranz, J.; Larouche, N.; Arruda, T. M.; Lefevre, M.; Jaouen, F.; Bogdanoff, P.; Fiechter, S.; Abs-Wurmbach, I.; Mukerjee, S. Structure of the Catalytic Sites in Fe/N/C-Catalysts for O 2-Reduction in PEM Fuel Cells. *Phys. Chem. Chem. Phys.* **2012**, *14* (33), 11673–11688.
13. Lv, H.; Li, D.; Strmcnik, D.; Paulikas, A. P.; Markovic, N. M.; Stamenkovic, V. R. Recent Advances in the Design of Tailored Nanomaterials for Efficient Oxygen Reduction Reaction. *Nano Energy* **2016**, *29*, 149–165.
14. YS-Horn, W. C.; Sheng, S. C.; PJ, F.; EF, H. D. Morgan. *Top Catal* **2007**, *46*, 285.
15. Yang, X.; Roling, L. T.; Vara, M.; Elnabawy, A. O.; Zhao, M.; Hood, Z. D.; Bao, S.; Mavrikakis, M.; Xia, Y. Synthesis and Characterization of Pt–Ag Alloy Nanocages with Enhanced Activity and Durability toward Oxygen Reduction. *Nano Lett.* **2016**, *16* (10), 6644–6649.

16. Choi, C. H.; Lim, H.-K.; Chung, M. W.; Chon, G.; Sahraie, N. R.; Altin, A.; Sougrati, M.-T.; Stievano, L.; Oh, H. S.; Park, E. S. The Achilles' Heel of Iron-Based Catalysts during Oxygen Reduction in an Acidic Medium. *Energy Environ. Sci.* **2018**, *11* (11), 3176–3182.
17. Tse, E. C.; Schilter, D.; Gray, D. L.; Rauchfuss, T. B.; Gewirth, A. A. Multicopper Models for the Laccase Active Site: Effect of Nuclearity on Electrocatalytic Oxygen Reduction. *Inorg. Chem.* **2014**, *53* (16), 8505–8516.
18. Thiyagarajan, N.; Janmanchi, D.; Tsai, Y.-F.; Wanna, W. H.; Ramu, R.; Chan, S. I.; Zen, J.-M.; Yu, S. S.-F. A Carbon Electrode Functionalized by a Tricopper Cluster Complex: Overcoming Overpotential and Production of Hydrogen Peroxide in the Oxygen Reduction Reaction. *Angew. Chem.* **2018**, *130* (14), 3674–3678.
19. Haile, S. M. Fuel Cell Materials and Components☆☆☆The Golden Jubilee Issue—Selected Topics in Materials Science and Engineering: Past, Present and Future, Edited by S. Suresh. *Acta Mater.* **2003**, *51* (19), 5981–6000.
20. Ducros, V.; Brzozowski, A. M.; Wilson, K. S.; Østergaard, P.; Schneider, P.; Svendson, A.; Davies, G. J. Structure of the Laccase from Coprinus Cinereus at 1.68 Å Resolution: Evidence for Differenttype 2 Cu-Depleted'isoforms. *Acta Crystallogr. D Biol. Crystallogr.* **2001**, *57* (2), 333–336.
21. Artyushkova, K.; Serov, A.; Rojas-Carbonell, S.; Atanassov, P. Chemistry of Multitudinous Active Sites for Oxygen Reduction Reaction in Transition Metal–Nitrogen–Carbon Electrocatalysts. *J. Phys. Chem. C* **2015**, *119* (46), 25917–25928.
22. Pegis, M. L.; Martin, D. J.; Wise, C. F.; Brezny, A. C.; Johnson, S. I.; Johnson, L. E.; Kumar, N.; Raugei, S.; Mayer, J. M. Mechanism of Catalytic O2 Reduction by Iron Tetraphenylporphyrin. *J. Am. Chem. Soc.* **2019**, *141* (20), 8315–8326.

23. Fonseca, S.; Pinto, L. M. de C. Oxygen Reduction Reaction on a CuII Complex of 3, 5-Diamino-1, 2, 4-Triazole: A DFT Approach. *ACS Omega* **2020**, *5* (3), 1581–1585.
24. Cui, L.; Cui, L.; Li, Z.; Zhang, J.; Wang, H.; Lu, S.; Xiang, Y. A Copper Single-Atom Catalyst towards Efficient and Durable Oxygen Reduction for Fuel Cells. *J. Mater. Chem. A* **2019**, *7* (28), 16690–16695.
25. Bhagi-Damodaran, A.; Michael, M. A.; Zhu, Q.; Reed, J.; Sandoval, B. A.; Mirts, E. N.; Chakraborty, S.; Moënne-Loccoz, P.; Zhang, Y.; Lu, Y. Why Copper Is Preferred over Iron for Oxygen Activation and Reduction in Haem-Copper Oxidases. *Nat. Chem.* **2017**, *9* (3), 257–263.
26. Pedersen, J. Z.; Steinkühler, C.; Weser, U.; Rotilio, G. Copper-Glutathione Complexes under Physiological Conditions: Structures in Solution Different from the Solid State Coordination. *Biometals* **1996**, *9* (1), 3–9.
27. Yin, S.-N.; Liu, Y.; Zhou, C.; Yang, S. Glutathione-Mediated Cu (I)/Cu (II) Complexes: Valence-Dependent Effects on Clearance and In Vivo Imaging Application. *Nanomaterials* **2017**, *7* (6), 132.
28. Peng, Y.; Liu, Y.-N.; Zhou, F. Voltammetric Studies of the Interactions Between Ferrocene-Labeled Glutathione and Proteins in Solution or Immobilized onto Surface. *Electroanal. Int. J. Devoted Fundam. Pract. Asp. Electroanal.* **2009**, *21* (16), 1848–1854.
29. Wang, C.; Jiang, K.; Xu, Z.; Lin, H.; Zhang, C. Glutathione Modified Carbon-Dots: From Aggregation-Induced Emission Enhancement Properties to a “Turn-on” Sensing of Temperature/Fe 3+ Ions in Cells. *Inorg. Chem. Front.* **2016**, *3* (4), 514–522.
30. Martos-Maldonado, M. C.; Casas-Solvas, J. M.; Téllez-Sanz, R.; Mesa-Valle, C.; Quesada-Soriano, I.; García-Maroto, F.; Vargas-Berenguel, A.; García-Fuentes, L. Binding

Properties of Ferrocene–Glutathione Conjugates as Inhibitors and Sensors for Glutathione S-Transferases. *Biochimie* **2012**, *94* (2), 541–550.

31. Mitamura, K.; Sogabe, M.; Sakanashi, H.; Watanabe, S.; Sakai, T.; Yamaguchi, Y.; Wakamiya, T.; Ikegawa, S. Analysis of Bile Acid Glutathione Thioesters by Liquid Chromatography/Electrospray Ionization–Tandem Mass Spectrometry. *J. Chromatogr. B* **2007**, *855* (1), 88–97.
32. Barile, C. J.; Edmund, C. M.; Li, Y.; Sobyra, T. B.; Zimmerman, S. C.; Hosseini, A.; Gewirth, A. A. Proton Switch for Modulating Oxygen Reduction by a Copper Electrocatalyst Embedded in a Hybrid Bilayer Membrane. *Nat. Mater.* **2014**, *13*, 619–623.
33. Collman, J. P.; Boulatov, R. Electrocatalytic O_2 Reduction by Synthetic Analogues of the Heme/Cu Site of Cytochrome Oxidase Incorporated in a Lipid Film. *Angew. Chem. Int. Ed.* **2002**, *41*, 3487-3489.
34. Pirie, N. W.; Pinhey, K. G. The Titration Curve of Glutathione. *J. Biol. Chem.* **1929**, *84*, 321–333.
35. Thorseth, M. A.; Letko, C. S.; Tse, E. C.; Rauchfuss, T. B.; Gewirth, A. A. Ligand Effects on the Overpotential for Dioxygen Reduction by Tris (2-Pyridylmethyl) Amine Derivatives. *Inorg. Chem.* **2013**, *52*, 628–634.
36. Zeng, T.; Wu, H.-L.; Li, Y.; Edmund, C. M.; Barile, C. J. Physical and Electrochemical Characterization of a Cu-Based Oxygen Reduction Electrocatalyst inside and Outside a Lipid Membrane with Controlled Proton Transfer Kinetics. *Electrochimica Acta* **2019**, *320*, 134611.

37. Liu, C.; Lei, H.; Zhang, Z.; Chen, F.; Cao, R. Oxygen Reduction Catalyzed by a Water-Soluble Binuclear Copper (Ii) Complex from a Neutral Aqueous Solution. *Chem. Commun.* **2017**, *53*, 3189–3192.
38. Gautam, R. P.; Lee, Y. T.; Herman, G. L.; Moreno, C. M.; Tse, E. C. M.; Barile, C. J. Controlling Proton and Electron Transfer Rates Enhances the Activity of an Oxygen Reduction Electrocatalyst. *Angew. Chem. Int. Ed.* **2018**, *57*, 13480-13483.
39. Fonseca, S.; Pinto, L. M. de C. Oxygen Reduction Reaction on a CuII Complex of 3, 5-Diamino-1, 2, 4-Triazole: A DFT Approach. *ACS Omega* **2020**, *5*, 1581–1585.
40. McCrory, C. C.; Devadoss, A.; Ottenwaelder, X.; Lowe, R. D.; Stack, T. D. P.; Chidsey, C. E. Electrocatalytic O2 Reduction by Covalently Immobilized Mononuclear Copper (I) Complexes: Evidence for a Binuclear Cu_2O_2 Intermediate. *J. Am. Chem. Soc.* **2011**, *133*, 3696–3699.
41. Speisky Cosoy, H.; López Alarcón, C.; Olea Azar, C.; Sandoval-Acua, C.; Aliaga, M. E. Role of Superoxide Anions in the Redox Changes Affecting the Physiologically Occurring Cu (I)-Glutathione Complex. **2011**.
42. Ngamchuea, K.; Batchelor-McAuley, C.; Compton, R. The Copper (II)-Catalyzed Oxidation of Glutathione. *Chem.- Eur. J.* **2016**, *22*.
43. Edmund, C. M.; Barile, C. J.; Kirchschlager, N. A.; Li, Y.; Gewargis, J. P.; Zimmerman, S. C.; Hosseini, A.; Gewirth, A. A. Proton Transfer Dynamics Control the Mechanism of O 2 Reduction by a Non-Precious Metal Electrocatalyst. *Nat. Mater.* **2016**, *15*, 754–759.

Chapter Three

Electrocatalytic Oxygen Reduction by Cu Complexes of Tripeptide Derivatives of Glutathione

3.1 Introduction.

The O_2 reduction reaction (ORR) is a central reaction in fuel cells, air batteries, and corrosion.[1–3] Although fuel cells have been used commercially since the 1960's, they have not been adopted on a large scale due to the slow kinetics and extensive overpotential of the ORR, which limits the energy efficiency and operating voltage of fuel cells. This large overpotential originates from the high strength of the O=O double bond (489 kJ/mol).[4]

A wide variety of different catalysts have been studied to decrease ORR overpotential. Pt-based ORR catalysts are the most successful with an overpotential of ∼300 mV.[4–6] However, the high cost of Pt-based catalysts has prevented their widespread adoption. For this reason, a large amount of research has focused on the development of efficient non-precious metal ORR catalysts.[7-16] Biological systems indicate that it is possible to develop non-precious metal ORR catalysts that operate at low overpotentials. For example, laccase, a multicopper protein, exhibits diffusion-limited O_2 reduction with an overpotential of only ∼70 mV.[17,18] Unfortunately, laccase is not stable over a wide pH range, and its large volume results in a low current density.[19-21]

The development of synthetic small-molecule Cu complexes is a promising strategy to produce inexpensive ORR catalysts with high current densities.[22-24] Beyond the ORR, Cu-based catalyst have emerged as promising non-precious metal catalysts in general.[25-28] Anson and co-workers demonstrated that Cu complexes of 1,10-phenanthroline (phen) on graphite catalyze the four-electron reduction of O_2 to H_2O.[29-31] Chidsey and co-workers synthesized mononuclear Cu complexes with modified phen-based ligands and determined relationships between the electronic and steric properties of the ligands and the O_2 reduction performances.[32] Karlin and co-workers developed a mononuclear Cu(II) complex that efficiently catalyzes the four-electron reduction of O_2 to H_2O via a peroxodicopper(II) complex that is chemically reduced in the presence of decamethylferrocene.[33] Cao and co-works described a dinuclear Cu complex with pyridine and polyamide motifs for the four-electron reduction of O_2 to H_2O.[34]

In chapter two, we have discussed the ORR activities of Cu complexes of a simple tripeptide, glutathione (GSH).[35] In particular, we synthesized a ferrocene-modified glutathione that facilitates fast electron transfer to Cu, which results in higher selectivity for the four-electron reduction of O_2 to H_2O than the unmodified Cu-GSH complex. These results imply that glutathione can serve as an appropriate scaffold for efficient Cu ORR catalysts if properly modified.

In this chapter, to further pursue the strategy of using GSH as a research direction for creating active Cu ORR catalysts, we systematically study the relationship between tripeptide compositional relatives of GSH and the O_2 reduction activities of their Cu complexes. We rationalize the observed electrochemical trends by using physicochemical models that account for Cu^{2+}-peptide binding constants and molecular aggregation quantified using FTIR spectroscopy.

3.2 Methods.

3.2.1 General Procedures

Peptide syntheses are described in the section below. All other chemicals were procured from commercial sources and used without purification. All electrochemical studies were performed using a VSP-300 Biologic potentiostat. A four-electrode cell was utilized in which modified glassy carbon served as the disc working electrode, Pt ring served as the ring electrode, a graphite rod functioned as the counter electrode, and a Ag/AgCl/3 M KCl (eDaq, Inc.) electrode was used as the counter electrode. Glassy carbon electrodes were polished using a suspension of 0.05 μm alumina followed by sonication for 8 min in water. The Pt ring electrodes (Pine Research

Instrumentation, Inc.) were cleaned electrochemically in 15 mL of 0.1 M $HClO_4$ solution by cycling from -0.4 V to +1.7 V vs. Ag/AgCl at 100 mV/s until the oxide stripping at ~0.35 V remained constant.[24]

3.2.2 Peptide Synthesis

3.2.2.1 *Glutathione Amide Synthesis*

Glutathione amide (GSHAmide) was synthesized via a two-step process based on a slightly modified literature procedure.[36] Briefly, in the first step to form the monoethyl ester, 2 g of reduced glutathione (GSH) was dissolved in 25 mL of 1.8 M methanolic HCl. The mixture was continuously stirred for 3 hours at room temperature. The resulting solution was cooled at 0°C, and 180 mL of ice-cold diethyl ether was added. After letting the reaction mixture stand for 1.5 hours at 0°C, the ether was decanted. The precipitate was then washed two times with 60 mL of ice-cold water and dried under reduced pressure. 1.8 g GSH-ester (90% yield) was produced in the first step. ^1H NMR (MeOD-*d_4*) δ 4.52 (t, 1H, CysCH), 4.02 (m, 3H, $GlyCH_2$, GluCH), 3.75 (s, 3H, $-OCH_3$), 2.91 (dd, 2H, $CysCH_2$), 2.57 (m, 2H, $-CH_2C\mathbf{H}_2CO-$), 2.20 (m, 2H, $-C\mathbf{H}_2CH_2CO-$). In the second step, which is an aminolysis reaction with ammonia, we followed the literature procedure to produce GSHAmide.

3.2.2.2 *Syntheses of Other Peptides: Glutamic Acid-Cysteine-Glycine (ECG), Asparagine-Cysteine-Glycine (NCG), and Glutamine-Cysteine-Glycine (QCG)*

ECG, NCG, and QCG peptides were synthesized using standard Fmoc-protocols employing Knorr resin on a PS3 automated peptide synthesizer (Protein Technologies, Inc., Woburn, MA). The crude peptides were cleaved from the resin by addition of 92.5% trifluoroacetic acid (TFA), 2.5% distilled water, 2.5% triisopropylsilan, and 2.5% 1,2-ethanedithiol with stirring for 3 hours. Then, the peptides were purified by reverse-phase high-performance liquid chromatography (HPLC, Waters) using a Vydac C18 column. The residual TFA from the peptide cleavage and purification was then removed by subsequent reconstitutions with 0.1% HCl followed lyophilization.

The peptides structures are characterized by matrix-assisted laser desorption ionization (MALDI) mass spectroscopy (Bruker Microflex Daltonics, Inc., Billerica, MA). First, a saturated matrix, α-cyano-4-hydroxycinnamic acid, was prepared in 55%/44% water/acetonitrile solution. For the MALDI mass spectra, a drop of a saturated matrix was added and left to dry on the MALDI plate. Then, a drop of one of the diluted peptides (~1 mM water/acetonitrile solution) was added to the MALDI plate and left to dry. Figure 3.1 shows MALDI mass spectra of QCG, ECG, and NCG peptides and the spectral regions zoomed containing the peptide masses. Panel D of Figure 3.1 shows the MALDI spectrum of matrix, α-cyano-4-hydroxycinnamic acid, alone.

Upon careful inspection, the peaks in the mass spectra of QCG, ECG, and NCG can be accounted for by direct comparison to the matrix mass spectrum by itself. It should be noted that the intensities of the matrix peaks can vary due to application to the MALDI plate. Any small peak contributions to the mass spectrum can further be accounted for by residual sample left on the MALDI plate after cleaning. It should be noted that the total masses corresponding to QCG isotopes were also found at *m/z* 307.067, 308.045, 309.04, and *m/z* 310.037. A single peak corresponding to the total mass of NCG was observed at m/z 293.087. Note, the peaks corresponding to the isotopic distribution of the NCG peptide does not appear in the MALDI mass spectrum due to overlap with the matrix. The total mass and corresponding isotopic distribution of ECG was detected at *m/z* 308.028, 309.04, 310.037, and *m/z* 311.036 (Figure 1).

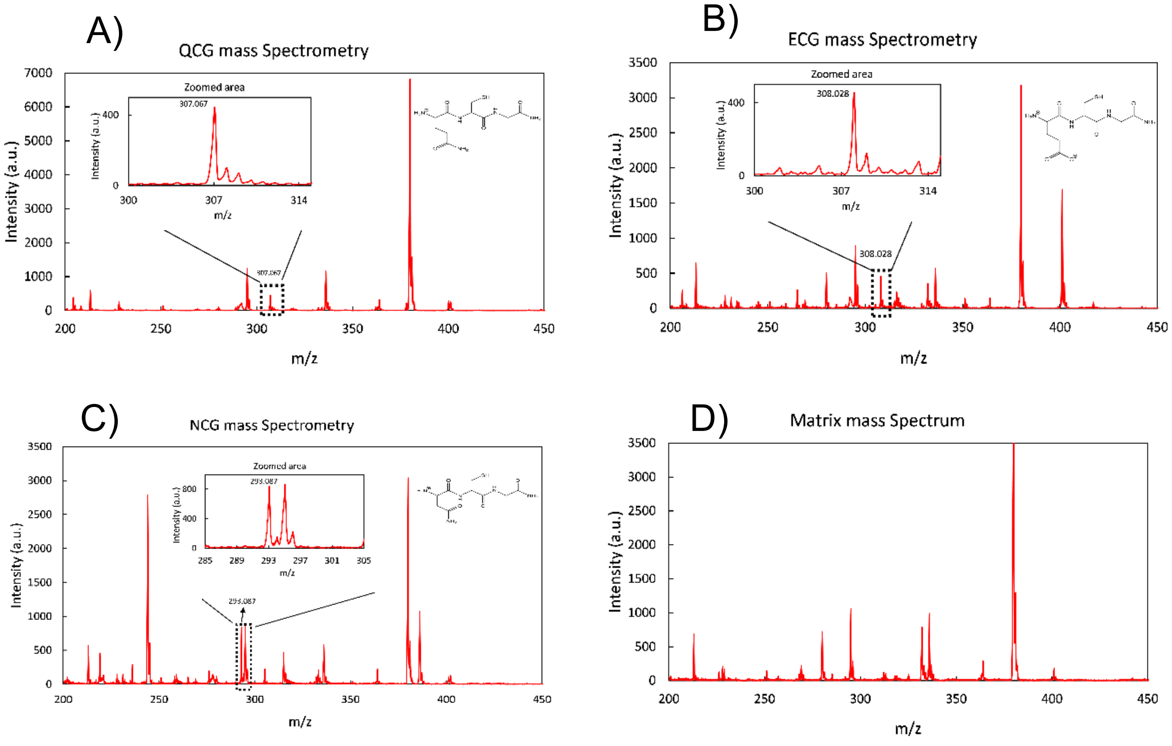

Figure 3.1: MALDI mass spectra of QCG, ECG, NCG, and matrix.

3.2.3 Binding Constant Determination

A Shimadzu UV-2550 spectrometer was used to measure the binding constants of Cu^{2+} to the various peptides. An aqueous peptide solution (0.4 mL of 2 mM except for GSHAmide, which was 10 mM) was used, and an aqueous $CuSO_4$ solution (0.5 M for ECG, 0.4 M for QCG and NCG, 0.1 M for GSHAmide) was added in intervals of 2.5 μL. UV-Vis absorbances were measured in the 200-500 nm range, and the absorbance peak at ~225 nm was plotted versus the number of equivalents of Cu^{2+} added. To calculate the binding constants, fits to these plots were obtained using the single ligand binding saturation macro ($y = B_{max}x/(K_d + x)$, where K_d is the dissociation constant, in SigmaPlot.

3.2.4 Electrochemical Experiments

Peptide (3.0 mg), $CuSO_4$ (3.0 mg), carbon (5.0 mg, Vulcan XC-72), and Nafion solution (30 µL, 5 wt %, D520, Fuel Cell Store, Inc.) were mixed and vortexed for 5 minutes. After vortexing, 5.0 mL MeOH was added, and the mixture was sonicated for 10 minutes to give a homogeneous suspension. About 80 µL of the suspension was drop cast on the glassy carbon electrode (5 mm in diameter) and dried using a custom-built upright rotator at a rotation speed of 8 rpm to ensure uniform film formation. This modified electrode was then used as the working electrode for rotating ring-disk electrode (RRDE) experiments using an electrode rotator (MSRX, Pine Research, Inc.). The ring potential was held constant at +1.5 V vs. Ag/AgCl during RRDE experiments. 1.2 M Britton-Robinson buffers (400 mM H_3BO_3, 400 mM H_3PO_4, 400 mM CH_3COOH) were used and adjusted to the desired pH using NaOH. Voltammetry was performed with 45 mL of buffer solution after it was sparged with O_2 for at least 10 minutes. Onset potentials were determined by calculating the voltage at which the current density for each voltammogram is equal to 10% of the current density at -1 V vs. Ag/AgCl. All reported error bars represent standard errors obtained from experiments that were at least duplicated. Potentials were converted to RHE using the following equation: V (vs. RHE) = V (vs. Ag/AgCl) + 0.21 + 0.059*pH.

3.2.5 FTIR Experiments

Deuterium exchange of the amide residues was achieved by performing 2-3 reconstitutions in D_2O followed by lyophilization. Additional 1.2 M Britton-Robinson buffer solutions were prepared with $CuSO_4$ (6 mg of $CuSO_4$ in 10 mL buffer solution) and exchanged with D_2O. Following the final deuterium exchange, the samples were reconstituted in D_2O, sonicated for 15 minutes, and then filtered with a 0.2 µm syringe filter.

For the FTIR experiments, a stock solution for each peptide was prepared by dissolving ~20-30 mg of peptide in 10 mL of D_2O (~0.1 OD at 1650 cm^{-1}). This stock solution was separated equally among twelve vials and lyophilized to maintain a similar amount of product in each container. Each Cu^{2+} peptide complex and peptide alone was suspended in equal volumes of the prepared buffer solutions at different pHs and sonicated for 15 minutes.

FTIR spectra were obtained using a ThermoNicolet 6700 FTIR spectrometer equipped with a liquid nitrogen-cooled mercury cadmium telluride (MCT) detector. To collect higher sensitivity spectra and correct the baseline more accurately, the IR beam was routed into a home-built temperature-controlled setup.[37] A homemade CaF_2 sample holder was divided into two compartments with a 50 μm Teflon spacer for better background subtraction (i.e., buffer) under identical conditions. An automated translation stage moves the sample cell between the reference and the sample side collecting a single beam spectrum to account for drift and stability. All measurements were carried out in a nitrogen-purged chamber at ambient temperatures of 20°C. The sample and background spectra were averaged over 128 scans.

3.2.6 ICP-MS Analysis

A peptide solution in EtOAc (3 mM) was mixed with an equal volume of an aqueous solution of $Cu(ClO_4)_2$. The Cu complex of the peptide that formed in the EtOAc layer was separated from the aqueous layer and dried over anhydrous Na_2SO_4. The organic solvent was subsequently removed via reduced pressure. Inductively coupled plasma-mass spectrometry (ICP-MS) was performed to quantify the Cu and S in the complex.

3.2.7 Modeling

FTIR data were utilized to quantify the total amount of peptide aggregation as a function of sequence as well as over a variety of pHs for each peptide alone and the Cu^{2+} peptide complexes. The vibrational spectra were decomposed into component peaks using a fitting method that included a sum of Gaussian functions, $y = A * e^{-4*\ln(2)*\frac{(x-x_c)^2}{w^2}}$, where x_c is the center frequency, A is the amplitude, and w is the full-width at half maximum (FWHM). Then, the total amount of aggregation was quantified by taking the product of the FWHM and the amplitude of the peaks at ~1620 cm^{-1} and ~1680 cm^{-1}, corresponding to anti-parallel beta sheets aggregates.[38-40] Linear combinations of the relative populations of each vibrational transition were screened during modeling, and a linear combination of 66% of the 1620 cm^{-1} and 34% of the 1680 cm^{-1} yielded the best-fit to the models.

Binding constants, which were obtained from UV-Vis spectra as described above, were measured at unadjusted pH. Binding constants could not be determined experimentally at different pH values due to the poor solubility of the Cu complexes in water. For this reason, the binding constants at different pH values were estimated by considering how the denticity of the peptide changes with pH. The amine group ($-NH_2$) on the N-terminus of each peptide and the carboxylate group (COO^-) on peptides containing a glutamate residue, both of which readily bind to Cu^{2+}, were each considered to increase the denticity of the peptide by one vis-à-vis peptides that do not contain these groups or contain protonated forms of these groups (i.e. $-NH_3^+$ and $-COOH$). Binding constants at different pH values were then calculated assuming the binding constants increased by a factor of 100 per increase in denticity, which is a reasonable approximation for Cu^{2+} complexes of aminocarboxylate ligands.[41] The denticity values were adjusted at the various pH values according to the relative populations of protonated and deprotonated forms according to the Henderson-Hasselbalch equation.

The aggregation and binding constant values were then normalized on a scale from 0 to 1. Similarly, the number of electrons transferred per mole of O_2 reduced as determined by RRDE and the logarithms of the maximum magnitude of the ORR currents measured during voltammetry per mole of catalyst were normalized on a scale from 0 to 1. The current per mole of catalyst was determined by first calculating the amount of catalyst loaded on each disc electrode. These values were determined by integrating the Cu(II)/Cu(I) redox couple measured during voltammetry under the assumption that each peptide binds to Cu in a 1:1 ratio, as determined by ICP-MS results. The maximum magnitude of ORR current was then divided by the calculated moles of Cu catalyst.

The models compared the normalized electrochemistry data to linear combinations of the normalized aggregation and binding constant values. Normalized values are referred to as “scores” from 0 to 1 throughout the manuscript. Each model consisted of a different linear combination with a weighting of $0 \leq x \leq 1$ for the aggregation values and a weighting of $0 \leq 1\text{-}x \leq 1$for the binding constant values. An increment of 1% was used for x to give 101 different sets of weighting values. For each of these 101 weighting values, positive and negative correlations were evaluated. In other words, four different sets of models were considered, those that compared the electrochemistry data to 1) increasing aggregation and increasing binding constant, 2) increasing aggregation and decreasing binding constants, 3) decreasing aggregation and increasing binding constants, and 4) decreasing aggregation and decreasing binding constants. Therefore, in total, 404 (101 x 4) models were considered. For both the number of electron and current data, the selected best-fit models were the ones that possessed the lowest residues between the modeled values and experimental electrochemistry data.

3.3 Results and Discussion.

3.3.1 Structure and Synthesis of Peptides

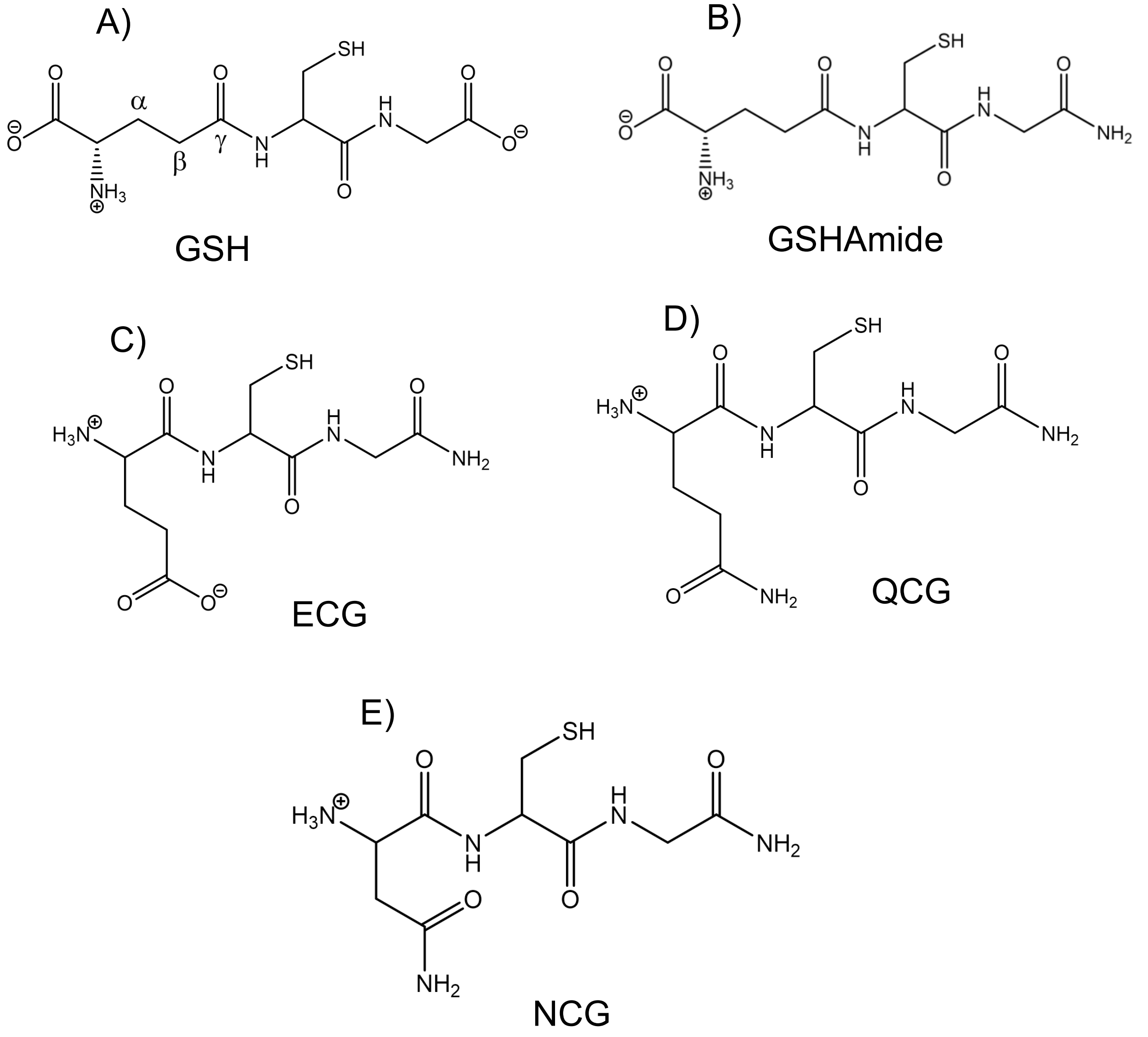

Figure 3.2: Predominant chemical structures of GSH (A), GSHAmide (B), ECG (C), QCG (D), and NCG (E) at neutral pH.

The Cu complexes of five different peptides were evaluated as ORR catalysts. The baseline catalyst is the previously studied Cu complex of glutathione (Cu-GSH). Glutathione is a tripeptide with a gamma linkage between the side chain of glutamate and the amine group of cysteine (Figure 3.2A). Three additional peptides in this work were synthesized using standard Fmoc-based solid-phase peptide synthesis with rink amide resin, which results in amidation of the C-terminal glycine residue (Figures 3.2C-3.2E). An additional peptide, GSH-carboyxamide (GSHAmide), was synthesized from the amidation of the C-terminus of glutathione (Figure 3.2B). Together, the four amidated peptides allow for a fair set of comparison of catalytic activities for the Cu complexes. Previous studies demonstrate that the carboxylate on the glycine of glutathione does not bind to Cu^{2+}, and we therefore hypothesize that modification of the glycine with an amide would not significantly affect the Cu^{2+} binding constants of the peptides. Indeed, measurements discussed in detail later in this chapter indicate that the binding constants of Cu-GSH and GSHAmide are similar. The Cu complex of ECG (Cu-ECG) was considered because ECG is a glutathione analog in which the glutamate residue is attached via a normal peptide linkage to cysteine instead of a gamma linkage (Figure 3.2C). We also evaluate Cu-QCG and Cu-NCG. QCG is a glutamine analog of ECG in which the carboxylate side chain is replaced by an amide (Figure 3.2D), and NCG (Figure 3.2E) contains one less methylene group on the sidechain than QCG. These peptides allow us to investigate the effects of carboxylate versus amide side chains of different lengths in the binding pocket of Cu^{2+} and the resulting effects on ORR catalysis.

3.3.2 Rotating Ring-Disc Electrochemistry

First, we investigated the ORR catalysis of different Cu^{2+}-peptide complexes by rotating ring-disc electrode (RRDE) experiments using O_2-saturated Britton-Robinson buffers at different pH values ranging from 2.5-10 (Figures 3.3-3.10). For all catalysts studied and at all pH values, the ORR onset potentials for each Cu^{2+}-peptide complex were significantly more positive than those of the corresponding peptide without Cu (Table 3.1). These results indicate that Cu is needed to increase ORR activity.

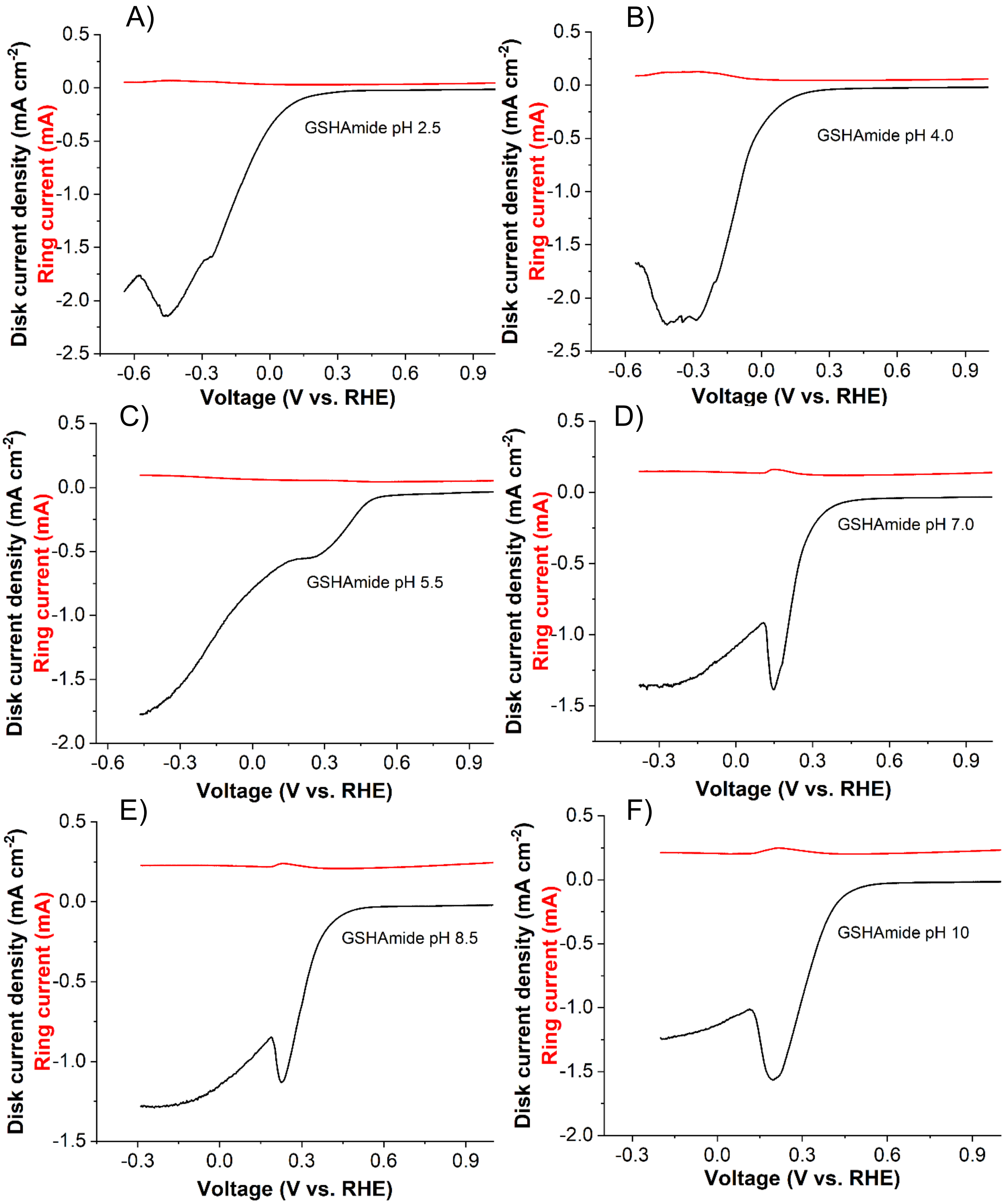

Figure 3.3: Electrocatalytic O_2 reduction by GSHAmide at pH 2.5 (A), pH 4 (B), pH 5.5 (C), pH 7 (D), pH 8.5 (E), and pH 10 (F) on a rotating ring-disk electrode at 10 mV s^{-1} at 500 rpm.

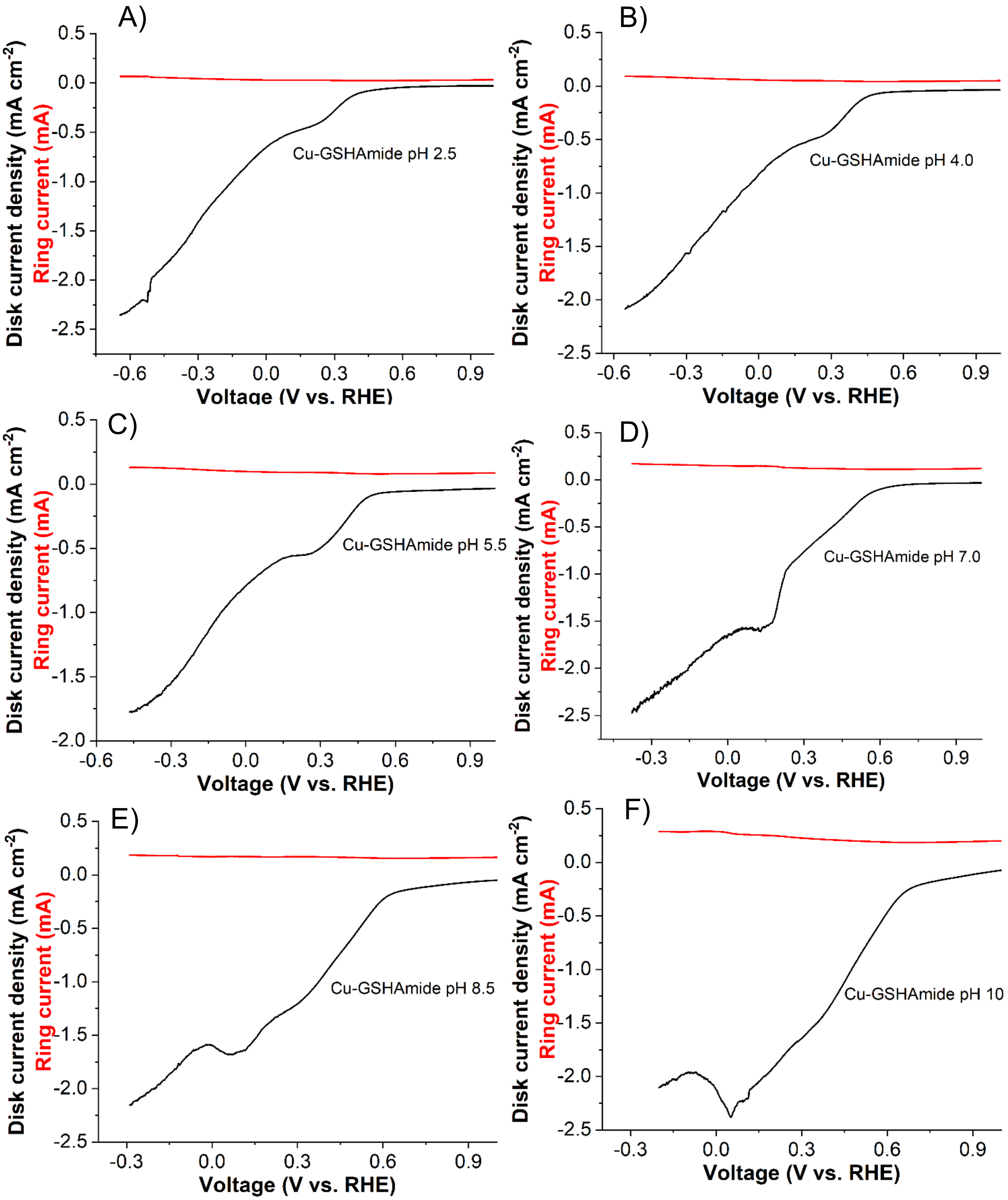

Figure 3.4: Electrocatalytic O_2 reduction by Cu-GSHAmide at pH 2.5 (A), pH 4 (B), pH 5.5 (C), pH 7.0 (D), pH 8.5 (E), and pH 10 (F) on a rotating ring-disk electrode at 10 mV s^{-1} at 500 rpm.

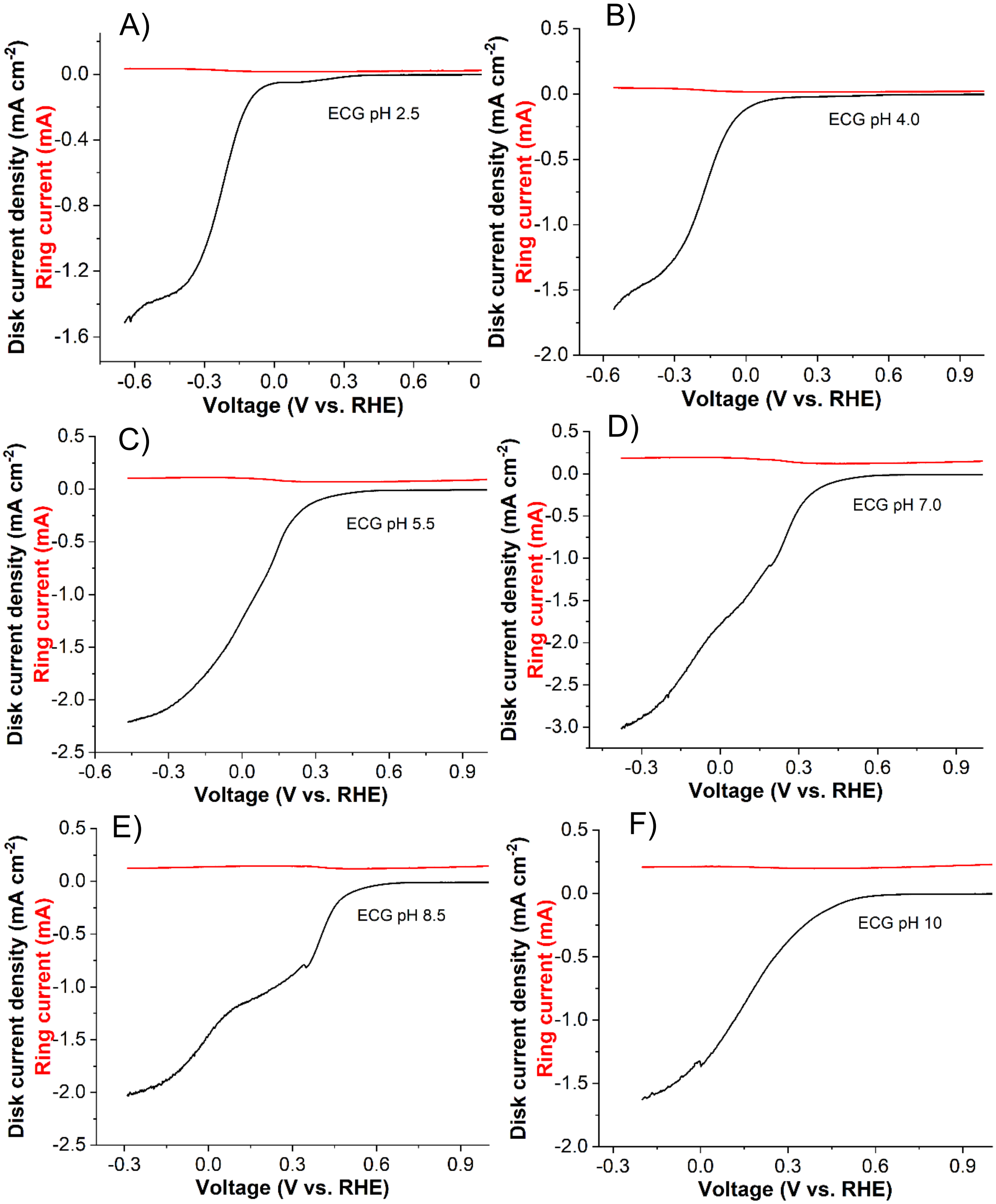

Figure 3.5: Electrocatalytic O_2 reduction by ECG at pH 2.5 (A), pH 4 (B), pH 5.5 (C), pH 7 (D), pH 8.5 (E), and pH 10 (F) on a rotating ring-disk electrode at 10 mV s^{-1} at 500 rpm.

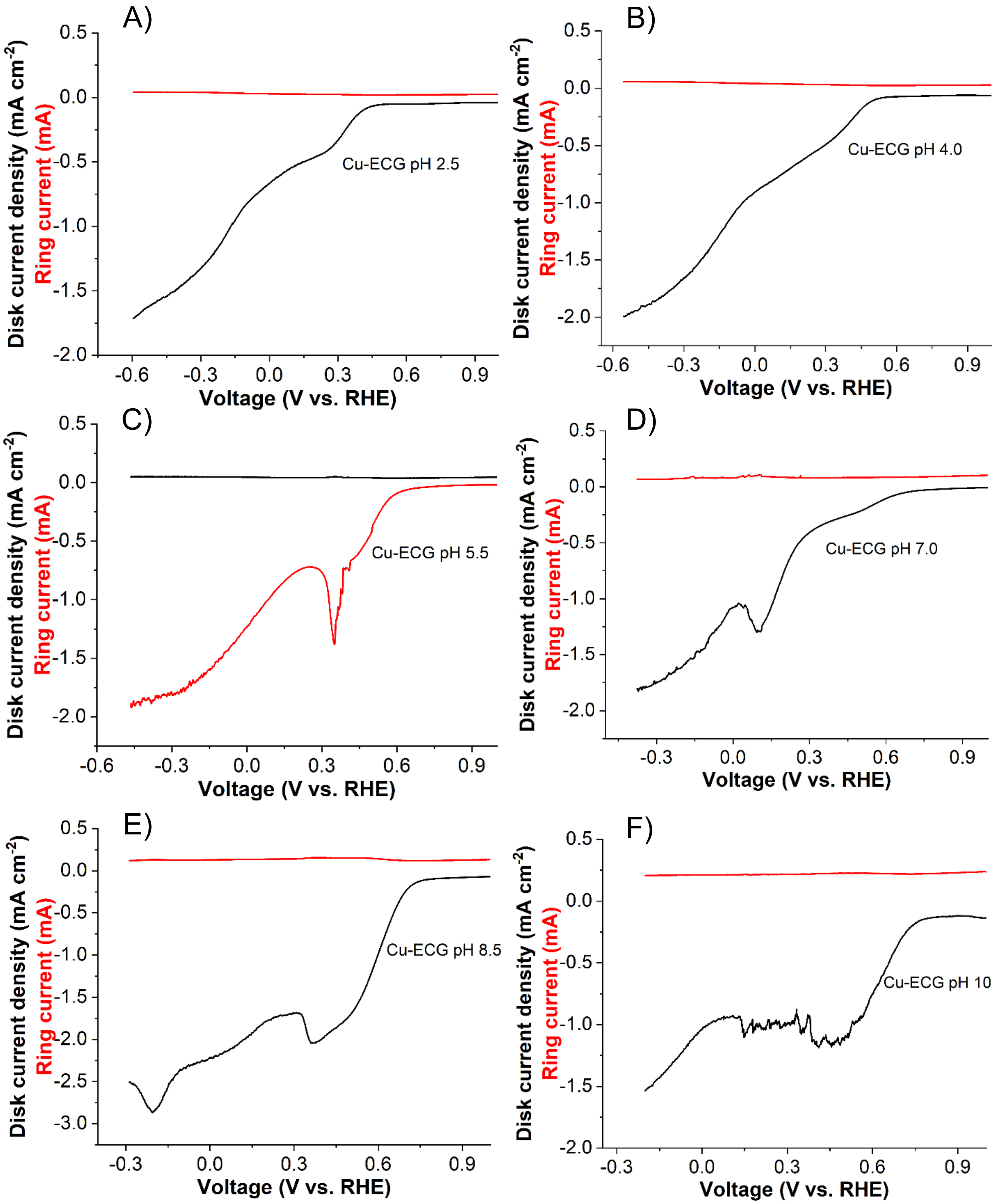

Figure 3.6: Electrocatalytic O_2 reduction by Cu-ECG at pH 2.5 (A), pH 4 (B), pH 5.5 (C), pH 7.0 (D), pH 8.5 (E), and pH 10 (F) on a rotating ring-disk electrode at 10 mV s^{-1} at 500 rpm.

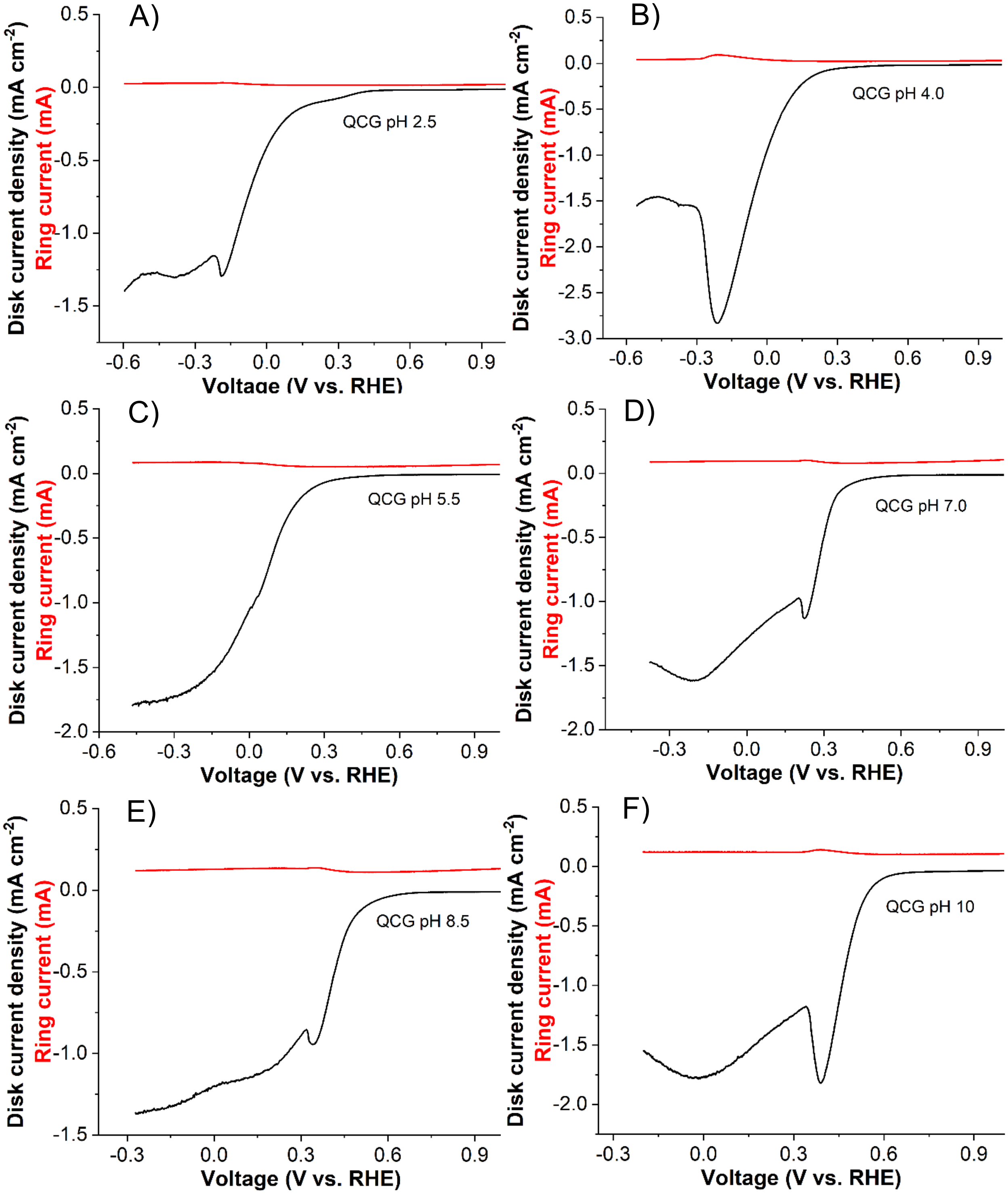

Figure 3.7: Electrocatalytic O_2 reduction by QCG at pH 2.5 (A), pH 4 (B), pH 5.5 (C), pH 7 (D), pH 8.5 (E), and pH 10 (F) on a rotating ring-disk electrode at 10 mV s^{-1} at 500 rpm.

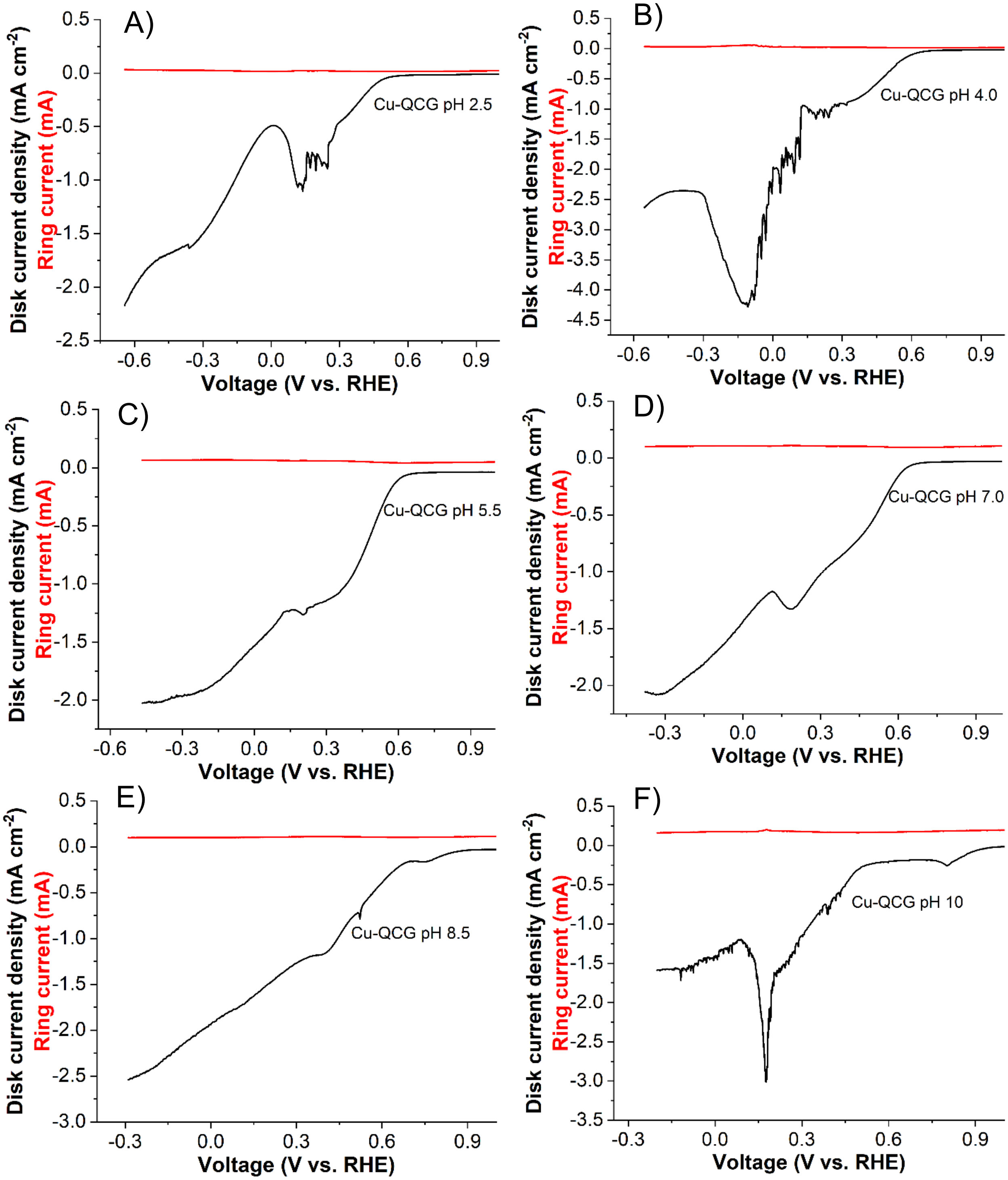

Figure 3.8: Electrocatalytic O_2 reduction by Cu-QCG at pH 2.5 (A), pH 4 (B), pH 5.5 (C), pH 7 (D), pH 8.5 (E), and pH 10 (F) on a rotating ring-disk electrode at 10 mV s^{-1} at 500 rpm.

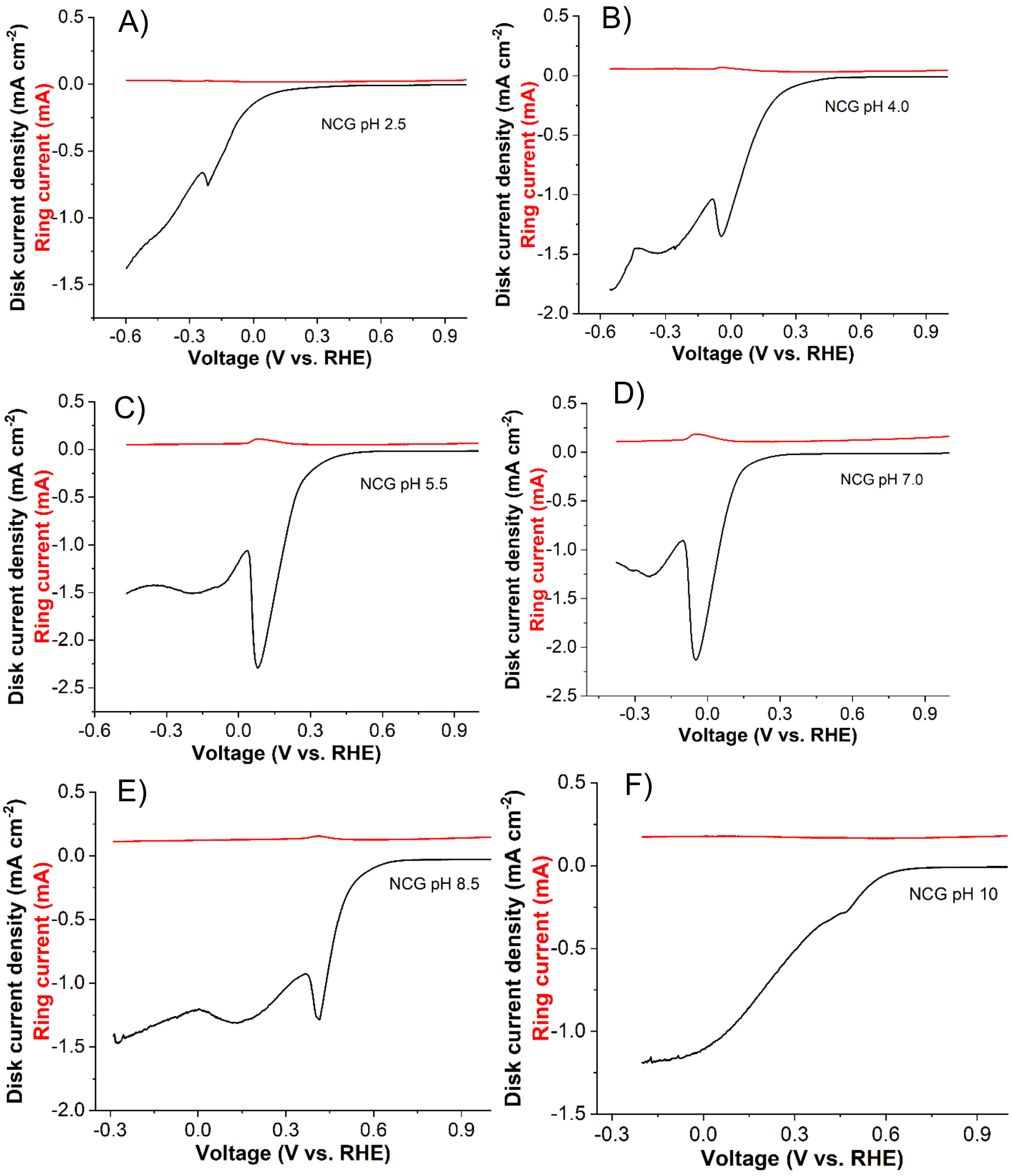

Figure 3.9: Electrocatalytic O_2 reduction by NCG at pH 2.5 (A), pH 4 (B), pH 5.5 (C), pH 7 (D), pH 8.5 (E), and pH 10 (F) on a rotating ring-disk electrode at 10 mV s^{-1} at 500 rpm.

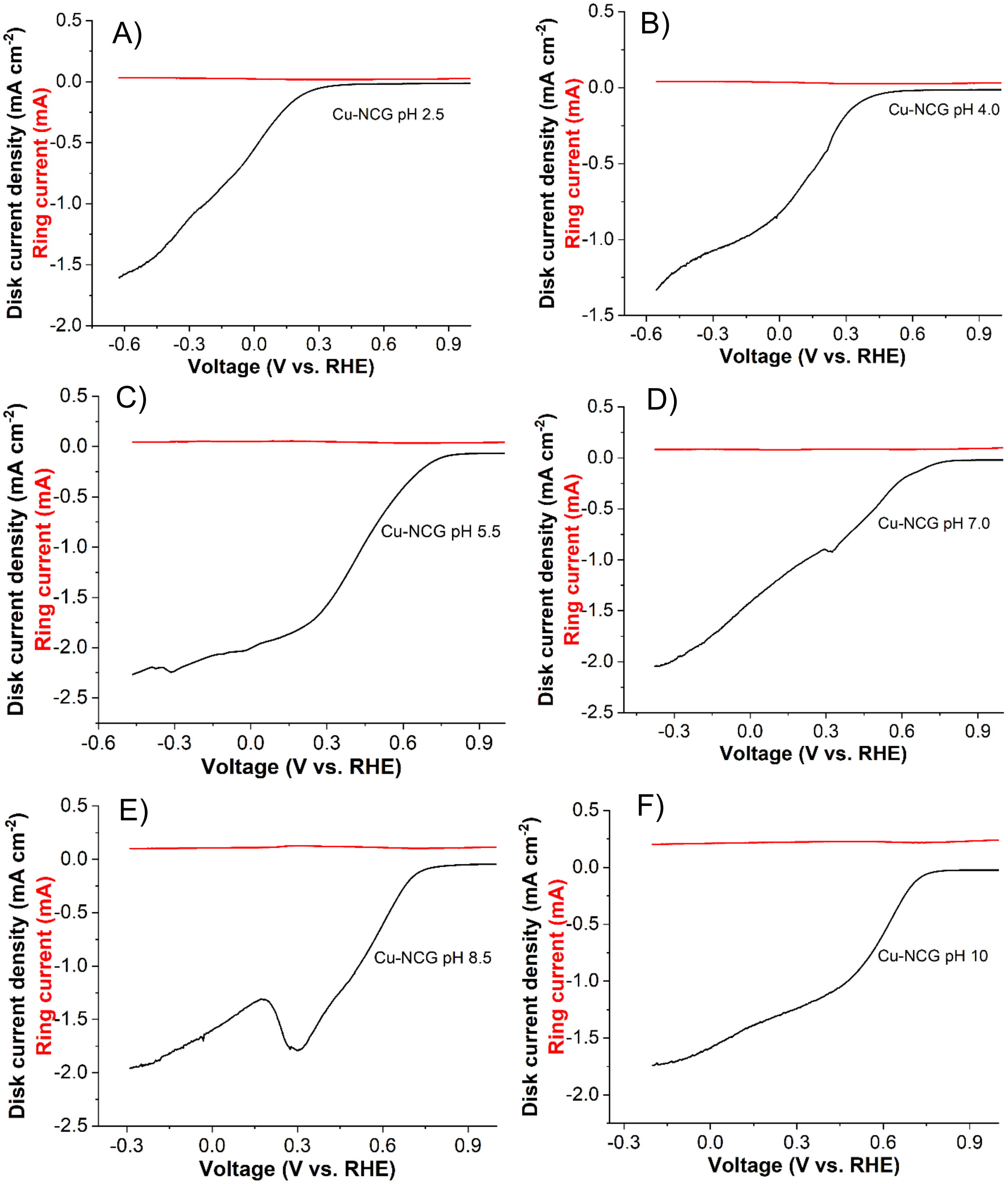

Figure 3.10: Electrocatalytic O_2 reduction by Cu-NCG at pH 2.5 (A), pH 4 (B), pH 5.5 (C), pH 7.0 (D), pH 8.5 (E), and pH 10 (F) on a rotating ring-disk electrode at 10 mV s^{-1} at 500 rpm.

Table 3.1: Onset potentials for peptide and Cu^{2+} peptide complexes vs. RHE as obtained from RRDE experiments.

pH	GSHAmide	Cu-GSHAmide	ECG	Cu-ECG	QCG	Cu-QCG	NCG	Cu-NCG
2.5	0.08	0.33	-0.10	0.37	0.13	0.31	0.00	0.21
4.0	0.10	0.39	-0.03	0.45	0.19	0.54	0.22	0.33
5.5	0.23	0.44	0.23	0.54	0.20	0.56	0.34	0.59
7.0	0.34	0.51	0.32	0.53	0.35	0.58	0.18	0.60
8.5	0.41	0.60	0.46	0.69	0.48	0.78	0.56	0.69
10	0.45	0.71	0.41	0.77	0.57	0.85	0.54	0.69

Representative RRDE plots for different Cu^{2+}-peptide complexes at pH 5.5 are displayed in Figure 3.11. Interestingly, there is a sharp peak in the O_2 reduction curve for the Cu-ECG complex at about -0.2 V, and although the origin of this peak is unknown, it is present at other pH values as well (Figure 3.6). Among the five Cu^{2+}-peptide catalysts studied, there are significant differences in ORR activity. For example, the maximum cathodic ORR current density at -0.45 V vs. RHE follows the order of Cu-NCG > Cu-QCG > Cu-ECG > Cu-GSHAmide ~ Cu-GSH. The observation that the disc voltammetry curves between Cu-GSHAmide and Cu-GSH are the most similar to one another is consistent with the interpretation that the active sites of the two catalysts are the same, and the modified glycine residue does not participate in Cu^{2+} binding. For this reason, we focus on relationships among the four catalysts with a C-terminal amide group (Cu-GSHAmide, CuECG, Cu-QCG, and Cu-NCG).

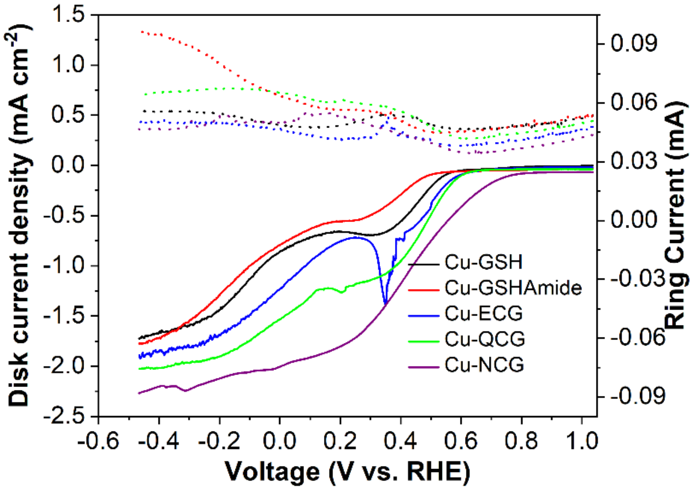

Figure 3.11: Electrocatalytic O_2 reduction by Cu-GSH (black line), Cu-GSHAmide (red line), Cu-ECG (blue line), Cu-QCG (green line) and Cu-NCG (purple line) in 1.2 M O_2-saturated Britton-Robinson Buffer at pH 5.5 using RRDE at 10 mV s^{-1} at 500 rpm. Solid line and dotted lines indicate the disk current density and ring current, respectively.

At this level of analysis, however, there is no obvious relationship between the structure of the five catalysts and their ORR current densities. In an attempt to determine the molecular origin of the differences in ORR current, we analyzed the measured currents on per mole of catalyst bases. The number of moles of catalyst in each case was calculated by integrating the Cu(II)/Cu(I) redox couple measured during voltammetry. Representative figure of Cu(II)/Cu(I) redox couple is shown in figure 3.12. We assumed that each peptide binds to Cu in a 1:1 ratio, which has been demonstrated previously to be true for CuGSH and a related Cu tripeptide complex.[31] ICP-MS measurements on the Cu complexes corroborate this assumption, which indicate that the Cu:S ratios in Cu-QCG, Cu-ECG, Cu-NCG, and Cu-GSHAmide are 1.02, 1.03, 0.94, and 1.04, respectively, all of which are close to the expected 1:1 ratio.

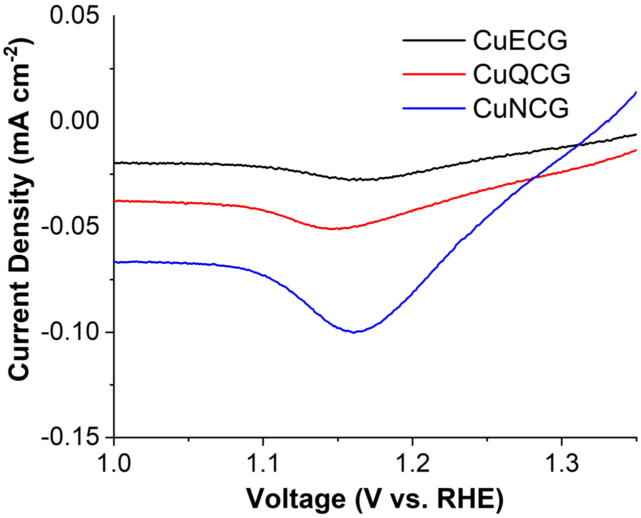

Figure 3.12: Representative LSVs at pH 5.5 showing the Cu(II) to Cu(I) transition that occurs before ORR.

At pH 5.5, the ORR currents per mole of catalyst follows the order of Cu-QCG > Cu-ECG > Cu-NCG > Cu-GSHAmide (figure 3.13). Although this order is different than the raw current density data, there is still no obvious trend (e.g. carboxylate side chains vs. amide side chains) between peptide structure and current. The complete set of data at all pH values for each current per mole of catalyst is displayed in Figure 3.13. The currents per mole of catalysts vary by a factor of more than 1,000. By comparison, the diffusion coefficients of the catalysts as determined by the Levich equation vary less than twofold, which is expected given the generally similar structure of the catalysts. Interestingly, the order of the currents across the five catalysts is different for each of the six pH values studied. These results suggest that there is a complicated relationship between catalyst activity, structure, and pH. Later in this chapter, we develop a model that takes into account Cu^{2+}-peptide binding strength and peptide aggregation to rationalize the observed trends in ORR current as a function of pH.

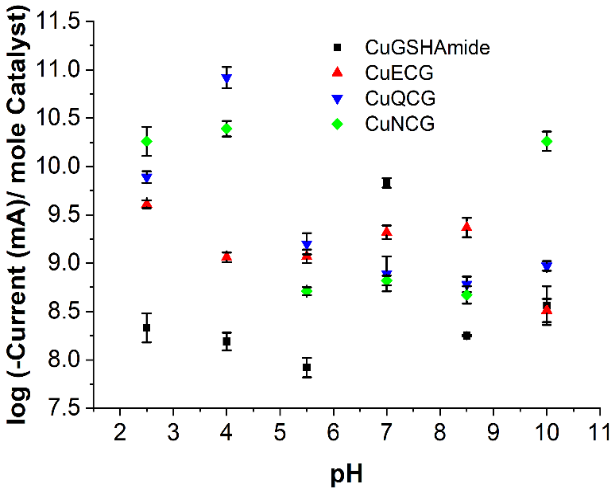

Figure 3.13: Logarithms of maximum ORR cathodic current per mole of catalyst measured during RRDE for Cu-GSHAmide (black), Cu-ECG (red), Cu-QCG (blue), and Cu-NCG (green) at different pH values.

In addition to the changes in the RRDE disc currents across the five catalysts that are reflective of ORR activity, there are also significant differences in the RRDE ring currents, which are reflective of ORR selectivity.[42-44] In aqueous electrolytes, the ORR can occur via a four-electron reduction pathway to produce H_2O or a two-electron reduction pathway to produce H_2O_2. The one-electron reduction of O_2 to superoxide generally does not occur in aqueous systems.[45] In fuel cells, the four-electron pathway to H_2O is desired because it gives the highest voltage output, and the reactivity of H_2O_2 limits device durability. By comparing the ring and disc currents and accounting for the collection efficiency of the ring, the average number of electrons transferred per O_2 during ORR can be determined assuming only the two- and four-electron pathways are operative.

Figure 3.14 displays the average number of electrons transferred per O_2 as calculated from the RRDE experiments at -0.9 V vs. Ag/AgCl across all five Cu^{2+}-peptide catalysts and pH values. In general, the number of electrons transferred per O_2 increases with pH. This trend indicates that the selectivities of the Cu^{2+}-peptide catalysts for H_2O production increase in higher pH electrolytes.

Enhanced selectivity with increasing pH has been observed previously for other classes of molecular Cu and other ORR catalysts.[46-51] For both Cu-GSH and Cu-GSHAmide, the number of electrons transferred increases from pH 2.5 to pH 5.5, then slightly decreases at pH 7 before increasing at higher pH values (Figure 3.14A). The observation that the trends of Cu-GSH and Cu-GSHAmide for ORR selectivities are the same across pH further supports the notion that modification of the glycine residue outside the Cu^{2+}-binding pocket does not significantly affect ORR activity.

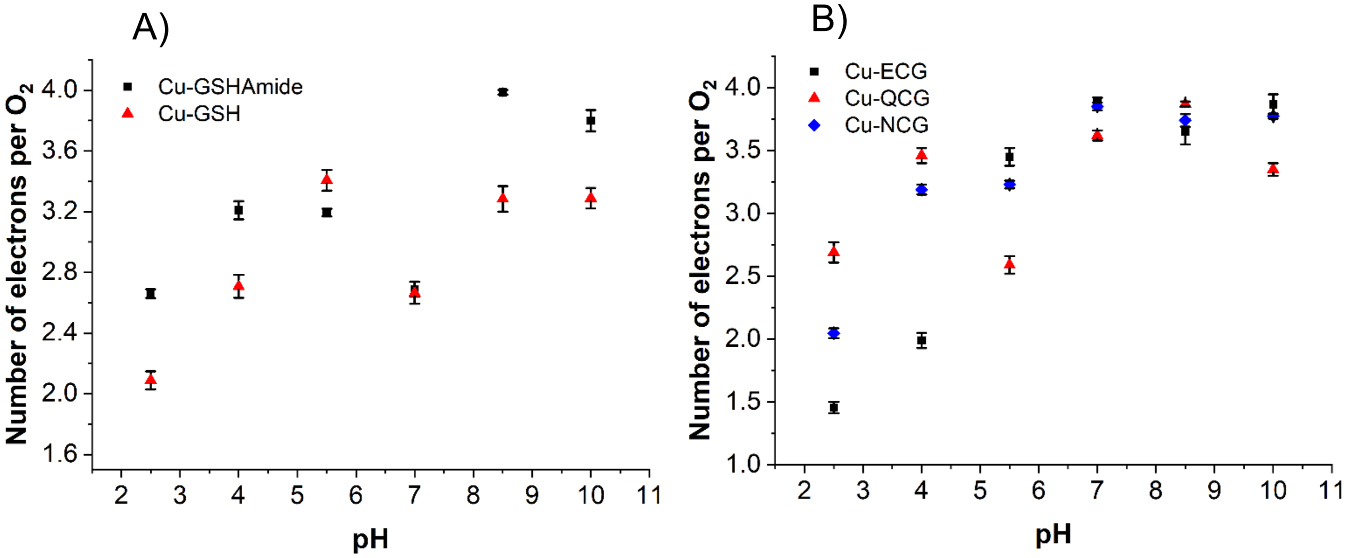

Figure 3.14: Number of electrons transferred per O_2 at -0.9 V vs. Ag/AgCl by Cu-GSHAmide (A, black points), Cu-GSH (A, red points), Cu-ECG (B, black points), Cu-QCG (B, red points), and Cu-NCG (B, blue points) as calculated from RRDE experiments.

The selectivities for the other three Cu^{2+} peptide catalysts also vary widely as a function of pH (Figure 3.14B). Notably, the number of electrons transferred for Cu-QCG at pH 4 is 3.46 ± 0.06, which is the highest value among the five catalysts at this pH. This result indicates that the Cu-QCG catalyst exhibits good selectivity for the four-electron reduction of O_2 to H_2O despite the low pH, which is uncommon for Cu-based ORR catalysts.[52,53]

3.3.3 Cu^{2+}-peptide Binding Measurements

In an attempt to understand the various relationships between pH, peptide structure, and catalyst performance, we first measured the Cu^{2+}-peptide binding constants using UV-Vis spectroscopy. Absorbance vs. mole equivalent of Cu^{2+} from UV-Vis spectroscopy for different peptides are shown in Figure 3.15 for the complexes.

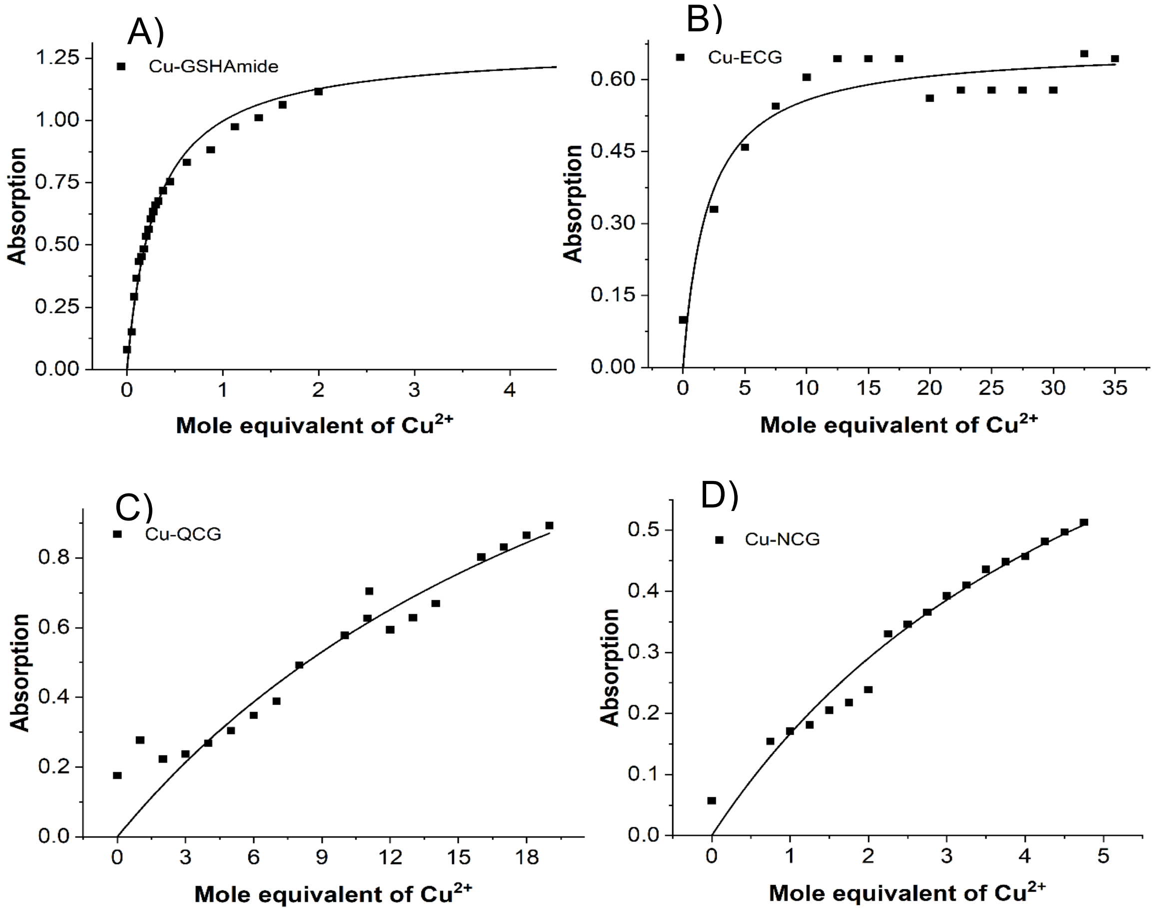

Figure 3.15: Absorbance vs. mole equivalent plots of Cu^{2+} with GSHAmide (A), ECG (B), QCG (C), and NCG (D).

Cu^{2+}-peptide binding constants values calculated from UV-Vis spectroscopy is represented in figure 16. Cu^{2+} binding to GSH is known to occur in a pocket that involves the thiol group of cysteine and the carboxylate and amine of glutamate. We find that the Cu^{2+}-binding constants to GSH and GSHAmide are similar, which is expected given that the two peptides only differ in whether or not the glycine residue, which is not directly involved in binding, contains an amide cap. In contrast, the Cu^{2+}-binding constant to ECG is significantly smaller than that of GSHAmide. Although the structures of these two peptides are similar, ECG contains a normal glutamate linkage, while GSHAmide contains a gamma glutamate linkage. This difference causes the amine group of the glutamate residue, which is protonated at neutral pH, to be closer to the thiol on the cysteine in ECG. Because protonated amines do not bind to Cu^{2+} due to electrostatic repulsion, this effect results in a decreased binding constant for Cu-ECG as compared to Cu-GSHAmide. Furthermore, the Cu^{2+}-binding constants for QCG and NCG are the lowest among all five Cu complexes. The weaker binding constants for these two peptides arise from the lack of carboxylate on the side chain of the N-terminal residue. In the other three Cu complexes, the carboxylate binds to Cu^{2+}, leading to increased binding constants. Lastly, the Cu^{2+}-binding constant to QCG is significantly lower than to NCG due to differences in the distance of the amide side chain to the Cu^{2+}-binding site. The amide is further away from the Cu^{2+}-binding site in QCG, which decreases the overall binding constant.

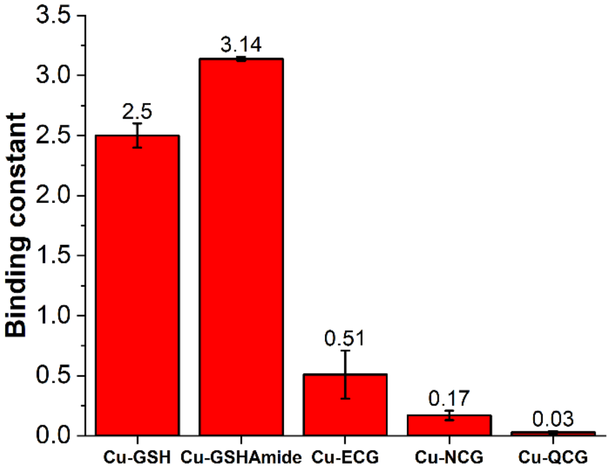

Figure 3.16: Binding constant of different Cu^{2+}-peptide complexes.

3.3.4 3.3.4. Infrared Spectroscopy and Peptide Aggregation

In addition to evaluating Cu^{2+}-peptide binding constants, we utilized infrared spectroscopy to quantify the total peptide aggregation as the main peptide structural component. Since the amide

I absorption band is primarily derived from backbone carbonyl stretching vibrations with some NH bending, it has been extensively used to characterize the amount of native structure present in protein and peptide systems including aggregation.[52-54] This sensitivity to peptide structure results from the excitonic coupling of the carbonyl modes along the backbone,[55,56] hydrogen bonding,[57] and degrees of hydration.[58,59] Upon aggregation, it is therefore expected that the peptide stacking, increased hydrogen bonding, and the degree of exposure to water of the amide group of the peptide will have a profound effect on, not only the vibrational frequency of the amide I, but also the FWHM of the observed peaks.

Two of the main absorption bands, observed at ~1620 cm^{-1} and ~1680 cm^{-1} in the infrared spectrum, correspond to the formation of in-phase and out-of-phase anti-parallel β-sheets, respectively. The vibrational frequency and amplitude of the transition at ~1680 cm^{-1} are not sensitive to the size of the sheets. However, the opposite is true of the ~1620 cm^{-1} band, which is sensitive to the dimensions of the sheets.[39,60,61] This effect is largely due to the in-phase oscillation of the residues in-register between strands having a transition dipole perpendicular to the β-strands.[61] To quantify the amount of aggregation present, the parameters associated with these two absorption bands are determined by Gaussian peak fitting of the infrared spectrum. Although both absorption bands are often present in the infrared spectrum of aggregates, it appears that out-of-phase anti-parallel β-sheets were more pronounced in the spectra of the peptide alone, while the infrared spectra of the peptide bound to the Cu^{2+} in the complex showed more in-phase anti-parallel β-sheets.

In Figure 3.17, the fitting of the lower frequency aggregation band as a function of pH is shown for the Cu-NCG complex in D_2O exchanged Britton-Robinson buffer solution.

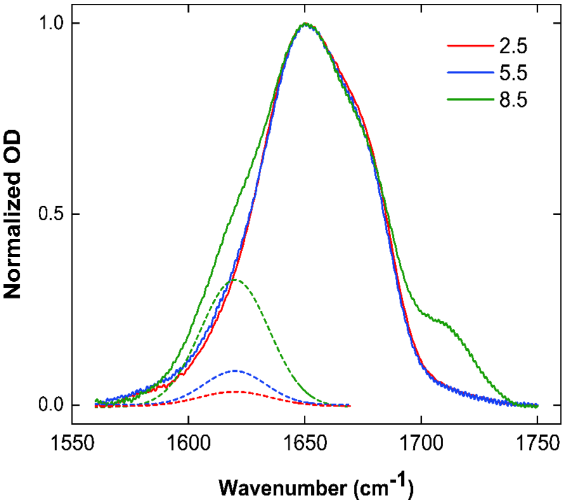

Figure 3.17: Representation of typical normalized infrared spectrum of peptide complexes, Cu^{2+}-NCG. The dotted lines demonstrate the increase of the aggregation peak, 1620 cm-1, at the indicated pH values.

The total peak fitting reveals three distinct absorption bands: the two aggregation bands at ~1620 cm^{-1} and ~1680 cm^{-1} with another absorption band at ~1650 cm^{-1} due to the presence of random coil.[53,62] The pH dependency of aggregations bands and Gaussian peak fitting of different components of the amide I band for different tripeptides and Cu^{2+}-tripeptides complexes are discussed in bellow:

Figure 3.18 shows the pH dependency of aggregation bands at 1620 cm^{-1} and 1605 cm^{-1} of GSHAmide and Cu-GSHAmide in 0.1 M Britton-Robinson Buffer solution, respectively. The GSHAmide peptide and Cu^{2+}-peptide complex aggregation increased significantly with increasing pH.

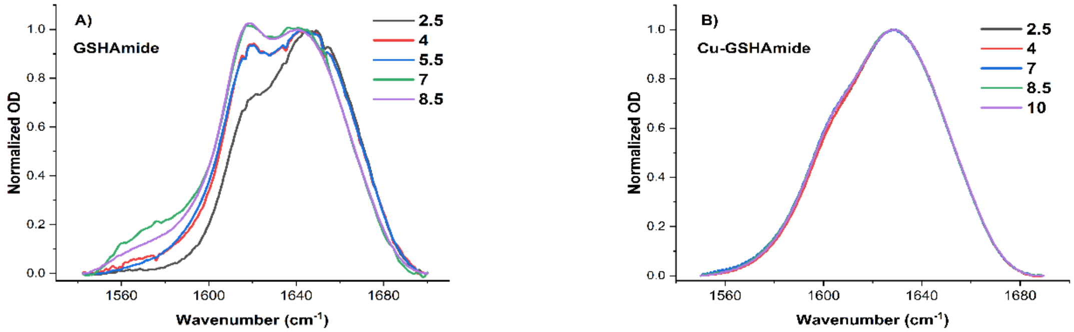

Figure 3.18: Normalized IR spectra of GSHAmide and the Cu-GSHAmide complex at different pHs.

Figure 3.19 shows the results of the Gaussian peak fitting of the different components of the amide I band of GSHAmide as a function of pH in D_2O exchanged Britton-Robinson Buffer solution. The graphs below show an increase in in-phase aggregation with increasing buffer pH at 1620 cm^{-1}.

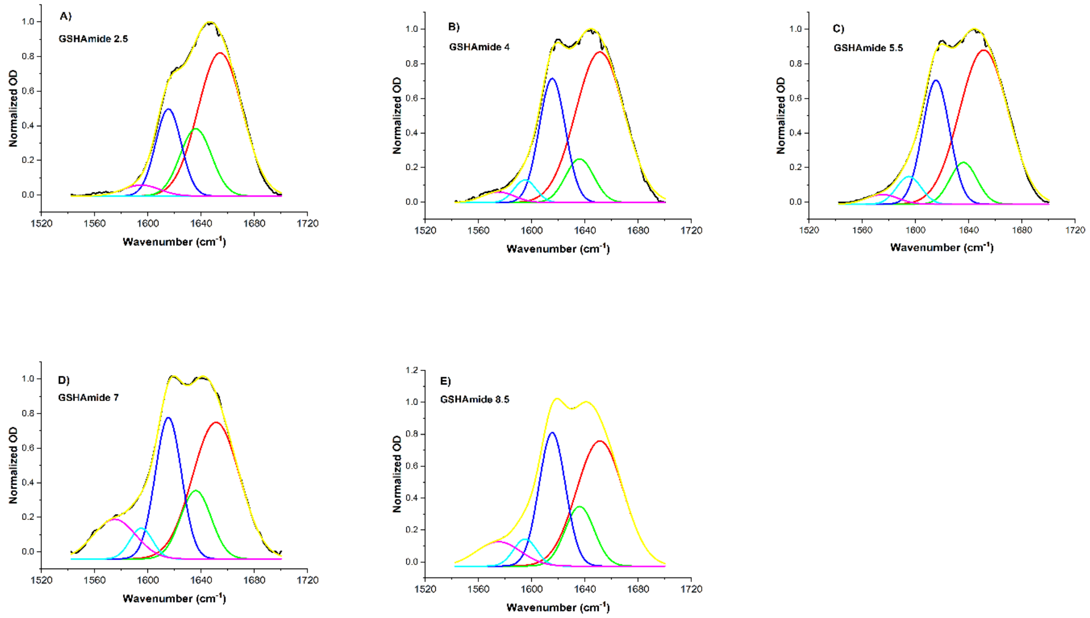

Figure 3.19: Gaussian peak fitting of the infrared spectra of GSHAmide at different pHs.

Figure 3.20 shows the Gaussian peak fittings of the amide I bands of Cu-GSHAmide as a function of pH in D_2O exchanged Britton-Robinson Buffer solution. Based on the graphs below, in-phase aggregation at 1605 cm^{-1} increases with increasing pH. Note that the in-phase aggregation band slightly shifted to lower frequencies in the Cu-GSHAmide complexes as opposed to the 1620 cm^{-1} band observed for other peptides and complexes.

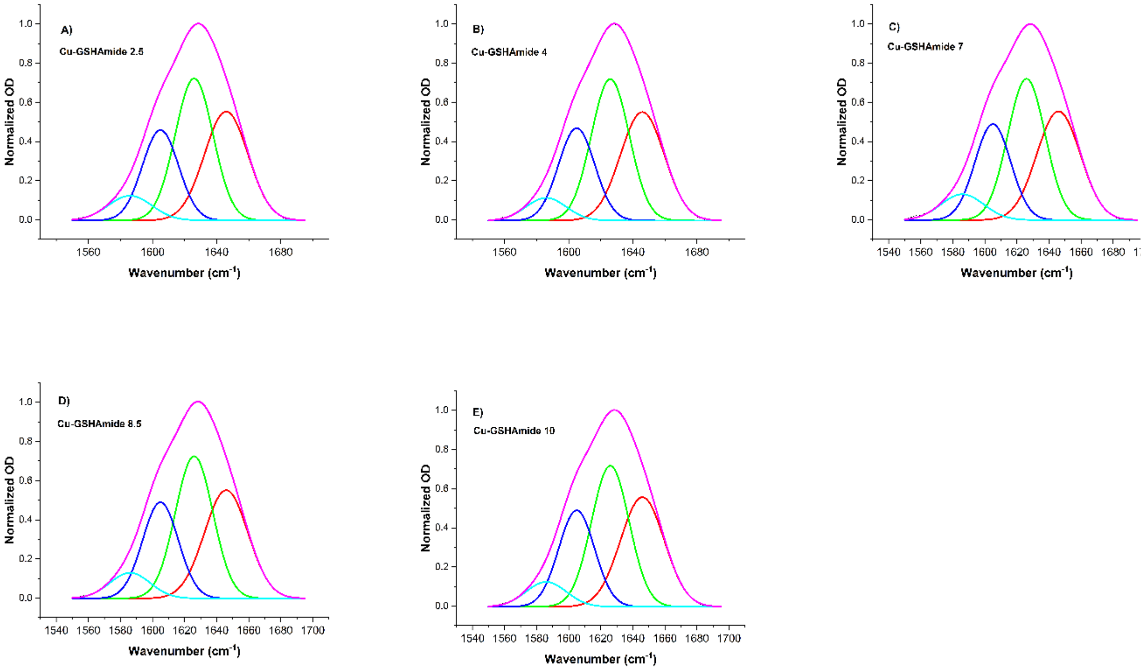

Figure 3.20: Gaussian peak fitting of the infrared spectra of Cu-GSHAmide at different pHs

Figure 3.21 displays pH-dependent aggregation bands of ECG and Cu-ECG in 0.1 M Britton-Robinson Buffer solution at 1680 cm^{-1} and 1620 cm^{-1}, respectively. Increasing pH significantly decreased peptide and Cu^{2+}-peptide aggregation at 1680 cm^{-1}. Cu-ECG showed the opposite direction in terms of pH dependence for the in-phase distribution of species, i.e. aggregation decreased as pH increased.

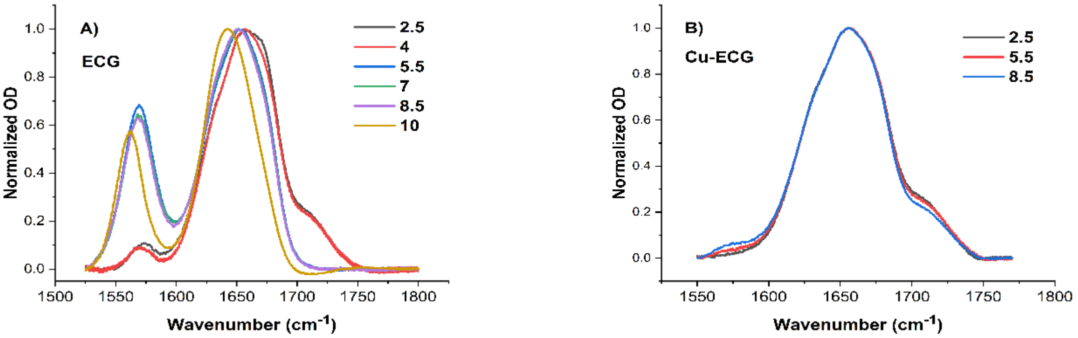

Figure 3.21: Normalized IR spectra of ECG and Cu-ECG complex at different pHs.

Figure 3.22 shows the results of the Gaussian peak fitting of the different components of the amide I band of ECG as a function of pH in D_2O exchanged Britton-Robinson Buffer solution. The graphs below shows a decrease in out-of-phase aggregation with increasing buffer pH at 1680 cm^{-1}. The 1620 cm^{-1} aggregation band remained relatively unchanged with respect to pH.

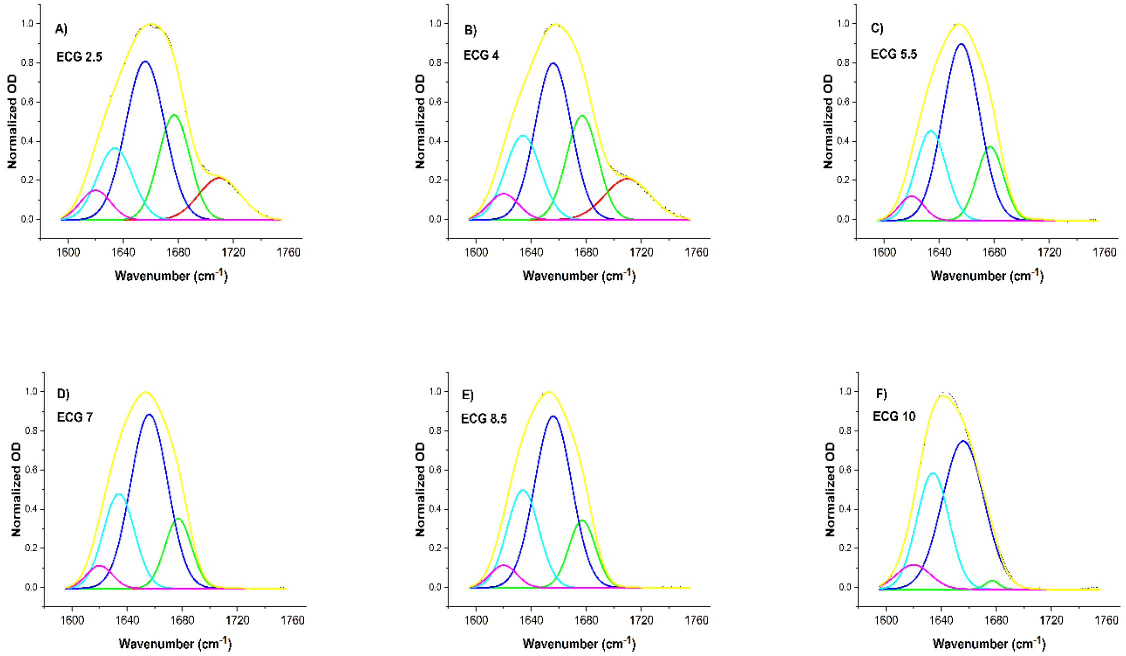

Figure 3.22: Gaussian peak fitting of the infrared spectra of ECG at different pHs.

Figure 3.23 shows the results of the Gaussian peak fitting of the different components of the amide I band of Cu-ECG complex as a function of pH in D_2O exchanged Britton-Robinson Buffer solution.

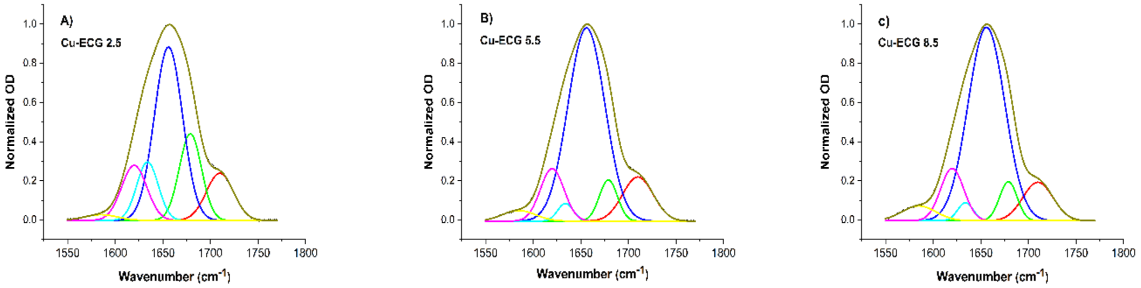

Figure 3.23: Gaussian peak fitting of the infrared spectra of Cu-ECG at different pHs

Figure 3.24 shows pH-dependent aggregation bands of QCG and Cu-QCG in 0.1 M Britton-Robinson Buffer solution. For QCG in solution, the aggregation band at 1680 cm^{-1} grows as the pH increases. Cu-QCG did not show significant change in aggregation with respect to pH.

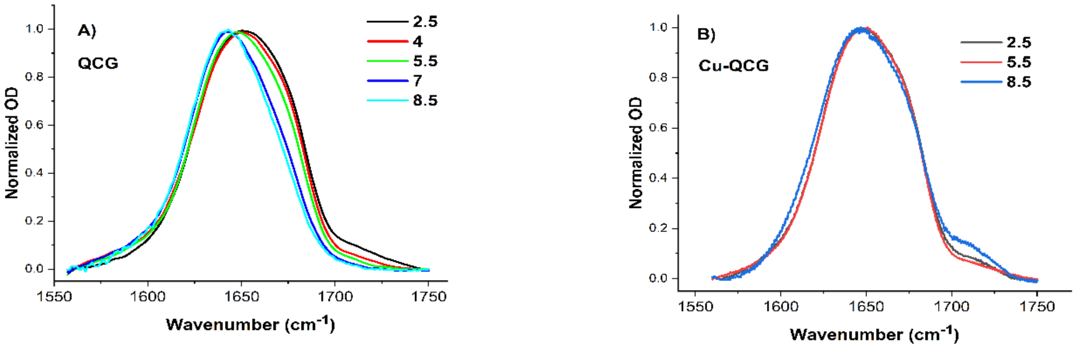

Figure 3.24: Normalized IR spectra of QCG and Cu-QCG complex at different pHs.

Figure 3.25 shows the results of the Gaussian peak fitting of the different components of the amide I band of QCG as a function of pH in D_2O exchanged Britton-Robinson Buffer solution. The QCG peptide demonstrated the least amount of aggregation for both the 1620 cm^{-1} and 1680 cm^{-1} bands.

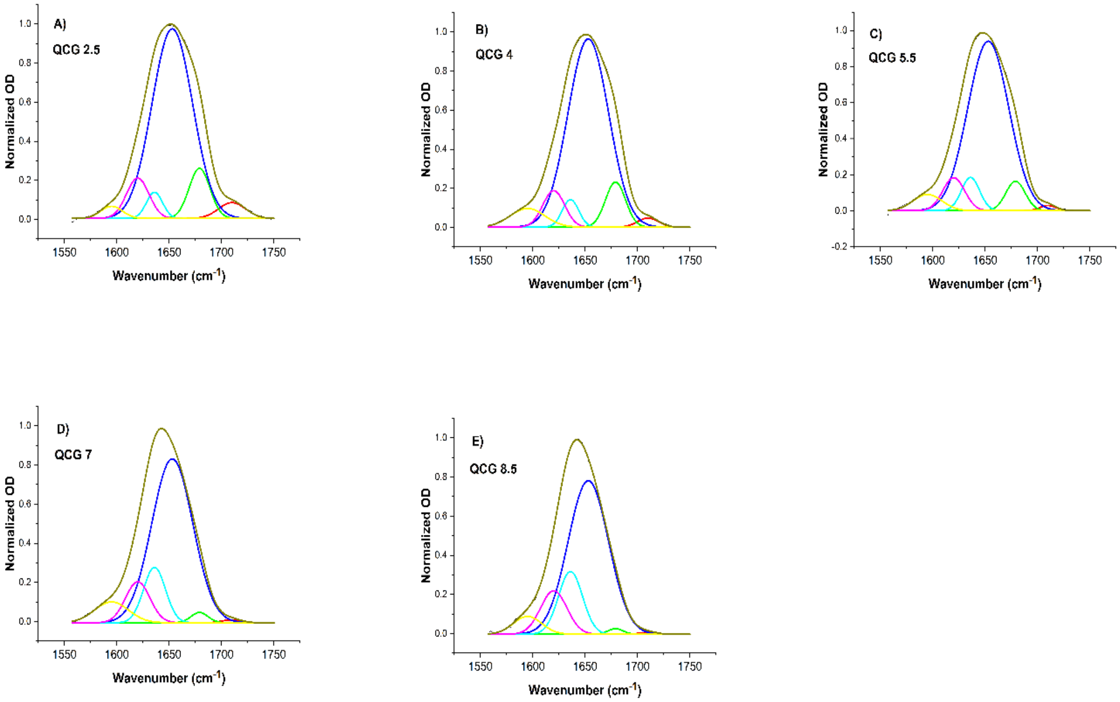

Figure 3.25: Gaussian peak fitting of the infrared spectra of QCG at different pHs.

Figure 3.26 shows the results of the Gaussian peak fitting of the different components of the amide I band of the Cu-QCG complex as a function of pH in D_2O exchanged Britton-Robinson Buffer solution. Cu-QCG shows minimal changes with respect to pH.

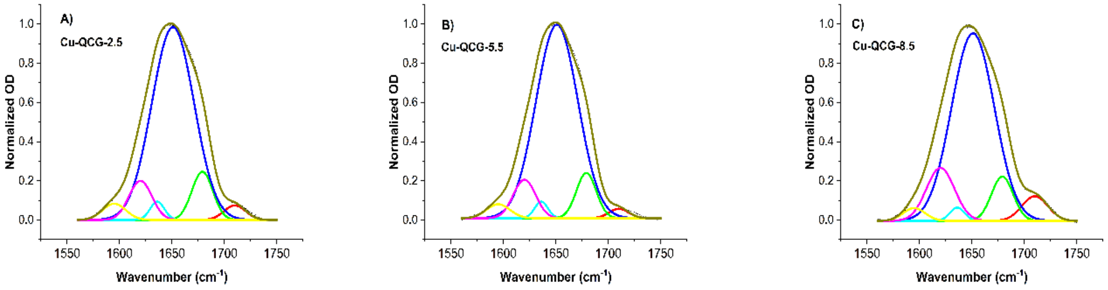

Figure 3.26: Gaussian peak fitting of the infrared spectrum of Cu-QCG at different pHs.

Figure 3.27 shows pH-dependent aggregation bands of NCG and Cu-NCG in 0.1 M Britton-Robinson Buffer solution. While NCG alone shows a significant pH dependency for the out-of-phase aggregation band at 1680 cm^{-1}, the Cu-NCG complex showed the highest aggregation amount at 1620 cm^{-1}.

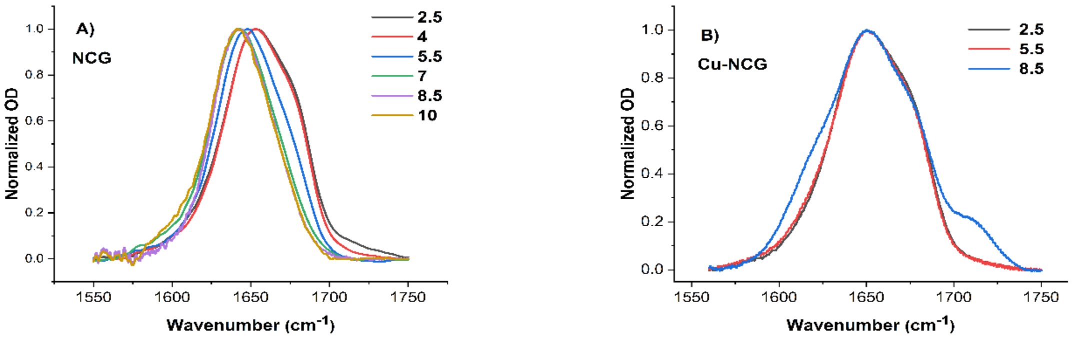

Figure 3.27: Normalized IR spectra of NCG and Cu-NCG complex at different pHs.

Figure 3.28 shows the results of the Gaussian peak fitting of the different components of the amide I band of NCG as a function of pH in D_2O exchanged Britton-Robinson Buffer solution.

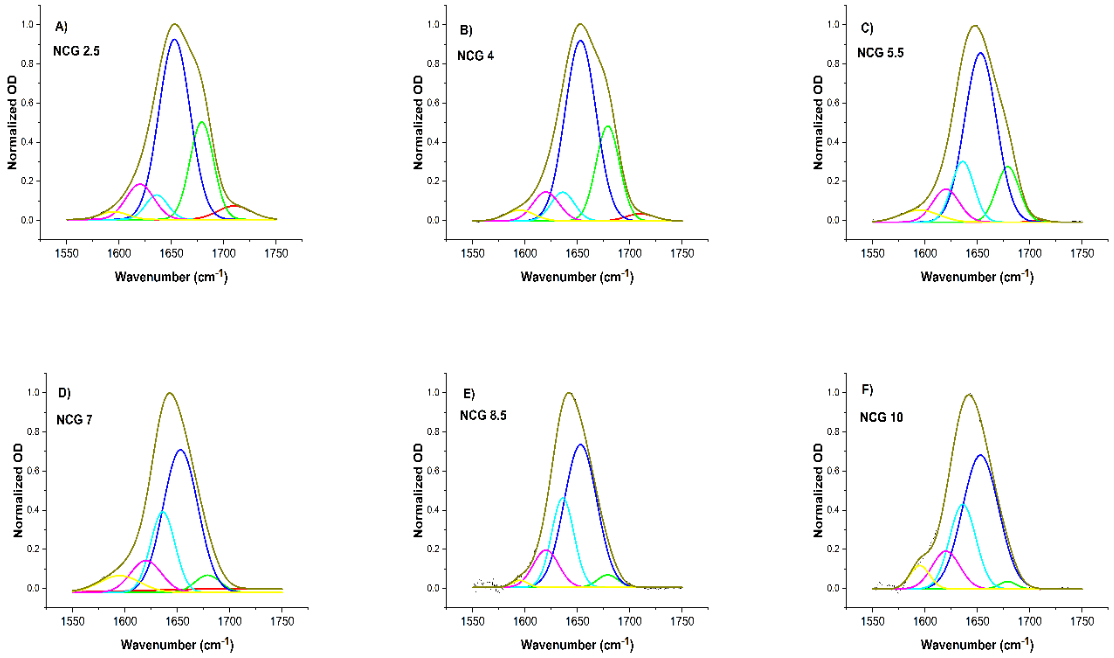

Figure 3.28: Gaussian peak fitting of the infrared spectra of NCG at different pHs.

Figure 3.29 shows the results of the Gaussian peak fitting of the different components of the amide I band of the Cu-NCG complex as a function of pH in D_2O exchanged Britton-Robinson Buffer solution.

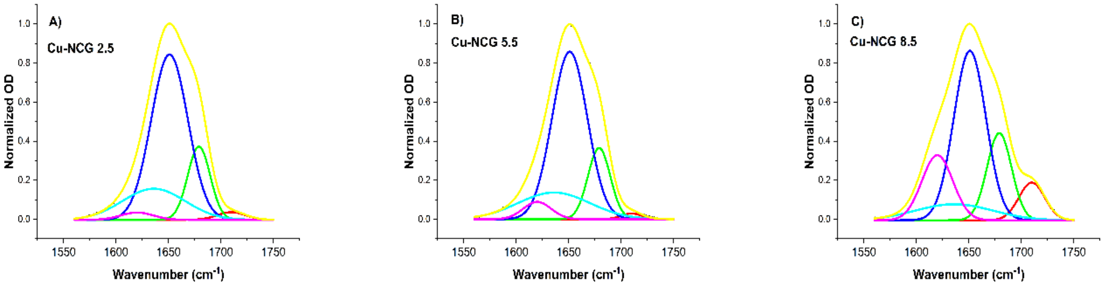

Figure 3.29: Gaussian peak fitting of the infrared spectra of Cu-NCG at different pHs.

In figure 3.17, two smaller additional absorption bands are observed at ~1710 cm^{-1} and <1600 cm^{-1} originating from the carboxylic group protonation and deprotonation states, respectively. The infrared spectra of the GSHAmide, ECG, and QCG peptides exhibited similar number of peaks at the same frequencies, but different amplitudes and FWHM for the varying levels of aggregation.

According to aggregation analysis of QCG, NCG, ECG, and GSHAmide peptides alone (without Cu^{2+} present), the absorption bands, observed at ~1680 cm^{-1} and ~1620 cm^{-1}, clearly show a dependence on pH. At an initial pH, the infrared spectrum of each peptide was divided into Gaussian components via least squares fitting. Then, the peptide aggregation level was quantified by fixing the vibrational frequencies of the peaks for all amide I transitions and varying the amplitude and FWHM of each peak for a given pH (Figures 3.30-3.31).

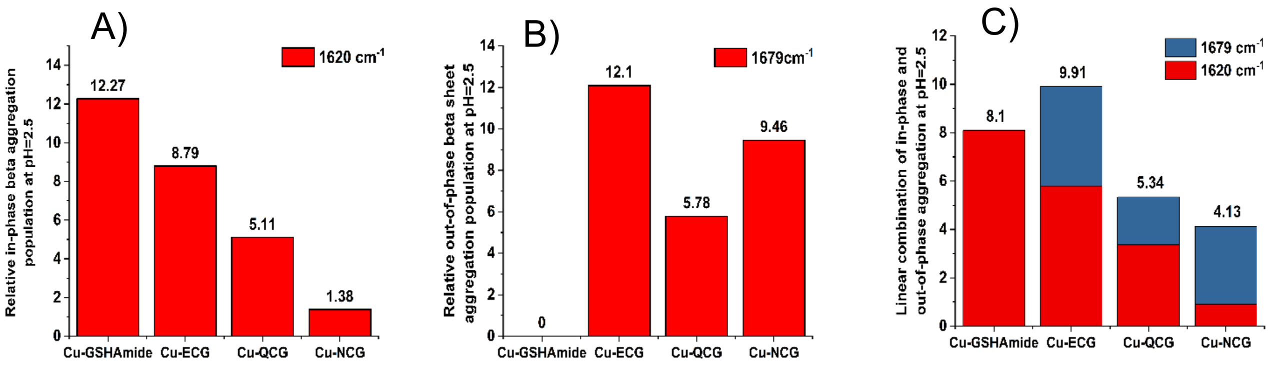

Figure 3.30: Relative aggregation analysis for Cu^{2+}-peptide complexes at pH=2.5

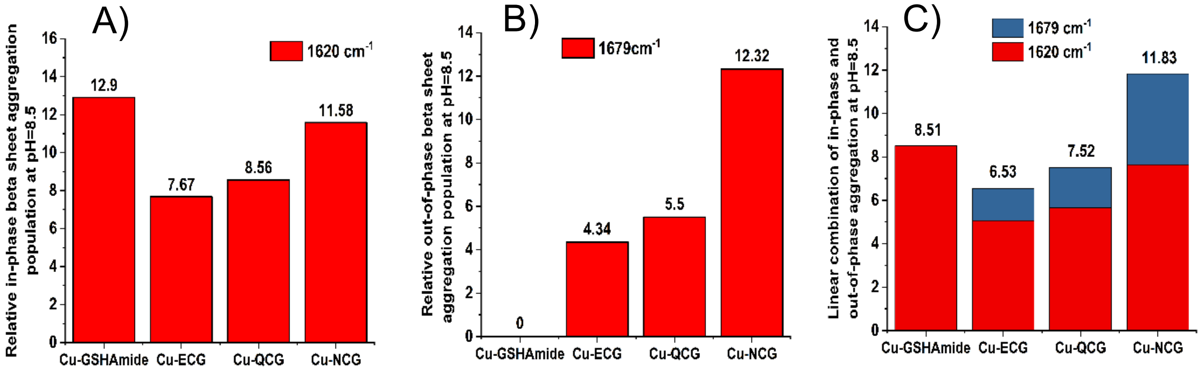

Figure 3.31: Relative aggregation analysis for Cu^{2+}-peptide complexes at pH=8.5

When the pH was decreased from 10 to 2.5 for the NCG, QCG, and ECG peptides, an increase in intensity of the out-of-phase antiparallel β-sheet transition, 1680 cm^{-1}, was observed (Figure 3.32B). However, the 1620 cm^{-1} transition remained mostly invariant, likely due to the peptides in solution forming small sized less ordered aggregates (Figure 3.32A).[61] NCG demonstrates the most sensitivity to pH changes followed by ECG, while QCG had the least variation as well as the least total aggregation population. These results indicate that the aggregate formation is likely aided by the neutralization of the charges on the sidechains at lower pHs for easier β-strand stacking despite steric effects of the longer sidechains. On the other hand, the shorter asparagine (N) sidechain of NCG acts as another possible hydrogen bond to stabilize the β-sheet stacking.

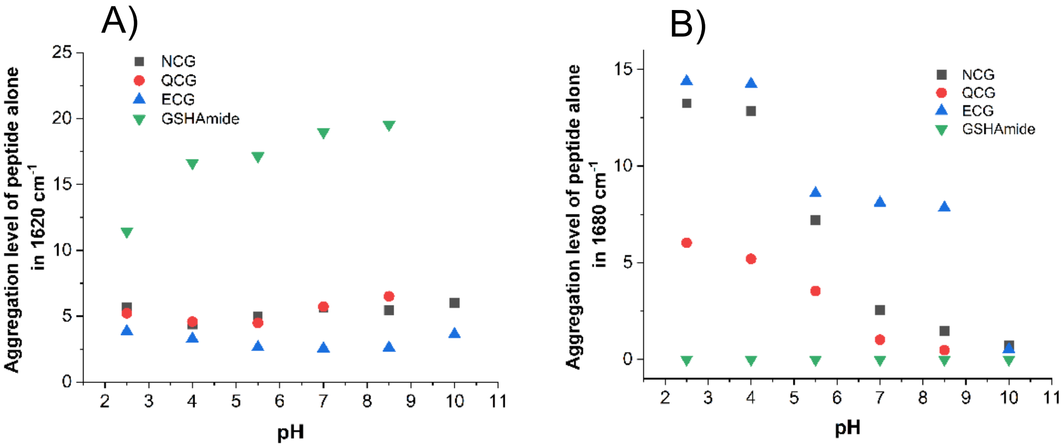

Figure 3.32: Aggregation level analysis of peptides in 0.1 M Britton-Robinson Buffer solution at different pHs.

In contrast to NCG, QCG, and ECG peptides, the infrared spectra of the GSHAmide peptide displays in-phase aggregation at ~1620 cm^{-1} without the presence of the 1680 cm^{-1} absorption band. This result suggests that the gamma linkage may allow for better stacking of the β sheets in solution and provides better ordering of hydrogen bonding. As further evidence of this phenomenon, the GSHAmide peptide aggregation showed reverse dependence on change of pH, increasing significantly with higher pH. As in the NCG above, the higher pH would afford more in-register hydrogen bonding across the gamma linkage providing better β-strand stacking. In general, Figure 3.33 illustrates the highest total aggregation population of each peptide in solution varies in the following way: GSHAmide > NCG > ECG > QCG. This overall trend coincides with the physical interpretations discussed above.

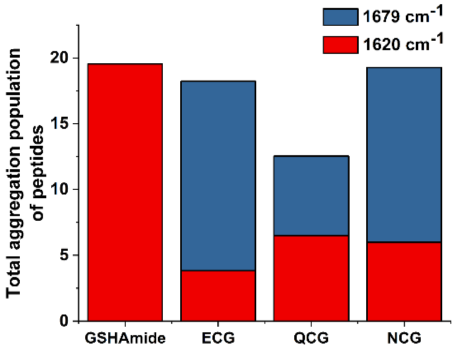

Figure 3.33: Total aggregation population of peptides in 0.1 M Britton-Robinson Buffer solution.

In the presence of Cu^{2+}, the peptides undergo significant changes in the types of aggregates formed, indicated by the increase in the absorption band at ~1620 cm^{-1}. As mentioned above, the amplitudes of the 1620 cm^{-1} transitions signify the presence of a much larger size and ordered β-strand stack.[61] The ability of the metals to trigger aggregation formation is not uncommon, especially for Cu^{2+} ions.[63-66] Using a similar aggregation analysis as above, the Cu^{2+}-peptide complexes were assessed for the total population aggregation. In QCG, ECG, and NCG Cu^{2+}-peptide complexes, the in-phase beta-sheet (frequency distributions at ~1620 cm^{-1}) increases as the pH increases with the exception of ECG. Cu-ECG, due to the repulsive effect of the carboxylate sidechain at high pH, demonstrates the most aggregation at lower pH. The 1680 cm^{-1} aggregation band remains relatively independent of the protonation states of surrounding solvent molecules. Cu-ECG demonstrates the most sensitivity to pH as observed in this high frequency aggregation band due to the removal of the charge of the carboxylate sidechain leading to the highest total aggregation population at low pH (Figure 3.30C).

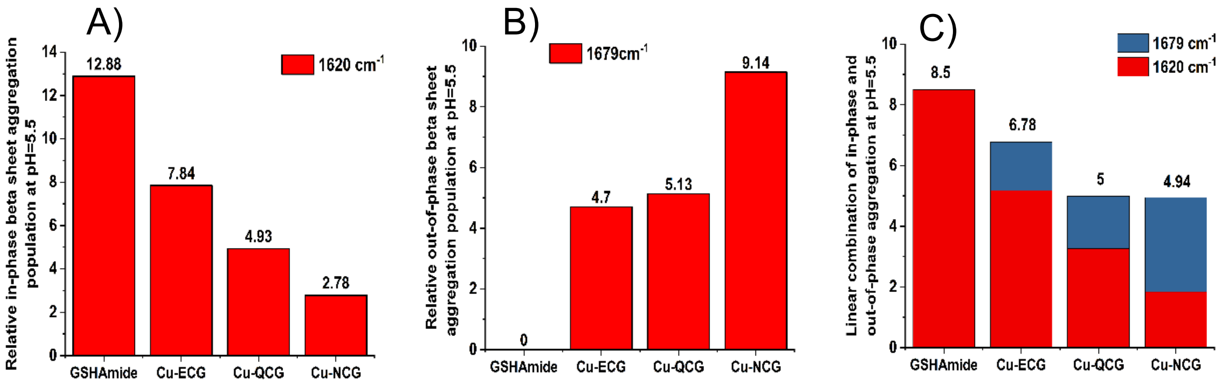

Figure 3.34: Relative aggregation analysis for Cu^{2+}-peptide complexes at pH=5.5

To compare the total aggregation population in the all Cu^{2+}-peptide complexes, the percentages (i.e. coefficients) of each contributing aggregation band were obtained from the model of the catalytic behavior. A resultant linear combination of 66% and 34% of the two aggregation bands were used to assess the overall trends in total aggregation population at pH = 5.5 (Figure 3.34C) (other pHs are shown in Figures 3.30C and 3.31C). This analysis at pH = 5.5 indicates the following ordering of total aggregation population: Cu-GSHAmide > Cu-ECG > Cu-QCG > Cu-NCG (Figure 3.34C). However, the Cu^{2+}-NCG peptide displayed the highest aggregation potential overall at high pH (Figure 3.31C), while the Cu^{2+}-GSHAmide was equally large independent of the pH (Figure 3.30C and 3.31C). This trend is similar to the peptides alone, and overall expected because the gamma linkage and the shorter sidechain would likely enhance the in-register hydrogen bonding during stacking. The Cu^{2+}-ECG has the next largest aggregation population at the lowest pH, which becomes inhibited at higher pHs due to repulsion of the carboxylate. Lastly, the Cu-QCG tends to be the least prone to aggregation.

Finally, after understanding the above trends of the peptides with sequence and pH, we wanted to determine if the aggregation of the peptides in solution correlated to the total aggregation population of the Cu^{2+}-peptide complexes. As seen in Figure 3.35, a clear trend was observed between the smaller unordered solution phase aggregates and the larger ordered aggregates found in the Cu^{2+}-peptide complexes. Figure 3.35 was produced by applying point for point analysis of each peptide starting at the highest aggregation population found in solution versus the highest total aggregation population found in the complex. Then, the next highest aggregation points were added to the plot and so on. This linear correlation plot indicates that the short peptides can first be assessed for their likelihood to aggregate in solution alone to screen the one most advantageous ones for catalytic behavior. For example, later in this manuscript, we demonstrate how a model accounting for catalyst aggregation is a good predictor of catalytic current. Ultimately, these relationships between peptide aggregation, Cu^{2+}-peptide complex aggregation, and catalyst activity could allow for a reduction in the number of systems needed for screening to discover new active catalysts.

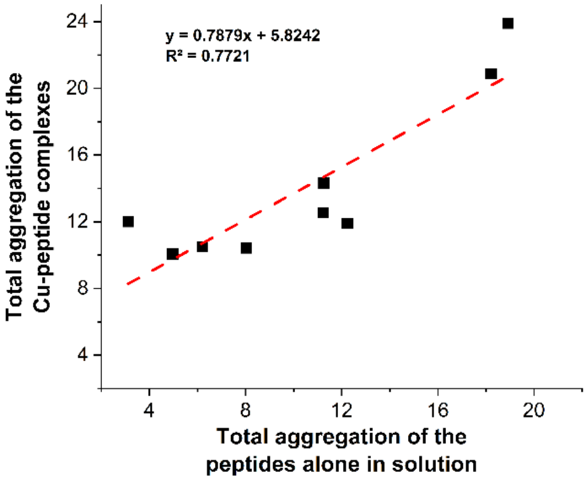

Figure 3.35: Total aggregation population of the Cu^{2+}-peptide complexes vs total aggregation population of the peptide alone.

3.3.5 Modeling Catalyst Performance

Considering both the Cu^{2+}-binding constants and aggregation of the Cu^{2+}-peptide complexes, we now seek to understand the physicochemical origins of the various electrocatalytic activities of the Cu^{2+}-peptide catalysts in different pH buffers. To more readily identify possible trends between catalytic activity, binding constants, and the degrees of complex aggregation, we quantified all of these attributes on a normalized scale from 0 to 1 across the four Cu complexes with C-terminal amide-capped peptides and across varying pH. For Cu^{2+}-binding constants and complex aggregation metrics, a value of 0 represents the weakest binding constant and smallest amount of aggregation, while a value of 1 represents the strongest binding constant and largest quantity of aggregation. Similarly, electrocatalytic ORR metrics were also normalized. A value of 0 represents the lowest selectivity for H_2O production and the lowest current on a per catalyst basis, while a value of 1 represents the highest selectivity for H_2O production and the highest current on a per catalyst basis. We call these sets of normalized values "scores."

When considered individually, there is no evident correlation between catalyst selectivity scores or catalyst current scores and binding constant scores or aggregation scores. For this reason, we considered linear combinations of binding constant and aggregation scores to model the electrochemical data. Specifically, we considered all possible linear combinations of binding constant and aggregation scores with weighting values in increments of 1% for both catalyst selectivity and catalyst current (see the "Modeling" portion of the "Experimental" section for more details).

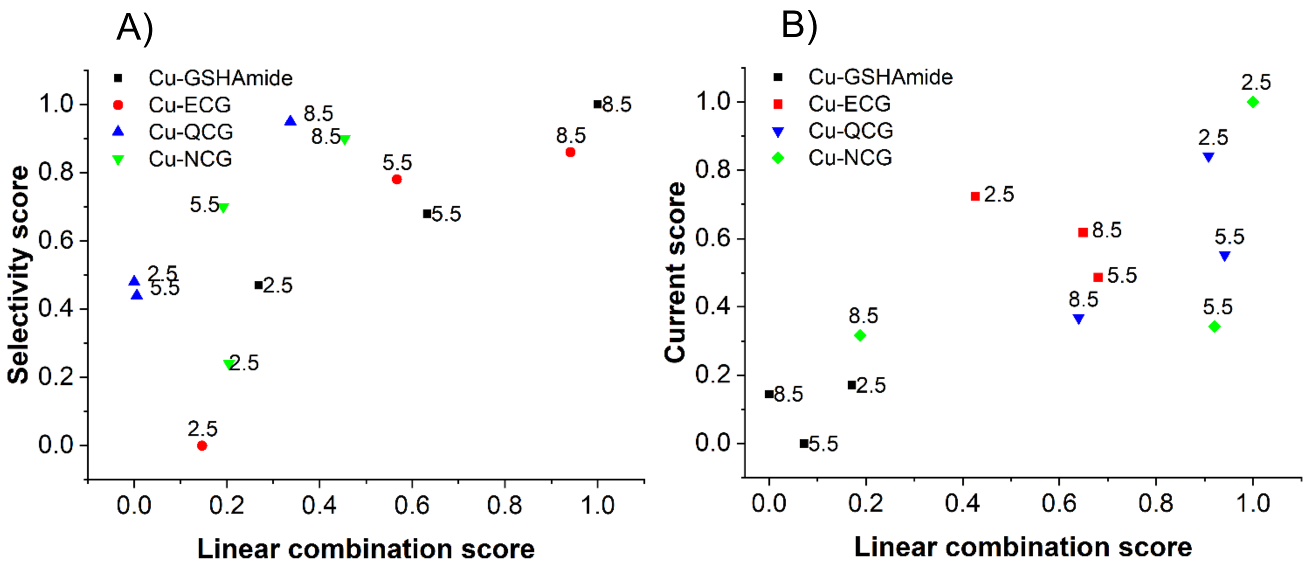

Figure 3.36: Comparison of catalyst ORR selectivity scores (A) and ORR current scores (B) of the four Cu complexes with C-terminal amide-capped peptides at various pH values and scores calculated from best-fit models that account for the strength of Cu^{2+} binding and peptide aggregation.

For catalyst selectivity, the best-fit model is a linear combination consisting of a 89% weighting for the binding constant scores and a 11% weighting for the aggregation scores. In this model, the binding constants increase as the selectivities increase, and the degrees of aggregation decrease as the selectivities increase. For catalyst current, the best-fit model is a linear combination consisting of a 16% weighting for the binding constant scores and a 84% weighting for the aggregation scores. In this model, both the binding constants and the degrees of aggregation decrease as the currents increase. These two models based on binding constant and aggregation fairly accurately predict catalyst selectivity and catalyst current (Figure 3.36).

Aside from being predictive of electrocatalytic activity, the results of these two models can be rationalized from a physical chemistry perspective. First, the selectivity model suggests that well-defined Cu complexes with stronger Cu^{2+}-binding constants that are relatively non-aggregated possess a narrower range of reactivity, which results in more selective ORR catalysis (Figure 3.36A). Second, the current model suggests that loose binding and less aggregation allows for fast electron transfer, which enhances catalytic current (Figure 3.36B). In other words, tightly bound Cu adducts have a lower propensity to bind to O_2, which decreases current. Similarly, more aggregated active sites could both decrease O_2 mass transfer and decrease electron transfer, also decreasing current.

3.3.6 Design Rules for Cu^{2+}-peptide ORR Catalysts

These models give rise to important and clear design rules for promising ORR fuel cell catalysts based on Cu^{2+}-peptide complexes that are both highly selective for the four-electron reduction of O_2 to water and that can operate at high rates. To design selective catalysts, complexes with relatively strong Cu^{2+} binding constants and weak peptide aggregation should be targeted. This set of design rules should also lead to catalysts that display relatively fast ORR kinetics. Even though strong Cu^{2+} binding constants are predicted to decrease catalytic current density, the weighting factor of the current density model as it relates to binding is small (16%), and so the advantageous effect of weak peptide aggregation in promoting catalytic current should outweigh the detrimental effect of tighter binding. In other words, our results imply that researchers should target Cu^{2+}-peptide complexes with strong binding constants and weak peptide aggregation to further develop a promising class of non-precious metal ORR catalysts that simultaneously exhibit high selectivity and fast kinetics.

3.4 Conclusions.

A series of novel Cu^{2+} complexes of tripeptides, inspired by glutathione, were investigated as electrocatalytic ORR catalysts using rotating ring-disk electrochemistry. The tripeptide complexes studied and compared are Cu-GSH, Cu-GSHAmide, Cu-ECG, Cu-NCG, and Cu-QCG, each of which has varying catalytic activity with respect to solution pH. The selectivity and kinetic parameters of the catalysts were evaluated using rotating ring-disk electrochemistry. Using binding constant measurements and quantitative peptide aggregation measurements obtained from infrared spectroscopy, we explain trends in both the selectivities and current densities of the Cu^{2+}-peptide electrocatalysts. In particular, our modeling indicates that Cu^{2+}-peptide complexes with relatively strong binding constants and weak peptide aggregation facilitates fast and selective catalyst formation for the four-electron reduction of O_2 to water. We anticipate that this fundamental insight into catalyst design should aid in the development of future highly-active non-precious metal ORR electrocatalysts based on molecular Cu complexes.

3.5 References.

1. Ghobadi, S.; Işıkel Şanlı, L.; Bakhtiari, R.; Alkan Gürsel, S. Green Composite Papers via Use of Natural Binders and Graphene for PEM Fuel Cell Electrodes. *ACS Sustain. Chem. Eng.* **2017**, *5*, 8407–8415.
2. Carrette, L.; Friedrich, K. A.; Stimming, U. Fuel Cells: Principles, Types, Fuels, and Applications. *ChemPhysChem* **2000**, *1*, 162–193.
3. Prater, K. B. Polymer Electrolyte Fuel Cells: A Review of Recent Developments. *J. Power Sources* **1994**, *51*, 129–144.
4. Gewirth, A. A.; Thorum, M. S. Electroreduction of Dioxygen for Fuel-Cell Applications: Materials and Challenges. *Inorg. Chem.* **2010**, *49*, 3557–3566.
5. Gasteiger, H. A.; Panels, J. E.; Yan, S. G. Dependence of PEM Fuel Cell Performance on Catalyst Loading. *J. Power Sources* **2004**, *127*, 162–171.
6. Gasteiger, H. A.; Kocha, S. S.; Sompalli, B.; Wagner, F. T. Activity Benchmarks and Requirements for Pt, Pt-Alloy, and Non-Pt Oxygen Reduction Catalysts for PEMFCs. *Appl. Catal. B Environ.* **2005**, *56*, 9–35.
7. Bashyam, R.; Zelenay, P. A Class of Non-Precious Metal Composite Catalysts for Fuel Cells. *Nature* **2006**, *443*, 63–66.
8. Jaouen, F.; Lefèvre, M.; Dodelet, J.-P.; Cai, M. Heat-Treated Fe/N/C Catalysts for O_2 Electroreduction: Are Active Sites Hosted in Micropores? *J. Phys. Chem. B* **2006**, *110*, 5553–5558.
9. Wang, B.; Feng, J.; Gao, C. Surface Wettability of Compressed Polyelectrolyte Multilayers. *Colloids Surf. Physicochem. Eng. Asp.* **2005**, *259*, 1–5.

10. Jaouen, F.; Dodelet, J.-P. O_2 Reduction Mechanism on Non-Noble Metal Catalysts for PEM Fuel Cells. Part I: Experimental Rates of O_2 Electroreduction, H_2O_2 Electroreduction, and H_2O_2 Disproportionation. *J. Phys. Chem. C* **2009**, *113*, 15422–15432.
11. Matter, P. H.; Ozkan, U. S. Non-Metal Catalysts for Dioxygen Reduction in an Acidic Electrolyte. *Catal. Lett.* **2006**, *109*, 115–123.
12. Xie, L.; Zhang, X.; Zhao, B.; Li, P.; Qi, J.; Guo, X.; Wang, B.; Lei, H.; Zhang, W.; Apfel, U.; Cao, R. Enzyme-inspired Iron Porphyrins for Improved Electrocatalytic Oxygen Reduction and Evolution Reactions. *Angew. Chem. Int. Ed.* **2021**, *60*, 7576-7581.
13. Lv, H.; Guo, H.; Guo, K.; Lei, H.; Zhang, W.; Zheng, H.; Liang, Z.; Cao, R. Substituent Position Effect of Co Porphyrin on Oxygen Electrocatalysis. *Chin. Chem. Lett.* **2021**, *32*, 2841-2845.
14. Wang, Y.; Huang, W.; Wan, L.; Yang, J.; Xie, R.; Zheng, Y.; Tan, Y.; Wang, Y.; Zaghib, K.; Zheng, L.; Sun, S.; Zhou, Z.; Sun S. Identification of the Active Triple-phase Boundary of a non-Pt Catalyst Layer in Fuel Cells. *Sci. Adv.* **2022**, *8*, eadd8873-eadd8882.
15. Wei, Z.; Zhu, Y.; Liu, J.; Zhang, Z.; Hu, W.; Xu, H.; Feng, Y.; Ma, J. Recent Advances in Single-atom Catalysis. *Rare Metals* **2021**, *40*, 767-789.
16. Zhou, Y.; Wang, N.; Xing, L.; Zhang, X.; Zhong, R.; Peng, Y.; Chen, Y.; Ye, S.; Xie, X.; Du, L. The Emerging Coupled Low-PGM and PGM-free Catalysts for Oxygen Reduction Reaction. *Chem. Catalysis* **2022**, *3*, 100484-100490.
17. Schweiger, H.; Vayner, E.; Anderson, A. B. Why Is There Such a Small Overpotential for O_2 Electroreduction by Copper Laccase? *Electrochem. Solid-State Lett.* **2005**, *8*, A585.
18. Mano, N.; Soukharev, V.; Heller, A. A Laccase-Wiring Redox Hydrogel for Efficient Catalysis of O_2 Electroreduction. *J. Phys. Chem. B* **2006**, *110*, 11180–11187.

19. Shleev, S.; Tkac, J.; Christenson, A.; Ruzgas, T.; Yaropolov, A. I.; Whittaker, J. W.; Gorton, L. Direct Electron Transfer between Copper-Containing Proteins and Electrodes. *Biosens. Bioelectron.* **2005**, *20*, 2517–2554.
20. Hussein, L.; Rubenwolf, S.; Stetten, F. von; Urban, G.; Zengerle, R.; Krueger, M.; Kerzenmacher, S. A Highly Efficient Buckypaper-Based Electrode Material for Mediatorless Laccase-Catalyzed Dioxygen Reduction. *Biosens. Bioelectron.* **2011**, *26*, 4133–4138.
21. Zloczewska, A.; Jönsson-Niedziolka, M.; Rogalski, J.; Opallo, M. Vertically Aligned Carbon Nanotube Film Electrodes for Bioelectrocatalytic Dioxygen Reduction. *Electrochimica Acta* **2011**, *56*, 3947–3953.
22. Gautam, R. P.; Lee, Y. T.; Herman, G. L.; Moreno, C. M.; Tse, E. C. M.; Barile, C. J. Controlling Proton and Electron Transfer Rates to Enhance the Activity of an Oxygen Reduction Electrocatalyst. *Angew. Chem. Int. Ed.* **2018**, *57*, 13480–13483.
23. Tse, E. C. M.; Barile, C. J.; Kirchschlager, N. A.; Li, Y.; Gewargis, J. P.; Zimmerman, S. C.; Hosseini, A.; Gewirth, A. A. Proton Transfer Dynamics Control the Mechanism of O_2 Reduction by a Non-Precious Metal Electrocatalyst. *Nat. Mater.* **2016**, *15*, 754–759.
24. Barile, C. J.; Tse, E. C. M.; Li, Y.; Sobyra, T. B.; Zimmerman, S. C.; Hosseini, A.; Gewirth, A. A. Proton Switch for Modulating Oxygen Reduction by a Copper Electrocatalyst Embedded in a Hybrid Bilayer Membrane. *Nat. Mater.* **2014**, *13*, 619–623.
25. Chang, F.; Xiao, M.; Miao, R.; Liu, Y.; Ren, M.; Jia, Z.; Han, D.; Yuan, Y.; Bai, Z.; Yang, L. Copper-based Catalysts for Electrochemical Carbon Dioxide Reduction to Multicarbon Products. *Electrochem. Energ. Rev.* **2022**, *5*, 1-35.

26. Zhao, J.; Xue, S.; Barber, J.; Zhou, Y.; Meng, J.; Ke, X. An Overview of Heterogeneous Electrocatalysts for CO_2 Reduction. *J. Mater. Chem. A* **2020**, *8*, 4700-4734.
27. Mondol, P.; Thind, J. K.; Barile, C. J. Selective Electrocatalytic Nitrate Reduction to Ammonia using Nafion-Modified Cu Electrodeposits. *J. Phys. Chem. C* **2023**, *127*, 8054-8061.
28. Mondol, P.; Panthi, D.; Albarran Ayala, A. J.; Odoh, S. O.; Barile, C. J. Membrane-modified Electrocatalysts for Nitrate Reduction to Ammonia with High Faradaic Efficiency. *J. Mater. Chem. A* **2022**, *10*, 22428-22436.
29. Lei, Y.; Anson, F. C. Dynamics of the Coordination Equilibria in Solutions Containing Copper(II), Copper(I), and 2,9-Dimethyl-1,10-Phenanthroline and Their Effect on the Reduction of O_2 by Cu(I). *Inorg. Chem.* **1995**, *34*, 1083–1089.
30. Lei, Y.; Anson, F. C. Mechanistic Aspects of the Electroreduction of Dioxygen as Catalyzed by Copper-Phenanthroline Complexes Adsorbed on Graphite Electrodes. *Inorg. Chem.* **1994**, *33*, 5003–5009.
31. McCrory, C. C.; Devadoss, A.; Ottenwaelder, X.; Lowe, R. D.; Stack, T. D. P.; Chidsey, C. E. Electrocatalytic O_2 Reduction by Covalently Immobilized Mononuclear Copper (I) Complexes: Evidence for a Binuclear Cu_2O_2 Intermediate. *J. Am. Chem. Soc.* **2011**, *133*, 3696–3699.
32. McCrory, C. C. L.; Ottenwaelder, X.; Stack, T. D. P.; Chidsey, C. E. D. Kinetic and Mechanistic Studies of the Electrocatalytic Reduction of O_2 to H_2O with Mononuclear Cu Complexes of Substituted 1,10-Phenanthrolines. *J. Phys. Chem. A* **2007**, *111*, 12641–12650.

33. Fukuzumi, S.; Kotani, H.; Lucas, H. R.; Doi, K.; Suenobu, T.; Peterson, R. L.; Karlin, K. D. Mononuclear Copper Complex-Catalyzed Four-Electron Reduction of Oxygen. *J. Am. Chem. Soc.* **2010**, *132*, 6874–6875.
34. Liu, C.; Lei, H.; Zhang, Z.; Chen, F.; Cao, R. Oxygen Reduction Catalyzed by a Water-Soluble Binuclear Copper(II) Complex from a Neutral Aqueous Solution. *Chem. Commun.* **2017**, *53*, 3189-3192.
35. Mondol, P.; Barile, C. J. Four-Electron Electrocatalytic O_2 Reduction by a Ferrocene-Modified Glutathione Complex of Cu. *ACS Appl. Energy Mater.* **2021**, *4*, 9611–9617.
36. Anderson, M. E.; Powrie, F.; Puri, R. N.; Meister, A. Glutathione Monoethyl Ester: Preparation, Uptake by Tissues, and Conversion to Glutathione. *Arch. Biochem. Biophys.* **1985**, *239*, 538–548.
37. Chalyavi, F.; Hogle, D. G.; Tucker, M. J. Tyrosine as a Non-Perturbing Site-Specific Vibrational Reporter for Protein Dynamics. *J. Phys. Chem. B* **2017**, *121*, 6380–6389.
38. Cheatum, C. M.; Tokmakoff, A.; Knoester, J. Signatures of β-Sheet Secondary Structures in Linear and Two-Dimensional Infrared Spectroscopy. *J. Chem. Phys.* **2004**, *120*, 8201–8215.
39. Demirdöven, N.; Cheatum, C. M.; Chung, H. S.; Khalil, M.; Knoester, J.; Tokmakoff, A. Two-Dimensional Infrared Spectroscopy of Antiparallel β-Sheet Secondary Structure. *J. Am. Chem. Soc.* **2004**, *126*, 7981–7990.
40. Ganim, Z.; Chung, H. S.; Smith, A. W.; DeFlores, L. P.; Jones, K. C.; Tokmakoff, A. Amide I Two-Dimensional Infrared Spectroscopy of Proteins. *Acc. Chem. Res.* **2008**, *41*, 432–441.

41. Martell, A. E. Chelating Agents for Metal Buffering and Analysis in Solution. **1978**, *50*, 813–829.
42. Sunarso, J.; Torriero, A. A. J.; Zhou, W.; Howlett, P. C.; Forsyth, M. Oxygen Reduction Reaction Activity of La-Based Perovskite Oxides in Alkaline Medium: A Thin-Film Rotating Ring-Disk Electrode Study. *J. Phys. Chem. C* **2012**, *116*, 5827–5834.
43. Jung, E.; Shin, H.; Lee, B.-H.; Efremov, V.; Lee, S.; Lee, H. S.; Kim, J.; Hooch Antink, W.; Park, S.; Lee, K.-S. Atomic-Level Tuning of Co–N–C Catalyst for High-Performance Electrochemical H_2O_2 Production. *Nat. Mater.* **2020**, *19*, 436–442.
44. Lu, Z.; Chen, G.; Siahrostami, S.; Chen, Z.; Liu, K.; Xie, J.; Liao, L.; Wu, T.; Lin, D.; Liu, Y. High-Efficiency Oxygen Reduction to Hydrogen Peroxide Catalysed by Oxidized Carbon Materials. *Nat. Catal.* **2018**, *1*, 156–162.
45. Song, C.; Zhang, J. Electrocatalytic Oxygen Reduction Reaction. In PEM Fuel Cell Electrocatalysts and Catalyst Layers: Fundamentals and Applications; Zhang, *J., Ed.; Springer London: London*, **2008**, 89–134.
46. Noffke, B. W.; Li, Q.; Raghavachari K.; Li, L. A Model for the pH-Dependent Selectivity of the Oxygen Reduction Reaction Electrocatalyzed by N-Doped Graphitic Carbon. *J. Am. Chem. Soc.* **2016**, *138*, 13923–13929.
47. Bai, J.; Zhu, Q.; Lv, Z.; Dong, H.; Yu, J.; Dong, L. Nitrogen-doped Graphene as Catalysts and Catalyst Supports for Oxygen Reduction in Both Acidic and Alkaline Solutions *Int. J. Hydrog. Energy* **2013**, *38*, 1413–1418.
48. (48) Iwazaki, T.; Oninata, R.; Sugimoto, W.; Takasu, Y. High Oxygen-reduction Activity of Silk- derived Activated Carbon. *Electrochem. Commun.* **2009**, *11*, 376–378.

49. Park, J.; Nabae, Y.; Hayakawa, T. Kakimoto, M. Highly Selective Two-electron Oxygen Reduction Catalyzed by Mesoporous Nitrogen-doped Carbon. *ACS Catal.* **2014**, *4*, 3749–3754.
50. Thorseth, M. A.; Letko, C. S.; Tse, E. C. M.; Rauchfuss, T. B.; Gewirth, A. A. Ligand Effects on the Overpotential for Dioxygen Reduction by Tris(2-pyridylmethyl) Amine Derivatives. *Inorg. Chem.* **2013**, *52*, 628-634.
51. Thorseth, M. A.; Tornow, C. E.; Tse, E. C. M.; Gewirth, A. A. Cu Complexes that Catalyze the Oxygen Reduction Reaction *Coord. Chem. Rev.* **2013**, *257*, 130-139.
52. Ghosh, A.; Tucker, M. J. Gai, F. 2D IR Spectroscopy of Histidine: Probing Side-Chain Structure and Dynamics via Backbone Amide Vibrations. *J. Phys. Chem. B* **2014**, *118*, 7799–7805.
53. (54) DeFlores, L. P.; Ganim, Z. Nicodemus, R. A.; Tokmakoff, A. Amide I′−II′ 2D IR Spectroscopy Provides Enhanced Protein Secondary Structural Sensitivity. *J. Am. Chem. Soc.* **2009**, *131*, 3385–3391.
54. (54) Barth, A.; Zscherp, C. What Vibrations Tell about Proteins *Q. Rev. Biophys.* **2002**, *35*, 369–430.
55. (55) Buchanan, L. E.; Carr, J. K.; Fluitt, A. M.; Hoganson, A. J.; Moran, S. D.; de Pablo, J. J.; Skinner, J. L.; Zanni, M. T. Structural Motif of Polyglutamine Amyloid Fibrils Discerned with Mixed-isotope Infrared Spectroscopy. *Proc. Natl. Acad. Sci.* **2014**, *111*, 5796–5801.
56. (56) Strasfeld, D. B., Ling, Y. L.; Gupta, R.; Raleigh, D. P., Zanni, M. T. Strategies for Extracting Structural Information from 2D IR Spectroscopy of Amyloid: Application to Islet Amyloid Polypeptide. *J. Phys. Chem. B* **2009**, *113*, 15679–15691.

57. (57) Torii, H. Amide I Vibrational Properties Affected by Hydrogen Bonding Out-of-Plane of the Peptide Group. *J. Phys. Chem. Lett.* **2015**, *6*, 727–733.

58. (58) Walsh, S. T.; Cheng, R. P.; Wright, W. W.; Alonso, D. O.; Daggett, V.; Vanderkooi, J. M.; DeGardo, W. F. The Hydration of Amides in Helices: A Comprehensive Picture from Molecular Dynamics, IR, and NMR. *Protein Sci.* **2003**, *12*, 520–531.

59. (59) Hundertmark, M.; Popova, A. V.; Rausch, S.; Seckler, R.; Hincha, D. K. Influence of Drying on the Secondary Structure of Intrinsically Disordered and Globular Proteins. *Biochem. Biophys. Res. Commun.* **2012**, *417*, 122–128.

60. (60) Kwac, K.; Lee, H.; Cho, M. Non-Gaussian Statistics of Amide I Mode Frequency Fluctuation of N-methylacetamide in Methanol Solution: Linear and Nonlinear Vibrational Spectra *J. Chem. Phys*. **2004**, *120*, 1477-1490.

61. (61) Lomont, J. P.; Ostrander, J. S.; Ho, J. J.; Petti, M. K.; Zanni, M. T. Not All β-Sheets Are the Same: Amyloid Infrared Spectra, Transition Dipole Strengths, and Couplings Investigated by 2D IR Spectroscopy. *J. Phys. Chem. B*. **2017**, *121*, 8935–8945.

62. (62) Kong, J.; YU, S. Fourier Transform Infrared Spectroscopic Analysis of Protein Secondary Structures. *Acta Biochimica et Biophysica Sinica* **2007**, *39*, 549–559.

63. (63) Sharma, C.; Srivastava, A. K.; Sharma, D.; Joshi, R. K. Iron- and Copper-based Bifunctional Catalysts for the Base- and Solvent-free C–N Coupling of Amines and Aryl/benzyl Chlorides under Aerobic Conditions *New J. Chem.*, **2022**, **46**, 8551-8556.

64. (64) Suh, M. J.; Kim, G.; Kang, J.; Lim, M. H. Strategies Employing Transition Metal Complexes To Modulate Amyloid-β Aggregation. *Inorg. Chem.* **2019**, *58*, 8–17.

65. (65) Faller, P.; Hureau, C .; Berthoumieu, Olivia, B. Role of Metal Ions in the Self-assembly of the Alzheimer's Amyloid-β Peptide. Inorg. Chem. **2013**, 52, 12193–12206.

66. (66) Miura, T.; Suzuki, K.; Kohata, N.; Takeuchi, T. Metal Binding Modes of Alzheimer's Amyloid β-Peptide in Insoluble Aggregates and Soluble Complexes *Biochemistry* **2000**, *39*, 7024–7031.

Chapter Four

Membrane-modified Electrocatalysts for Nitrate Reduction to Ammonia with High Faradaic Efficiency

4.1 Introduction.

Ammonia (NH_3) is an extremely important chemical feedstock and is used extensively in the fertilizer, pharmaceutical, and dye industries.[1-4] As a result, NH_3 is the fifth most produced chemical in the world by volume.[5] Additionally, NH_3 has recently been considered as an alternative renewable fuel in fuel cells.[6,7] The most well-established route to generate NH_3 on an industrial scale is the Haber-Bosch process.[6,8-11] Because the Haber-Bosch process is energy intensive and because a massive quantity of NH_3 is generated annually, NH_3 production is responsible for 1-2% of total world energy consumption and causes ~1% of global anthropogenic CO_2 emissions.[2,12-14] Another route to produce NH_3 is through the electrochemical generation of H_2 from water coupled with subsequent N_2 reduction.[1] However, there are several large challenges associated with electrochemical N_2 reduction including low selectivity, low current densities, low N_2 solubility in water, and the high dissociation energy of the N≡N bond, all of which have prevented the use of electrochemical N_2 reduction to NH_3 outside of research settings.[13,15]

Alternatively, NH_3 can be produced electrochemically from the nitrate anion (NO_3^-). In many respects, NO_3^- is a better source of nitrogen because of its high water solubility and the low dissociation energy of the N=O bond compared to N≡N, which allows for faster reaction kinetics.[16] Another value of using NO_3^- is its high natural abundance, [17,18] particularly in agricultural settings where it is a major environmental pollutant. Thus, the electrochemical generation of NH_3 from NO_3^- under ambient conditions has the potential not only to save energy consumption vis-à-vis the Haber-Bosch process, but it could also play an important role in environmental remediation. For example, high concentrations of NO_3^- in drinking water cause several health problems including blue baby syndrome, thyroid disease, birth defects, and cancer.[19] For this reason, the United States Environmental Protection Agency (EPA) has set a limit of 10 mg/L of NO_3^- in drinking water. [20,21] In contrast, NH_3 is comparatively less toxic, and the EPA has not established a threshold for NH_3 concentration in drinking water.

Previous research has demonstrated the activity of monometallic catalysts such as Pd,[22] Pt,[22] Ag,[23] Cu,[23] Sn,[24] and Rh for NO_3^- and/or nitrite (NO_2^-) reduction.[23] Bimetallic catalysts including Pt-Cu,[22,25] Pd-Cu,[22] Pd-Sn,[26] Sn-Rh,[27] Sn-Ru,[27] and Sn-Ir[27] have also been used. Nonetheless, selectivity remains a challenge, and for NO_3^- to NH_3 catalysts, N_2 and H_2 are common side products that diminish NH_3 Faradaic efficiency.[28]

Electrocatalyst selectivity is a concern for all reactions involving multiple proton and electron transfer steps and is not just limited to the NO_3^- reduction reaction. For example, our group designed new membrane-modified catalysts that can be used to increase the selectivity of the CO_2 reduction reaction.[29,30] In particular, we demonstrated that when the fluoropolymer Nafion is used as an overlayer that interfaces the catalyst and bulk solution, a bound CO intermediate is activated on the catalyst surface.[30] This activation of CO allows it to be further reduced to CH_4, the most highly reduced form of carbon.

Based on these previous results, we hypothesize that a similar strategy can be used to increase the selectivity of NO_3^- to NH_3 catalysts. In NO_3^- reduction, NH_3 is the most reduced product, making it the direct analog of CH_4 in CO_2 reduction. Furthermore, the electronic and structural properties of NO and CO are similar, and NO is a key intermediate in the NO_3^- reduction reaction just as CO is an important intermediate in CO_2 reduction.[31-34] For these reasons, we speculate that a metal-NO intermediate could be activated by a Nafion overlayer to increase the selectivity of NH_3 production. This chapter provides experimental and computational evidence in support of this central hypothesis.

Nafion is a widely used fluoropolymer that is often mixed with electrocatalysts to facilitate proton transport or used as a separator between two half reaction compartments in full NO_3^- reduction devices.[35,36] In contrast to these uses of Nafion, this work studies different metallic electrodes covered by Nafion overlayers. In this architecture, Nafion affects the reactivity of intermediates at the catalyst surface, and thus its role here is fundamentally different from the other common uses of fluoropolymers in electrocatalyst research.

4.2 Experimental procedures.

4.2.1 Materials and Electrode Preparation

Nafion D520 dispersion was purchased from Fuel Cell Store, Inc. Cu foil (99.99%) was purchased from All-Foils, Inc. Ti foil (99.99%) was purchased from Stanford Advanced Materials, Pb foil was purchased from KRT Distributions (99.9%), and Zn foil (99.99%) was purchased from Belmont Metals. $NaNO_3$ (> 99%) and Na_2SO_4 (> 99%) were purchased from Sigma Aldrich. $NaNO_2$ (98%) was purchased from Oakwood Chemicals, Inc. The pH of solutions was measured using a Go Direct pH sensor (Vernier, Inc.). The unadjusted pH of the electrolytes was approximately 5.5 due to the presence of atmospheric CO_2 in the water. More acidic electrolytes were pH adjusted with sulfuric acid. Nafion-modified electrodes were fabricated by drop-casting the Nafion dispersion directly onto the metal surfaces. To modify the thickness of the Nafion layer, multiple rounds of drop-casting were performed. In between each round of drop-casting, the Nafion dispersion was dried in an oven for 7 min at 65 °C.

4.2.2 Electrochemical Measurements

A VSP-300 Biologic potentiostat was used for electrochemical studies. All electrochemical studies were performed in a three-electrode system in which metal surfaces, a platinized-titanium electrode (Rio Grande, Inc.), and a leakless Ag/AgCl/3 M KCl (eDaq, Inc.) were the working, counter, and reference electrodes, respectively. Current densities are reported with respect to the geometric area of the working electrode. The metal electrodes were rinsed with acetone and subsequently washed with deionized water several times before use. For evaluating NO_3^- reduction activities of each thin film, the working electrodes were studied in 10 mL of 50 mM $NaNO_3$ and 100 mM Na_2SO_4 (unless otherwise mentioned) in a two-compartment cell. The cell consisted of a 25 mL glass beaker separated by a Nafion 117 membrane (H^+ form, 183 μm, Fuel Cell Store, Inc.). The working and reference electrodes were in one compartment, while the counter electrode was placed in the second compartment. The onset potential was determined by calculating the potential at which the current density reached 10% of the maximum current density for each LSV.

For electrochemical NO_2^- reduction, we used 10 mL 50 mM $NaNO_2$ and 100 mM Na_2SO_4 in a two-compartment electrochemical cell and followed a procedure analogous to those used for NO_3^-. For electrochemical NO reduction, we used 10 mL 100 mM Na_2SO_4. This electrolyte was sparged with NO gas for 10 minutes before running chronoamperometry. NO was synthesized from $NaNO_2$ and dilute sulfuric acid according to literature procedures.[37] The concentration of NO in a saturated aqueous solution is about 2 mM.[38] For experiments with groundwater, water was obtained from a domestic well in Silver Springs, NV and was used directly in experiments without any pretreatment step.

4.2.3 Materials Characterization

X-ray photoelectrons spectroscopy (XPS) data was obtained using a Thermo Fischer Scientific Nexsa G2 Surface Analysis System using a monochromatic Al X-ray source and a spot size of 400 μm. The energy of the spectra was calibrated against the C 1s peak of adventitious carbon at 248.6 eV. Scanning electron microscope (SEM) images and energy-dispersive X-ray

(EDX) analysis were obtained for each sample using a JEOL JSM-7100F field emission SEM operated using an accelerating voltage of 15 kV. X-ray diffraction (XRD) spectra were recorded using a Bruker D2 X-ray diffractometer. A Renishaw in Via confocal Raman microscope was used to collect Raman spectra of the electrodes. For surface-enhanced Raman spectroscopy experiments with NO gas, NO was sparged for 10 minutes on the Cu surface before collecting the spectra. The Nafion-modified Cu substrates had a thickness of about 100 nm. Although we also collected spectra on Cu with the micron-thick Nafion overlayers used for electrochemical experiments, these spectra only possessed Nafion peaks and could not be used to probe the Cu-Nafion interface due to their large thicknesses. Before all of the experiments, the instrument was calibrated with a Si standard. Spectra were collected with a 10x objective lens and averaged over 10 scans. A 514 nm laser with a power of approximately 11 mW was used to illuminate the samples.

4.2.4 Product Detection

The concentration of NH_3, NO_2^-, and NO_3^- after 1 hour of chronoamperometry were each evaluated using well-established colorimetric methods. For most electrodes, the voltage values used during chronoamperometry were selected such that the current density was approximately 5 mA cm^{-2}. For experiments with Pb electrodes, the current density decreased significantly over the course of 1 hr, and so a high voltage of -2.0 V was used in accordance with previous literature methods.[39] NH_3 was qualitatively detected according to a literature method using iodine.[40] After chronoamperometry, 1 mL of the electrolyte adjusted to pH 13 with NaOH was poured onto a 3 mg iodine crystal in a small glass vial. A black precipitate of NH_4I_3 upon stirring confirms the presence of NH_3 in electrolyte. The amount of NH_3 was quantified from the electrolyte using the indophenol method.[41] All the reagents were purchased from Sigma Aldrich and were used without any further purification. 0.5 mL of the catholyte was taken in a glass vial, and 2 mL of a 1 M NaOH solution containing 5 wt. % salicylic acid and 5 wt. % sodium citrate was added. Then, 1 mL of 0.5 M NaClO and 0.2 mL of 1 wt. % sodium nitroferricyanide were added to the same vial. After waiting for 1 hr at room temperature, UV-Vis spectroscopy was performed (Shimadzu UV-2550 spectrometer). The concentration of NH_3 in the electrolyte was determined using the maximum absorbance at 670 nm along with an appropriate calibration curve produced using NH_3 solutions of known concentrations.

NO_3^- and NO_2^- were evaluated using Griess reagents with and without VCl_3.[42] N-(1-Naphthyl)ethylenediamine dihydrochloride (NEDD) and sulfanilamide were purchased from Sigma Aldrich. A 200 mL 0.5 M Hydrochloric acid solution containing 2 wt. % NEDD and 2 wt. % sulfanilamide was first prepared to make the Griess reagents.

To quantify NO_2^-, 10 μL of reaction electrolyte was diluted with 2 mL of deionized water, and 0.8 mL of the Griess reagents were added. The solution was let to stand at room temperature for 30 minutes. The absorbances of the resulting solutions were measured using UV-VIS spectroscopy. The concentration of NO_2^- was calculated from the absorbance at 540 nm along with an appropriate calibration curve using NO_2^- solutions of known concentrations.

To detect the amount of NO_3^- consumed during electrochemistry, we used a similar procedure as for NO_2^- detection, except the 200 mL Griess reagent solution contained 0.5 g VCl_3 (Sigma Aldrich). NO_3^- is reduced into NO_2^- by VCl_3 through a relatively slow process, so the reaction was allowed to go to completion by letting the reaction mixture stand at room temperature for 6-10 hours. Finally, the amount of NO_3^- was subtracted from NO_2^- to determine the amount of NO_3^- remaining after electrochemistry.

4.2.5 Faradaic Efficiency Calculations

To calculate the Faradic efficiency (% FE) of NH_3 and NO_2^- production, we used the following formula.

$$\% \text{ FE} = \frac{Actual\ Yield}{Theoritical\ Yield} \times 100 \qquad \text{………………… (1)}$$

The Faradic efficiencies of N_2 and H_2 production were calculated from equations considering the feasible NO_3^- reduction products, which are as follows.

$2H^+ + 2e^- \rightarrow H_2$ ………………….. (2)
$9H^+ + NO_3^- + 8e^- \rightarrow NH_3 + 3H_2O$ ……………..…… (3)
$12H^+ + 2NO_3^- + 10e^- \rightarrow N_2 + 6H_2O$ ……………..……. (4)
$2H^+ + NO_3^- + 2e^- \rightarrow NO_2^- + H_2O$ …………………..… (5)

The catalysts studied in this work did not produce any measurable quantities (Faradaic efficiency > 0.1%) of NO, N_2O, or N_2H_4. NO and N_2O were detected using an Agilent Technologies GC-MS instrument equipped with a 7890A GC system and 5975C inert MSD with a Triple-Axis Detector. N_2H_4 was detected using the para-dimethylaminobenzaldehyde method.[43] In the absence of NO, N_2O, and N_2H_4 production, the number of moles of N_2 can be quantified by determining the amount of NO_3^- consumed (Equation 7). The Faradaic efficiency of N_2 was then calculated from Equation (1).

$n_{NO_3^-}$ (initial) = $n_{NO_3^-}$ (final) + $n_{NO_3^-}$ (consumed)
$n_{NO_3^-}$ (consumed) = $n_{NH_3} + 2n_{N_2} + n_{NO_2^-}$ …………… (6)

$n_{N_2} = 0.5\, n_{NO_3^-}$ (consumed) $- 0.5\, n_{NH_3} - 0.5\, n_{NO_2^-}$ ……………. (7)

H_2 production was calculated by subtracting the total Faradaic efficiency for nitrogen-containing products from 100%. The values obtained from H_2 production were also corroborated by pH measurements conducted on both compartments of the cell because the number of protons transferred for each nitrogen-containing product is known.

4.2.6 DFT Calculations

All calculations were performed with the PBE-D3 density functional in the Quantum Espresso package. We used large cells and were thus able to sample the Brillouin zone only at the Γ-point. Specifically, we used a 4 * 4 cell with three layers. Scalar-relativistic Projector Augmented Wave (PAW) pseudopotentials were employed with kinetic and charge cut-offs of 50.0 Ry and 420.0 Ry, respectively, while converging all energies to a 10^{-7} Ry threshold.

4.3 Results and Discussion.

4.3.1 Electrocatalytic NO_3^- Reduction of Bare Cu and 6-µm Nafion Modified Cu Electrodes

We proceeded to evaluate the electrochemical activity of Cu electrodes for NO_3^- reduction using linear sweep voltammetry (LSV) with and without NO_3^- or NO_2^- in the electrolyte. On an unmodified Cu electrode, the cathodic current increases as the voltage is swept negative in a NO_3^- electrolyte (Figure 4.1A, black line). The onset potential of electrocatalytic reduction, defined as the potential at which the current reaches 10% of its maximum value during the LSV, is -0.93 V vs. Ag/AgCl. The same unmodified Cu electrode in a NO_2^- electrolyte (Figure 4.1A, red line) exhibits a similar amount of current as the NO_3^- curve with a slightly more positive onset potential of -0.92 V. These results match previous literature showing that the ability of Cu to reduce NO_2^- at a more positive potential than NO_3^- indicates that Cu is a more effective NO_3^- reduction catalyst than most other metals.[44] A LSV without NO_3^- or NO_2^- containing solely the Na_2SO_4 supporting electrolyte catalyzes the H_2 evolution reaction at a much more negative onset potential of -1.42 V.

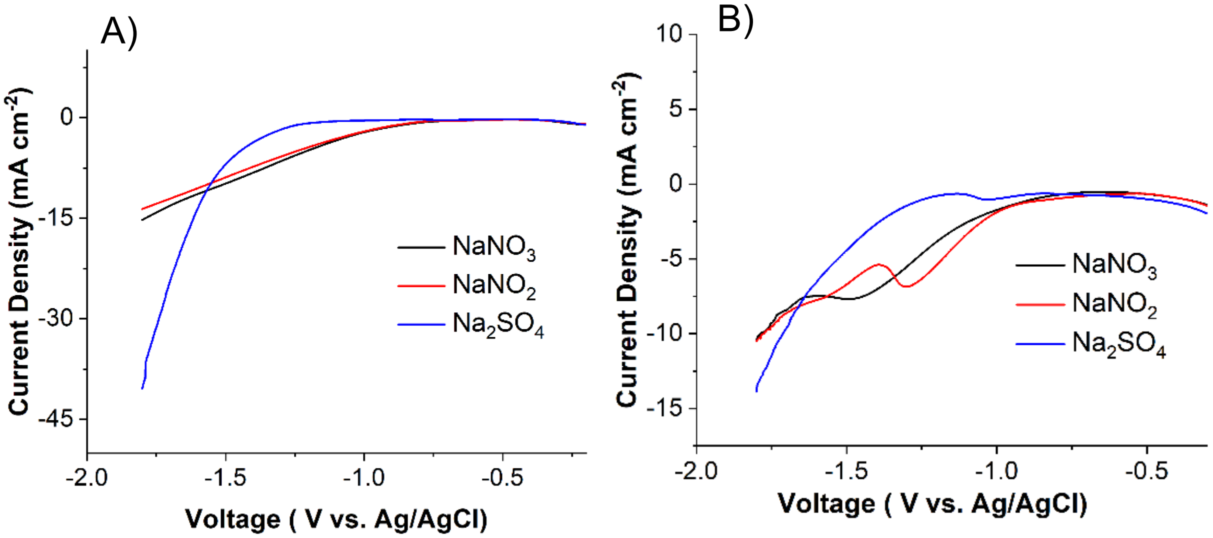

Figure 4.1: Linear sweep voltammograms at a scan rate of 10 mV s^{-1} of unmodified Cu (A) and Cu modified with 6 µm of Nafion (B) in 50 mM $NaNO_3$ and 100 mM Na_2SO_4 (black line), 50 mM $NaNO_2$ and 100 mM Na_2SO_4 (red line), and 100 mM Na_2SO_4 (blue line).

LSVs in the same three electrolytes with Cu electrodes modified with 6 µm of Nafion (Figure 4.1B) differ in two important ways from LSVs of unmodified Cu. Firstly, the current densities of the LSVs decrease upon addition of Nafion. This result is expected because the Nafion membrane slows down mass transport from the bulk solution to the electrode. Secondly, and more interestingly, the onset potentials for both NO_3^- (-0.88 V) and NO_2^- (-0.86 V) reduction shift to more positive values in the presence of the Nafion overlayer. This finding indicates that NO_3^- reduction is more thermodynamically favorable with the Nafion. Furthermore, the onset potential for NO_3^- reduction consistently shifts to more positive values as the thickness of the Nafion membrane increases from 3 µm to 10 µm (Figure 4.2). The onset potentials of these LSVs curves (defined as the potential at which 10% of the maximum current is attained) are -1.04 V, -0.88 V, -0.83 V, and -0.75 V for the 3 µm, 6 µm, 8 µm, and 10 µm Nafion layers, respectively. As with the unmodified electrode, the Nafion-modified electrode still exhibits a slightly more positive onset potential for NO_2^- compared to NO_3^-, which indicates that the unique NO_3^- reactivity on Cu discussed in the previous paragraph is maintained in the presence of Nafion.

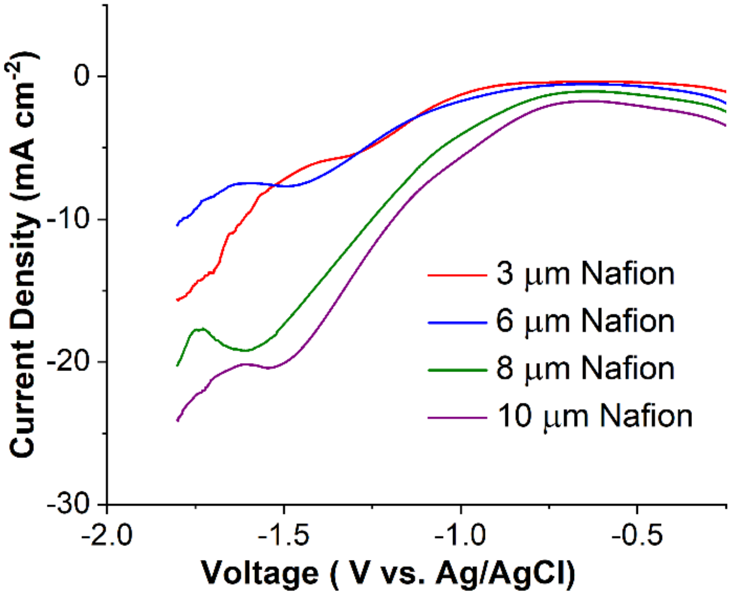

Figure 4.2: Linear sweep voltammograms at a scan rate of 10 mV s^{-1} in 50 mM $NaNO_3$ and 100 mM Na_2SO_4 of Cu modified with 3 μm (red line), 6 μm (blue line), 8 μm (green line), and 10 μm (purple line) of Nafion.

4.3.2 pH Effect Investigation

Given the increase in thermodynamic feasibility of NO_3^- reduction with the Nafion-modified Cu electrode, we wondered if the acidic nature of the sulfonate groups of Nafion altered the reactivity of the electrode through a pH effect. To explore this hypothesis, we conducted LSVs in pH 1 electrolytes on unmodified Cu electrodes (Figure 4.3A). Although the onset potential of the LSV (-0.65 V) in the pH-adjusted NO_3^- electrolyte (pH 1) shifts positive compared to the unaltered NO_3^- electrolyte (pH 5.5), the current density for the pH 1 electrolyte in the absence of NO_3^- (Figure 4.3A, blue line) is more than double that of the LSV in the presence of NO_3^- at pH 1 (Figure 4.3A, black line) at most potentials. This dramatic increase in current density in the absence of NO_3^-, which does not occur with the Nafion-modified electrodes (Figure 4.1B, blue line), suggests that the H_2 evolution reaction is accelerated at pH 1. In both pH experiments (pH 1.0 and pH 3.0), because no nitrogen-containing products other than NH_3 and NO_2^- were detected, the Faradaic efficiencies for the H_2 evolution reaction are high.

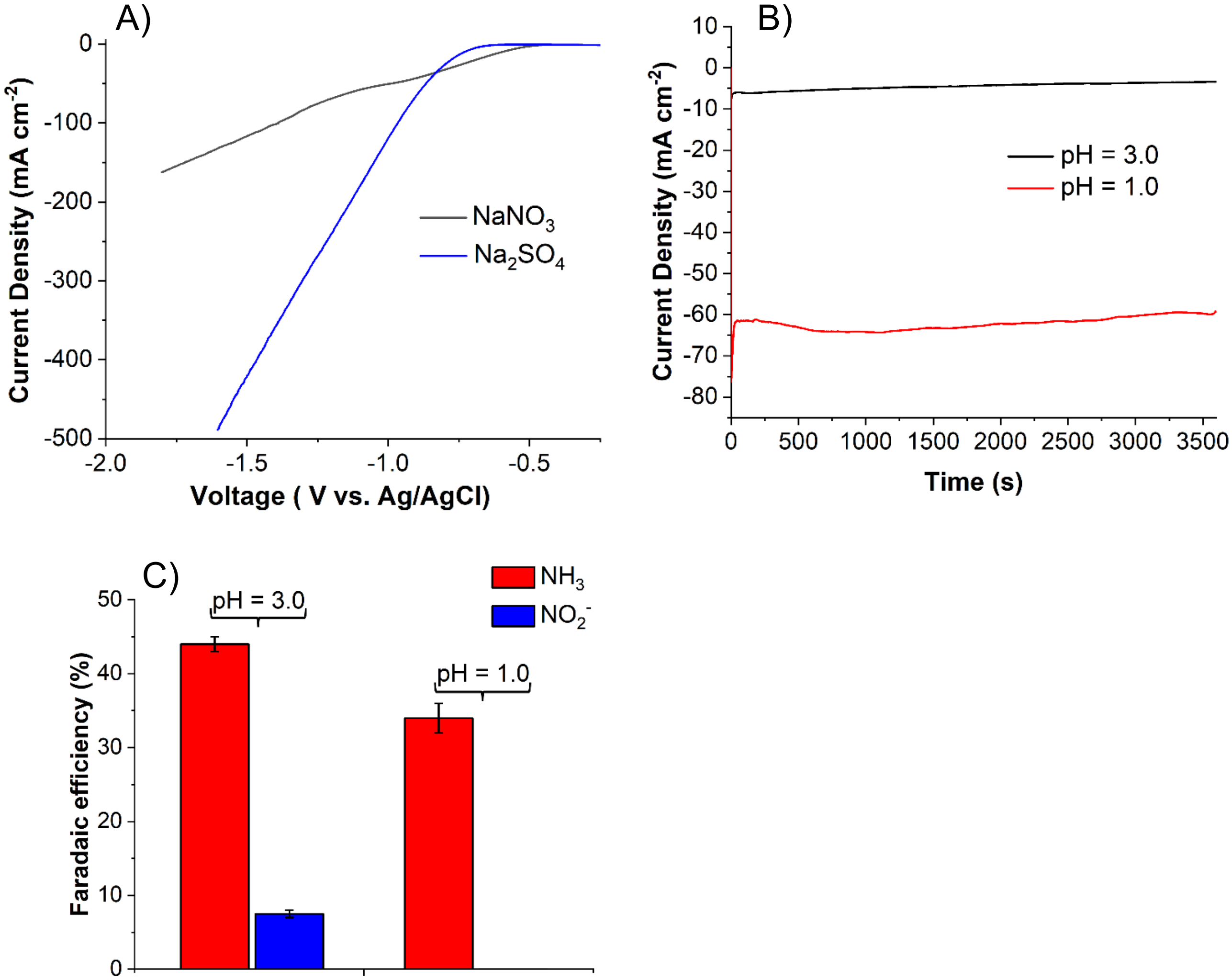

Figure 4.3: Linear sweep voltammograms (A) at a scan rate of 10 mV s^{-1} of unmodified Cu electrodes at pH 1.0 with 50 mM $NaNO_3$ and 100 mM Na_2SO_4 (A, black line) and 100 mM Na_2SO_4 (A, blue line). Chronoamperometry of unmodified Cu electrodes in 50 mM $NaNO_3$ and 100 mM Na_2SO_4 at pH 3.0 (B, black line) and pH 1.0 (B, red line) and Faradaic efficiencies of NH_3 (red bars) and NO_2^- (blue bars) production after chronoamperometry (C).

Indeed, product detection analysis at both pH 1 and 3 demonstrates that the yield of H_2 is significantly higher for these unmodified electrodes (Figure 4.3C) as compared to the Nafion-modified electrode (*vide infra*). In summary, the differences in both the LSVs and product distributions between the Nafion-modified Cu electrode at pH 5.5 and the unmodified Cu electrode under more acidic conditions indicate that the changes in the electrochemical behavior upon addition of the Nafion layer cannot be fully rationalized by pH changes at the electrode-electrolyte interface. Systemic electrochemical analysis, Raman spectroscopy, and density functional theory (DFT) calculations presented later in this chapter suggest that it is the activation of a Cu-NO intermediate by Nafion that is responsible for the positive shift in the onset potential for NO_3^- reduction on Nafion-modified Cu electrodes.

4.3.3 NH_3 Selectivity from NO_3^- Reduction Using Bare Cu and 6-μm Nafion Modified Cu Electrocatalysts

We next evaluated the NO_3^- product distribution for unmodified and Nafion-modified metal electrodes (Figure 4.4). After one hour of chronoamperometry, analytical techniques were used to assess for a wide variety of nitrogen-containing reduction products including NH_3, NO_2^-, N_2, N_2H_4, NO, and N_2O. None of the electrodes studied produced any detectable quantities (Faradaic efficiencies > 0.1%) of N_2H_4, NO, and N_2O. With the exception of the unmodified Pb electrode which yielded (16 ± 2) % N_2, all electrodes generated NH_3 and NO_2^- as the only nitrogen-containing products. For the unmodified metal electrodes studied, these results are in agreement with previous literature reports.[39] Because NH_3 and NO_2^- are the only nitrogen-containing products, H_2, a common side product in NO_3^- reduction experiments, is assumed to be the remaining product.[46] At -1.4 V vs. Ag/AgCl, the Cu electrode modified with 6 μm of Nafion produces a strikingly high yield of NH_3, (91 ± 2) %, a value that is higher than the (62 ± 2) % NH_3 Faradaic efficiency for unmodified Cu.

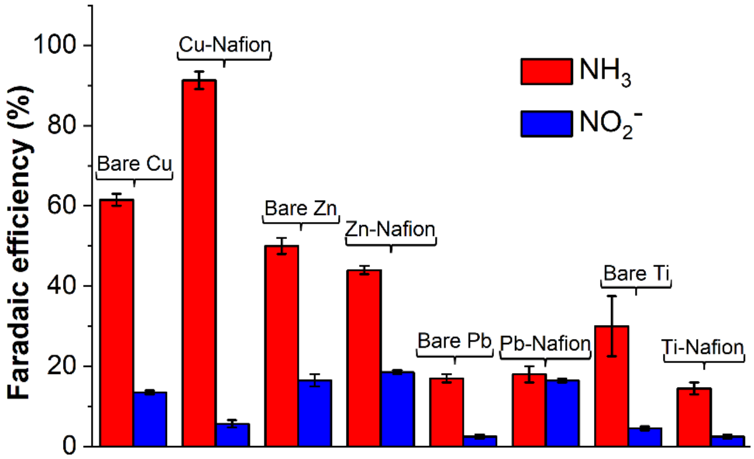

Figure 4.4: Faradaic efficiencies of NH_3 (A, red bars) and NO_2^- (A, blue bars) production after 1 hour of chronoamperometry from unmodified (bare) and metal electrodes modified with 6 μm of Nafion.

4.3.4 Optimization of Reduction Voltages and Nafion Thickness

Systematic variations in the thickness of Nafion used and the applied voltage show that the highest yield of NH_3, (91 ± 2) %, is obtained with 6 μm of Nafion at -1.4 V (Figure 4.5).

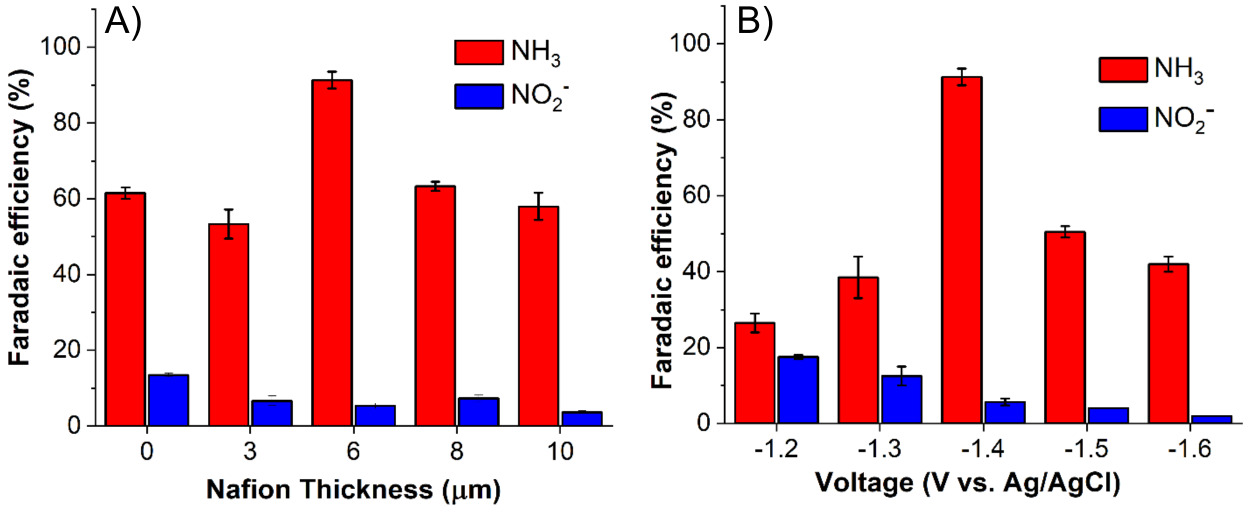

Figure 4.5: Faradaic efficiencies of NH_3 (red bars) and NO_2^- (blue bars) production after 1 hour of chronoamperometry at -1.4 V vs. Ag/AgCl from Cu electrodes modified with different thickness Nafion (A) and after 1 hour of chronoamperometry at different voltage with 6 μm Nafion (B).

Figure 4.6 demonstrate the chronoamperometry and UV-Vis spectra of Bare Cu and also Nafion modified Cu with varying thickness.

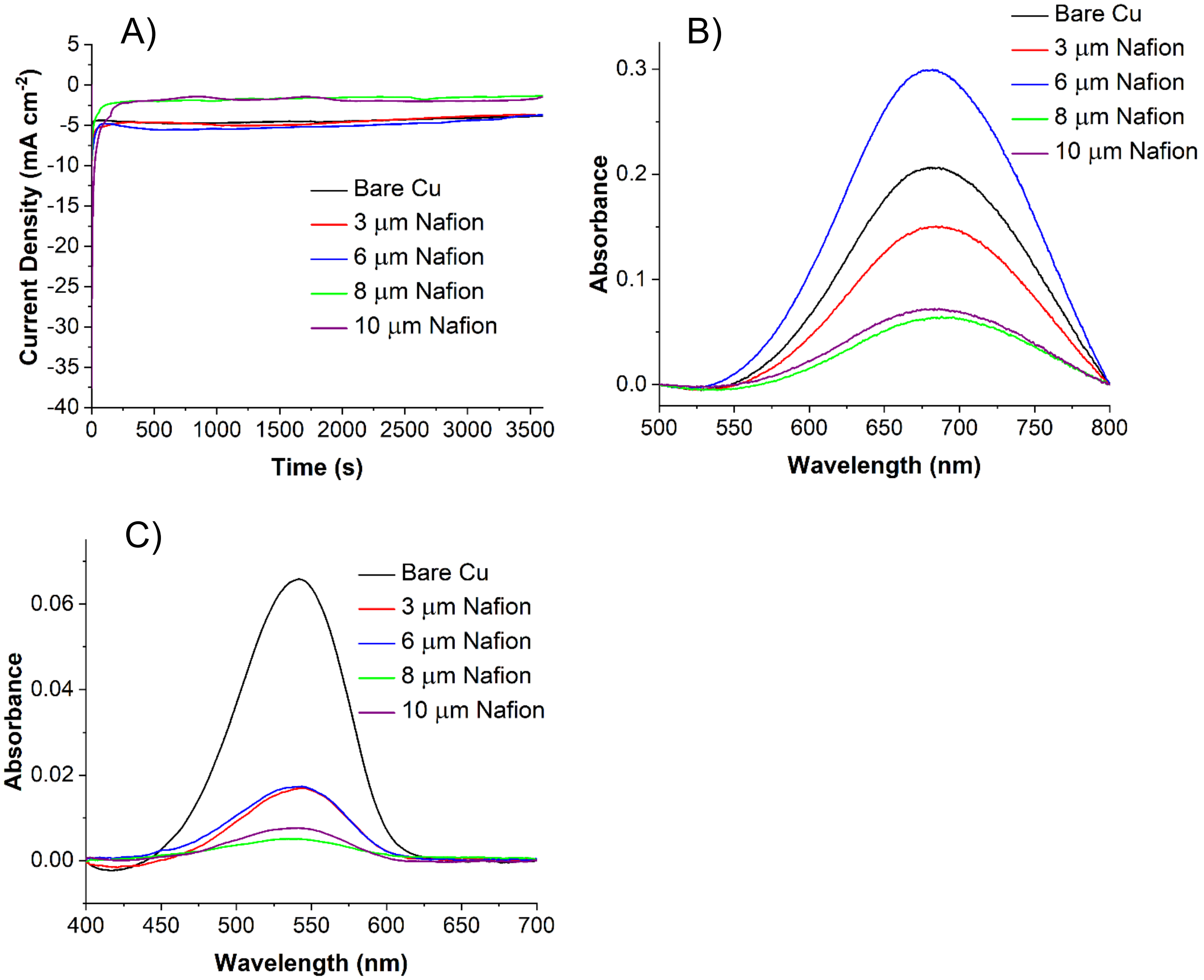

Figure 4.6: Chronoamperometry curves of unmodified (bare) Cu (black line) and Cu modified with 3 μm (red line), 6 μm (blue line), 8 μm (green line), and 10 μm (purple line) of Nafion at -1.4 V in 50 mM $NaNO_3$ and 100 mM Na_2SO_4 (A), and UV-Vis absorption spectra after chronoamperometry for NH_3 (B) and NO_2^- (C) detection.

Figure 4.7 demonstrate the chronoamperometry and UV-Vis spectra of Bare Cu and 6-μm Nafion modified Cu with changing applied voltages.

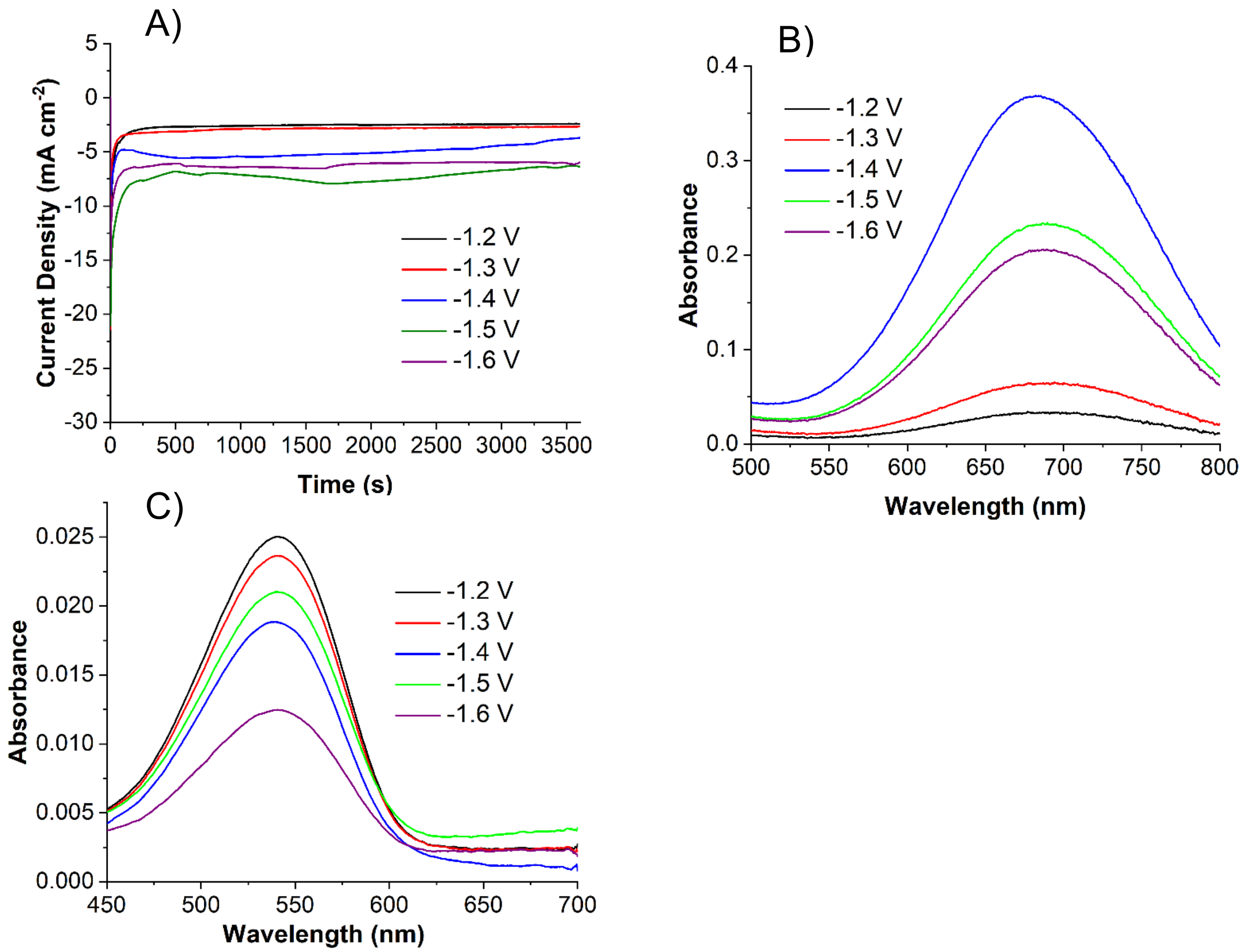

Figure 4.7: Chronoamperometry curves of Cu modified with 6 μm of Nafion at -1.2 V (black line), -1.3 V (red line), -1.4 V (blue line), -1.5 V (green line), and -1.6 V (purple line) in 50 mM $NaNO_3$ and 100 mM Na_2SO_4 (A), and UV-Vis absorption spectra after chronoamperometry for NH_3 (B) and NO_2^- detection.

This NH_3 yield with the Cu electrode with 6 μm of Nafion is among the highest reported across all previous literature reports (Table 4.1). Compared to the rather complex synthetic protocols used to synthesize many of these previous catalysts, the Nafion-modified Cu catalyst reported here is produced using a simple dropcasting protocol. Due to the high NH_3 Faradaic efficiency using 6 μm of Nafion, we used this Nafion thickness for all subsequent experiments.

Table 4.1: Previous literature reports of NH_3-producing NO_3^- reduction catalysts compared to the Nafion-modified Cu electrode presented in this work.

Catalyst	Electrolyte	NH_3 Faradaic Efficiency
This work (Nafion-modified Cu)	50 mM $NaNO_3$ and 100 mM Na_2SO_4	91 ± 2 %
Fe single atom[47]	500 mM KNO_3 and 100 mM K_2SO_4	75 %
PTCDA/O-Cu[48]	100 mM PBS NO_3^- reduction	77 ± 3 %
Pd-In / c-Al_2O_3[49]	3.28 mM $NaHCO_3$ NO_3^- reduction	71.5 %
Pt[36]	3000 mg L^{-1} NO_3^-	49 %
30 % Cu – 70 % Pd[50]	50 mM KNO_3	58 %
Pd-In / $TinO_{2n-1}$ Pd-Cu / $TinO_{2n-1}$ Pd-Cu / REM[51]	10 mM $NaHCO_3$ buffer NO_3^- reduction	19 ± 1 % 22 ± 2 % < 2.3 %
Co-NAs[52]	1 M KOH 1700 ppm NO_3^-	≥ 96 %
CuFe[53] $Pt_{78}Ru_{22}$/C	100 mM K_2SO_4 100 mM H_2SO_4 1700 ppm NO_3^-	94.5 % ≥ 93.0%
Bi_2O_3-CC[54]	500 mM Na_2SO_4 750 ppm NO_3^-	84.9 %
Co/CoO NSA[55]	100 mM K_2SO_4 200 ppm NO_3^-	93.8 %
Co_3O_4/NiO HNTs[56]	500 mM Na_2SO_4 200 ppm NO_3^-	55 %
Thiourea/Au[57]	500 mM $NaNO_3$	85 %
Co_3O_4/Ti[58]	1 M KOH 50 ppm NO_3^-	80 %
Ir NTs[59]	100 mM $HClO_4$ 17000 ppm NO_3^-	84.7 %

4.3.5 Effect of Hydrophobicity of Fluoropolymers

We also investigated dropcasting a mixture of polyvinylidene fluoride (PVDF) and Nafion onto the Cu electrodes. PVDF is a hydrophobic polymer that is impermeable to protons, and if used in a pure form as a catalyst overlayer, PVDF completely inhibits electrocatalysis.[30] For this reason, we used mixtures of PVDF and Nafion to explore the effect of the resulting catalysts that contain more hydrophobic fluoropolymer overlayers. With a Cu electrode at -1.4 V with an overlayer consisting of 10 wt. % PVDF in Nafion, the Faradaic efficiencies for NH_3 and NO_2^- are (41 ± 1) % and (26.6 ± 0.1) %, respectively. The same system with a 50 wt. % PVDF in Nafion overlayer yields NH_3 and NO_2^- with Faradaic efficiencies of (22 ± 3) % and (18 ± 4) %, respectively. These results demonstrate that increasing the hydrophobicity of the fluoropolymer overlayer does not increase NH_3 Faradaic efficiency.

4.3.6 Understanding the Catalysts Surface for NO_3^- Reduction

To understand how the Nafion layer, in the absence of PVDF, improves the selectivity of Cu for NH_3 production, we first determined the interface at which NO_3^- reduction occurs on Nafion-modified electrodes. In principle, NO_3^- reduction could occur at the polymer-electrolyte interface, the electrode-polymer interface, or the electrode-electrolyte interface. The uniform nature of the Nafion overlayer (Figure 4.16A, cross sectional SEM image) suggests that NO_3^- reduction does not occur at the electrode-electrolyte interface. Experiments with Nafion-modified metals other than Cu demonstrate that the product distributions vary depending upon the identity of the metal (Figure 4.4). These results indicate that NO_3^- reduction does not occur at the polymer-electrolyte interface because in this case, we would expect to obtain similar Faradaic efficiencies regardless of the metal buried below the polymer. As a result, we conclude that NO_3^- reduction occurs at the electrode-polymer interface.

4.3.7 NO_3^- Reduction Activity of Zn and Pb Electrodes with or without Nafion Overlayer

Unlike Cu, Nafion-modified Zn and Pb electrodes do not exhibit significantly altered NH_3 Faradaic efficiencies relative to their unmodified metal counterparts (Figures 4.4). Figure 4.8 demonstrate the chronoamperometry and UV-Vis spectra for the NO_3^- reduction using Zn and 6-μm Nafion modifed Zn electrode.

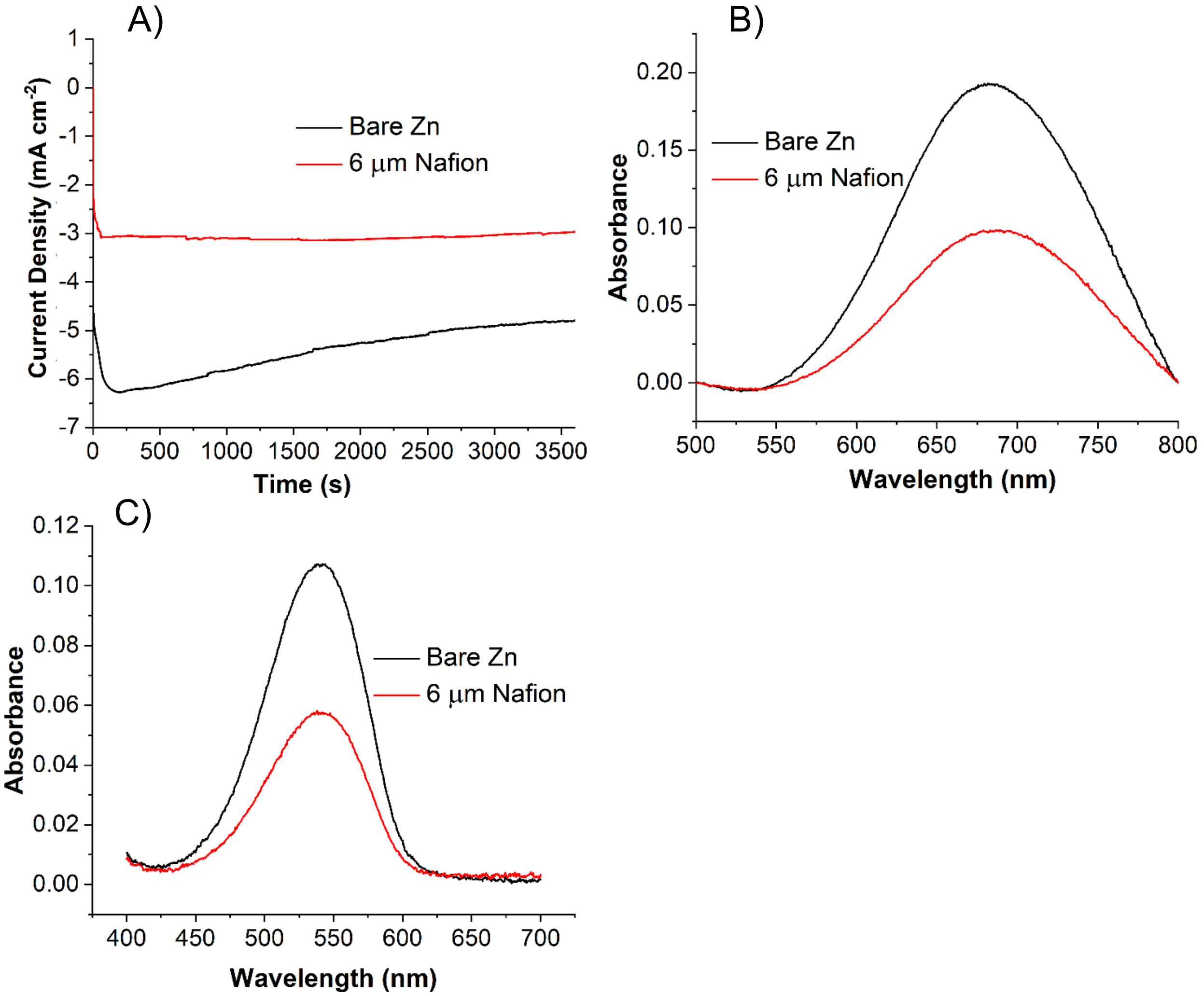

Figure 4.8: Chronoamperometry curves of unmodified (bare) Zn (black line) and Zn modified with 6 μm of Nafion (red line) at -1.5 V in 50 mM $NaNO_3$ and 100 mM Na_2SO_4 (A), and UV-Vis absorption spectra after chronoamperometry for NH_3 (B) and NO_2^- (C) detection.

Figure 4.9 demonstrates the chronoamperometry and UV-Vis spectra for the NO_3^- reduction using Pb and 6-μm Nafion modifed Pb electrode.

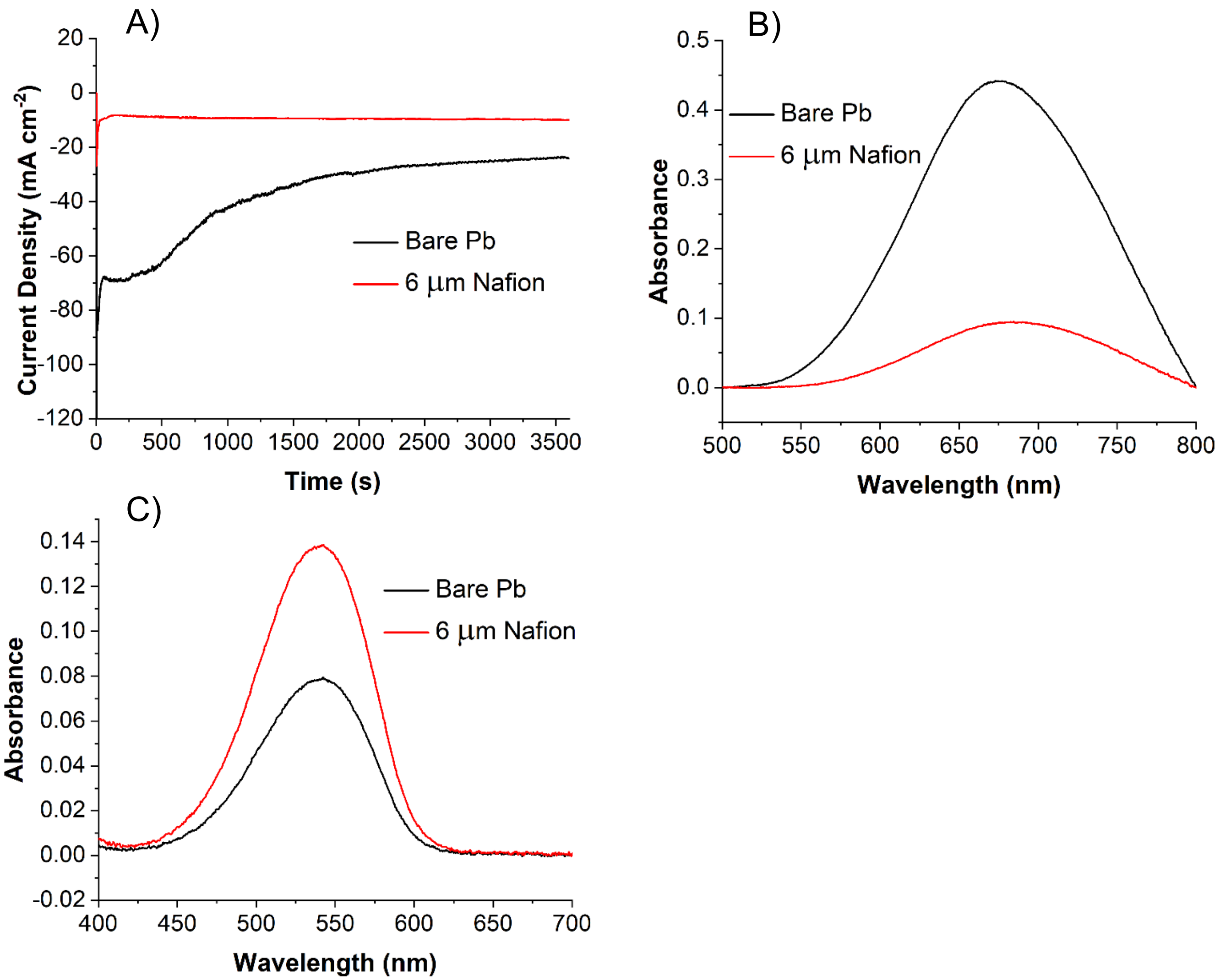

Figure 4.9: Chronoamperometry curves of unmodified (bare) Pb (black line) and Pb modified with 6 μm of Nafion (red line) at -2.0 V in 50 mM $NaNO_3$ and 100 mM Na_2SO_4 (A), and UV-Vis absorption spectra after chronoamperometry for NH_3 (B) and NO_2^- (C) detection.

The electrochemical behavior of Nafion-modified Zn and Pb electrodes also differ from Nafion-modified Cu in that the LSV onset potentials of the membrane-modified electrodes do not change significantly compared to those of the corresponding unmodified metals (Figure 4.10). In the presence of 50 mM $NaNO_3$ and 100 mM Na_2SO_4, the onset potentials of the LSVs curves (defined as the potential at which 10% of the maximum current is attained) are -1.24 V, -1.23 V, -0.5 V and -0.49 V for the unmodified Zn, Nafion-modified Zn, unmodified Pb and Nafion-modified Pb electrodes, respectively.

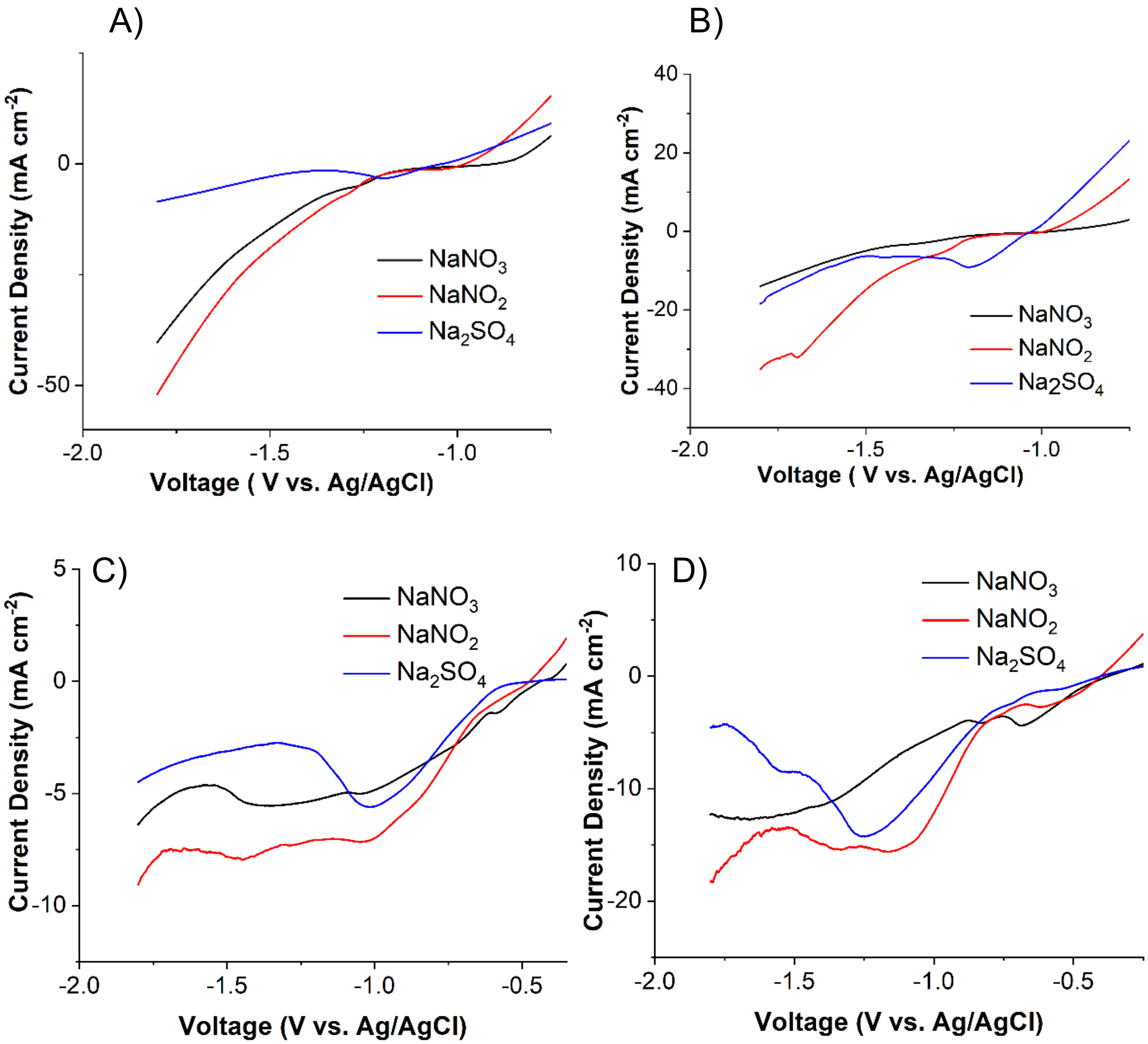

Figure 4.10: Linear sweep voltammograms at a scan rate of 10 mV s^{-1} of unmodified Zn (A), Zn modified with 6 µm of Nafion (B), unmodified Pb (C) and Pb modified with 6 µm of Nafion (D) in 50 mM $NaNO_3$ and 100 mM Na_2SO_4 (black line), 50 mM $NaNO_2$ and 100 mM Na_2SO_4 (red line), and 100 mM Na_2SO_4 (blue line).

4.3.8 NO_3^- Reduction Activity of Ti and Nafion-modified Ti Electrodes

Furthermore, a Nafion-modified Ti electrode generates a lower yield of NH_3 compared to unmodified Ti (Figures 4.4). Figure 4.11 demonstrates the chronoamperometry and UV-Vis spectra for the NO_3^- reduction using Ti and 6-µm Nafion modifed Ti electrode.

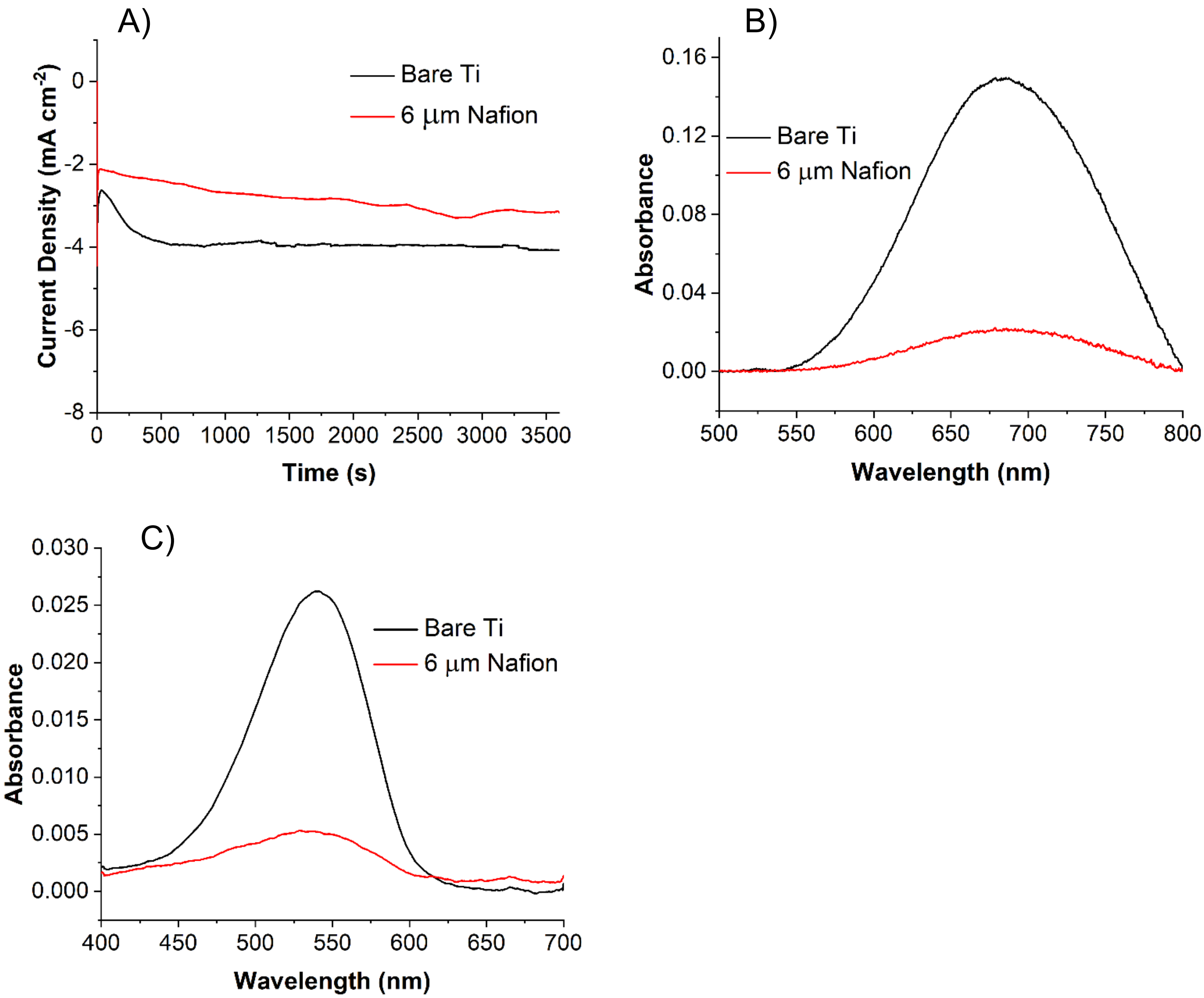

Figure 4.11: Chronoamperometry curves of unmodified (bare) Ti (black line) and Ti modified with 6 µm of Nafion (red line) at -1.6 V in 50 mM $NaNO_3$ and 100 mM Na_2SO_4 (A), and UV-Vis absorption spectra after chronoamperometry for NH_3 (B) and NO_2^- (C) detection.

In the case of the Ti LSVs, the LSV for the Nafion-modified electrolyte possesses a significantly more negative onset potential than the LSV of unmodified Ti (Figure 4.12). As, in the presence of 50 mM $NaNO_3$ and 100 mM Na_2SO_4, the onset potentials of the LSVs curves (defined as the potential at which 10% of the maximum current is attained) are -1.45 V and -1.48 V for the unmodified and Nafion-modified Ti electrodes, respectively.

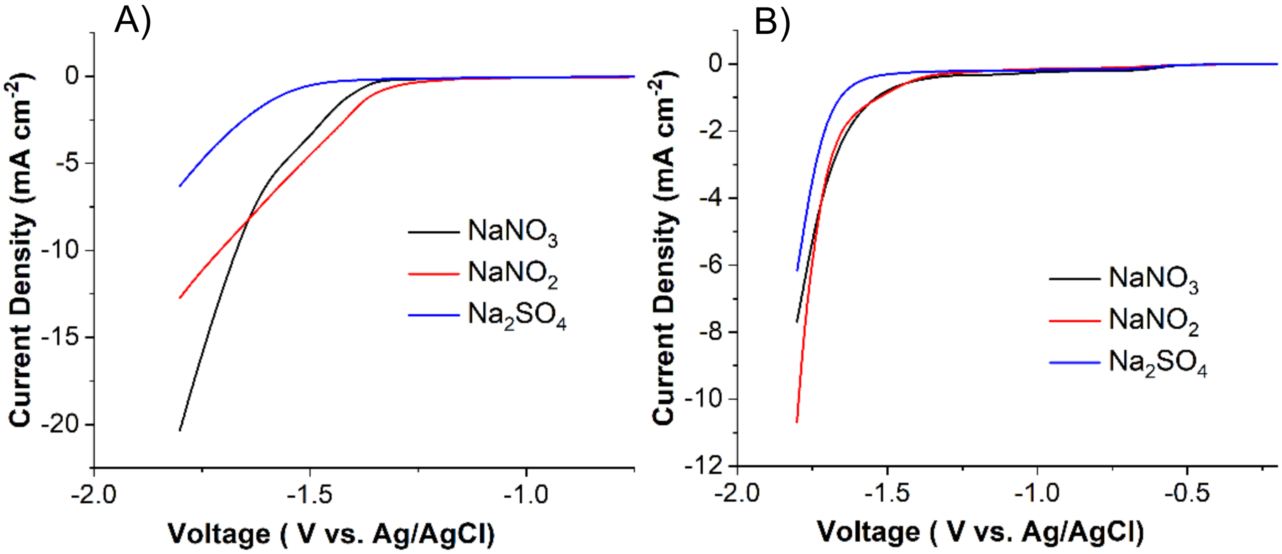

Figure 4.12: Linear sweep voltammograms at a scan rate of 10 mV s^{-1} of unmodified Ti (A) and Ti modified with 6 µm of Nafion (B) in 50 mM $NaNO_3$ and 100 mM Na_2SO_4 (black line), 50 mM $NaNO_2$ and 100 mM Na_2SO_4 (red line), and 100 mM Na_2SO_4 (blue line).

4.3.9 Effect of Nafion Overlayer on Thermodynamic Potential in Electrocatalytic NO_3^- Reduction Reaction

Comparing the LSV and NH_3 yield results across the four metal electrodes reveals a conspicuous trend. There is a correlation between the differences in onset potentials (ΔE_{onset}) and the differences in NH_3 Faradaic efficiencies (ΔFE_{NH_3}) between the Nafion-modified and unmodified electrodes (Figure 4.13). In particular, the ΔE_{onset} (+40 mV) and ΔFE_{NH_3} (+30%) values for Cu are both much greater than zero, the ΔE_{onset} (+10 mV) and ΔFE_{NH_3} (-6% for Zn and 0% for Pb) values for Zn and Pb are both near zero, and the ΔE_{onset} (-30 mV) and ΔFE_{NH_3} (-15%) for Ti are both much less than zero. This simple relationship could be used as a guide for future experimental and computational work striving to design new NO_3^- reduction catalysts that selectively produce NH_3. Since Cu and 6-µm Nafion modified Cu electrodes show the promising

Faradaic efficiency of NH_3 production, the subsequent studies are done based on these two electrodes unless mention other electrodes.

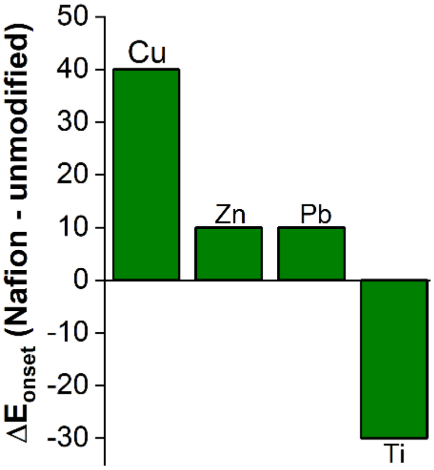

Figure 4.13: Differences in onset potentials (ΔE_{onset}) of LSVs of NO_3^- reduction between Nafion-modified and unmodified electrodes.

4.4 Electrodes Characterization.

4.4.1 X-Ray Photoelectrons Spectroscopy (XPS)

Surface composition of Cu metal electrodes (Cu foils) was characterized by XPS. Cu 2p spectra demonstrates that electrode contains mostly Cu metals and small amount of Cu(II) oxide (Figure 4.14A). Oxide can be also detected from O 1s XPS spectra (Figure 14B)

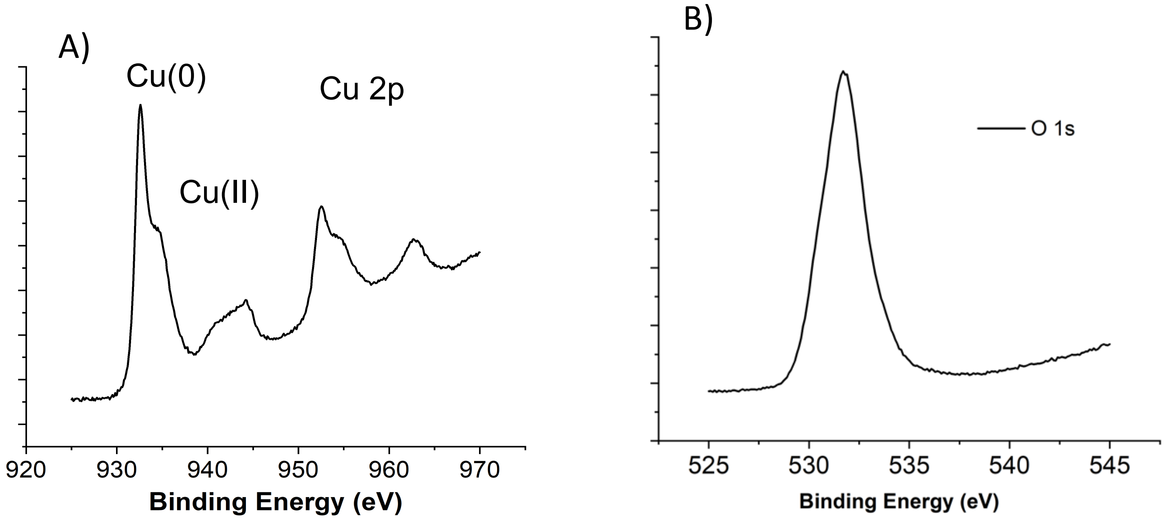

Figure 4.14: XPS spectra of bare Cu electrode.

4.4.2 X-Ray Diffraction (XRD) Study

Polycrystalline Cu foil was used as the bare Cu electrode. We have done XRD of Cu foil to understand the crystals faces presents in the Cu electrode. Figure 4.15 represents the XRD spectrum of Bare Cu foil which demonstrates that the (220) face is the most predominate crystal faces in Cu foil. Previous experiments with single crystal Cu electrodes demonstrate that the electrocatalytic properties of NO_3^- reduction vary depending upon the crystal face used.[45] So, we are assuming that Cu (220) faces are the most active faces to produce NH_3 selectively from NO_3^- reduction (For details see chapter 5).

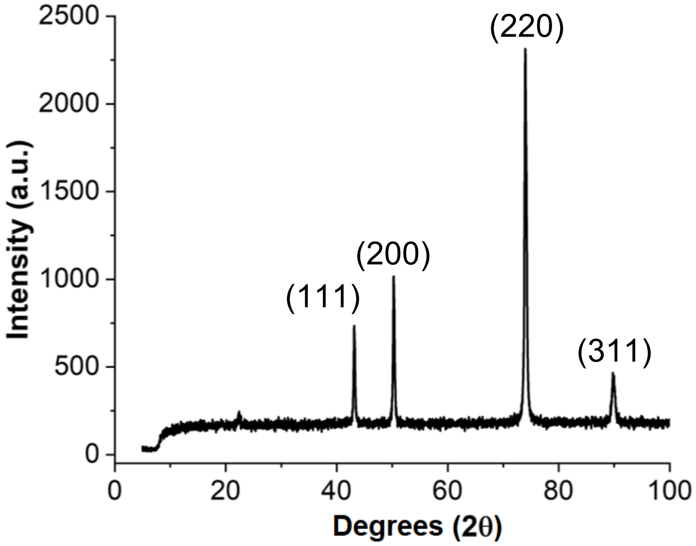

Figure 4.15: XRD spectrum of an unmodified Cu electrode.

4.4.3 Scanning Electron Microscopy (SEM) and Energy Dispersive X-ray Spectroscopy (EDX)

SEM-EDX analysis demonstrates the successful fabrication of metal electrodes with uniform layers of Nafion with thicknesses ranging from 3-10 μm using a simple dropcasting method (Figures 4.16A and 4.17). Figure 4.16A represents the cross sectional SEM image of 6-μm Nafion modified Cu electrode. Figure 4.16B is the EDX spectra for this electrode. This EDX spectra demonstrates that this electrode contains Cu, F, S, C, and O. While Cu originates from the Cu electrode, C, S and F come from the Nafion Structure and O come from both sources. EDX elemental mapping of Cu and F reveals that the Nafion overlayer is distributed uniformly on the top of the Cu electrode (Figures 4.16C and 4.16D, respectively).

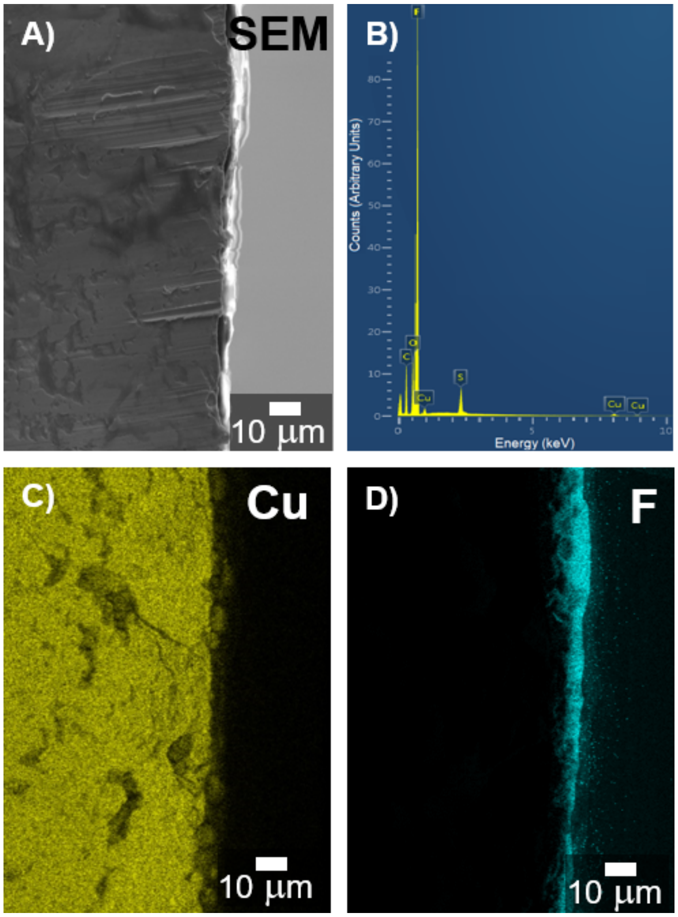

Figure 4.16: Cross-sectional SEM image of a Cu electrode modified with 6 µm of Nafion (A). The EDX spectrum of this electrode (B). EDX elemental mapping of Cu (C) and F (D) of this electrode.

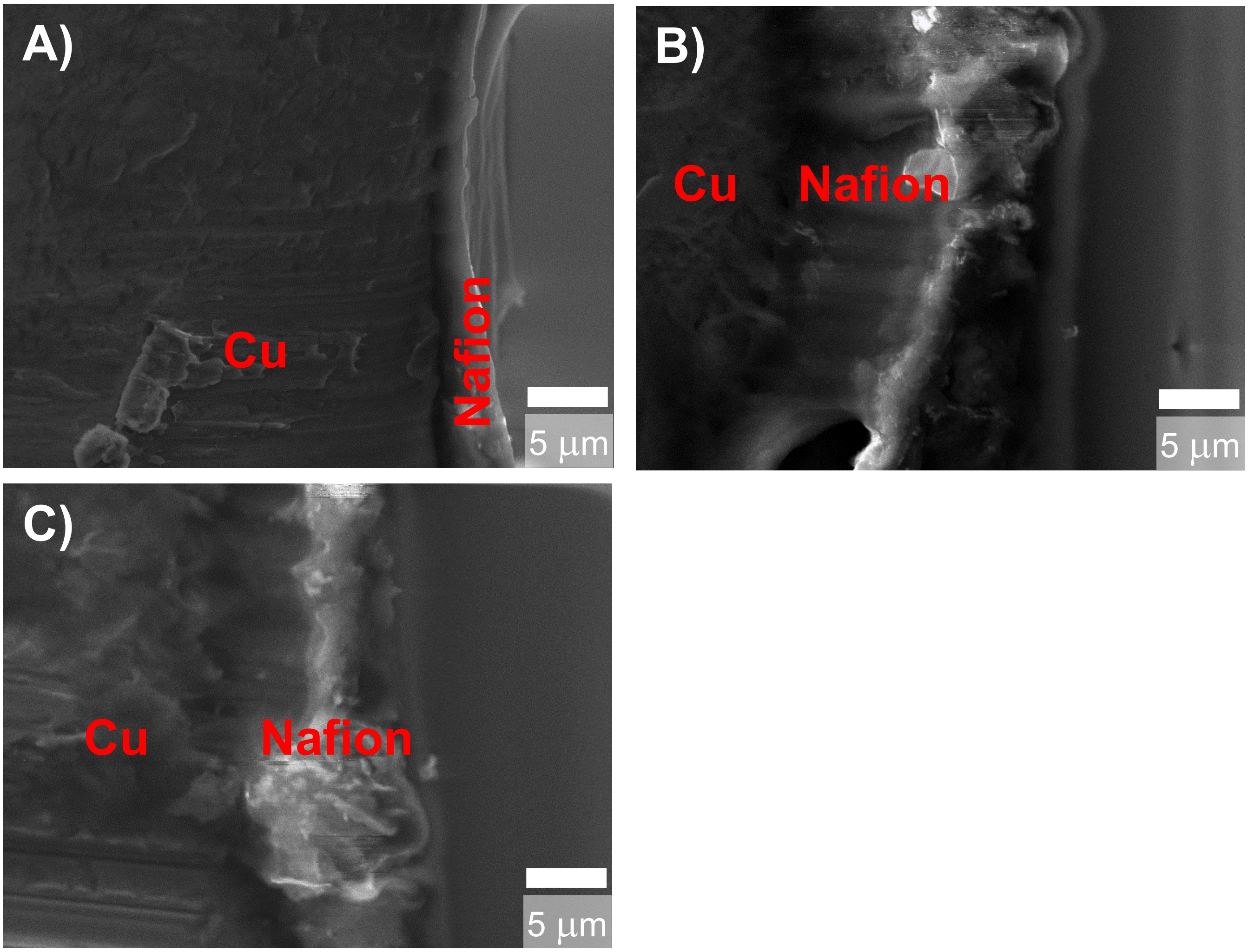

Figure 4.17: Cross-sectional SEM images of Cu electrodes modified with Nafion layers with thicknesses of about 3 µm (A), 8 µm (B) and 10 µm (C).

4.4.4 Electrochemical Impedance Spectroscopy (EIS)

To calculate the charge stores on the surface of electrodes, we have done electrochemical impedance spectroscopy (EIS). EIS was performed on unmodified Cu and Nafion-modified Cu electrodes (Figure 4.18A) in 100 mM aq. KCl in open circuit potential (OCP). While a standard Randles circuit is used to model the EIS data of the unmodified Cu electrode (Figure 4.18B), a

Randles circuit with one more resistor and capacitor is used to model the EIS data of the Nafion-modified Cu electrode to account for the Nafion layer (Figure 4.18C). R1 is the solution resistance in both circuit diagrams, and it has similar values in both experiments (12 Ω and 11 Ω for bare Cu and Nafion-modified Cu, respectively). This similarity is expected because the presence of Nafion does not significantly alter the resistance of the bulk electrolyte. R2 = 48 Ω and R3 = 52 Ω are the charge transfer resistances of the bare Cu and Nafion-modified Cu electrodes, respectively, which are also similar. The added resistance due to the Nafion is reflected in the R2 = 20 Ω component of the equivalent circuit for the Nafion-modified Cu electrode. So, the total calculated resistance of the Nafion-modified Cu is higher than the unmodified electrode, which is expected due to the addition of the resistive Nafion layer.

C1 = 95 µF and C2 = 230 µF are the double layer capacitances of the bare Cu and Nafion-modified Cu electrodes, respectively. The Nafion-modified Cu electrode possesses a higher double layer capacitance due to the charged nature of the Nafion layer, which increases the quantity of ions that are stored in the double layer above the Nafion. The C1 = 6 nF for the Nafion-modified Cu electrode indicates that some charge is also stored inside the Nafion layer. equivalent circuits used for fitting the data of bare Cu and Nafion-modified Cu are shown in panels B and C, respectively.

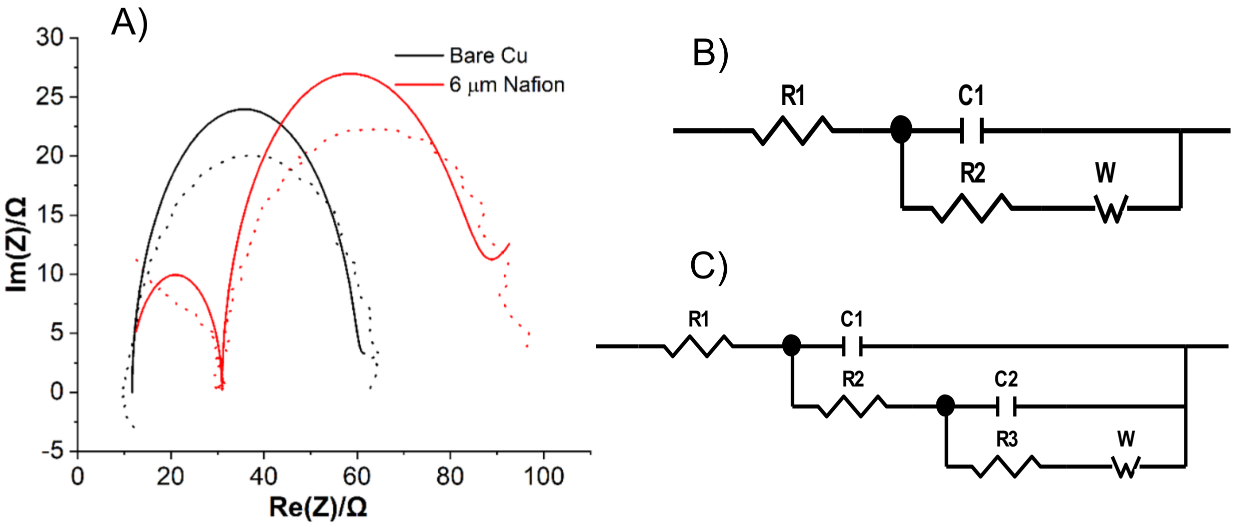

Figure 4.18: EIS spectra of bare Cu (A, black points) and Cu modified with 6 μm of Nafion (A, red points) in 100 mM KCl at open circuit potential. The best fits are displayed as the solid lines.

4.5 Mechanistic Studies of NO_3^- Reduction.

4.5.1 Electrochemical NO_3^-, NO_2^-, and NO Reduction

To further understand the origin of the significant increase in NH_3 selectivity upon Nafion modification of the Cu electrode, we performed a series of experiments aimed at probing the mechanisms of NO_3^- reduction on Nafion-modified and unmodified Cu. Previous literature indicates that NH_3 production from NO_3^- on Cu occurs via the successive production of metal-bound NO_2^- and NO intermediates.[47] As with NO_3^- reduction, we find that NO_2^- reduction at the same concentration of electrolyte (50 mM) on Cu results in a greater Faradaic efficiency in the presence of the Nafion layer (Figure 4.19, middle two bars). Figure 20, A and B demonstrates the chronoamperometry and UV-Vis spectra of this NO_2^- reduction experiments. Similarly, NO reduction from a NO-saturated Na_2SO_4 electrolyte on the Nafion-modified Cu electrode produces NH_3 with greater selectivity than on unmodified Cu (Figure 4.19, rightmost two bars). Figure 20, C and D demonstrates the chronoamperometry and UV-Vis spectra of this NO reduction experiments. These results suggest that the Nafion-induced increase in NH_3 selectivity observed for NO_3^- reduction is due, at least in part, to an increase in the kinetics of NO conversion to NH_3.

This interpretation that NO reactivity on Cu is activated by Nafion is further supported by DFT calculations (*vide infra*).

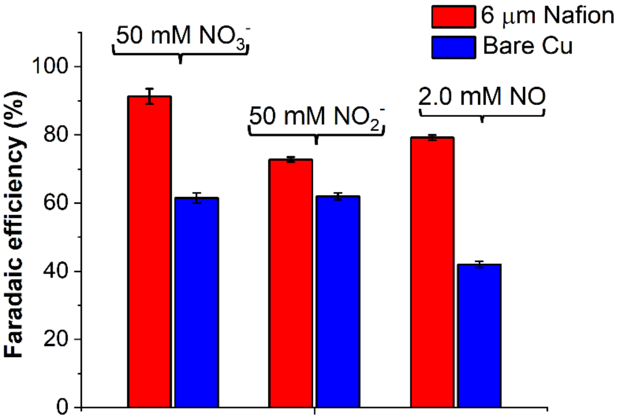

Figure 4.19: Comparison of Faradaic efficiencies for NH_3 production from NO_3^- reduction (leftmost two bars), NO_2^- reduction (middle two bars), and NO reduction (rightmost two bars) using Cu electrodes modified with 6 µm of Nafion (red bars) and unmodified Cu electrodes (blue bars) after 1 hour of chronoamperometry at -1.4 V. The solutions used contain 100 mM Na_2SO_4 as a supporting electrolyte.

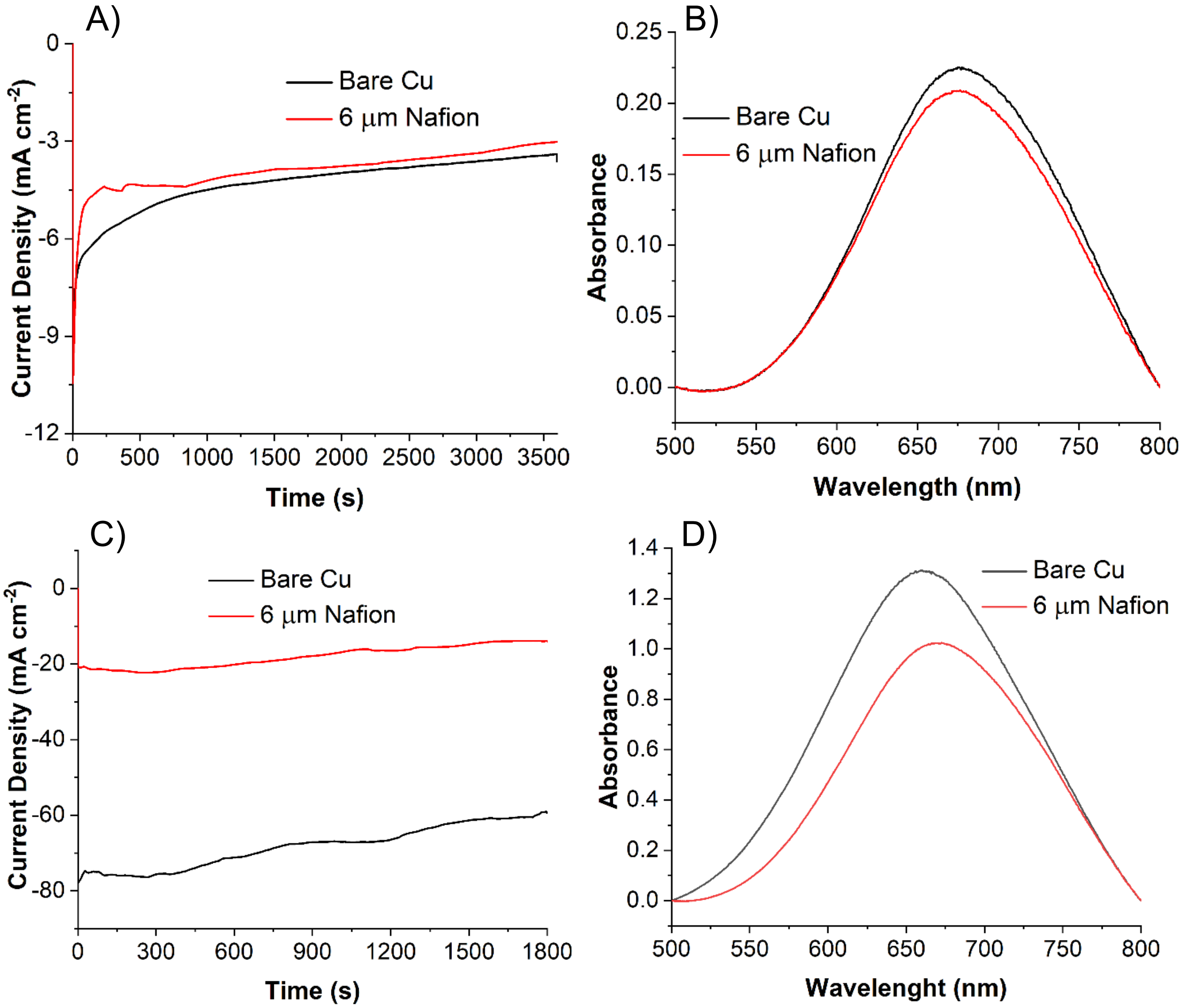

Figure 4.20: Chronoamperometry curves of unmodified (bare) Cu (black line) and Cu modified with 6 μm of Nafion (red line) at -1.4 V in 50 mM $NaNO_2$ (A) and 2 mM NO (C) containing 100 mM Na_2SO_4 and UV-Vis absorption spectra after chronoamperometry for NH_3 (B and D) detection.

Although the Faradaic efficiencies for NH_3 are all greater with Nafion as compared to unmodified Cu for NO_3^-, NO_2^-, and NO reduction, there is variation in the NH_3 yields for the Nafion-modified electrodes across the three electrolytes (Figure 4.19, red bars). In particular, the Nafion-modified electrode possess a lower selectivity for NH_3 during NO_2^- reduction, (72.8 ± 0.7) %, compared to NO_3^- reduction, (91 ± 2) %. When a Nafion-modified Cu electrode in an electrolyte containing 25 mM $NaNO_3$ and 25 mM $NaNO_2$ is used, the Faradaic efficiency for NH_3, (71 ± 1) %, is the same within experimental error as when the electrolyte contains 50 mM $NaNO_2$, (72.8 ± 0.7) %. These results indicate that NO_3^- reduction to NH_3 is inhibited in the presence of NO_2^-, which is consistent with previous findings for other Cu-based catalysts that show NH_3 production can be affected by bulk NO_2^-.[41] Furthermore, the Nafion-modified Cu electrode also exhibits decreased NH_3 selectivity for NO reduction as compared to NO_3^- reduction due to the lower concentration of NO in a NO-saturated electrolyte (2 mM) compared to the NO_3^- electrolyte (50 mM). Indeed, both NO_3^- and NO_2^- reduction on unmodified Cu electrodes with lower concentration electrolytes (i.e. 2 mM NO_3^- or 2 mM NO_2^-) result in significantly diminished NH_3 yields, (13 ± 1) % and (11 ± 1) %, for NO_3^- and NO_2^-, respectively.

4.5.2 Surface Enhance Raman Spectroscopy

To further investigate the mechanism of NO_3^- reduction on Nafion-modified Cu, we used surface-enhanced Raman spectroscopy (Figure 4.21). First, we collected the Raman spectrum of an unmodified Cu substrate, which does not contain any peaks (Figure 4.21, black line). After NO was sparged across the Cu surface, the spectrum possesses two broad peaks centered around 1600 cm^{-1} and 1350 cm^{-1} (Figure 4.21, blue line). The more intense peak at 1600 cm^{-1} is assigned to a NO stretching mode in Cu-NO, the frequency of which is similar to previously reported metal-nitrosyl complexes.[60] The broader peak centered around 1350 cm^{-1} is assigned to NO stretching in bridging species with multiple Cu sites such as Cu_2-(μ-NO). As is the case here, the vibrational modes of analogous bridging metal-NO and metal-CO species have significantly lower wavenumbers than their unbridged counterparts.[61,62] The relative broadness of both peaks is likely due to the presence of multiple NO binding modes and crystal faces of the polycrystalline Cu substrates.

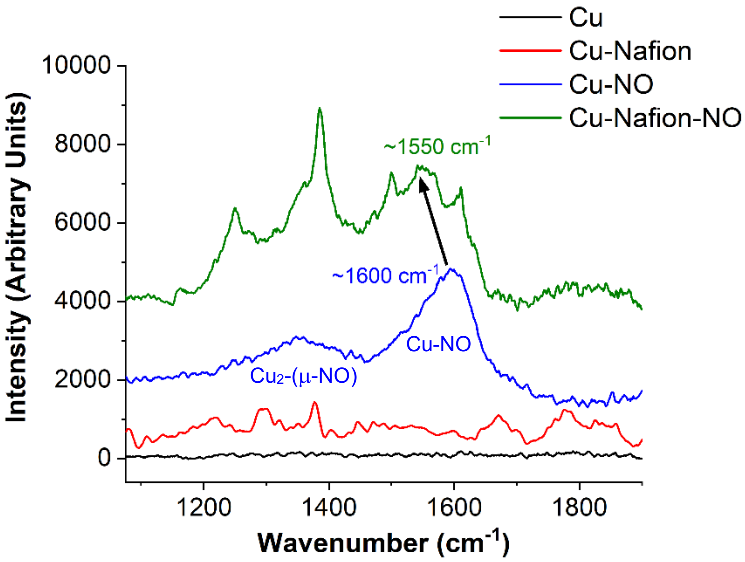

Figure 4.21: Surface-enhanced Raman spectra of an unmodified Cu electrode (black line), a Nafion-modified Cu electrode (red line), a Cu electrode exposed to NO (blue line), and a Nafion-modified Cu electrode exposed to NO (green line) at open circuit potential.

The Raman spectrum of a Nafion-modified Cu substrate possesses a series of weak, but relatively sharp peaks from 1200 cm^{-1} to 1800 cm^{-1} due to various vibrational modes arising from Nafion. After NO was sparged across the Nafion-modified Cu surface, sharp peaks corresponding to Nafion are still observed, however, the broad NO peak at 1600 cm^{-1} on unmodified Cu shifts to 1550 cm^{-1} in the presence of Nafion. This decrease in the frequency of NO stretching on the Nafion-modified electrode indicates that the NO bond is weakened when it is covered by the polymer. This weaker NO bond explains why a Nafion overlayer increases NH_3 selectivity on a Cu electrode. In other words, the Nafion layer activates the NO bond, which increases the kinetics of NH_3 formation. Next, we use DFT calculations to further understand the reactivity of NO inside Nafion-modified Cu and to corroborate the Raman spectroscopy results.

4.5.3 4DFT Calculations

4.5.3.1 Characteristic of N-O Bonds

Periodic DFT PBE-D3 calculations were performed on a 4×4 slab of Cu(111) with three layers while holding atoms in the bottom layer fixed.[63,64] Spurious interactions of images were prevented by using a length of 50 Å in the direction perpendicular to the slab surface. Nafion was modeled with $[CF_3O(CF_2)_2SO_3]^-[H_3O]^+(H_2O)_2$; ergo an hydronium and two explicit water molecules are associated with the sulfonate group. Without Nafion, we considered absorption with a water trimer (Figure 4.22A). In both cases, there are hydrogen-bonding interactions between explicit water molecules and NO. The N-O bond distance is 1.247 Å on Cu(111), becoming slightly elongated to 1.252 Å when NO interacts with explicit water molecules associated with the sulfonate and hydronium of Nafion. The Nafion also causes NO to be more closely bound to the surface, 1.227 Å, versus 1.235 Å. These structural differences lead to lowered wavenumbers for the N-O vibrational stretching mode in the presence of Nafion (Figure 4.22). Indeed, the calculated difference in these stretching frequencies, $\Delta\upsilon$ = 45 cm^{-1}, between the Nafion-modified and unmodified Cu(111) surfaces agrees well with the experimental Raman data ($\Delta\upsilon \sim 50$ cm^{-1}, Figure 4.21), although the absolute values of the calculated harmonic frequencies underestimate the values measured experimentally. This underestimation is expected and has been observed previously for vibrational calculations using the PBE-D3 functional.[65]

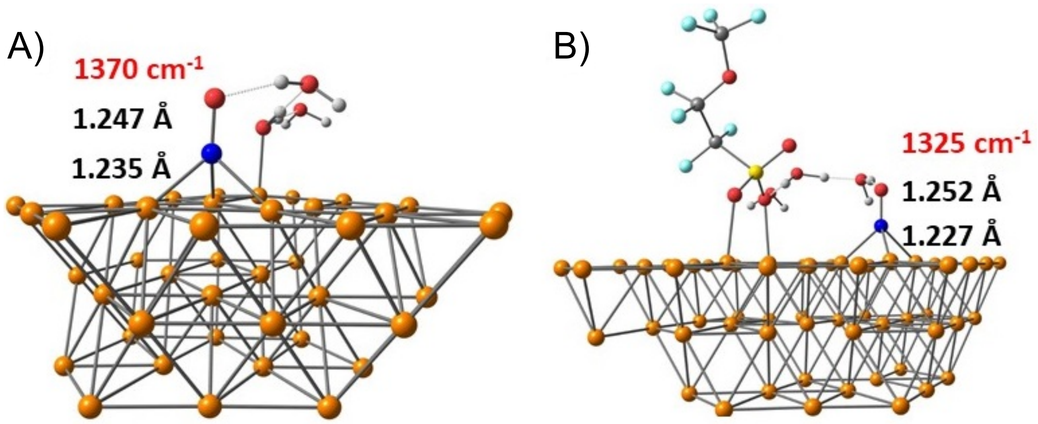

Figure 4.22: Structural properties of NO adsorbed at the Cu(111) surface with (A) water and (B) a model for Nafion, an associated hydronium, and water molecules.

4.5.3.2 4.5.3.2. Potential Steps Determination for NH_3 Production

The reaction path for the NO → NH_3 process was calculated on Cu(111) and Nafion-coated Cu(111) (Figure 4.23). We used a hydronium ion solvated by three water molecules and an excess electron, $[H_9O_4]$, as the source of protons and electrons; following the recommendations of Rossmeisl et al.[66] We then added an additional H atom after each reduction step. In the presence of Nafion, reaction energies of the $^*NO \rightarrow {}^*NOH$, $^*NOH \rightarrow {}^*N + H_2O$, $^*N \rightarrow {}^*NH$, $^*NH \rightarrow {}^*NH_2$, and $^*NH_2 \rightarrow {}^*NH_3$ steps are all lowered. Interestingly, the greatest impact is found for the first hydrogenation step, the potential-limiting step, indicating that Nafion and the water around its associated proton sufficiently perturb surface-adsorbed NO to affect energetics of NO reduction to NH_3.[67] Analogous computations on Zn(001) and Nafion-coated Zn(001) surfaces provide $^*NO \rightarrow {}^*NOH$ reaction energies of -0.90 eV and -1.02 eV, respectively. Thus for Zn(001), Nafion has an impact of -0.13 eV, a factor of 4.1 smaller than the impact on Cu(111) (Figure 4.23), which agrees with our experimental data indicating that a Nafion-modified Zn electrode does not display a significantly altered NO_3^- reduction product distribution as compared to unmodified Zn (Figure 4.4). Taken together, these results demonstrate that it is the activation of the NO bond by Nafion that enables the Nafion-modified Cu electrode to display enhanced selectivity for NH_3 production.

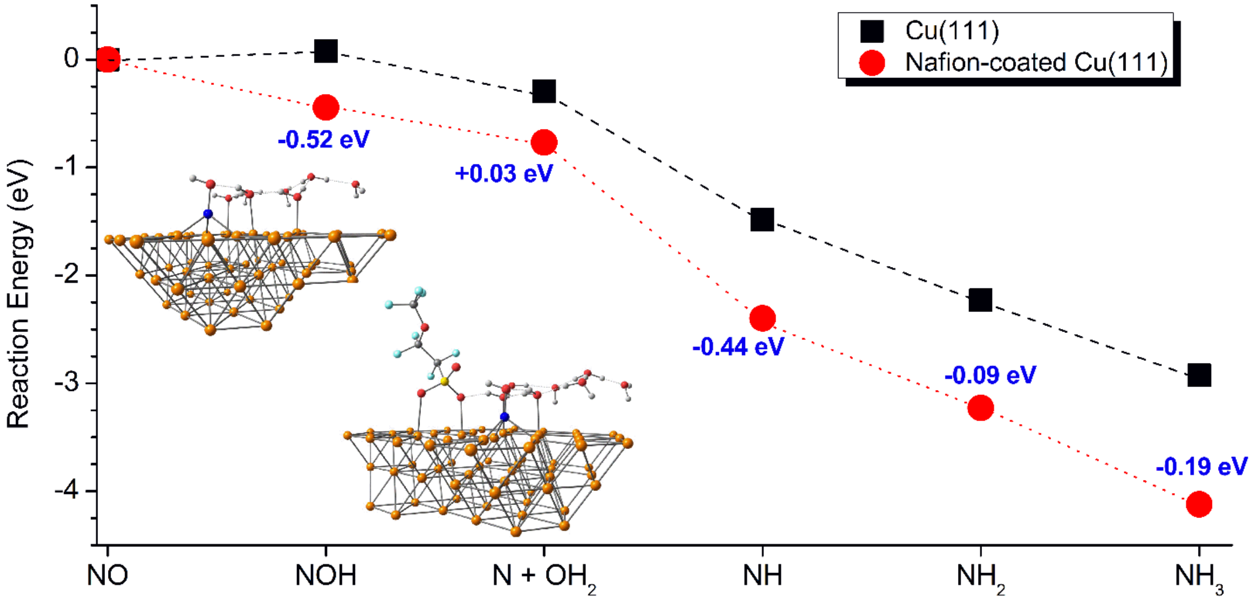

Figure 4.23: Calculated reaction path for NO reduction to NH3 on Cu(111) and Nafion-coated Cu(111) obtained from DFT. The impact of Nafion on reaction energies are given in blue and insets show optimized structures of the *NOH species.

4.6 Denitrification of Groundwater.

Lastly, we tested the practicality of the Nafion-modified Cu electrode by using it to remove NO_3^- from a real-world groundwater sample. We obtained groundwater from a rural residential well in Silver Springs, Nevada, which is located in an agricultural valley 30 miles east of Reno, Nevada. Groundwater NO_3^- contamination is common in regions like these due to agricultural runoff from fertilizers. The NO_3^- concentration measured in the well water was 0.24 ppm, which is more than double the 0.10 ppm average for commercially treated water in Reno.[68]

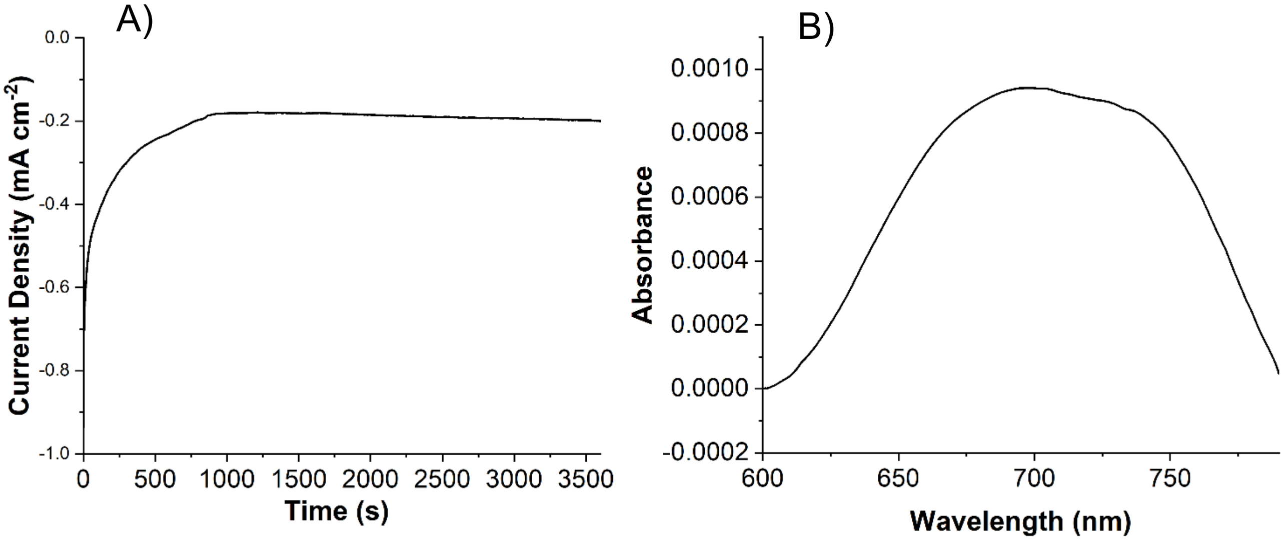

Figure 4.24: Chronoamperometry curve of Cu modified with 6 μm of Nafion at -1.4 V in groundwater obtained from a well in Silver Springs, Nevada, United States, and UV-Vis absorption spectrum after chronoamperometry for NH_3 detection (B).

We used the Nafion-modified Cu electrode to denitrify the well water directly without the addition of a supporting electrolyte. After one hour of chronoamperometry at -1.4 V vs. Ag/AgCl, the NO_3^- concentration in the water decreased from 0.24 ppm to 0.008 ppm, which represents a 97% NO_3^- removal efficiency (Figure 4.24). These results demonstrate that the Nafion-modified Cu catalyst has potential for practical use in water purification.

4.7 Conclusions.

In summary, this work discusses electrochemical NO_3^- reduction to NH_3 using simple Nafion-modified metal catalysts. For the case of Nafion-modified Cu, which produces NH_3 with excellent selectivity, the Nafion overlayer activates the NO bound in a Cu-NO intermediate, which accelerates NH_3 generation. This interpretation is supported by surface-enhanced Raman spectroscopy data and DFT calculations. In addition to demonstrating the practical applicability of these catalysts for water purification, this work opens up a new research direction for the development of selective NO_3^- reduction catalysts using membrane-modified electrodes.

4.8 References.

1. Foster, S. L.; Bakovic, S. I. P.; Duda, R. D.; Maheshwari, S.; Milton, R. D.; Minteer, S. D.;Janik, M. J.; Renner, J. N.; Greenlee, L. F. Catalysts for nitrogen reduction to ammonia. *Nat. Catal.,* **2018**, *1,* 490–500.
2. Tang, C.; Qiao, S. Z. How to explore ambient electrocatalytic nitrogen reduction reliably and insightfully. *Chem Soc Rev.,* **2019**, *48,* 3166–3180.
3. Service, R. F. New recipe produces ammonia from air, water, and sunlight. *Science,* **2014**, *345,* 610-610.
4. Ashida, Y.; Arashiba, K.; Nakajima, K.; Nishibayashi, Y. Molybdenum-catalysed ammonia production with samarium diiodide and alcohols or water. *Nature*, **2019**, *568*, 536–540.
5. Bhown, A.; Cussler, E.; Mechanism for selective ammonia transport through poly (vinylammonium thiocyanate) membranes. *J. Am. Chem. Soc.,* **1991**, *113,* 742–749.
6. Jiao, F.; Xu, B. Electrochemical ammonia synthesis and ammonia fuel cells. *Adv. Mater*., **2019,** *31,* 1805173.
7. Afif, A.; Radenahmad, N.; Cheok, Q.; Shams, S.; Kim, J. H.; Azad, A. K. Ammonia-fed fuel cells: a comprehensive review. *Renew. Sustain. Energy Rev,* **2016**, *60,* 822–835.
8. Ertl, G. Primary steps in catalytic synthesis of ammonia. *J. Vac. Sci. Technol. Vac. Surf. Films,* **1983**, *1,* 1247–1253.
9. Kyriakou, V.; Garagounis, I.; Vasileiou, E.; Vourros, A.; Stoukides, M. Progress in the electrochemical synthesis of ammonia. *Catal. Today.,* **2017**, *286*, 2–13.
10. Wu, T.; Fan, W.; Zhang, Y.; Zhang, F. Electrochemical synthesis of ammonia: Progress and challenges. *Mater. Today Phys.,* **2021**, *16,* 100310–100332.

11. Kyriakou, V.; Garagounis, I.; Vourros, A.; Vasileiou, E.; Stoukides, M. An electrochemical haber-bosch process. *Joule,* **2020**, *4,* 142–158.
12. Wan, Y.; Xu, J.; Lv. R. Heterogeneous electrocatalysts design for nitrogen reduction reaction under ambient conditions. *Mater. Today.,* **2019**, *27,* 69–90.
13. Suryanto, B. H.; Du, H. L.; Wang, D.; Chen, J.; Simonov, A. N.; MacFarlane, D. R. Challenges and prospects in the catalysis of electroreduction of nitrogen to ammonia. *Nat. Catal.,* **2019**, *2,* 290–296.
14. Guo, C.; Ran, J.; Vasileff, A.; Qiao, S. Z. Rational design of electrocatalysts and photo (electro) catalysts for nitrogen reduction to ammonia (NH_3) under ambient conditions. *Energy Environ. Sci,* **2018**, *1,* 45–56.
15. Chen, C. F.; Cao, X.; Wu, S.; Zeng, X.; Ding, L. X.; Zhu, M.; Wang, H. Ammonia Electrosynthesis with High Selectivity under Ambient Conditions via a Li^+ Incorporation Strategy. *J. Am. Chem. Soc.,* **2017**, 139*,* 9771–9774.
16. Stirling, A.; Papai, I.; Mink, J.; Salahub, D. R. Density functional study of nitrogen oxides. *J. Chem. Phys.,* **1994**, *100,* 2910–2923.
17. Menció, A.; Mas-Pla, J.; Otero, N.; Regàs, O.; Boy-Roura, M.; Puig, R.; Bach, J., Domènech, C.; Zamorano, M.; Brusi, D. Nitrate pollution of groundwater; all right…, but nothing else? *Sci. Total Environ.* **2016**, *539,* 241–251.
18. Gracia-Segura, S.; Lanzarini-Lopes, M.; Hristovski, K.; Westerhoff, P. Electrocatalytic reduction of nitrate: Fundamentals to full-scale water treatment applications. *Appl. Catal. B Environ.* **2018**, *236,* 546–568.

19. Ward, M. H.; Jones, R. R.; Brender, J. D.; De Kok, T. M.; Weyer, P. J.; Nolan, B. T.; Villanueva, C. M.; Van Breda, S. G. Drinking water nitrate and human health: An updated review, *Int. J. Environ. Res. Public. Health,* **2018**, *15*, 15-45.
20. Self, J. R.; Waskom, R. Nitrates in drinking water. *Colorado State University* Fact Sheet, No**1992**, *0517*, 1–3.
21. Kross, B. Nitrate toxicity and drinking water standards–A Review. *J Prev Med,* **2002**, *10,* 3–10.
22. Martínez, J.; Ortiz, A.; Ortiz, I. State-of-the-Art and perspectives of the catalytic and electrocatalytic reduction of aqueous nitrates. *Appl. Catal. B Environ.,* **2017,** *207*, 42–59.
23. Dima, G. E.; De Vooys, A. C. A.; Koper, M. T. M. Electrocatalytic reduction of nitrate at low concentration on coinage and transition-metal electrodes in acid solutions. *J. Electroanal. Chem. Lausanne Switz.,* **2003**, *554–555,* 15–23.
24. Katsounaros, I.; Kyriacou, G. Influence of nitrate concentration on its electrochemical reduction on tin cathode: Identification of reaction intermediates *Electrochimica Acta,* **2008**, *53,* 5477–5484.
25. Pronkin, S. N.; Simonov, P. A.; Zaikovskii, V.I.; Savinova, E. R. Model Pd-based bimetallic supported catalysts for nitrate electroreduction. *J. Mol. Catal. Chem.,* **2007**, *265,* 141–147.
26. Shimazu, K.; Goto, R.; Piao, S.; Kayama, R.; Nakata, K.; Yoshinaga, Y. Reduction of nitrate ions on tin-modified palladium thin film electrodes. *J. Electroanal. Chem.,* **2007**, *601,* 161–168.

27. Piao, S.; Kayama, Y.; Nakano, Y.; Nakata, K.; Yoshinaga, Y.; Shimazu, K. Nitrate reduction on tin-modified rhodium, ruthenium, and iridium electrodes. *J. Electroanal. Chem.* **2009**, *629,* 110–116.
28. Pérez-Gallent, E.; Figueiredo, M. C.; Katsounaros, I.; Koper, M. T. M. Electrocatalytic reduction of Nitrate on Copper single crystals in acidic and alkaline solutions. *Electrochimica Acta,* **2017**, *227,* 77–84.
29. Supakul, S. N.; Barile, Membrane-modified metal triazole complexes for the electrocatalytic reduction of oxygen and carbon dioxide. C. J. *Front. Chem.,* **2018**, *6,* 1-8.
30. Pan, H.; Barile, C. J. Electrochemical CO 2 reduction to methane with remarkably high Faradaic efficiency in the presence of a proton permeable membrane. *Energy Environ. Sci.,* **2020**, *13*, 3567–3578.
31. Lei, F.; Xu, W.; Yu, J.; Li, K.; Xie, J.; Hao, P.; Cui, G.; Tang, B. T. Electrochemical synthesis of ammonia by nitrate reduction on Indium incorporated in sulfur doped graphene. *Chem. Eng. J.,* **2021**, *426,* 131317–131323.
32. Katsounaros, I.; Dortsiou, M.; Polatides, C.; Preston, S.; Kypraios, T.; Kyriacou, G. Reaction pathways in the electrochemical reduction of nitrate on tin. *Electrochimica Acta,* **2012**, *71,* 270–276.
33. Hori, Y.; Kikuchi, K.; Suzuki, S. Production of CO and CH_4 in electrochemical reduction of CO_2 at metal electrodes in aqueous hydrogencarbonate solution. *Chem. Lett.,* **1985**, *14,* 1695–1698.

34. Kortleyer, R.; Shen, J.; Schouten, K. J. P.; Calle-Vallejo, F.; Koper, M. T. M. Catalysts and reaction pathways for the electrochemical reduction of carbon dioxide. *J. Phys. Chem. Lett.,* **2015**, 6*,* 4073–4082.

35. Hasnat, M. A.; Ishibashi, I.; Sato, K.; Agui, R.; Yamaguchi, T.; Ikeue, K.; Machida, M. Electrocatalytic Reduction of Nitrate Using Cu–Pd and Cu–Pt Cathodes/H^+-Conducting Solid Polymer Electrolyte Membrane Assemblies. *Bull. Chem. Soc. Jpn.,* **2008**, *81,* 1675–1680.

36. Machida, M.; Sato, K.; Ishibashi, I.; Hasnat, M. A.; Ikeue, K. Electrocatalytic nitrate hydrogenation over an H^+-conducting solid polymer electrolyte membrane–modified cathode assembly. *Chem. Commun.,* **2006**, *7,* 732–734.

37. Brauer, G. Inorganic chemistry: Vol. 1. Reed F. Riley, Ed. Academic Press, New York, NY **1963**.

38. Zacharia, I. G.; Deen, W. M. Diffusivity and solubility of nitric oxide in water and saline. *Ann. Biomed. Eng.,* **2005**, *33,* 214–222.

39. Polatides, C.; Kyriacou, G. Electrochemical reduction of nitrate ion on various cathodes–reactions kinetics on bronze cathode. *J. Appl. Electrochem.,* **2005**, *35,* 421–427.

40. (40) Furman, N. H. "Scott's Standard Methods of Chemical Analysis," 5th ed. D. Van Nostrand and Co., New York, NY, **1939**, pg. 630.

41. Chen, G. F.; Yuan, Y.; Jiang, H.; Ren, S. Y.; Ding, L. X.; Ma, L.; Wu, T.; Lu, J.; Wang, H. Electrochemical reduction of nitrate to ammonia via direct eight-electron transfer using a copper–molecular solid catalyst. *Nat. Energy,* **2020**, *5,* 605–613.

42. Schnetger,B.; Lehners, C. Determination of nitrate plus nitrite in small volume marine water samples using vanadium (III) chloride as a reduction agent. *Mar. Chem.,* **2014**, *160,* 91–98.
43. Watt, G.W.; Chrisp, J. D. Spectrophotometric method for determination of hydrazine. *Anal. Chem.* **1952**, *24,* 2006–2008.
44. Liu, H.; Park, J.; Chen, Y.; Oiu, Y.; Cheng, Y.; Srivastava, K.; Gu, S.; Shanks, B. H.; Roling, L. T.; Li, W. Electrocatalytic nitrate reduction on oxide-derived silver with tunable selectivity to nitrite and ammonia. *ACS Catal.,* **2021**, *11,* 8431–8442.
45. Butcher Jr. D. P.; Gewirth, A. A. Nitrate reduction pathways on Cu single crystal surfaces: Effect of oxide and Cl^-. *Nano Energ.,* **2016**, *29*, 457–465.
46. Yamauchi, M.; Abe, R.; Tsukuda, T.; Kato, K.; Takata, M. Highly Selective Ammonia Synthesis from Nitrate with Photocatalytically Generated Hydrogen on CuPd/TiO_2. *J. Am. Chem. Soc.,* **2011**, *133,* 1150–1152.
47. Wu, Z. Y.; Karamad, M.; Yong, X.; Huang, Q.; Cullen, D. A.; Zhu, P.; Xia, C.; Xia, Q.; Shakouri, M.; Chen, F. Y.; et al. Electrochemical ammonia synthesis via nitrate reduction on Fe single atom catalyst. *Nat. Commun.,* **2021**, *12*, 2870–2879.
48. Chen, G. F.; Yuan, Y.; Jiang, H.; Ren, S. Y.; Ding, L. X.; Ma, L.; Wu, T.; Lu, J.; Wang, H. Electrochemical reduction of nitrate to ammonia via direct eight-electron transfer using a copper–molecular solid catalyst. *Nat. Energy*., **2020**, *5,* 605–613.
49. Chaplin, B. P.; Shapley, J. R.; Werth, C. J. The Selectivity and Sustainability of a Pd–In/γ-Al_2O_3 Catalyst in a Packed-Bed Reactor: The Effect of Solution Composition. *Catal. Lett.,* **2009**, *130,* 56–62.

50. Hasnat, M. A.; Karim, M. R.; Machida, M. Electrocatalytic ammonia synthesis: role of cathode materials and reactor configuration. *Catal. Commun.,* **2009**, *10,* 1975–1979.
51. Gayen, P.; Spataro, J.; Avasarala, S.; Ali, A. M.; Cerrato, J. M.; Chaplin, B. P. Electrocatalytic Reduction of Nitrate Using Magnéli Phase TiO_2 Reactive Electrochemical Membranes Doped with Pd-Based Catalysts. *Environ. Sci. Technol.,* **2018**, *52,* 9370–9379.
52. Deng, X.; Yang, Y.; Wang, L.; Fu, X. Z.; Luo, J. L. Metallic Co Nanoarray Catalyzes Selective NH_3 Production from Electrochemical Nitrate Reduction at Current Densities Exceeding 2 A cm^2. *Adv. Sci.,* **2021**, *8,* 2004523–2004531.
53. Wang, C.; Liu, Z.; Hu, T.; Li, J.; Dong, L.; Du, F.; Li, C.; Guo, C. Metasequoia-like Nanocrystal of Iron-Doped Copper for Efficient Electrocatalytic Nitrate Reduction into Ammonia in Neutral Media. *ChemSusChem.,* **2021**, *14,* 1825–1829.
54. Wang, Y.; Xu, A.; Wang, Z.; Huang, L.; Li, J.; Li, F.; Wicks, J.; Luo, M.; Nam, D. H.; Tan, C. S.; et al. Enhanced Nitrate-to-Ammonia Activity on Copper–Nickel Alloys via Tuning of Intermediate Adsorption. *J. Am. Chem. Soc.,* **2020**, *142*, 5702–5708.
55. Yu, Y.; Wang, C.; Yu, Y.; Wang, Y.; Zhang, B. Promoting selective electroreduction of nitrates to ammonia over electron-deficient Co modulated by rectifying Schottky contacts. *Sci. China Chem.,* **2020**, *63,* 1469–1476.
56. Wang, Y.; Liu, C.; Zhang, B.; Yu, Y. Self-template synthesis of hierarchically structured Co_3O_4@NiO bifunctional electrodes for selectivenitrate reduction and tetrahydroisoquinolines semidehydrogenation. *Sci. China Mater.,* **2020**, *63,* 2530–2538.
57. El-Deab, M. S. Electrochemical reduction of nitrate to ammonia at modified gold electrodes. *Electrochimica Acta.,* **2004**, *49,* 1639–1645.

58. Su, L.; Li, K.; Zhang, H.; Fan, M.; Ying, D.; Sun, T.; Wang, Y.; Jia, J. Electrochemical nitrate reduction by using a novel Co3O4/Ti cathode. *Water Res.* **2017**, *120*, 1–11.

59. Zhu, J. Y.; Xue, Q.; Xue, Y. Y.; Ding, Y.; Li, F. M.; Jin, P.; Chen, P.; Chen Y. Iridium nanotubes as bifunctional electrocatalysts for oxygen evolution and nitrate reduction reactions. *ACS Appl. Mater. Interfaces,* **2020**, *12,* 14064–14070.

60. Huheey, J. E.; Keiter, E. A.; Keiter, R. L. 4th Ed. *Pearson College Division*, New York, NY 1993.

61. De La Cruz, C.; Sheppard, N. A structure-based analysis of the vibrational spectra of nitrosyl ligands in transition-metal coordination complexes and clusters. *Spectrochim. Acta. A. Mol. Biomol. Spectrosc.,* **2011**, *78,* 7–28.

62. Schmitt, K. G.; Gewirth, A. A. In situ surface-enhanced Raman spectroscopy of the electrochemical reduction of carbon dioxide on silver with 3, 5-diamino-1, 2, 4-triazole. *J. Phys. Chem., C,* **2014**, *118,* 17567–17576.

63. Perdew, J. P.; Burke, K.; Ernzerhof, M. Generalized gradient approximation made simple. *Phys Rev Lett.,* **1996**, *77,* 3865–3868.

64. Grimme, S.; Antony, J.; Ehrlich, S.; Krieg, H. A consistent and accurate ab initio parametrization of density functional dispersion correction (DFT-D) for the 94 elements H-Pu. *J. Chem. Phys.,* **2010**, *132,* 154104.

65. Alecu, I. M.; Zheng, J.; Zhao, Y.; Truhlar, D. G. Computational thermochemistry: scale factor databases and scale factors for vibrational frequencies obtained from electronic model chemistries. *J. Chem. Theory Comput.,* **2010**, *6,* 2872–2887.

66. Rossmeisl, J.; Skúlason, E.; Björketun, M. E.; Tripkovic, V.; Nørskov, J. K. Modeling the electrified solid–liquid interface. *Chem. Phys. Lett.,* **2008**, *466,* 68–71.

67. Wan, H. Bagger, A.; Rossmeisl, J. Electrochemical nitric oxide reduction on metal surfaces. *Angew. Chem.,* **2021**, *133,* 22137–22143.

68. Foree, M.; 2021 Water quality report. *Truckee Meadows Water Authority,* **2021**, 1–5.

Chapter Five

Selective Electrocatalytic Nitrate Reduction to Ammonia using Nafion-covered Cu Electrodeposits

5.1 Introduction.

Nitrate (NO_3^-) conversion or removal is important to balance the nitrogen cycle in the environment. NO_3^- is a common pollutant from agricultural runoff and other industrial activities that has caused a misbalance in the natural nitrogen cycle. Excess NO_3^- is responsible for toxic algae blooms in waterways and also poses human health concerns.[1] For these reasons, the conversion of NO_3^- into other products is of great research interest.[2–5]

As the most important chemical in the nitrogen fertilizer industry, ammonia (NH_3) is a value-added product attainable from electrocatalytic NO_3^- reduction.[6–10] In fact, NH_3 is currently the fifth most produced chemical by volume in the world.[11] Because the Haber-Bosch process used to synthesize NH_3 is energy intensive and responsible for 1-2% of anthropogenic CO_2 production, alternative routes to generating NH_3 are needed.[12–15] Thus, electrocatalytic NO_3^- reduction to NH_3 is a potential pathway to both increase energy efficiency and remove environmental NO_3^- contamination. However, a major hurdle facing electrocatalytic NO_3^- reduction technology is poor catalyst selectivity. In particular, converting NO_3^- to NH_3 ($NO_3^- + 9\ H^+ + 8\ e^- \rightarrow NH_3 + 3H_2O$) requires the transfer of 9 H^+ and 8 e^-, and side products can be generated during this multistep process, which decreases the Faradaic efficiency of NH_3 production.[1,16–20]

To increase the catalyst activity and selectivity, researchers have explored various electrocatalysts including noble metal catalysts, transition metals, alloys, and non-metallic electrodes.[1,21–26] Among them, Cu-based catalysts have been emphasized due to their excellent NO_3^- adsorption properties.[5,27,28] For example, Kang et al. developed structure-activity relationships between different Cu materials including Cu nanosheets, nanocubes, nanoparticles, and foils.[27] Zhang et al. unveiled the active phase of Cu-based electrocatalysts and demonstrated that Cu/Cu_2O turns into CuO during NO_3^- reduction, which facilitates the formation of a *NOH intermediate and suppresses the H_2 evolution reaction.[5] Many reports have developed Cu catalysts with a second metal such as Ni or Pd, which significantly increase NH_3 production due to modulated electronic structure and synergistic effects.[22,29]

The fluoropolymer Nafion is commonly used as a separator between the two half compartments in full electrochemical devices and as a binder in catalyst inks.[30,31] In chapter four, I used Nafion in a different manner to increase the selectivity of NH_3 production from NO_3^- on flat polycrystalline metal electrodes in which a Nafion overlayer covered the electrocatalysts.[32] Surface-enhanced Raman spectroscopy and density functional theory calculations indicate that the metal-NO intermediate is activated in the presence of the Nafion layer. In this chapter, we expand upon this work by developing NO_3^- reduction catalysts using Nafion-modified Cu electrodeposits that display both enhanced current densities and NH_3 selectivities. We elucidate the physical and chemical parameters that give rise to this enhanced performance.

5.2 Methods.

5.2.1 General Procedures

A Nafion D520 dispersion was obtained from Fuel Cell Store, Inc. Cu foil (99.99%) was obtained from All-Foils, Inc. and was sonicated 8 min in acetone and 10 min in deionized water successively before use. $NaNO_3$ (> 99%) and Na_2SO_4 (> 99%) were procured from Sigma Aldrich, while $NaNO_2$ (98%) was purchased from Oakwood Chemicals, Inc. KH_2PO_4 and $Ru(NH_3)_6Cl_3$ were obtained from Fischer Scientific. Cu electrodeposits were formed on Cu foil using chronoamperometry for 30 min in 0.8 M $CuSO_4$ and 1 M H_2SO_4 solution at either -0.14 V or -0.5 V using a three-electrode electrochemical cell with the Cu foil serving as the working electrode, a leakless Ag/AgCl/ 3 M KCl (eDaq, Inc.) reference electrode, and a Pt wire counter electrode. After washing with water, the electrodeposited electrode was dried at room temperature in air overnight. Nafion-modified electrodes were fabricated by drop-casting the Nafion dispersion directly on each side of the electrodeposited Cu surfaces. Each side of the Nafion film was dried at room temperature for 15 min before use. The thickness of the Nafion was modulated by using multiple rounds of dropcasting and drying.

5.2.2 Electrochemical Measurements

Electrochemical studies were performed using a VSP-300 Biologic potentiostat. A three-electrode system was used with modified Cu surfaces, a Pt-coated Ti mesh electrode (Rio Grande, Inc.), and a leakless Ag/AgCl/ 3 M KCl (eDaq, Inc.) electrode were used as working, counter, and reference electrodes, respectively for all electrochemical experiments unless mentioned otherwise. All electrochemical potentials were reported with respect to a Ag/AgCl reference electrode. Current densities are calculated with respect to the electrochemically active surface area of the working electrodes. The electrochemically active surface areas of the electrodes were obtained by performing cyclic voltammetry (CV) in a 0.1 M pH 7.0 phosphate buffer solution containing 1 mM $Ru(NH_3)_6Cl_3$ from -0.1 V to 0.5 V at 50 mV/s in a one compartment cell (Figure 5.3). The second cycle of each CV was used to calculate the electrochemical surface area by integrating the charge under the Ru^{2+} to Ru^{3+} couple. The integrated charge for each surface was then compared to the integrated charge for a flat Cu electrode to determine the electrochemically active surface area.

A two-compartment cell containing 10 mL of 50 mM $NaNO_3$ and 100 mM Na_2SO_4 was used for studying NO_3^- reduction activities for different working electrodes. The Pt-coated Ti counter electrode was put in one compartment, which was separated from the working and reference electrodes by a Nafion 117 membrane (183 μm thick, Fuel Cell Store, Inc.). This membrane prevents possible reoxidation of NO_3^- reduction products formed on the working electrode by the positive potential of the counter electrode. For all linear sweep voltammetry (LSV) experiments, onset potentials were calculated by determining the voltage at which 10% of the maximum current density was attained.

For electrochemical NO_2^- reduction studies, an electrolyte containing 50 mM $NaNO_2$ and 100 mM Na_2SO_4 in a two-compartment cell was used following a procedure analogous to NO_3^- reduction. For electrochemical NO reduction, the electrolyte consisted of 100 mM Na_2SO_4 and was sparged with NO gas for 10 minutes before conducting electrochemistry in a two-compartment cell. NO gas was prepared from $NaNO_2$ and 1 M H_2SO_4 following literature procedures.[33] The produced NO_x species were washed with NaOH, which absorbs acidic NO_2, resulting in a NO stream. The NO concentration in solution before electrochemistry was 2 mM.[34]

5.2.3 Materials Characterization

Scanning electron microscope (SEM) images and energy-dispersive X-ray (EDX) analysis were obtained using a JEOL JSM-7100F field emission SEM operated using an accelerating voltage of 15 kV. Atomic force microscopy (AFM) images were obtained for each sample using a Nanosurf EasyScan 2 microscope operated in contact mode using a silicon tip with an aluminum reflective coating (ContAl-G, TedPella, Inc.). A Rame-Hart 100-00 goniometer was used to measure contact angles. 20 μL of distilled water was placed on each electrode surface using a micropipette. The contact angles were measured at room temperature within 5 s of dispensing the water droplet. Reported contact angles are calculated from the average of the left and right angles of the droplet, and each measurement was conducted three times. X-ray diffraction (XRD) data was collected with a Bruker D2 X-ray diffractometer.

5.2.4 Product Detection

Standard colorimetric methods were used to detect the concentration of NH_3, NO_2^-, and NO_3^- after chronoamperometry. The amount of NH_3 was quantified using the indophenol method.[35] Required reagents were purchased from Sigma Aldrich and used without further purification. In a typical preparation, 0.5 mL of the catholyte was taken in a glass vial, and 2 mL of a 1 M NaOH solution containing 5 wt. % salicylic acid and 5 wt. % sodium citrate was added. Then, 1 mL of 0.05 M NaClO and 0.2 mL of 1 wt. % sodium nitroferricyanide were added to the same vial. After this mixture was let to stand at 2 h at 4°C, UV-Vis spectroscopy was performed using a Shimadzu UV-2550 spectrometer. The concentration of NH_3 in the electrolyte was determined using the maximum absorbance at 670 nm along with an appropriate calibration curve produced using NH_3 solutions of known concentrations.

Griess reagents with and without VCl_3 were used to quantify the NO_3^- and NO_2^-, respectively.[36] The Griess reagent was first prepared by dissolving 2 wt. % NEDD (N-(1-naphthyl)ethylenediamine dihydrochloride) and 2 wt. % sulfanilamide in 200 mL of 0.5 M HCl solution.

10 μL of the catholyte was diluted with 2 mL water in a glass vial to quantify NO_2^- concentration. 0.8 mL of the Griess reagent was added in that vial, and the mixture was let to stand for 2 h at room temperature to allow the reaction to go to completion. The absorbance at 540 nm was used to calculate the NO_2^- concentration using an appropriate calibration curve constructed from NO_2^- solutions of known concentrations.

To calculate the amount of NO_3^- consumed after chronoamperometry, 5 μL of the catholyte was diluted with 2 mL of water. Then, 200 mL of the Griess reagents solution was made as described previously, and 0.5 g VCl_3 was added. 0.8 mL of this solution was added to the above mixture, and it was let to stand overnight at room temperature to allow the reaction to go to completion. NO_3^- is reduced to NO_2^- in the presence of VCl_3 and that total NO_2^- concentration was quantified using UV-Vis spectroscopy using the maximum absorbance at 540 nm. The total NO_2^- concentration was subtracted from the above NO_2^- concentration to determine the unconverted NO_3^- during chronoamperometry.

5.2.5 Faradaic Efficiency Calculations

Faradaic efficiency (% FE) values of NH_3 and NO_2^- production were calculated using the established procedures.[32] The catalysts studied in this project did not yield any measurable quantities (Faradaic efficiency > 0.1%) of N_2, NO, N_2O, or N_2H_4 as determined by previously described methods.[32] Faradaic efficiency for H_2 production was not explicitly reported, but it can be found by subtracting the Faradaic efficiency for all nitrogen-containing products from 100%.

5.3 Results and Discussion.

5.3.1 Electrode characterization

5.3.1.1 Scanning Electron Microscopy (SEM) of Electrodeposited Cu Electrodes

Figure 5.1 presents top-down SEM images of Cu electrodes modified with Cu electrodeposits produced using 30 min of electrodeposition at either -0.14 V or -0.5 V from a Cu electrodeposition bath. While the electrodeposits formed at -0.14 V are relatively smooth (Figures 5.1A and 5.1B), when the electrodeposits are formed using -0.5 V, the surface consists of large particles (> 10 μm) in a three-dimensional agglomerate-like structure (Figures 5.1C and 5.1D). Electrodeposition at higher overpotentials is known to give rise to larger particles sizes in many other contexts.[37]

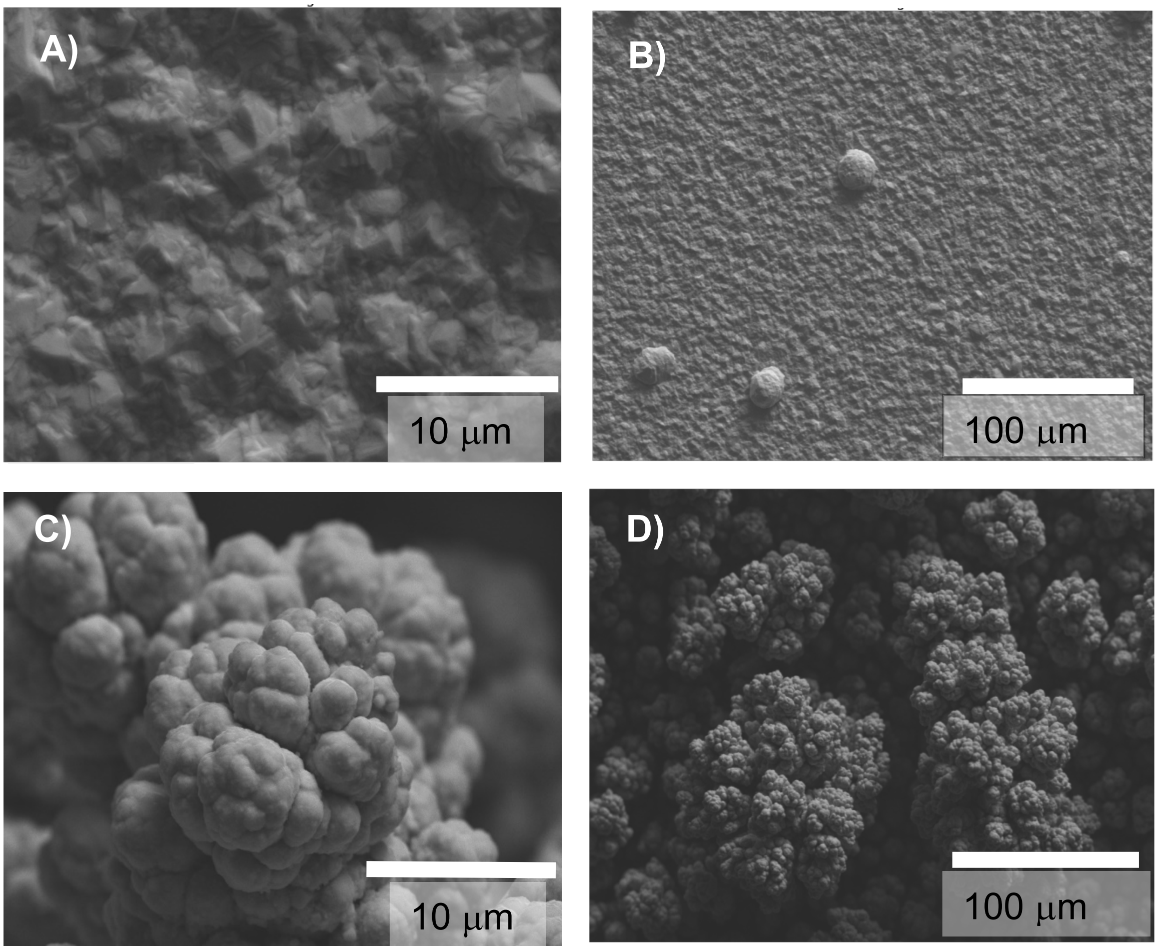

Figure 5.1: Top-down SEM images after 30 min of Cu electrodeposition on a Cu electrode using electrodeposition voltages of -0.14 V (A, B) and -0.5 V (C, D).

5.3.1.2 Atomic Force Microscopy (AFM)

To understand further the surface morphology of the electrodes modified with Cu electrodeposits, atomic force microscopy (AFM) images were also collected (Figure 5.2). AFM images of unmodified Cu (Figure 5.2A and 5.2B) show a relatively flat morphology. In contrast, the Cu electrode modified with the Cu electrodeposits are much rougher (Figure 5.2C and 5.2D).

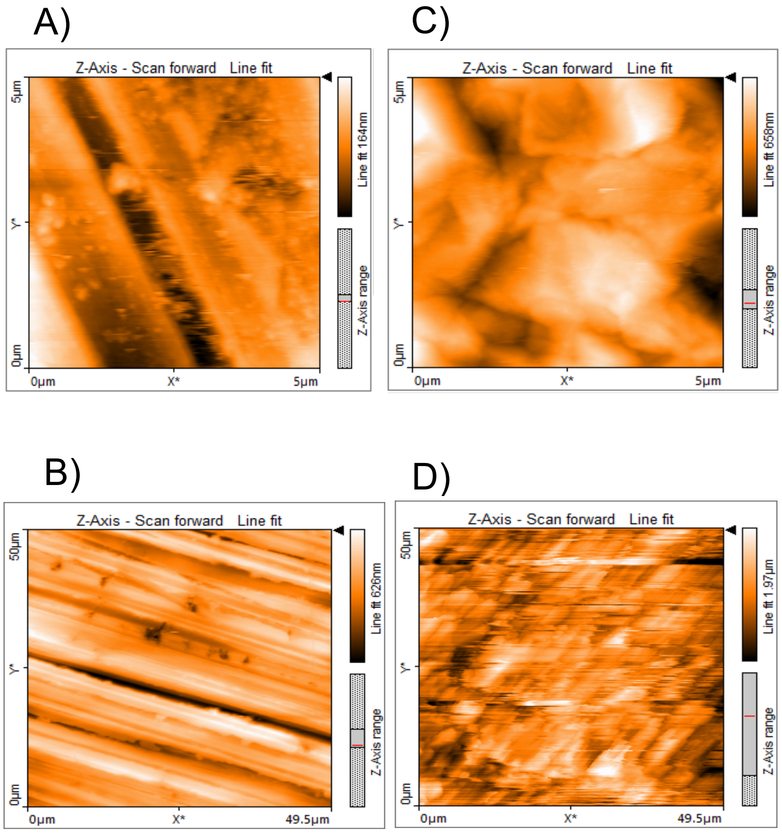

Figure 5.2: AFM images of an unmodified Cu electrode (A, B) and the Cu electrode after 30 min of Cu electrodeposition at -0.14 V (C, D).

5.3.1.3 Electrochemical Surface Area Measurement

The electrochemically active surface areas of the electrodes with Cu electrodeposits were measured by conducting CVs in a solution containing $Ru(NH_3)_6Cl_3$ (Figure 5.3), a standard reversible redox couple (E° = 0.10 V vs. NHE). The more positive potential of ferrocene (E° = 0.64 V) compared to Cu (E° = 0.34 V) renders ferrocene unsuitable for this experiment because the Cu surface will be oxidized to Cu^{2+} at the potentials needed to observe the ferrocene couple.[38] By integrating the charge under the Ru^{3+}/Ru^{2+} couple for the flat unmodified Cu electrode and comparing that value to the charge measured for the electrodes with Cu electrodeposits, the roughness factors and electrochemically active surface areas of these electrodes were determined. The roughness factors were calculated to be 1.84 and 4.92 for the electrodes with Cu electrodeposits formed at -0.14 V and -0.5 V, respectively. These measurements are consistent with the larger, rougher electrodeposits formed at -0.5 V as observed in the SEM images (Figure 5.1). Throughout the chapter, we use the electrochemically active surface areas to calculate and report current densities.

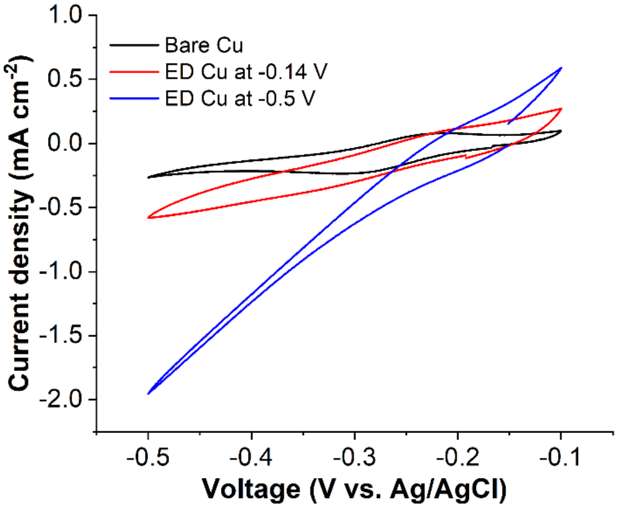

Figure 5.3: Cyclic voltammetry of unmodified Cu (black line), Cu modified with electrodeposition at -0.14 V (red line) and -0.5 V (blue line) at 50 mVs-1 in an electrolyte containing 0.1 M phosphate buffer (pH 7.0) and 1 mM $Ru(NH_3)_6Cl_3$.

5.3.1.4 Scanning Electron Microscopy (SEM) and Energy Dispersive X-Ray Spectroscopy (EDX) of Nafion-modifed Cu electrodeposit

The electrodes containing the Cu electrodeposits were also modified with a Nafion overlayer. Cross-sectional SEM-EDX images show that the Nafion overlayer forms a relatively uniform coating on the electrodeposited Cu surface with an approximate thickness of 6 µm (Figure 5.4A). This thickness of Nafion is chosen for all studies in this chapter because previous results indicate that thinner or thicker layers result in lower NH_3 Faradaic efficiencies on flat Cu electrodes.[32] The EDX spectrum (Figure 5.4B) of the Nafion-modified electrodeposits confirms that the major elemental component is Cu. The other elements present are C, F, O, and S, which originate from the Nafion layer. EDX mapping demonstrates that Cu is present underneath the Nafion overlayer (Figure 4.4C), and F is localized in the Nafion overlayer (Figure 5.4D).

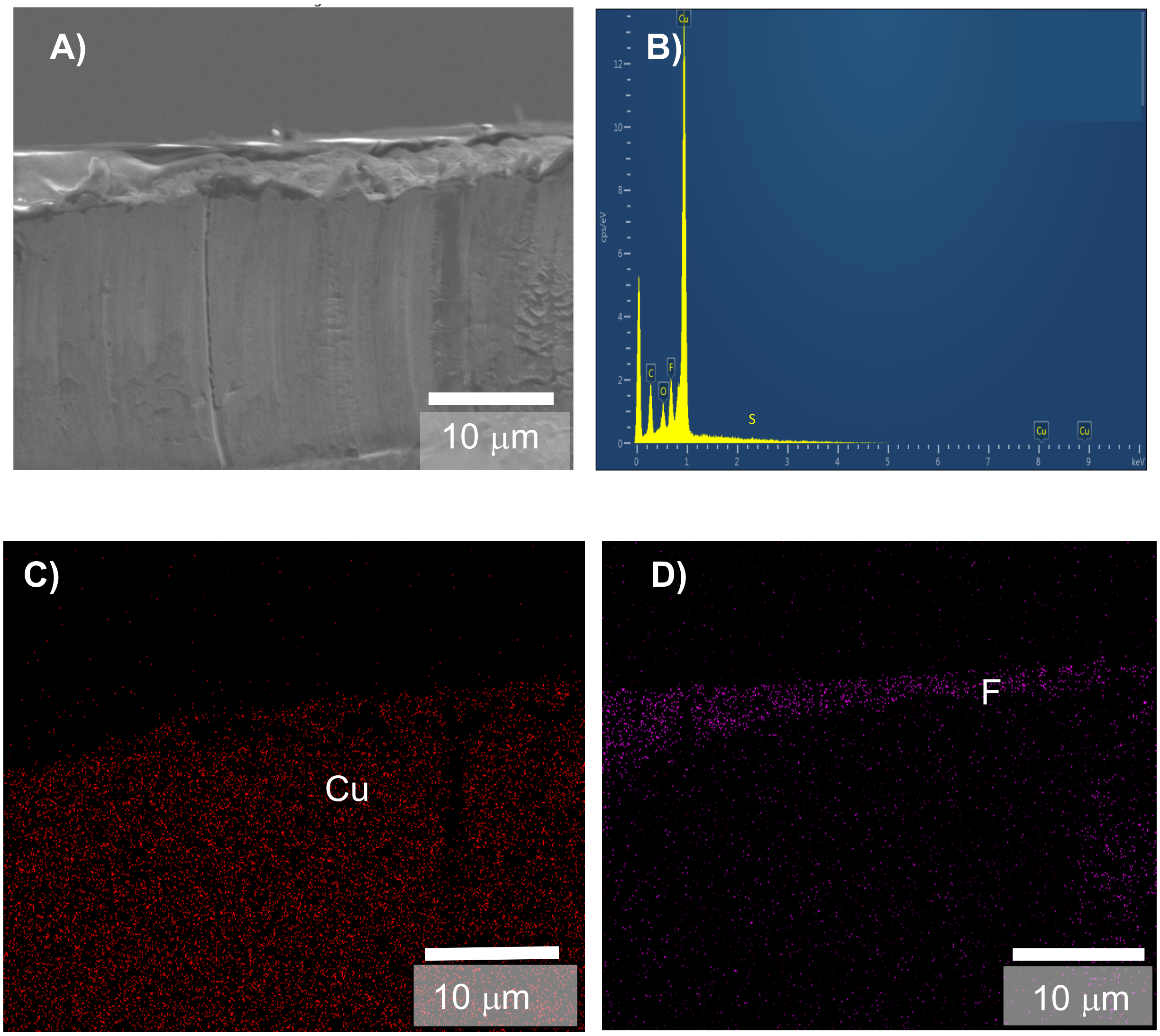

Figure 5.4: Cross-sectional SEM image of Cu electrode after 30 min of Cu electrodeposition at 0.14 V modified with a 6 μm Nafion overlayer (A). The EDX spectrum of this substrate (B). EDX elemental mapping of Cu (C) and F (D).

5.3.1.5 Water Contact Angles Measurement

Water contact angles were measured to compare the hydrophobicity characteristics of the different Cu electrodes (Table 5.1). The angle between an unmodified Cu surface and a water droplet is (67 ± 5)°. For the Cu electrodes modified with Cu electrodeposits, the contact angles decreased relative to the flat surface. This result is expected because according to the Wenzel equation, a rough surface exhibits a lower contact angle compared to a corresponding flat surface when the water droplet is wetting (contact angle less than 90°).[39] The finding that the water contact angle for the electrodeposits formed at -0.5 V is less than the angle on the electrodeposits formed at -0.14 V is consistent with the increased surface roughness of the -0.5 V electrodeposits as determined by SEM and electrochemically active surface area measurements described previously. When the electrodeposits are modified with Nafion, the water droplets on both of the electrodeposits are non-wetting (contact angle greater than 90°). In these Nafion-modified cases, the contact angle for the -0.5 V electrodeposits is greater than that of the -0.14 V electrodeposits, which again is consistent with the relative surface roughness values because the Wenzel equation indicates that rougher non-wetting surfaces exhibit greater contact angles. Together with the cross-sectional SEM imaging, these results suggest that the Nafion layer form a relatively uniform coating over the Cu electrodeposits.

Table 5.1: Water contact angles of various electrodes studied.

Electrode	Water Contact Angle (degrees)
Unmodified Cu	67 ± 5
Cu with electrodeposits formed using -0.14 V	55 ± 2
Cu with electrodeposits formed using -0.5 V	34 ± 5
Cu with electrodeposits formed using -0.14 V modified with Nafion	108 ± 1
Cu with electrodeposits formed using -0.5 V modified with Nafion	117 ± 2

5.3.2 Electrochemical NO_3^- Reduction

5.3.2.1 Electrocatalytic NO_3^- Reduction Activity

Electrochemical NO_3^- reduction activities of different Cu electrodes were tested using linear sweep voltammetry (LSV). Figure 5.5 represents the LSV of NO_3^- reduction on different metal or modified metal electrocatalysts. The current densities for the LSVs and all subsequent current densities reported in this chapter are normalized with respect to the electrochemically active surface areas of the electrodes. The unmodified Cu electrode has a maximum current density of -0.57 mA cm^{-2} at -1 V and an onset potential (defined as the potential at which 10% of the maximum current density is attained) of -0.43 V. We electrodeposited Cu particles onto the Cu electrode with the aim of increasing the current density for the NO_3^- reduction reaction. The current density for the electrodes modified with Cu electrodeposits increases significantly as compared to unmodified Cu due in part to the increased surface area imparted the Cu electrodeposits (see previous discussion on roughness values and electrochemically active surface areas). Interestingly, the current density for the electrodes with Cu electrodeposits is still larger than that of the unmodified Cu even when taking into account the larger electrochemical active surface areas of the electrodes with electrodeposits (Figure 5.5, red and blue lines compared to Figure 5.5, black line). These results indicate that the Cu electrodeposits are intrinsically more kinetically active catalysts for NO_3^- reduction than unmodified Cu. The enhanced activity of the Cu electrodeposits is not directly related to the distribution of crystal faces in the electrode materials because the Cu electrodeposits formed at -0.14 V and -0.5 V have significantly different XRD spectra (*vide infra*). However, the electrodeposits likely possess more defects than flat Cu electrodes, and we therefore hypothesize that the enhanced current densities of the Cu electrodeposits originate from these defect sites.

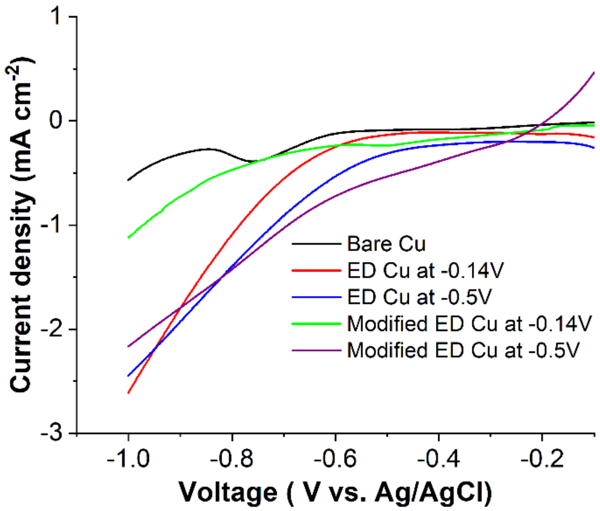

Figure 5.5: Linear sweep voltammograms in 50 mM $NaNO_3$ and 100 mM Na_2SO_4 at a scan rate of 10 mV s^{-1} of unmodified Cu (black line), Cu with Cu electrodeposits (ED) formed at -0.14 V (red line) or at -0.5 V (blue line), and Nafion-modified Cu with Cu electrodeposits formed at -0.14 V (green line) and at -0.5 V (purple line).

After modifying the Cu electrodeposits with a 6 μm Nafion overlayer, the current density at -1.0 V decreases as compared to the Cu electrodeposits without Nafion (Figure 5.5, green line vs. red line and Figure 5.5, purple line vs. blue line). This decrease in current density likely occurs due to hindered mass transport of NO_3^- from the bulk solution to the electrode surface by the Nafion layer. Interestingly, the differences between the current densities at -1.0 V for the electrodeposits produced at -0.5 V is less than for the electrodeposits produced at -0.14 V. The exact origin of this difference is unknown, but it is likely related to differences in the morphologies of the electrodeposits in the two cases. Additionally, the onset potentials of the LSVs for the Nafion-modified electrodes for both the electrodeposits formed at -0.14 V and -0.5 V each shift positive compared to the corresponding electrodes without Nafion (Table 5.2). These positive shifts in onset potential upon addition of Nafion match previous experiments with Nafion-modified flat Cu electrodes and can be attributed to the activation of a Cu-NO intermediate through sulfonate groups on the Nafion, which increases the thermodynamic feasibility of NO_3^- reduction in the presence of Nafion.[32]

Table 5.2: NO_3^- reduction onset potentials as obtained from linear sweep voltammetry for different electrodes.

Electrode	Onset potential vs. Ag/AgCl without chloride (V)	Onset potential vs. Ag/AgCl with chloride (V)	Difference in potential (V)
Unmodified Cu	-0.58	-0.55	0.03
Cu with electrodeposits formed using -0.14 V	-0.61	-0.60	0.01
Cu with electrodeposits formed using -0.5 V	-0.42	-0.51	-0.07
Cu with electrodeposits formed using -0.14 V modified with Nafion	-0.34	-0.46	-0.12
Cu with electrodeposits formed using -0.5 V modified with Nafion	-0.28	-0.01	0.27

5.3.2.2 Products Distribution

We next calculated the Faradaic efficiencies of NH_3 and NO_2^- production from NO_3^- electroreduction after 1 h chronoamperometry at -1.4 V using different Cu electrodes (Figure 5.6A). Figure 5.7 demonstrates the chronoamperometry and UV-Vis spectrum for the NO3- reduction using unmodified and modified Cu electrocatalysts. The Faradaic efficiency of NH_3 production from an unmodified Cu electrode is (62 ± 2) % as reported before (Figure 5.6A, leftmost blue bar).[32] The Faradaic efficiency for NH_3 is similar for Cu with electrodeposits formed using -0.5 V, while the yield is slightly higher for the electrodeposits formed at -0.14 V (Figure

5.6A, three leftmost blue bars). Strikingly, after modifying the electrodeposits formed at -0.14 V with a 6-µm-thick Nafion overlayer, the Faradaic efficiency for NH_3 production increases to (97.0 ± 0.3) %. This NH_3 yield is among the highest reported for NO_3^- reduction catalysts, making it one of the most selective electrocatalysts for NH_3 production (Table 5.3). Furthermore, this NH_3 Faradaic efficiency is significantly higher than the (91 ± 2) % obtained with a flat Cu electrode modified with Nafion. The electrochemically active surface area of the electrodes were used when calculating the products rates.

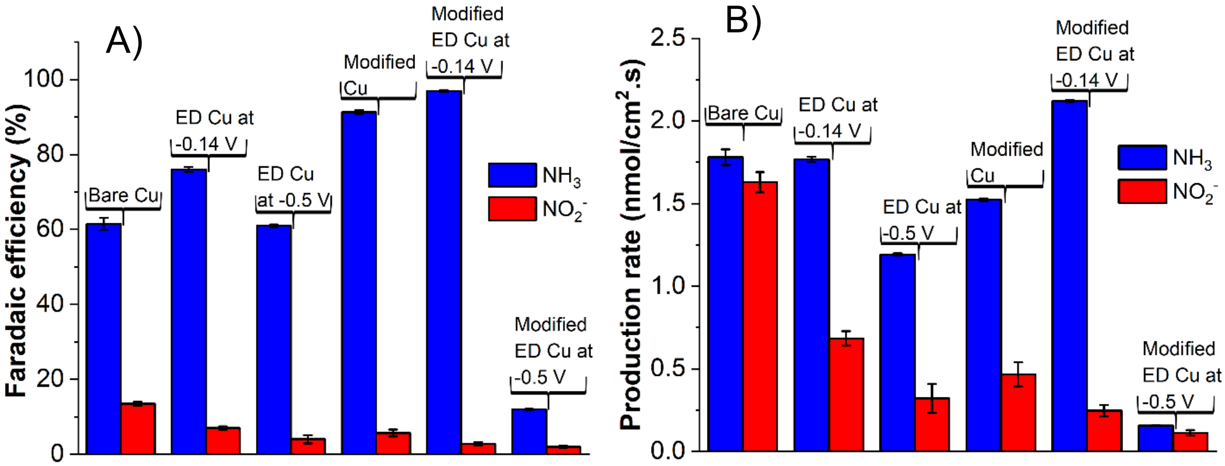

Figure 5.6: Faradaic efficiencies (A) and rate of production rate (B) of NH_3 (blue bars) and NO_2^- (blue bars) after 1 h of chronoamperometry at -1.4 V from unmodified (bare) Cu, Cu modified with electrodeposits (ED), and Cu modified with ED and Nafion.

We fabricated electrodes with Cu electrodeposits formed at -0.14 V modified with Nafion layers that are 3 µm, 8 µm, 10 µm, 12 µm, or 30 µm thick. The Faradaic efficiencies of NH_3 produced from these electrodes are 77%, 71%, 65%, 57%, and 5%, respectively. Because the 6-µm-thick Nafion layer exhibits the highest activity towards NH_3 production (97%), we used this Nafion thickness for the remaining studies in this chapter.

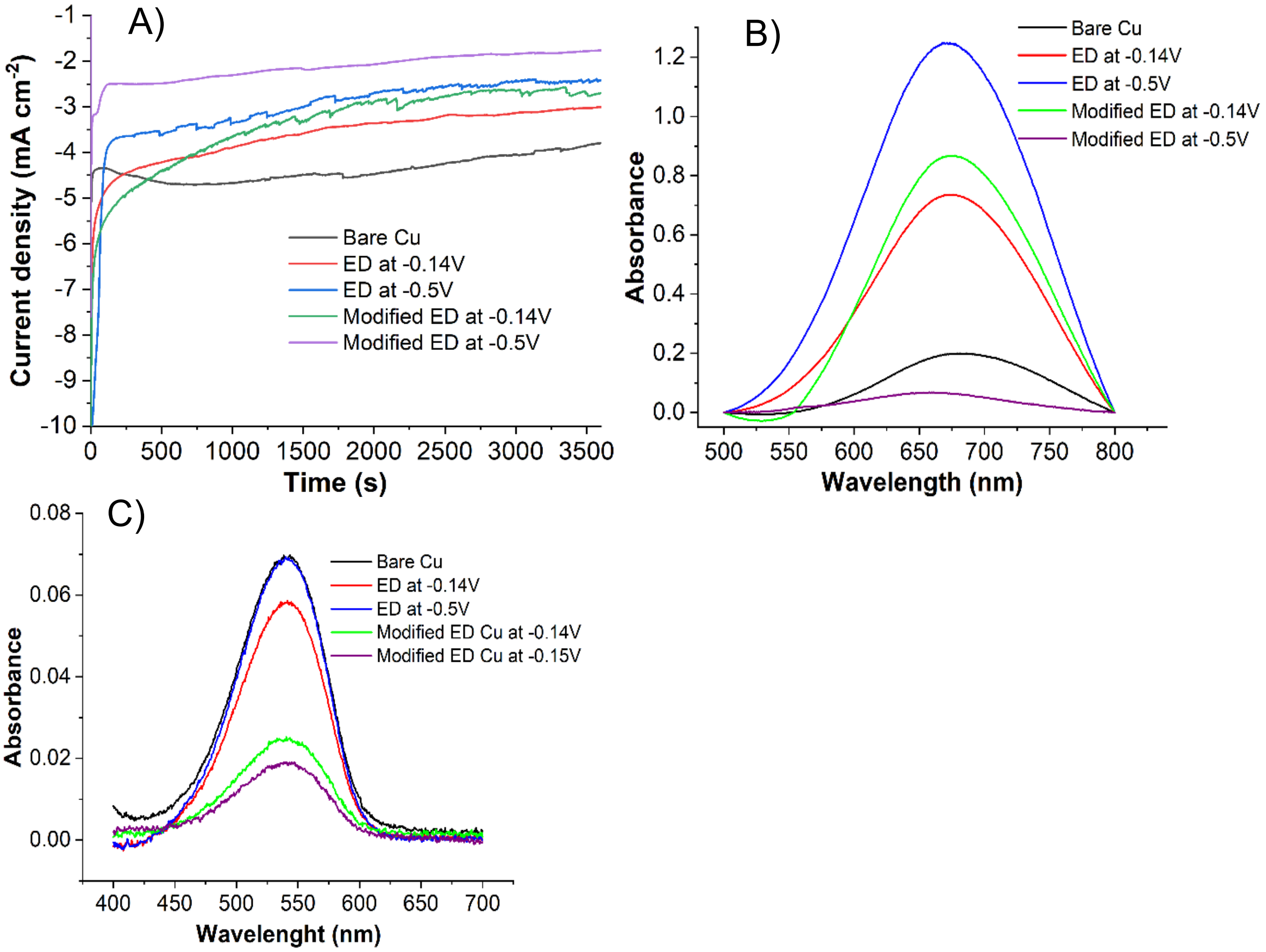

Figure 5.7: Chronoamperometry curves (A) performed at -1.4 V in 50 mM $NaNO_3$ and 100 mM Na_2SO_4 at -1.4 V of unmodified Cu (black line), Cu modified with 30 min of Cu electrodeposition at -0.14 V (red line), at -0.5 V (blue line), at -0.14 V with a 6 μm Nafion overlayer (green line), and at -0.5 V with a 6 mm Nafion overlayer (purple). UV-Vis absorption spectra after chronoamperometry for NH_3 (B) and NO_2^- (C) detection.

5.3.3 Nafion Effects Investigation for Selective NH_3 Production

Previous studies showed that the N-O bond in a Cu-NO intermediate is activated in the presence of Nafion. In particular, spectroscopic and density functional theory calculations indicate that the N-O bond length increases, which facilitates subsequent bond cleavage and NH_3 formation.[32]

Table 5.3: Faradaic efficiencies for NH_3 for NO_3^- reduction catalysts in the literature.

Catalyst	**Electrolyte**	**NH_3 Faradaic Efficiency**
This work (Cu with electrodeposits formed using -0.14 V modified with Nafion)	50 mM $NaNO_3$ 100 mM Na_2SO_4	97.0 ± 0.3 %
6-µm Nafion-modified Cu[32]	50 mM $NaNO_3$ 100 mM Na_2SO_4	91 ± 2 %
Co_3O_4/Co nanosheets[40]	0.1 M Na_2SO_4 1 mg mL^{-1} of KNO_3	88.7%
Fe_1/NC[41]	0.1 M K_2SO_4 0.5 M KNO_3	86%
Co/CoO NSA[42]	100 mM K_2SO_4 200 ppm NO_3^-	93.8%
Ir NTs[43]	100 mM $HClO_4$ 17000 ppm NO_3^-	84.7%
CuFe[3]	100 mM K_2SO_4 1700 ppm NO_3^-	94.5%
Co_3O_4/NiO HNTs[44]	500 mM Na_2SO_4 200 ppm NO_3^-	55%
FeB_2[45]	1 M KOH 0.1 M KNO_3	96.8%
Co@TiO2/TP[46]	0.1 M PBS and 0.1 M NO_3^-	96.7%
Au-Pd alloy nanocrystals with (331) high-index facets[47]	0.5 M K_2SO_4 0.05 M KNO_3	65%
Ce–MoS_{2-x}/CC[48]	0.5 M Na_2SO_4 0.1 M $NaNO_3$	96.6%

FeOOH/CP[49]	0.1 M PBS 0.1 M NaNO$_3$	92%
Pt[30]	3000 mg L^{-1} NO$_3^-$	49%
Cu (111) nano disks[50]	0.1 M KOH 0.2 10 mM KNO$_3$	81%
Cu–N$_4$[51]	0.1 M KOH 0.1 M KNO$_3$	84.7%

5.3.4 Durability

To evaluate the durability of the Nafion-modified Cu electrodeposits formed at -0.14 V, we performed chronoamperometry for 18 hours at -1.4 V (Figure 5.8). The NH$_3$ Faradaic efficiency for this long-term experiment was (85 ± 2) %, which indicates that the electrode is relatively stable over this time period and can support a high NH$_3$ Faradaic efficiency throughout the experiment. Note that for this longer experiment, only 300 uL of electrolyte was used for colorimetric analysis because of the greater quantity of products generated.

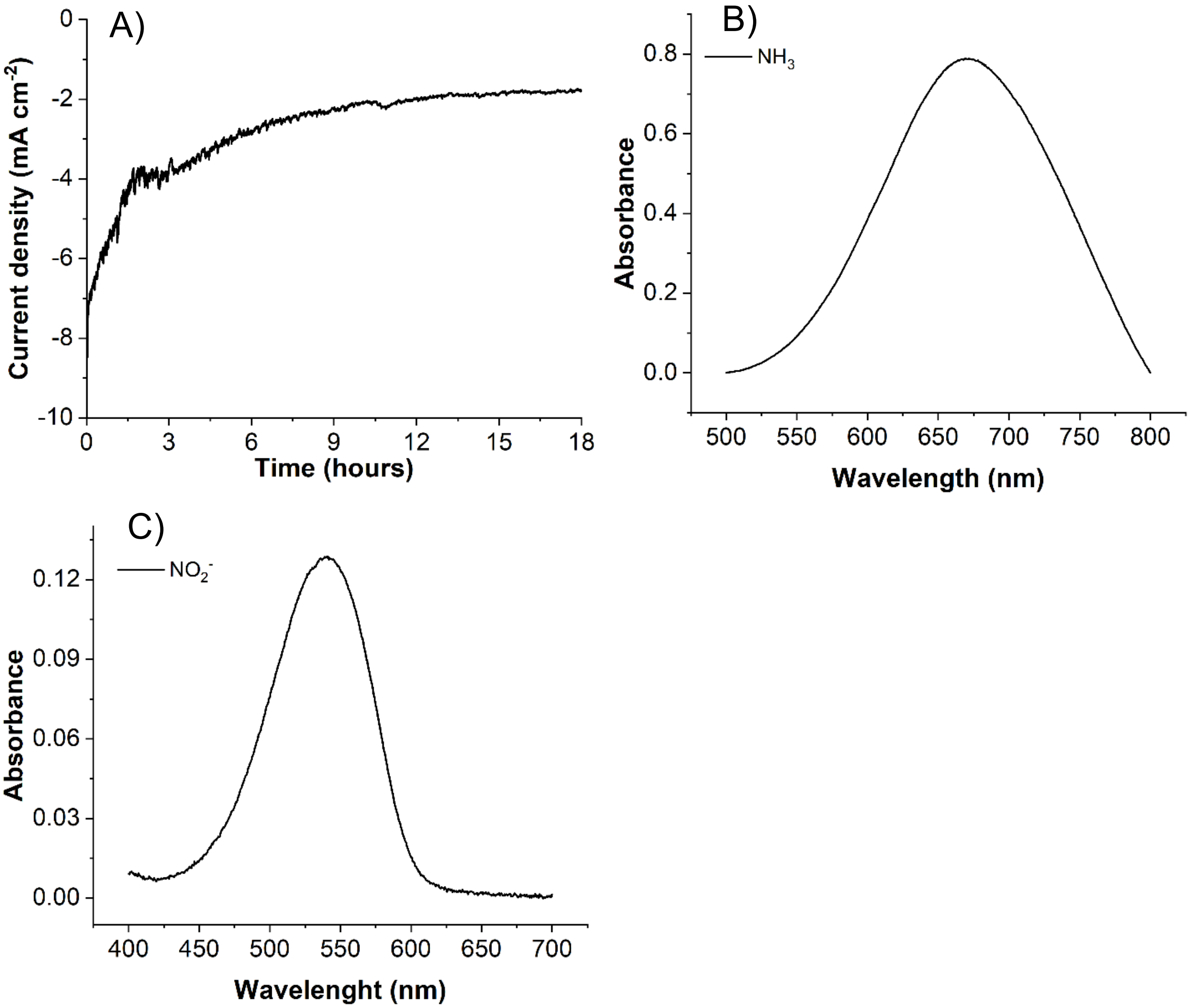

Figure 5.8: Chronoamperometry curve at -1.4 V for 18 h (A) of a Cu electrode modified with electrodeposited Cu at -0.14 V with a 6 µm Nafion overlayer in 50 mM $NaNO_3$ and 100 mM Na_2SO_4 (A), and UV-Vis absorption spectra after the chronoamperometry for NH_3 (B) and NO_2^- (C) detection.

Interestingly, the Faradaic efficiency for NH_3 production from Cu electrodeposits formed using -0.5 V drastically decreases to (11.1 ± 0.1) % upon Nafion modification unlike the electrodeposits formed at -0.14 V. The difference in NH_3 selectivity for the Nafion-modified electrodes with the two different electrodeposits could be due to differences in the crystal structure of the Cu electrodeposits as we will discuss later using XRD data. Figure 5.6B displays the NH_3 and NO_2^- production rates from the different Cu electrodes, and these production rates follow a similar trend as the Faradaic efficiencies.

5.3.5 Electrodes Fabrication System Optimization

Given the high NH_3 selectivity of the Nafion-modified electrode with Cu electrodeposits formed at -0.14 V, we focused on this electrode architecture for the remainder of our studies. In particular, we changed both the time employed to deposit the Cu particles and the voltage applied during the NO_3^- reduction reaction in an attempt to further optimize this system. NH_3 Faradaic efficiencies were 14% and 19% for the electrode electrodeposited at -0.14 V for 2 hours, without and with modification using Nafion overlayer, respectively. Although increasing the electrodeposition time for generating the Cu electrodeposits increases the surface area of the electrodeposits, the NH_3 Faradaic efficiency significantly decreases (Figure 5.9), so we focused on the Nafion-modified electrode formed using only 30 min of electrodeposition.

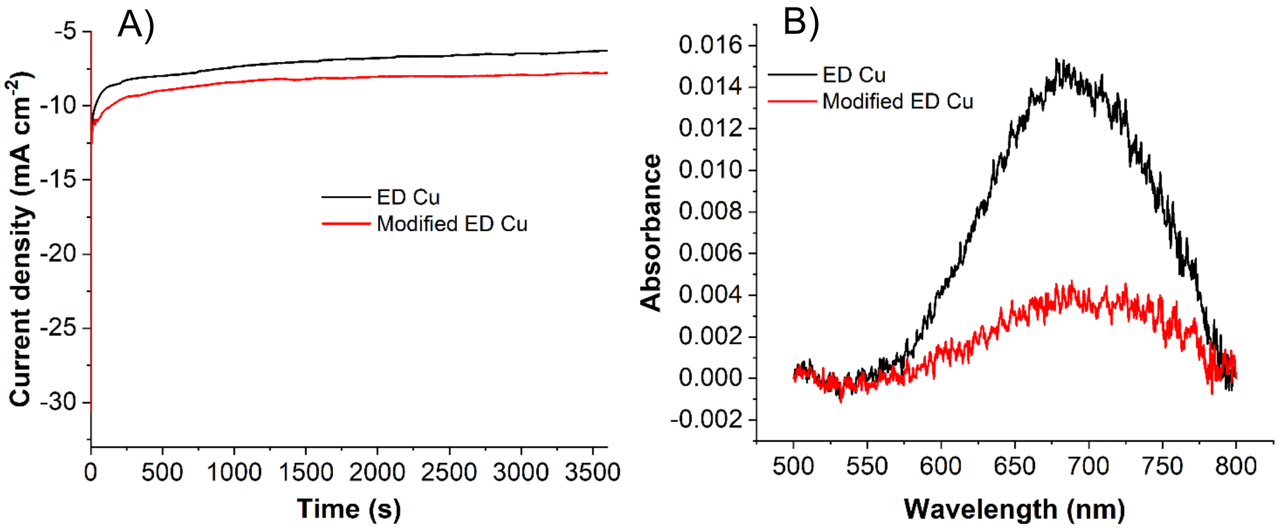

Figure 5.9: Chronoamperometry curves at -1.4 V in 50 mM $NaNO_3$ and 100 mM Na_2SO_4 (A) of Cu electrodes modified using two hours of Cu electrodeposition at -0.14 V (black line) with a 6 μm Nafion overlayer (red line). UV-Vis absorption spectra for NH_3 detection (B).

5.3.6 Voltage Optimization

We also assessed the effect of applied voltage on the electrocatalyst selectivity and kinetics (Figures 5.10 and 5.11). Increasing the magnitude of the cathodic voltage increases the NH_3 production rate per electrochemically active surface area of electrodes due to a greater applied overpotential (Figure 5.10B, blue bars). However, the NO_2^- production rates peak at -1.2 V, indicating that there is an optimal potential for NO_2^- generation (Figure 5.10B, red bars). At higher overpotentials, most of the NO_2^- produced at the electrode surface is converted to NH_3, which explains why the NO_2^- production rate decreases at more negative voltages. In terms of Faradaic efficiencies, the NO_2^- production decreases with increasing cathodic voltage with a corresponding rise in NH_3 Faradaic efficiency from -1 V to -1.4 V (Figure 5.10A). The NH_3 Faradaic efficiency decreases at voltages more negative than -1.4 V due to an increase in kinetically facile H_2 evolution at higher overpotentials.[35]

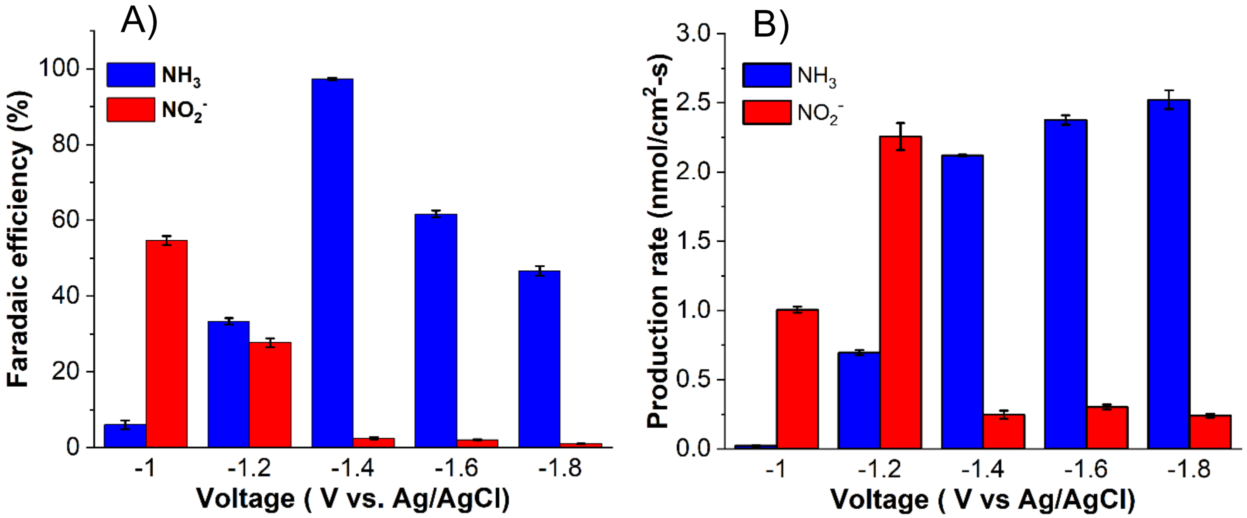

Figure 5.10: Faradaic efficiencies (A) and production rates (B) of NH_3 (blue bars) and NO_2^- (red bars) after 1 h of chronoamperometry at various voltages using Cu electrodes with Cu electrodeposits formed at -0.14 V modified with Nafion.

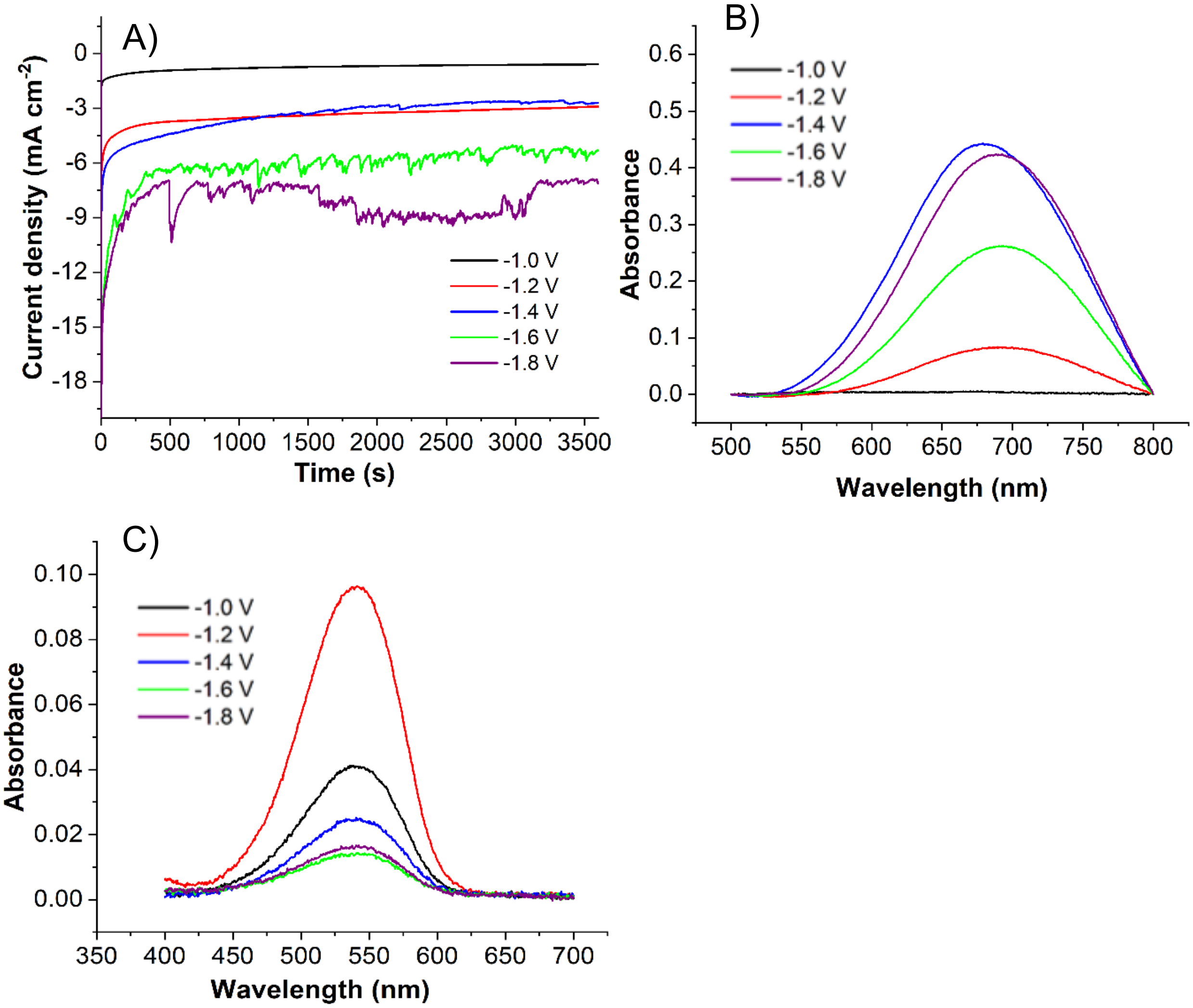

Figure 5.11: Chronoamperometry curves (A) in 50 mM $NaNO_3$ and 100 mM Na_2SO_4 of Cu electrodes modified with electrodeposited Cu at -0.14 V and a 6 μm Nafion overlayer. Voltages applied during chronoamperometry were -1.0 V (black line), -1.2 V (red line), -1.4 V (blue line), -1.6 V (green line), and -1.8 V (purple line) UV-Vis absorption spectra after chronoamperometry for NH_3 (B) and NO_2^- (C) detection.

5.4 Mechanistic Studies of NO_3^- Reduction.

To study the electrocatalytic NO_3^- reduction mechanism to produce NH_3, we performed three different chronoamperometry experiments using NO_3^-, NO_2^-, or NO-saturated electrolytes with the Cu electrodeposits formed at -0.14 V with and without Nafion modification. Figures 5.12 demonstrate the chronoamperometry and UV-Vis spectra of NO_2^- and NO reduction. The solutions used contained 100 mM Na_2SO_4 as a supporting electrolyte. Faradaic efficiencies and rates of NH_3 production are reported in Figures 5.13A and 5.13B, respectively for the electrochemical reduction of NO_3^-, NO_2^- and NO. In all three electrolytes, the NH_3 Faradaic efficiencies for the Nafion-modified electrode are significantly higher than those of the unmodified electrolyte. Furthermore, the Nafion-modified electrode exhibits high selectivity for NH_3 (> 90%) regardless of whether NO_3^-, NO_2^-, or NO is used as the precursor. These experiments suggest that both NO_2^- and NO are intermediates during NO_3^- reduction to NH_3 on the Nafion-modified Cu electrodeposits. A similar inference was discussed previously using flat Cu electrodes and is supported by surface-enhanced Raman spectroscopy and density functional theory calculations in our previous work.[32]

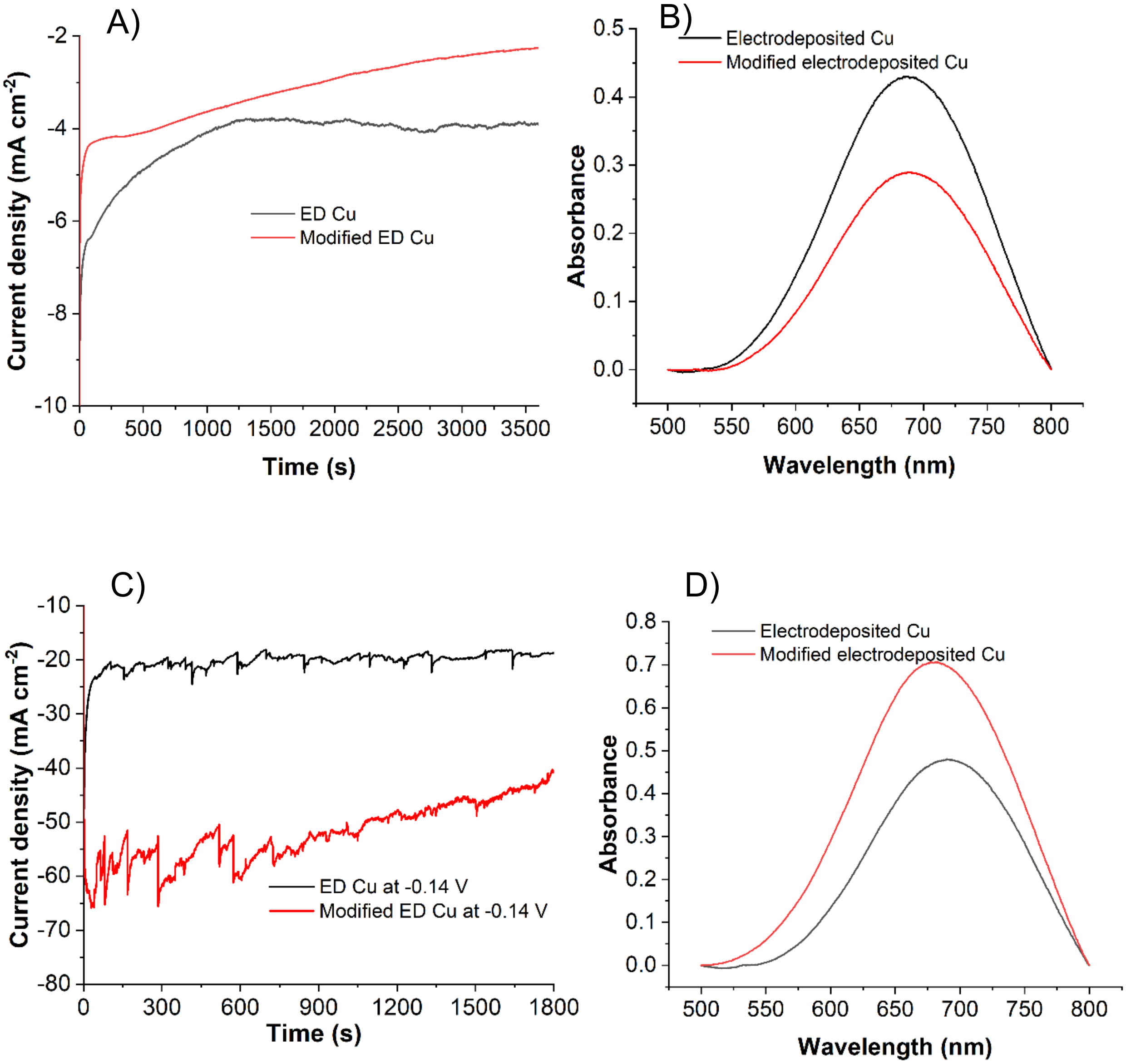

Figure 5.12: Chronoamperometry curves at -1.4 V in 50 mM $NaNO_2$ (A) and 2 mM NO (C) containing 100 mM Na_2SO_4 of Cu electrodes modified with electrodeposited Cu at -0.14 V without (black line) and with (red line) a 6 µm Nafion overlayer. UV-Vis absorption spectra after chronoamperometry for NH_3 (B and D) detection.

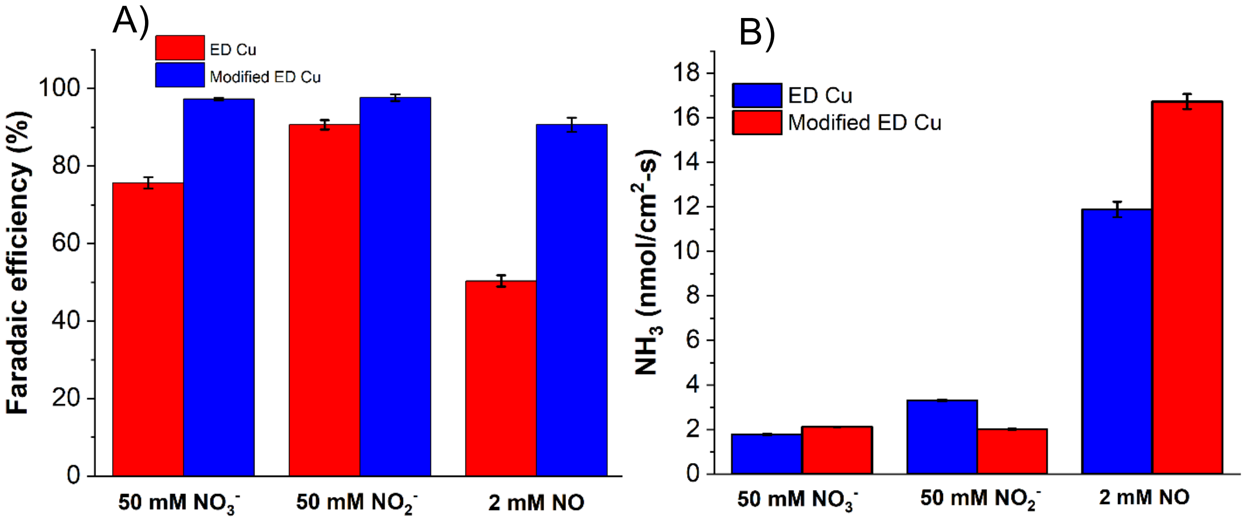

Figure 5.13: Faradaic efficiencies (A) and NH_3 production rates (B) from NO_3^- reduction (leftmost two bars), NO_2^- reduction (middle two bars), and NO reduction (rightmost two bars) using Cu electrodes with Cu electrodeposits (ED) formed at -0.14 V with (blue bars) and without (red bars) after 1 h of chronoamperometry at -1.4 V.

5.5 Responsible Crystal Faces to Produce NH_3 with High Faradaic Efficiency.

5.5.1 X-Ray Diffraction (XRD) Study

To understand the effect of electrodeposition voltage on the Cu electrodeposits, we performed XRD of the electrodeposits formed using -0.14 V and -0.5 V (Figure 5.14). In the spectrum of the electrodeposits formed at -0.14 V, the (111), (200), (220), and (311) crystal faces are present, and the intensity of the (220) face is largest (Figure 5.14A). In contrast, the (111) facet exhibits the greatest intensity in the spectrum of the electrodeposits formed at -0.5 V (Figure 5.14B). Based on these results, we attribute the high Faradaic efficiency for NH_3 production with the Nafion-modified Cu electrodeposits formed at -0.14 V to the predominance of (220) faces in the Cu electrodeposits. Previous reports demonstrate that the Cu (111) face is the most active for the H_2 evolution reaction,[52] which for NO_3^- reduction catalysts would reduce the NH_3 Faradaic efficiency. Additionally, the (111) facet has the highest atomic packing density in face centered cubic systems and hence the fewest number of dangling bonds on the surface. We hypothesize that the higher coordination number of Cu in the (111) faces inhibits its activity towards NO_3^-

reduction. This interpretation may explain why the Nafion-modified Cu electrodeposits formed at -0.5 V do not yield significant quantities of NH_3, while the Nafion-modified Cu electrodeposits formed using -0.14 V are highly selective for NH_3 generation.

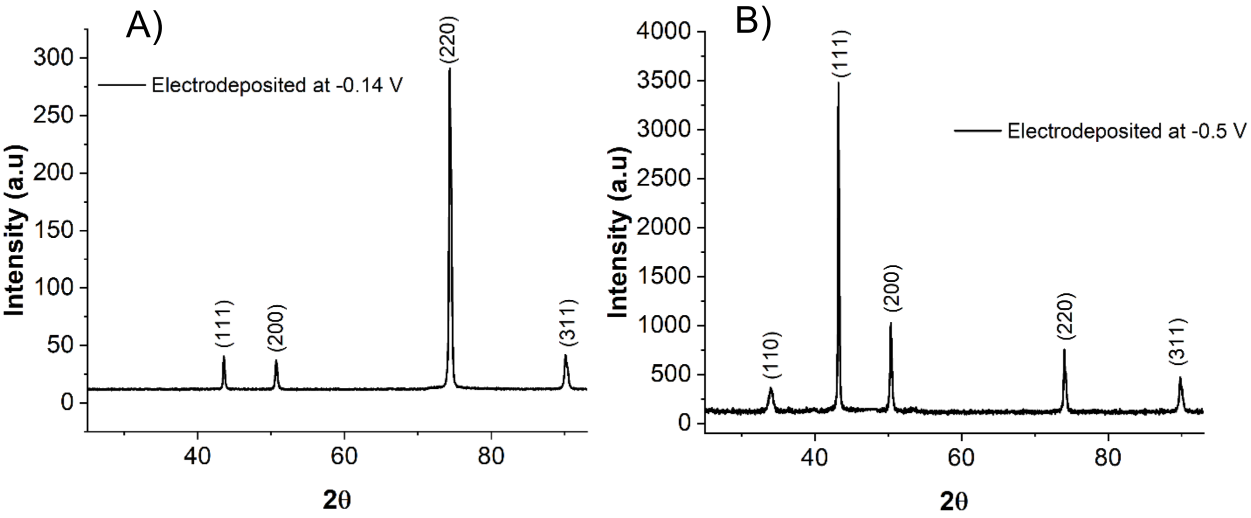

Figure 5.14: XRD spectra of Cu electrodes with Cu electrodeposits formed using -0.14 V (A) and 0.5 V (B).

5.5.2 Surface Poising

Through NO_3^- reduction experiments on Cu single crystals, Butcher Jr. and Gewirth previously determined that NO_3^- reduction leads to the partial oxidation of Cu surfaces during the catalytic cycle.[19] In particular, this oxidation facilitates NO_3^- reduction, and the reaction proceeds at lower overpotentials on crystal faces that are more readily oxidized. A corollary to this effect is that these same oxidizable crystal faces are poisoned by chloride because chloride etches copper oxides.[53] In the case of Cu electrodeposits, because the (220) face exhibits enhanced activity for NO_3^- reduction, we hypothesize that the electrodeposits formed using -0.14 V, which contain a predominance of the (220) face, would be poisoned by chloride as well. Indeed, a LSV of the Nafion-modified Cu electrodeposits formed using -0.14 V possesses an onset potential that is significantly shifted negative in a chloride-containing electrolyte (Figure 5.15A and Table 5.1). In contrast, the less active Nafion-modified Cu electrodeposits formed using -0.5 V exhibit the opposite trend (Figure 5.15B and Table 5.1).

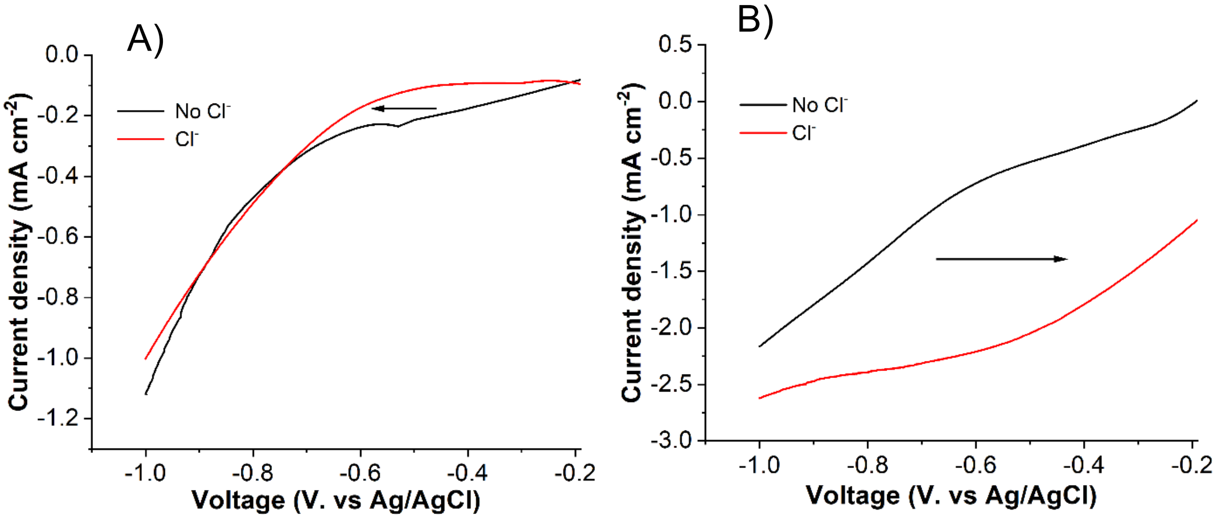

Figure 5.15: Linear sweep voltammograms at a scan rate of 10 mV s^{-1} of Nafion-modified Cu electrodes with Cu electrodeposits formed using -0.14 V (A) and -0.5 V (B) in 50 mM $NaNO_3$, 100 mM Na_2SO_4 (black line) and in 50 mM $NaNO_3$, 100 mM Na_2SO_4, and 10 mM NaCl (red line).

Taken together, these results further suggest that the Cu (220) face is responsible for the enhanced NH_3 production of the Nafion-modified Cu electrodeposits formed using -0.14 V, which is likely facilitated by the formation of copper oxides on the surface during catalysis.

5.6 Conclusions.

Although Nafion is commonly used as separator in two-compartment cells or as a binder in catalyst inks, here we modified Cu electrodeposits with a Nafion overlayer to enhance NH_3 production. Compared to previous reports using flat Cu electrodes, the Cu electrodeposits can both increase the NO_3^- reduction current density and the NH_3 Faradaic efficiency. In particular, the optimized catalyst reduces NO_3^- to NH_3 with a (97.0 ± 0.3) % Faradaic efficiency at a rate of (2.12 ± 0.01) nmol/cm^2-s. The structure and morphology of the electrodeposits were characterized using SEM-EDX, AFM, and XRD, and products were quantified in terms of electrochemically active surface areas. Along with the Nafion overlayer, the (220) face in the Cu electrodeposits suppresses

H_2 evolution and enhances NH_3 yield. These studies will aid future researchers in rationally developing the next generation of active NO_3^- reduction electrocatalysts.

5.7 References.

1. Li, J.; Zhan, G.; Yang, J.; Quan, F.; Mao, C.; Liu, Y.; Wang, B.; Lei, F.; Li, L.; Chan, A. W. M. et al. Efficient Ammonia Electrosynthesis from Nitrate on Strained Ruthenium Nanoclusters. *J. Am. Chem. Soc.* **2020**, *142*, 7036–7046.
2. Cerrón-Calle, G. A.; Fajardo, A. S.; Sánchez-Sánchez, C. M.; Garcia-Segura, S. Highly Reactive Cu-Pt Bimetallic 3D-Electrocatalyst for Selective Nitrate Reduction to Ammonia. *Appl. Catal. B Environ.* **2022**, *302*, 120844-120853.
3. Wang, C.; Liu, Z.; Hu, T.; Li, J.; Dong, L.; Du, F.; Li, C.; Guo, C. Metasequoia-like Nanocrystal of Iron-Doped Copper for Efficient Electrocatalytic Nitrate Reduction into Ammonia in Neutral Media. *ChemSusChem* **2021**, *14*, 1825–1829.
4. Zhang, Y.; Chen, X.; Wang, W.; Yin, L.; Crittenden, J. C. Electrocatalytic Nitrate Reduction to Ammonia on Defective Au1Cu (111) Single-Atom Alloys. *Appl. Catal. B Environ.* **2022**, *310*, 121346-121356.
5. Wang, Y.; Zhou, W.; Jia, R.; Yu, Y.; Zhang, B. Unveiling the Activity Origin of a Copper-based Electrocatalyst for Selective Nitrate Reduction to Ammonia. *Angew. Chem. Int. Ed.* **2020**, *59*, 5350–5354.
6. Kyriakou, V.; Garagounis, I.; Vourros, A.; Vasileiou, E.; Stoukides, M. An Electrochemical Haber-Bosch Process. *Joule* **2020**, *4*, 142–158.
7. Wu, T.; Fan, W.; Zhang, Y.; Zhang, F. Electrochemical Synthesis of Ammonia: Progress and Challenges. *Mater. Today Phys.* **2021**, *16*, 100310-100332.
8. Kyriakou, V.; Garagounis, I.; Vasileiou, E.; Vourros, A.; Stoukides, M. Progress in the Electrochemical Synthesis of Ammonia. *Catal. Today* **2017**, *286*, 2–13.

9. Ertl, G. Primary Steps in Catalytic Synthesis of Ammonia. *J. Vac. Sci. Technol. A* **1983**, *1*, 1247–1253.
10. Jiao, F.; Xu, B. Electrochemical Ammonia Synthesis and Ammonia Fuel Cells. *Adv. Mater.* **2019**, *31*, 1805173-1805177.
11. Bhown, A.; Cussler, E. Mechanism for Selective Ammonia Transport through Poly (Vinylammonium Thiocyanate) Membranes. *J. Am. Chem. Soc.* **1991**, *113*, 742–749.
12. Guo, C.; Ran, J.; Vasileff, A.; Qiao, S.-Z. Rational Design of Electrocatalysts and Photo(Electro)Catalysts for Nitrogen Reduction to Ammonia (NH_3) under Ambient Conditions. *Energy Env. Sci* **2018**, *11*, 45–56.
13. Suryanto, B. H. R.; Du, H.-L.; Wang, D.; Chen, J.; Simonov, A. N.; MacFarlane, D. R. Challenges and Prospects in the Catalysis of Electroreduction of Nitrogen to Ammonia. *Nat. Catal.* **2019**, *2*, 290–296.
14. Wan, Y.; Xu, J.; Lv, R. Heterogeneous Electrocatalysts Design for Nitrogen Reduction Reaction under Ambient Conditions. *Mater. Today* **2019**, *27*, 69–90.
15. Tang, C.; Qiao, S.-Z. How to Explore Ambient Electrocatalytic Nitrogen Reduction Reliably and Insightfully. *Chem Soc Rev* **2019**, *48*, 3166–3180.
16. Badea, G. E. Electrocatalytic Reduction of Nitrate on Copper Electrode in Alkaline Solution. *Electrochimica Acta* **2009**, *54*, 996–1001.
17. Yang, J.; Sebastian, P.; Duca, M.; Hoogenboom, T.; Koper, M. T. M. PH Dependence of the Electroreduction of Nitrate on Rh and Pt Polycrystalline Electrodes. *Chem Commun* **2014**, *50*, 2148–2151.

18. Siriwatcharapiboon, W.; Kwon, Y.; Yang, J.; Chantry, R. L.; Li, Z.; Horswell, S. L.; Koper, M. T. M. Promotion Effects of Sn on the Electrocatalytic Reduction of Nitrate at Rh Nanoparticles. *ChemElectroChem* **2014**, *1*, 172–179.
19. Butcher, D. P.; Gewirth, A. A. Nitrate Reduction Pathways on Cu Single Crystal Surfaces: Effect of Oxide and Cl−. *Nano Energy* **2016**, *29*, 457–465.
20. Duca, M.; Klugt, B. van der; Hasnat, M. A.; Machida, M.; Koper, M. T. M. Electrocatalytic Reduction of Nitrite on a Polycrystalline Rhodium Electrode. *J. Catal.* **2010**, *275*, 61–69.
21. Zhang, X.; Wang, Y.; Liu, C.; Yu, Y.; Lu, S.; Zhang, B. Recent Advances in Non-Noble Metal Electrocatalysts for Nitrate Reduction. *Chem. Eng. J.* **2021**, *403*, 126269-126283.
22. Simpson, B. K.; Johnson, D. C. Electrocatalysis of Nitrate Reduction at Copper-Nickel Alloy Electrodes in Acidic Media. *Electroanal. N. Y. N* **2004**, *16*, 532–538.
23. Gao, J.; Jiang, B.; Ni, C.; Qi, Y.; Zhang, Y.; Oturan, N.; Oturan, M. A. Non-Precious Co_3O_4-TiO_2/Ti Cathode Based Electrocatalytic Nitrate Reduction: Preparation, Performance and Mechanism. *Appl. Catal. B Environ.* **2019**, *254*, 391–402.
24. McEnaney, J. M.; Blair, S. J.; Nielander, A. C.; Schwalbe, J. A.; Koshy, D. M.; Cargnello, M.; Jaramillo, T. F. Electrolyte Engineering for Efficient Electrochemical Nitrate Reduction to Ammonia on a Titanium Electrode. *ACS Sustain. Chem. Eng.* **2020**, *8*, 2672–2681.
25. Jia, R.; Wang, Y.; Wang, C.; Ling, Y.; Yu, Y.; Zhang, B. Boosting Selective Nitrate Electroreduction to Ammonium by Constructing Oxygen Vacancies in TiO_2. *ACS Catal.* **2020**, *10*, 3533–3540.
26. Martínez, J.; Ortiz, A.; Ortiz, I. State-of-the-Art and Perspectives of the Catalytic and Electrocatalytic Reduction of Aqueous Nitrates. *Appl. Catal. B Environ.* **2017**, *207*, 42–59.

27. Fu, X.; Zhao, X.; Hu, X.; He, K.; Yu, Y.; Li, T.; Tu, Q.; Qian, X.; Yue, Q.; Wasielewski, M. R. et al. Alternative Route for Electrochemical Ammonia Synthesis by Reduction of Nitrate on Copper Nanosheets. *Appl. Mater. Today* **2020**, *19*, 100620-100625.
28. Wang, C.; Liu, Y.; Schmid, R. Rapid Nonovershooting Control for Simultaneous Infusion of Anesthetics and Analgesics. *IFAC-Pap.* **2021**, *54*, 1–6.
29. Nørskov, J. K.; Bligaard, T.; Rossmeisl, J.; Christensen, C. H. Towards the Computational Design of Solid Catalysts. *Nat. Chem.* **2009**, *1*, 37–46.
30. Machida, M.; Sato, K.; Ishibashi, I.; Hasnat, M. A.; Ikeue, K. Electrocatalytic Nitrate Hydrogenation over an H^+-Conducting Solid Polymer Electrolyte Membrane–Modified Cathode Assembly. *Chem. Commun.* **2006**, No. 7, 732–734.
31. Hasnat, M. A.; Ishibashi, I.; Sato, K.; Agui, R.; Yamaguchi, T.; Ikeue, K.; Machida, M. Electrocatalytic Reduction of Nitrate Using Cu–Pd and Cu–Pt Cathodes/H+-Conducting Solid Polymer Electrolyte Membrane Assemblies. *Bull. Chem. Soc. Jpn.* **2008**, *81*, 1675–1680.
32. Mondol, P.; Panthi, D.; Albarran Ayala, A. J.; Odoh, S. O.; Barile, C. J. Membrane-Modified Electrocatalysts for Nitrate Reduction to Ammonia with High Faradaic Efficiency. *J Mater Chem A* **2022**, *10*, 22428–22436.
33. Kay, J. G. Inorganic Chemistry: Handbook of Preparative Inorganic Chemistry. Vol. 1. Georg Brauer, Ed. Translated from the German Edition (Stuttgart, Ed. 2, 1960) by Scripta Technica. Reed F. Riley, Ed. Academic Press, New York, **1964**, *144*, 703–703.
34. Zacharia, I. G.; Deen, W. M. Diffusivity and Solubility of Nitric Oxide in Water and Saline. *Ann. Biomed. Eng.* **2005**, *33*, 214–222.

35. Chen, G.-F.; Yuan, Y.; Jiang, H.; Ren, S.-Y.; Ding, L.-X.; Ma, L.; Wu, T.; Lu, J.; Wang, H. Electrochemical Reduction of Nitrate to Ammonia via Direct Eight-Electron Transfer Using a Copper–Molecular Solid Catalyst. *Nat. Energy* **2020**, *5*, 605–613.
36. Schnetger, B.; Lehners, C. Determination of Nitrate plus Nitrite in Small Volume Marine Water Samples Using Vanadium (III) Chloride as a Reduction Agent. *Mar. Chem.* **2014**, *160*, 91–98.
37. Schlesinger, M.; Paunovic, M. *Modern Electroplating*; John Wiley & Sons: Hoboken, NJ, 2011.
38. Mondol, P.; Barile, C. J. Four-Electron Electrocatalytic O_2 Reduction by a Ferrocene-Modified Glutathione Complex of Cu. *ACS Appl. Energy Mater.* **2021**, *4*, 9611–9617.
39. Wolansky, G.; Marmur, A. Apparent Contact Angles on Rough Surfaces: The Wenzel Equation Revisited. *Colloids Surf. Physicochem. Eng. Asp.* **1999**, *156*, 381–388.
40. Zhao, F.; Hai, G.; Li, X.; Jiang, Z.; Wang, H. Enhanced Electrocatalytic Nitrate Reduction to Ammonia on Cobalt Oxide Nanosheets via Multiscale Defect Modulation. *Chem. Eng. J.* **2023**, *461*, 141960.
41. Liu, L.; Xiao, T.; Fu, H.; Chen, Z.; Qu, X.; Zheng, S. Construction and Identification of Highly Active Single-Atom Fe1-NC Catalytic Site for Electrocatalytic Nitrate Reduction. *Appl. Catal. B Environ.* **2023**, *323*, 122181.
42. Yu, Y.; Wang, C.; Yu, Y.; Wang, Y.; Zhang, B. Promoting Selective Electroreduction of Nitrates to Ammonia over Electron-Deficient Co Modulated by Rectifying Schottky Contacts. *Sci. China Chem.* **2020**, *63*, 1469–1476.

43. Zhu, J.-Y.; Xue, Q.; Xue, Y.-Y.; Ding, Y.; Li, F.-M.; Jin, P.; Chen, P.; Chen, Y. Iridium Nanotubes as Bifunctional Electrocatalysts for Oxygen Evolution and Nitrate Reduction Reactions. ACS Appl. Mater. Interfaces 2020, 12, 14064–14070.

44. Wang, Y.; Liu, C.; Zhang, B.; Yu, Y. Self-Template Synthesis of Hierarchically Structured Co_3O_4@NiO Bifunctional Electrodes for Selective Nitrate Reduction and Tetrahydroisoquinolines Semi-Dehydrogenation. *Sci. China Mater.* **2020**, *63*, 2530–2538.

45. Zhang, G.; Li, X.; Chen, K.; Guo, Y.; Ma, D.; Chu, K. Tandem Electrocatalytic Nitrate Reduction to Ammonia on MBenes. *Angew. Chem. Int. Ed. n/a* (n/a), e202300054.

46. Fan, X.; Zhao, D.; Deng, Z.; Zhang, L.; Li, J.; Li, Z.; Sun, S.; Luo, Y.; Zheng, D.; Wang, Y.; Ying, B.; Zhang, J.; Alshehri, A. A.; Lin, Y.; Tang, C.; Sun, X.; Zheng, Y. Constructing Co@TiO_2 Nanoarray Heterostructure with Schottky Contact for Selective Electrocatalytic Nitrate Reduction to Ammonia. *Small*, 2208036.

47. Liu, F.; Chen, C.; Jiang, X.; Guo, J.-Y.; Wei, Y.; Li, J.-W.; Sheng, T.; Zhao, X.; Wei, L. High-Index Surface Structure Engineering of Au–Pd Concave Triple-Octahedrons for Boosting Electrocatalytic Nitrate Reduction to Ammonia. *ACS Sustain. Chem. Eng.* **2023**, *11*, 1631–1637.

48. Luo, Y.; Chen, K.; Wang, G.; Zhang, G.; Zhang, N.; Chu, K. Ce-Doped MoS2-x Nanoflower Arrays for Electrocatalytic Nitrate Reduction to Ammonia. *Inorg. Chem. Front.* **2023**.

49. Liu, Q.; Liu, Q.; Xie, L.; Ji, Y.; Li, T.; Zhang, B.; Li, N.; Tang, B.; Liu, Y.; Gao, S.; Luo, Y.; Yu, L.; Kong, Q.; Sun, X. High-Performance Electrochemical Nitrate Reduction to Ammonia under Ambient Conditions Using a FeOOH Nanorod Catalyst. *ACS Appl. Mater. Interfaces* **2022**, *14*, 17312–17318.

50. Wu, K.; Sun, C.; Wang, Z.; Song, Q.; Bai, X.; Yu, X.; Li, Q.; Wang, Z.; Zhang, H.; Zhang, J.; Tong, X.; Liang, Y.; Khosla, A.; Zhao, Z. Surface Reconstruction on Uniform Cu Nanodisks Boosted Electrochemical Nitrate Reduction to Ammonia. *ACS Mater. Lett.* **2022**, *4*, 650–656.

51. Yang, J.; Qi, H.; Li, A.; Liu, X.; Yang, X.; Zhang, S.; Zhao, Q.; Jiang, Q.; Su, Y.; Zhang, L.;Li, J.-F.; Tian, Z.-Q.; Liu, W.; Wang, A.; Zhang, T. Potential-Driven Restructuring of Cu Single Atoms to Nanoparticles for Boosting the Electrochemical Reduction of Nitrate to Ammonia. *J. Am. Chem. Soc.* **2022**, *144*, 12062–12071.

52. Santos, E.; Pötting, K.; Lundin, A.; Quaino, P.; Schmickler, W. Hydrogen Evolution on Single-Crystal Copper and Silver: A Theoretical Study. *ChemPhysChem* **2010**, *11*, 1491–1495.

53. Touzé, E.; Cougnon, C. Study of the Air-Formed Oxide Layer at the Copper Surface and Its Impact on the Copper Corrosion in an Aggressive Chloride Medium. *Electrochim. Acta* **2018**, *262*, 206–213.